

Prying eyes on radio skies

Pushing the high-resolution low-frequency frontier with LOFAR

Proefschrift

ter verkrijging van
de graad van doctor aan de Universiteit Leiden,
op gezag van rector magnificus prof.dr.ir. H. Bijl,
volgens besluit van het college voor promoties
te verdedigen op donderdag 11 april 2024
klokke 13:45 uur
door

Frits Sweijen

geboren te Drachten, Nederland
in 1994

Promotor: Prof.dr. H. J. A. Röttgering

Co-promotor Dr. R. J. van Weeren

Promotiecommissie:

Prof.dr. I. A. G. Snellen

Prof.dr. K. H. Kuijken

Dr. L. K. Morabito (Durham University)

Prof.dr. R. Morganti (University of Groningen)

Dr. A. R. Offringa (ASTRON)

Prof.dr. R. A. Windhorst (Arizona State University)

ISBN: 000-00-0000-000-0

Front cover: the widefield radio image of the Lockman Hole field produced as part of this thesis. The left half is at the resolution of the Dutch array. The right half is at the resolution of the international array.

Rear cover: a contour image of 3C 295 as seen by the international radio telescope at sub-arcsecond angular resolution.

Front and back cover designed by the author.

Contents

1	Introduction	9
1.1	Discovering electromagnetic waves	9
1.2	The dawn of Radio astronomy	10
1.3	A zoo of radio sources	11
1.4	Radio telescopes and interferometry	17
1.4.1	Systematic surveys of the radio sky	20
1.4.2	Very long baseline interferometry	21
1.4.3	LOFAR	23
1.5	In this thesis	26
1.6	Outlook to the future	27
2	Technical primer	41
2.1	Interferometric imaging	41
2.1.1	Gridding	43
2.1.2	Deconvolution	43
2.2	Interferometric calibration	45
2.2.1	Systematic effects	47
2.2.2	Telluric effects	48
2.2.3	Direction-dependent effects and self-calibration	50
2.2.4	LOFAR calibration	51
3	High-resolution international LOFAR observations of 4C 43.15 – Spectral ages and injection indices in a high-z radio galaxy	63
3.1	Introduction	63
3.2	Observations	65
3.3	Data reduction	66
3.3.1	Dutch LOFAR calibration	66
3.3.2	International LOFAR calibration	67
3.3.3	LOFAR self-calibration	69
3.3.4	Archival VLA recalibration	72
3.3.5	Resolution matching and astrometric corrections	72
3.3.6	Spectral modelling	73
3.4	Results	74
3.4.1	A GHz steep-spectrum core	74
3.4.2	ILT radio morphology and measurements	74

3.4.3	Spectral index maps and model fitting	75
3.5	Discussion	76
3.5.1	What drives the lobe difference?	78
3.5.2	Core spectral index	79
3.5.3	Magnetic field strength	79
3.5.4	The $\alpha - z$ correlation	80
3.6	Conclusion	81
3.7	Acknowledgements	82
4	Deep sub-arcsecond widefield imaging of the Lockman Hole field at 144 MHz using the International LOFAR Telescope	93
4.1	Methods	97
4.1.1	Observation	97
4.1.2	Calibration and imaging	97
4.1.3	Source detection and catalogues	102
4.1.4	Astrometric corrections	102
4.1.5	Smearing	102
4.1.6	Flux scale corrections	103
5	Piercing the dusty veil of hyper-luminous infrared galaxies: Sub-arcsecond 144MHz ILT observations of HLIRGs in the Lockman Hole	113
5.1	Introduction	114
5.2	Data	116
5.2.1	Radio data	116
5.2.2	HLIRG sample	116
5.3	Methods	117
5.3.1	Radio excess	118
5.4	Results	118
5.4.1	Fraction of radio detections, brightness temperature	118
5.4.2	Brightness temperature compared to SED fitting	120
5.4.3	Brightness temperature compared to radio excess	123
5.4.4	Brightness temperature compared to IRAC detections	123
5.5	Discussion	126
5.5.1	Sensitivity to extended source structure and completeness and detection bias	129
5.5.2	Addressing the tension between HLIRGs and galaxy formation models	129
5.5.3	Brightness temperature as a dust-unobscured tracer of AGN activity	130
5.5.4	Co-evolution of black hole growth and star formation	131
5.6	Conclusion	132
5.7	Other code-model combinations	134
6	A low-frequency size distribution of radio galaxies in the Lockman hole	149
6.1	Introduction	150
6.2	Data	153
6.2.1	Radio data	153
6.2.2	Sample selection	154

6.3	Methods	155
6.3.1	Flood-fill size estimates	155
6.3.2	Curve-of-growth estimate	156
6.3.3	Gaussian fitting estimate	156
6.3.4	Visual inspection and cross-check	157
6.3.5	Down-scattering sources without reliable higher resolution fits	157
6.4	Results	158
6.4.1	Angular size distribution and flux density versus angular size	158
6.4.2	Radio power vs linear size	159
6.5	Discussion	159
6.5.1	Comparison with literature	159
6.5.2	Recovery of (diffuse) emissions	163
6.5.3	Definitions of size	166
6.6	Conclusions	166
6.7	Derivation of the size limits given a surface brightness limit	168
	Popular scientific summary	179
	Populairwetenschappelijke samenvatting	187
	List of publications	195
	Curriculum Vitae	199
	Acknowledgements	201

CONTENTS

CHAPTER 1

Introduction

You write something that is at the boundaries of your knowledge and call that “introduction”.

– M. S. S. L. Oei, 2023

Low-frequency radio astronomy explores some of the last electromagnetic waves that can still reach the Earth’s surface. For the longest part of human history, our studies of the night sky were limited by what our eyes could see. With the advent of photographic plates and cameras, we could leverage long exposures to capture objects invisible to even the best human eyes, but we remained tethered to but a sliver of the full electromagnetic spectrum. Staying within a single waveband is almost unthinkable these days. In less than a century astronomy has grown into a multi-spectral science. Each part of the electromagnetic spectrum, from the lowest frequency radio emission to the highest frequency gamma rays, tells its own story about the objects in the Universe that emitted them. But change can be slow, and new ideas may not be welcomed at first. Radio astronomy was no exception.

In this thesis, we explore the low-frequency radio sky in the hitherto largely unexplored parameter space of sub-arcsecond angular resolution resolving power with a survey-oriented twist to it. First, we briefly recollect the history

1.1 Discovering electromagnetic waves

At the forefront of radio astronomy is the discovery of extraterrestrial radio emission by Karl Guthe Jansky in the 1930s, but radio waves themselves have some history before that moment. We go back in time to 1846. In May of that year Michael Faraday published his “*Thoughts on Ray-vibrations*” (Faraday, 1846b) where he speculates about the nature of light (or “*radiant phaenomena*” as he calls it), pondering a wave-like nature of its propagation. Just under two decades later in 1865, James Clerk Maxwell published his “*dynamical theory of the electromagnetic field*” (Maxwell, 1865). Through his derivations, he mathematically demonstrated that electromagnetic disturbances would propagate as a wave. Not only that, the derived velocity at which these waves would propagate was in wondrous agreement with the experimentally measured speed of light. With a theory that predicted the existence of electromagnetic waves in place, only experimental evidence for their existence was missing.

Heinrich Hertz is the name that comes up most often when thinking about experimentally verifying the existence of EM waves. His publications provided us with the definitive proof that they existed, but others before him described experiments on how they could be generated, observations of sparks magnetising metal across thin air or even came close to rivalling Hertz’s discovery (Susskind, 1964). One such individual

was Sir Oliver Lodge. After he presented his experiments at the 1888 meeting of the British association in Bath, it became clear that he and Hertz had similarly proven the existence of em waves (Science., 1889). Lodge continued to build on Hertz's work by showing that, just like light as we knew then, these EM waves could be manipulated with lenses (Lodge et al., 1888). With this work he also discovered the so-called Hertzian dipole, finding that half-wavelength antennas made much better radiators (Garratt, 1994). Amusingly, no practical application of this wireless transmission was thought of at the time (Burns et al., 2004). A rich history of telecommunications unfolded after these discoveries, but we leave that for the interested reader to pursue on their own. It is from practical issues in the telecommunications industry that radio astronomy spuriously emerged.

1.2 The dawn of Radio astronomy

Karl G. Jansky is probably the most famous name around in radio astronomy. Jansky joined Bell Laboratories as a telecommunications engineer, where he was initially tasked with investigating sources of noise that could hinder telecommunications. For this purpose, he built a large rotating structure, as seen in Fig. 1.1, that allowed him to receive radio signals from different directions. The long antennas were sensitive to radio signals with a frequency of 20.5 MHz (corresponding to a wavelength of 14.6 m). His measurements revealed three sources of noise: local thunderstorms, distant thunderstorms and "*a steady hiss type static of unknown origin*" (K. Jansky, 1932). Perhaps even more surprising, this hiss appeared periodically, approximately every 24 hours. Although first thought to be associated with the Sun, more data revealed that it was associated with a fixed position among the stars (K. G. Jansky, 1933b). Only half a year later, Jansky published a follow-up study pinpointing the disturbance's position to 18 hours in right ascension and -20 degrees in declination (K. G. Jansky, 1933a): the galactic centre.

Not getting much traction, it took several years before another crucial measurement at radio frequencies would be taken. There was good reason for not seeing much merit in observations at radio wavelengths. Radio frequencies were already absurdly low frequencies in astronomical terms, which still occupied itself with little more than visible light at a few hundred nanometres, and Jansky's measurements were taken at just 23 MHz. That is low even in modern radio astronomical terms. At such low frequencies, Planck's law for thermal black-body radiation predicts a minuscule brightness compared to optical wavelengths, so it was not expected to be of much astronomical interest.

Nonetheless, Jansky's discovery grabbed the interest of Grote Reber. He started his measurements at a relatively high frequency of 3.3 GHz for both a stronger signal (thermal black-body radiation would be brighter at higher frequencies after all) and higher resolving power. Faced with a non-detection, he deployed a more sensitive detector at 900 MHz, but to no avail either. Two detections were finally made with an even more sensitive detector operating at a frequency of 162 MHz: one "*towards the Milky Way*", confirming Jansky's detection, and one coming "*from the great nebula in An-*

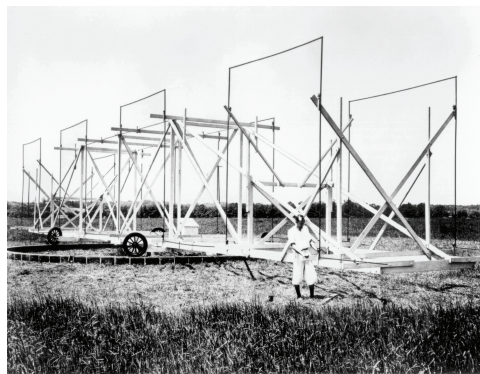


Figure 1.1: Karl Jansky at the telescope he built and used to study the origin of the noise on communication lines. Credit: NRAO/AUI/NSF

dromeda" (Reber, 1940). The wider astronomical community remained sceptical about the use of radio wavelengths, but the seeds were planted.

In the 1940s other sources of radio emission were started to be discovered. Hey et al., 1946b conducted a survey of the radio sky at a frequency of 64 MHz. This frequency was a compromise between signal strength, which increased towards lower frequencies, and angular resolution, which increased towards higher frequencies. As before, the strongest signal came from the Scorpio-Sagittarius region. They also noted another source close to Reber's "towards Andromeda" position, which they narrowed down to a location in Cygnus. Using the famous "single-dish cliff-side interferometer" approach by Pawsey et al., 1946, it was localised on the sky and constrained to a size of less than 8 arcminutes by Bolton et al., 1948b; Bolton et al., 1948a. Finally, Bolton, 1948 published the discovery of six new "discrete sources of radio noise", among which the famous radio sources Cygnus A (already discussing a double component nature), Taurus A, Virgo A (initially identified as Coma Berenices A, Robertson et al., 2014), Hercules A and Centaurus A. The addition "A" means they were the first radio source discovered in that constellation. These sources are informally often called "the A-team", but unfortunately for modern radio astronomers, they do more harm than good when they encroach on a telescope's field of view. Three of these sources were traced back to optical counterparts by Bolton (Bolton et al., 1949a; Bolton et al., 1949b). Although arguably by guessing and intuition (see Robertson et al., 2014, and references therein), he identified Taurus A with the Crab Nebula, Centaurus A with NGC 5128 and Virgo A with M 87. It were the more precise position and angular size measurements from Mills, 1952a and Mills, 1952c that solidified the identifications of these counterparts. The discovery of these sources and their (still contested) extragalactic nature rang the bell for a new era in astronomy.

1.3 A zoo of radio sources

A mystery that remained was what these radio sources were. The Crab Nebula was an already well-known galactic object, leaving no doubt about the association with Taurus A, but Bolton and his peers were apprehensive towards associating Centaurus A and Virgo A with NGC 5128 and M 87, respectively, given that their extra-galactic nature was not yet proven beyond all doubt (Bolton et al., 1949b; Robertson et al., 2014).

Neither of these objects have been resolved into stars, so there is little definite evidence to decide whether they are true extragalactic nebulae or diffuse nebulosities within our own galaxy. If the identification of these objects with the discrete sources of radio-frequency energy can be accepted, it would tend to favour the latter alternative, for the possibility of an unusual object in our own galaxy seems greater than a large accumulation of such objects at a great distance. – Bolton et al., 1949b

Another aspect that made source association difficult was the generally imprecise positions of the radio sources. Though impressive for the time, one can only do so much in terms of optical counterpart identification with a precision of a few arcminutes on radio source position measurements. The positions of Cygnus A and Cassiopeia A were measured more accurately by F. G. Smith (1951), narrowing it down to within 1 arcmin in declination and 15 arcseconds in right ascension. This allowed Baade et al. (1954a) to associate clear optical counterparts. Dewhirst (1959) discusses optical counterparts to 15 sources in the 3C catalogue, finding all of them to be associated with elliptical or peculiar galaxies (apart from Taurus A),

some of them in clusters or groups. They also already discussed that the radio emission could be related to a particular phase in the formation of those clusters. The large discrepancy between the radio size and the optical size led to the suggestion that the radio emission may come from a different, more complex double-component morphology instead of following the “true size” of the galaxy. Progress in our understanding of radio sources made a jump when in the early 1960s redshifts of the optical counterparts to bright radio sources in the 3C survey were being determined.

Quasars

3C 295’s redshift was measured by Minkowski (1960) to be $z = 0.4614$, associated with a cluster of galaxies. While 3C 295 was likened to Cygnus A, other sources like 3C 48, 196 and 286 were found to have “stellar” counterparts (Matthews et al., 1963). Lunar occultations allowed Hazard et al. (1963) to measure the position of 3C 273 with arcsecond accuracy, which allowed M. Schmidt (1963) to measure a spectrum of the only object near that position: a 13th magnitude “star” and the associated, now well-known, jet of optical synchrotron emission. Hydrogen lines in the spectrum revealed that this object resided at $z = 0.158$.

Only the detection of an irrefutable proper motion or parallax would definitely establish 3C 273 as an object within our Galaxy. At the present time, however, the explanation in terms of an extragalactic origin seems most direct and least objectionable. –M. Schmidt, 1963

Based on Schmidt’s results, Greenstein et al. (1963) interpreted 3C 48’s spectrum similarly as redshifted emission lines and estimated its redshift to be $z = 0.3675$. Both results from M. Schmidt (1963) and Greenstein et al. (1963) suggested that these “quasi-stellar radio sources” were the nuclear regions of galaxies. The short-hand term *quasar* was subsequently introduced by Chiu (1964). What the physical emission mechanism responsible for the radio waves we detect was, remained unclear, but it was obvious from the measurements by Reber (1940) already that it could not have a thermal origin. Alfvén et al. (1950) were the first to predict that charged particles could be accelerated in the magnetic field of a “radio star” and radiate at observable wavelengths. A few years later Shklovsky, 1953 published a theory of synchrotron radiation. Measurements of strongly polarised emission of the Crab Nebula (J. H. Oort et al., 1956) and M87’s jet (Baade, 1956) were seen as evidence supporting this synchrotron emission as the main emission mechanism behind radio sources. These ideas were expanded on to form more elaborate theories of non-thermal emission processes in radio sources (Kardashev, 1962; Pacholczyk, 1970; Jaffe et al., 1973). It allowed for the break in the spectrum of Cygnus A to be explained naturally in terms of energy losses in the relativistic electron population (Kardashev et al., 1962) and these models are still used to date in spatially-resolved spectral studies of radio sources (see e.g. Hardcastle et al., 2013; Jeremy J. Harwood et al., 2013).

With an emission mechanism finally identified, it came down to identifying the underlying driver. Possibilities like the collapse of massive or numerous stars, emitting gas clouds or other non-thermal sources were explored (Shklovsky, 1964; Burbidge, 1970; M. J. Rees, 1971), but crucial to progressing our understanding was the idea that quasars might be the drivers behind the powerful radio galaxies observed, by ejecting clouds of relativistic particles (Martin Ryle et al., 1967) and that varying the timescale between episodes of activity could drastically change their appearance across parts of the electromagnetic spectrum (M. Ryle, 1968). One of the major remaining open questions was how those bursts of intense activity would be produced. Quasars release an enormous amount of energy, outshining their host galaxy with energy produced in a relatively tiny nuclear region. At the end of the 1960s, Lynden-Bell (1969) proposed that such a small region would be possible:

[discussing black holes] We would be wrong to conclude that such massive objects in spacetime should be unobservable, however. It is my thesis that we have been observing them indirectly for many years. –Lynden-Bell (1969)

The idea of an accretion disk funnelling material to a black hole in the nucleus, which would ultimately release large amounts of energy and eject material out of the galaxy took shape. In this paradigm, quasars represent a phase of rapid accretion.

Powerful radio galaxies

A plethora of labels have since been assigned to radio sources after the discovery of quasars. The catch-all term for any radio source associated with black hole activity from the centres of galaxies has become *active galactic nucleus* (AGN). Among the AGNs, there are many different types of objects based on various properties such as emission lines, jet or lobe morphology, spectral properties or combinations thereof. An extensive review of AGN nomenclature, summarising many of the labels we attach to them, is given by P. Padovani et al. (2017) in table 1.

Among the compact radio objects one finds, for example, the quasars, blazars, peaked spectrum (PS) sources and compact steep spectrum (CSS) sources (Christopher P. O’Dea et al., 2021) or ultra-steep spectrum (USS) sources (De Breuck et al., 2000). PS sources are objects that have peaked radio spectra. CSS sources are compact objects with a steep spectral index $\alpha \lesssim -0.5$ (Christopher P. O’Dea et al., 2021). The USS sources have even steeper spectral indices of $\alpha \lesssim -1.0$ or steeper (e.g. Roettgering et al., 1994; De Breuck et al., 2000). Finally, there are the Seyfert galaxies, which are similar to quasars and are characterised by intense nuclear emission with strong emission lines present (Seyfert, 1943). The presence of emission lines is also used in general, to distinguish between high-excitation and low-excitation sources (Heckman et al., 2014).

Sources that launch powerful jets and have lobe structures were originally labelled “Class I” or “Class II” by Fanaroff et al. (1974), typically called FR Is and FR IIs nowadays. FR Is have most of their intensity close to the centre, gradually fading towards the edges (edge-darkened). FR IIs are the opposite and have most of their intensity in hotspots and lobes towards the edges (edge-brightened). Two classic examples are 3C 31 for FR Is and Cygnus A for FR IIs. This distinction seemed to not be purely morphological, and their host galaxies appeared to inhabit different parts of parameter space in terms of optical magnitude or radio power (e.g. Fanaroff et al., 1974; Ledlow et al., 1996; Capetti et al., 2017a; Capetti et al., 2017b) or accretion mode Heckman et al., 2014. Whether this dichotomy is real, what its driver would be, or whether it is due to selection effects is actively debated in the literature, however. The discovery of hybrid morphology sources displaying both morphologies for either jet (Gopal-Krishna et al., 2000; Jeremy J Harwood et al., 2020), a population of “FR 0”s that have properties similar to FR Is, yet are more compact (Baldi et al., 2015), distinct sources in general (e.g. Mingo et al., 2019) and a large population of low-luminosity FR IIs (e.g. Mingo et al., 2022), for example, at the very least paint a picture that is more complicated than the original divide.

Radio-quiet AGNs and star-forming galaxies

The type of radio sources discussed above fall in the group of “powerful radio AGNs”. To help quantify this further, the concept of “radio loudness” was introduced. This qualifier takes on various forms in the literature—such as a ratio of radio-to-optical flux (Maarten Schmidt, 1970; K. I. Kellermann et al., 1989), a radio power threshold (Peacock et al., 1986), radio-to-x-ray luminosity ratio (Terashima et al., 2003) or

showing (large-scale) relativistic jets (Hardcastle et al., 2019)—but all manifest as some criterion for the radio emission that if met makes them “radio loud” (RL) and otherwise “radio quiet” (RQ).

The low-power radio sources are not just RQ AGNs, however, but also star-forming galaxies (SFGs). While RL AGNs form the dominant population of radio sources above $S_{150\text{MHz}} \sim 1 \text{ mJy}$, below this flux density the SFGs and RQ AGNs take over (P N Best et al., 2023) as the dominant population. For the former the emission, isn’t driven by black hole activity in the nucleus, but by star formation activity. This originates from free-free emission ($s_\nu \propto \nu^{-0.1}$) from HII regions and synchrotron radiation ($s_\nu \propto \nu^{-0.7}$) from, for example, relativistic electrons accelerated by supernova explosions (Condon, 1992; Klein et al., 2018).

Lacking a strongly dominating radio component, RQ AGNs provide a valuable laboratory for studying weak jets, winds and star formation (see e.g. The review by Panessa et al., 2019). At the same time, lacking strong extra-galactic jets as identifying features makes it hard to separate the two in spatially unresolved observations. This makes it challenging to determine the extent of the AGN’s contribution to the radio emission in radio surveys that do not spatially resolve them. One way to do so is through high-resolution radio observations. Those allow precise association of radio emission with the nucleus. Additionally, one can calculate a threshold for the maximum brightness star formation would be able to reach (e.g. Condon, 1992), by calculating the brightness temperature. This is the temperature an object would have, assuming it is all black-body radiation. A radio-emitting component exceeding this threshold would therefore likely be AGN driven. This approach is used in Chapter 5 to identify AGNs in hyperluminous infrared galaxies, which are presumed to have both extreme star formation and an AGN.

Table 1.1: A summary of radio surveys below 1 GHz with published catalogues of discrete radio sources.

Year	No. sources	Frequency	Survey	References
1933	1	23.5 MHz	Galactic centre	K. G. Jansky, 1933a
1940	2		Andromeda	Reber, 1940
1946	3		Cygnus A	Hey et al., 1946a
1948	9		Tau A, Cen A, Vir A, Her A	Bolton, 1948 ¹
1950	9		M31 again	Brown et al., 1950
1953	23			Hanbury Brown et al., 1953b
1955	38		Jupiter, IAU list of <i>verified</i> sources	Pawsey, 1955
1955	1936		2C, $-38^\circ < \delta < 83^\circ$	Shakeshaft et al., 1955 ²
1958	471	159 MHz	3C, $-22^\circ < \delta < 71^\circ$	Edge et al., 1958
1958	1,159	85.5 MHz	$-20^\circ < \delta < 10^\circ$, $00\text{h} < \alpha < 08\text{h}$	Mills et al., 1958
1961	910		4C early results	Scott et al., 1961
1962	328	178 MHz	3CR catalogue	Bennett et al., 1962
1963	–		3C 48, 3C 273 get redshifts	
1964	297	400 MHz	Parkes Radio Catalogue $-20^\circ < \delta < -60^\circ$	Bolton et al., 1964
1965	247	400 MHz	Parkes Radio Catalogue $-60^\circ < \delta < -90^\circ$	Price et al., 1965
1965	1219	178 MHz	4C, $20^\circ < \delta < 40^\circ$	Pilkington et al., 1965
1966	564	408 MHz	Parkes Radio Catalogue $0^\circ < \delta < 20^\circ$	Day et al., 1966
1966	628	408 MHz	Parkes Radio Catalogue $0^\circ < \delta < -20^\circ$	Shimmins et al., 1966
1966	1,069	48 MHz	Mullard Radio Astronomy Observatory, $\delta > -10^\circ$	Williams et al., 1966
1967	3,624	178 MHz	4C, $-07^\circ < \delta < 20^\circ$ and $40^\circ < \delta < 80^\circ$	Gower et al., 1967
1968	297	635 MHz	Parkes Radio Catalogue $20^\circ < \delta < 27^\circ$	Shimmins et al., 1968
1969	1,780	408 MHz	Parkes Radio Catalogue $20^\circ < \delta < -90^\circ$	Ekers, 1969
1974	2,882		Compilation of sources thusfar	Véron et al., 1974
1981	12,141	408 MHz	Molongolo Reference Catalogue	Large et al., 1981
1983	–	178 MHz	3CRR catalogue	

1985	1,761	151 MHz	6C I, $\delta > 80^\circ$	Baldwin et al., 1985
1988	8,278	151 MHz	6C II, $30^\circ < \delta < 51^\circ$, $08\text{h}30\text{m} < \alpha < 17\text{h}30\text{m}$	S. E. G. Hales et al., 1988
1990	8,749	151 MHz	6C III, $48^\circ < \delta < 68^\circ$, $05\text{h}25\text{m} < \alpha < 18\text{h}17\text{m}$	S. E. G. Hales et al., 1990
1990	5,859	38 MHz	8C	N. Rees, 1990
1991	5,421	151 MHz	6C IV, $67^\circ < \delta < 82^\circ$, $00\text{h}00\text{m} < \alpha < 24\text{h}00\text{m}$	S. E. G. Hales et al., 1991
1993	3,458	151 MHz	6C V, $48^\circ < \delta < 68^\circ$, $01\text{h}34\text{m} < \alpha < 06\text{h}14\text{m}$ $48^\circ < \delta < 68^\circ$, $17\text{h}16\text{m} < \alpha < 20\text{h}24\text{m}$	S. E. G. Hales et al., 1993b
1993	6,752	151 MHz	6C VI, $30^\circ < \delta < 51^\circ$, $00\text{h}00\text{m} < \alpha < 09\text{h}05\text{m}$ $30^\circ < \delta < 51^\circ$, $22\text{h}00\text{m} < \alpha < 24\text{h}00\text{m}$	S. E. G. Hales et al., 1993c
1996	66,841	365 MHz	Texas 365 MHz survey, $-35.5^\circ < \delta < 71.5^\circ$	Douglas et al., 1996
1997	229,420	325 MHz	WENSS	Rengelink et al., 1997
1999	43,683	151 MHz	7C	McGilchrist et al., 1990; Visser et al., 1995; S. E. G. Hales et al., 2007 ³
2003	107,765	843 MHz	SUMMS	Mauch et al., 2003
2006	68,311	74 MHz	VLSS	A. S. Cohen et al., 2006
2014	92,964	74 MHz	VLSSr	Lane et al., 2014
2017	307,455	72 – 231 MHz	GLEAM, $\delta < 30^\circ$	Hurley-Walker et al., 2017
2017	623,604	150 MHz	TGSS ADR1, $\delta > -53^\circ$	Intema et al., 2017
2019	325,694	144 MHz	LoTSS DR1	Shimwell et al., 2019
2021	2,123,638	843 MHz	RACS, $-80^\circ < \delta < +30^\circ$	Hale et al., 2021
2022	4,396,228	144 MHz	LoTSS DR2	Shimwell et al., 2022

¹ Two unnamed detections remain debatable as to whether they were physical radio sources or artificial from e.g. side lobes.

² The 2C survey would later turn out to be unreliable, which led to a vast overestimate of the number of sources.

³ The 7C survey was published over multiple years.

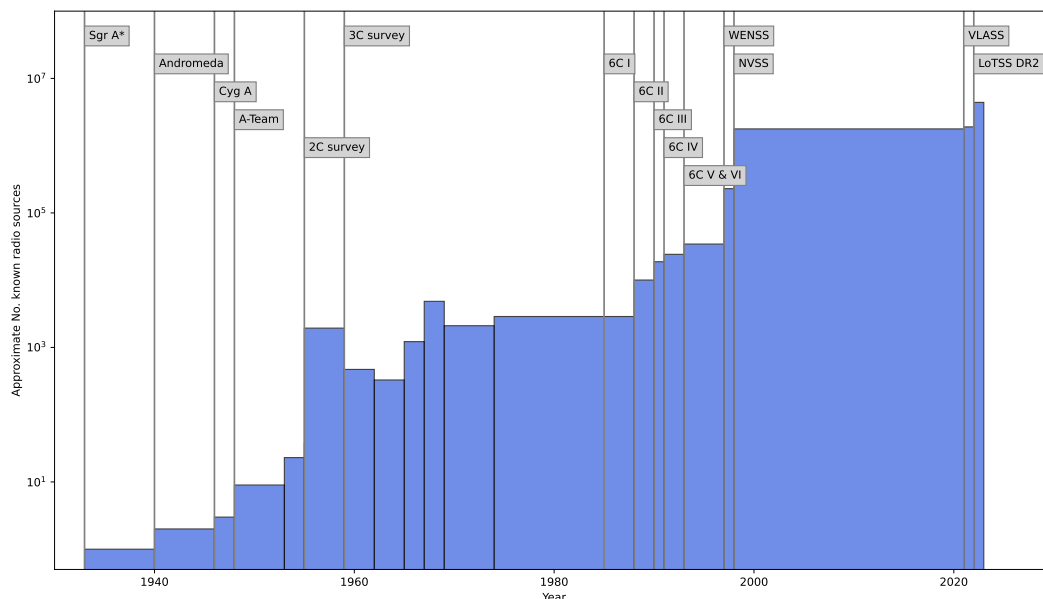


Figure 1.2: Table 1.1 visualised. The height of each bar indicates the number of known or published (once large surveys start going) sources and the width corresponds to the time between successive entries.

1.4 Radio telescopes and interferometry

Single-dish telescopes

Probably the simplest way of doing radio astronomy is to simply record the power received from the sky with an antenna. To make it more practical, such an antenna can be mounted at the focal point of a dish to record the radio power coming from a specific direction in the sky. The bane of single-dish radio telescopes, however, is the practical limit to their size that inadvertently limits their achievable angular resolution. For a given diameter D of a dish or mirror, the diffraction limit tells us that the angular resolution θ at an observing wavelength λ is given by

$$\theta = 1.22 \frac{\lambda}{D} \quad (1.1)$$

where the factor 1.22 comes from an Airy disk diffraction pattern. It becomes painfully clear why low-frequency radio telescopes suffer in the resolution department: the long observing wavelengths need to be offset by large dishes, a costly endeavour. Table 1.2 lists the diameters of significant single-dish radio telescopes. In the optical band, HST's diffraction limit is already around 50 mas with a relatively modest 2.4 m mirror. In comparison, even the *Five-hundred-meter Aperture Spherical radio Telescope* (FAST), with its massive 500 m dish making it the world's biggest single-dish radio telescope as of this moment, is limited to an angular resolution of just $50''$ in the best case scenario by Eqn. 1.1. Telescopes of such a size become impractical to build in the first place, but also exceed the practical limits for building a *steerable* telescope. Giant dishes like Arecibo and FAST implement a drift-scan approach. The secondary "mirror",

Table 1.2: Notable single-dish radio telescopes that are or have been used for astronomical purposes.

Telescope	Diameter [m]	Frequency [MHz]
Reber's dish	9.6	160, 910, 3300
Dwingeloo	25	1375 – 1425, 1580 – 1725
Murriyang	64	80 – 20,000
DSS-43	70	1628 – 27,000
Effelsberg	100	300 – 90,000
GBT	100 × 110	300 – 100,000
Arecibo	300	50 – 11,000
FAST	500	70 – 3000

where the receiver is housed, allows for some freedom in pointing the telescope, but they otherwise stare up and observe while the Earth's rotation makes the sky drift across their field of view. Radio astronomy thus needed a new approach to increase its resolving power and to start exploring the radio sky at a grander scale.

Interferometers

Some things are greater than the sum of their parts. If we can't build a single dish large enough for our needs, can we overcome that limitation by combining two or more of them? That is the basic premise of radio interferometry. Combine two waves and you get constructive or destructive interference increasing or decreasing the intensity of light, depending on the relative phase of the waves. The resulting patterns are called interference patterns or "fringes". That is what lies at the heart of interferometry. This idea was first put to astronomical use by Albert A. Michelson and Francis G. Pease to measure the diameter of the star Betelgeuse in 1920. In 1946 this was expanded to the radio domain by Martin Ryle and D. D. Vonberg to try and measure the radio size of Sunspots (M. Ryle *et al.*, 1946). Using two antennas they published two measurements: one where they were separated by 17 m and one with a separation of 140 m, which provided an angular resolution of 30 arcmin. An illustration of the antenna's sensitivity and the received signal is given in Fig. 1.3. Through clever exploitation of the fringe's behaviour as the antenna is moved across the source, they estimated an angular size of 10 arcmin for the emitting region. Additionally, over 90% of the radiation received during intense solar activity was found to be circularly polarised, supporting the idea that this emission was of non-thermal origin. This concludes one of the first, if not the first, low-frequency radio interferometric measurements of the sky.

Since this experiment, we have expanded interferometric arrays far beyond two antennas. In 1968 the *Westerbork Synthesis Radio Telescope* (WSRT) came online in Dwingeloo, The Netherlands. Operating at 1.4 GHz and consisting of 12 antennas with a diameter of 25 m, it was a revolutionary instrument for radio astronomy. Its maximum baseline of 1.6 km meant it could achieve an angular resolution of 24'' (Hogbom *et al.*, 1974). Soon after, in 1978, the *Very Large Array* (VLA) came online in New Mexico, USA. Its 27 movable 25 m antennas offer baselines of up to 36.4 km. This gives the array a 1.5'' resolving power at 1.4 GHz, going to sub-arcsecond levels at higher frequencies. Arrays like the WSRT and VLA, and many others, revolutionised radio astronomy. It was no longer confined to one-dimensional interference patterns and high-resolution images could now be made over large areas of the sky.

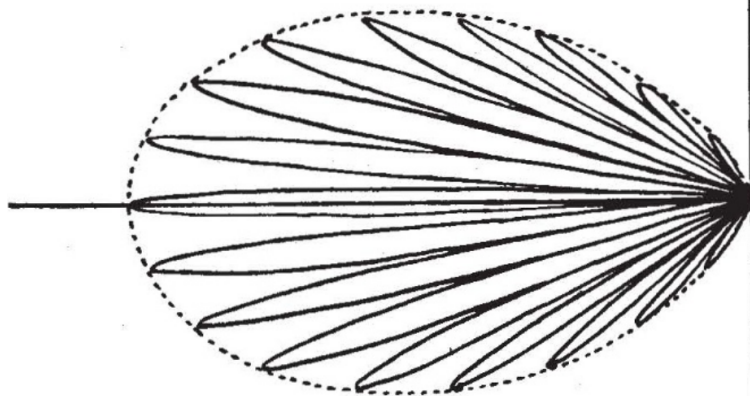


FIG. 1 POLAR DIAGRAM OF TWO 8-ELEMENT AERIAL SYSTEMS WITH SEPARATION OF 10λ

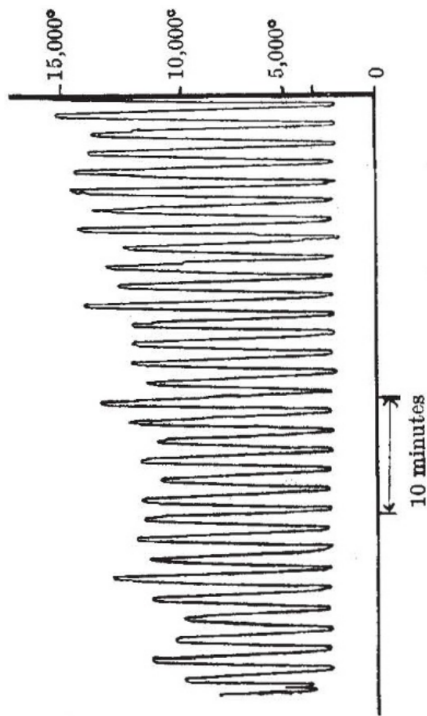


FIG. 3. RECORD OBTAINED WITH 140λ SEPARATION (JULY 26, 1946).

Figure 1.3: Figures 1 and 3 from M. Ryle et al., 1946 illustrating the sensitivity pattern of the antenna pair (*left*) and detected fringes during high solar activity (*right*). Figures reproduced with permission from Springer Nature.

1.4.1 Systematic surveys of the radio sky

During the 1950s interest in radio sources from an astronomical perspective gained traction and three major radio astronomy groups arose: Martin Ryle’s group in Cambridge, Bernard Lovell’s in Manchester and Joe Pawsey’s in Sydney, Australia. Results from early surveys sparked great debate and controversy between various groups and people about the reliability of the measurements and the credibility of the idea that “radio stars” might in fact be distant galaxies, for example, which was proposed by e.g. Mills, 1952b, but initially (heavily) opposed by others such as Bolton and Ryle (Goss et al., 2023).

One reason for such debates was that the results from radio surveys started challenging cosmological notions; notably, that of the Steady State model. Source counts that plot the observed number of sources as a function of flux density produced a slope that was inconsistent with the slope predicted by a Steady State cosmology, sparking debate (e.g. M. Ryle et al., 1955; Pawsey, 1957; Scott et al., 1961; Hoyle et al., 1961; Sciamia, 1963). A Steady State universe would have a constant density, so a possible explanation for the steep observed number counts was an evolution in density Davidson, 1961; Gower, 1966. While the first two iterations of Cambridge radio surveys had caveats, eventually M. Ryle et al., 1961 used the more reliable 4C survey (Scott et al., 1961) to find “conclusive evidence against the steady-state model”. This is just one example of the impact of radio astronomy on astronomy as a whole, but it is an important highlight of how exploring new parameter space can lead to profound new insights.

In Tab. 1.1, visualised in Fig. 1.2, we summarise some of the largest low-frequency radio surveys since Jansky first discovered galactic radio emission. At the end of the 1950s, we got one of the first reliable large radio surveys: the 3C survey at 159 MHz (Edge et al., 1958). This confusion-limited survey and its later revisions yielded the famous (and possibly equally notorious) “3C sources”. Soon after the 178 MHz 4C survey came about Pilkington et al., 1965; Gower et al., 1967 covering sources brighter than 2 Jy. For almost two decades this would remain the largest sample of radio sources until the 6C survey started in the 1980s (Baldwin et al., 1985). This remained the largest radio survey for another decade, before the Texas 365 MHz survey almost doubled the record with 66,841 sources. At the end of the millennium the famous surveys of today started taking shape. In 1997 the *Faint Images of the Radio Sky at Twenty-cm* (FIRST, R. L. White et al., 1997, 138,665 sources at first) and the *Westerbork Northern Sky Survey* (WENSS, Rengelink et al., 1997, 11,299 sources initially and ultimately 229,420 sources) surveys, conducted with the *vla* at 1.4 GHz and the WSRT at 325 MHz respectively, released large catalogues. Only a year later, this record was obliterated by the NRAO VLA Sky Survey (NVSS). This 1.4 GHz catalogue of the sky above declination -40° contains over 1.7 million sources. In terms of low-frequency surveys, however, interest waned. Not for a lack of scientific interest, but because higher frequency facilities were able to offer (much) higher angular resolution and were easier to calibrate due to lesser to little ionospheric effects. In the southern hemisphere the *Sydney University Molonglo Sky Survey* (SUMSS, Mauch et al. 2003) 843 mhz survey had a fairly high angular resolution, comparable to FIRST at $45'' \cos \delta$. The *Galactic and Extragalactic All-Sky MWA* (GLEAM, Hurley-Walker et al. 2017) survey pushed down to 200 MHz, but with an angular resolution of only $2'$. It wasn’t until the *TGSS Alternative Data Release 1* (TGSS ADR1, Intema et al. 2017) that a survey of the low-frequency sky with a reasonably high angular resolution of $25''$ became available. It covers 90% of the entire sky at a frequency 150 MHz, making it the largest radio survey in terms of sky area, containing over 600,000 sources. It is rivalled by the *Rapid ASKAP Continuum Survey* (RACS, Hale et al. 2021); another southern survey at a frequency of 887.5 MHz with over 2.1 million sources and the same angular resolution. The only other low-frequency survey that comes close is the recent second data release of the *LOFAR Two-metre Sky Survey* (LoTSS, Shimwell et al. 2022): a deep 144 MHz survey of the northern sky. With almost 4.4 million sources in the second data release, it is the

largest radio survey to date in terms of raw numbers and has an unprecedented resolution for low-frequency surveys of $6''$. With its pan-European baselines, it opens up possibilities for even higher resolution all-sky surveys at arcsecond and sub-arcsecond angular resolution.

1.4.2 Very long baseline interferometry

Physics does not favour radio astronomy below 1 GHz when it comes to resolution. As such, sub-arcsecond or higher angular resolutions require enormous baselines that approach notable fractions of the Earth's diameter. The use of long baselines to push the angular resolution to the highest regimes is aptly called *very long baseline interferometry*, or VLBI. Perhaps the most famous example of it by now is the *Event Horizon Telescope* (EHT) reaching micro-arcsecond resolution to image M87's black hole ([Event Horizon Telescope Collaboration et al., 2019](#)). The fact that radio telescopes can be separated by a mostly arbitrary distance allows VLBI to offer the highest angular resolution in astronomy.

For low-frequency instruments, long baselines practically become a necessity to compete with the (sub)-arcsecond angular resolution easily attained by telescopes operating at gigahertz frequencies and optical telescopes (with the help of adaptive optics). Unfortunately, for real-time correlation of the signals coming from a pair of antennas, it is important that phase stability is maintained over the connection between antennas, which becomes increasingly challenging over longer distances. With an unstable connection, signals can not be added coherently, causing decorrelation and information loss. A first design improvement to deal with this was described (and demonstrated) by [Hanbury Brown et al., 1952](#) at Jodrell Bank. Instead of transporting the incoming signal directly, a superheterodyne receiver was used to produce a low-frequency output that would be much easier to transmit over long distances. Their setup was subsequently used by [Jennison et al., 1953](#) to derive the resolved structure of Cygnus A for the first time, as shown in [Fig. 1.4](#). Combined with the findings that radio sources appeared to have compact structure on arcsecond scales or smaller (e.g. [L. R. Allen et al., 1960](#)), it did not take long for the first survey-oriented long baseline interferometry studies to start ([L. R. Allen et al., 1962b](#); [Elgaroy et al., 1962](#)).

Having to record antenna signals at a central location, or at all, becomes another problem once distances become large enough. To overcome this, [Brown et al., 1954](#) had proposed a different kind of interferometer:

A new type of interferometer for measuring the diameter of discrete radio sources is described and its mathematical theory is given. The principle of the instrument is based upon the correlation between the rectified outputs of two independent receivers at each end of a baseline

...

The most obvious advantage of the new instrument is that the technical problem of combining the signals from two widely spaced receivers is relatively simple, since there is no need to maintain the high degree of phase stability in the link which is required if the radio-frequency phase of the signals must be preserved. – Brown et al., 1954

Recording signals separately removes the need for a stable real-time link between the antennas and the correlator during the observation, or even a link at all (sometimes called “offline correlation”). A development that was foreshadowed in their concluding remarks

Indeed it should be possible to eliminate the transmission link altogether and to record the low-frequency outputs of the two receivers on, say, magnetic tape. The records could be compared subsequently in a correlator and it seems that by the use of this technique a baseline of indefinite length could be used. – Brown et al., 1954

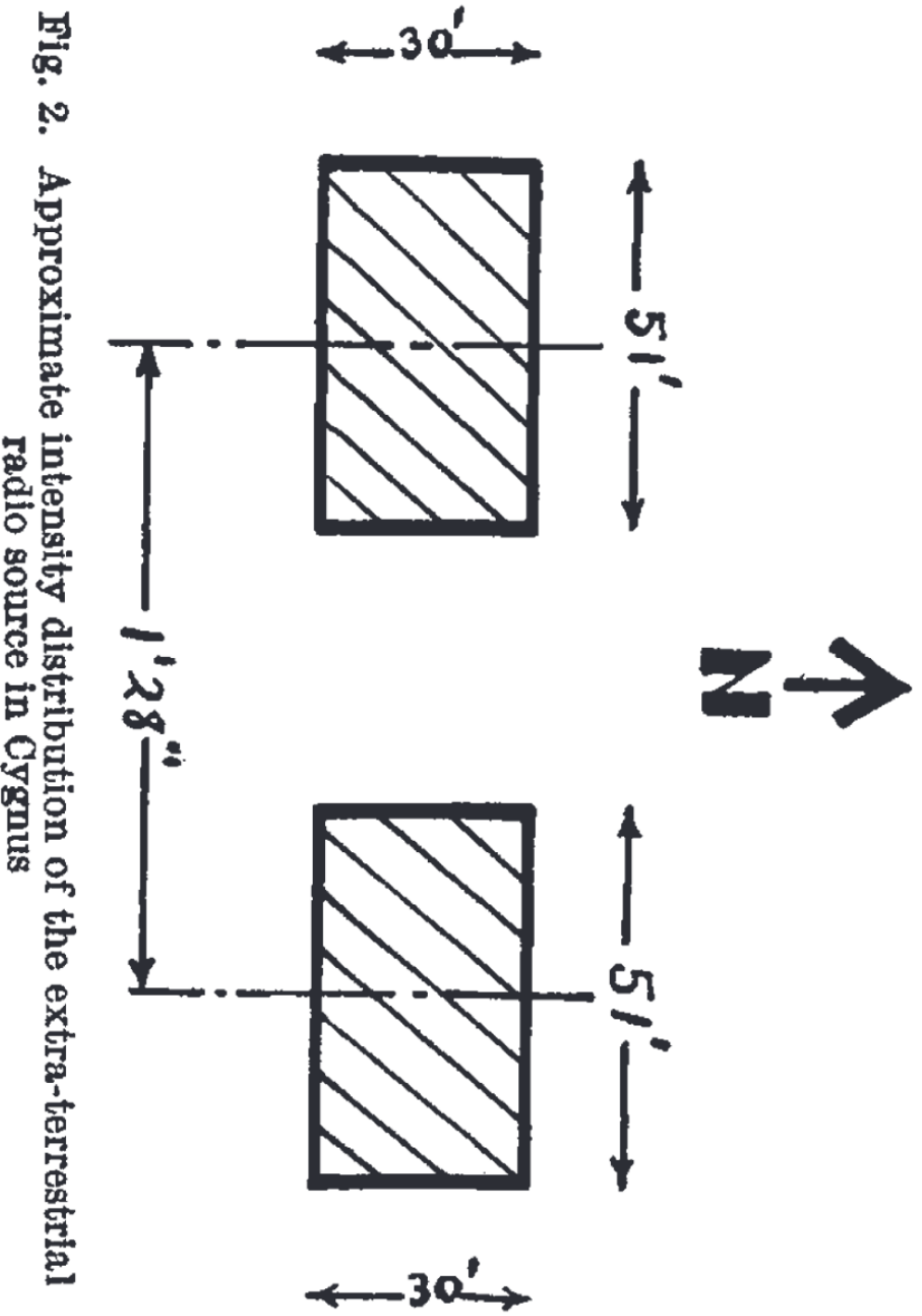


Fig. 2. Approximate intensity distribution of the extra-terrestrial radio source in Cygnus

Figure 1.4: The first resolved intensity distribution of Cygnus A as derived by Jennison et al., 1953. Figure reproduced with permission from Springer Nature.

A proof of concept was demonstrated by [Jennison et al., 1956a](#) who used it to measure the angular size of the Sun. Afterwards, the full-scale instrument was built and it was used to measure angular sizes of Cyg A and Cas A ([Jennison et al., 1956b](#)). It was further demonstrated in practice later (e.g. [Bare et al., 1967](#)). During the 1960s this technique was used to study decameter bursts from Jupiter ([Carr et al., 1970](#)), going one step further and eliminating the real-time link between the antennas entirely. Their setup was described as:

We recorded on tape the outputs of the receivers at the ends of the baseline to eliminate the necessity for real-time transmission of data over the length of the baseline. The interferometer was a VLBI in the technical sense; it recorded the two receiver outputs separately. The playback oscillograms of the Jupiter noise from the two tapes were aligned with the aid of time marks which had also been recorded. – Carr et al., 1970

These experiments also immediately set the record for decameter VLBI¹ that still stands today: a 7900 km baseline at a frequency of 18 MHz. Note that this instrument was an “intensity interferometer” and thus only recorded the total power. [B. Clark, 1968](#) later discussed a middle ground between such an interferometer and a full correlating interferometer, allowing for better performance while still lowering the required phase stability. During the same period, other experiments demonstrated the technique at a higher frequency of 480 MHz ([Brotten et al., 1967a](#); [Brotten et al., 1967b](#)) using baselines as long as 3,074 km and 6,833 km. These high resolutions allowed direct measurements of sources that were inferred to be compact from interplanetary scintillation measurements ([M. H. Cohen et al., 1967](#)). A plethora of high-resolution studies followed from these advances, studying burst phenomena on Jupiter ([Carr et al., 1970](#); [Ratner, 1976](#)), variable sources ([Readhead et al., 1977](#)), compact sources ([Wilkinson et al., 1979](#)) and, of course, the resolved structure of radio galaxies and quasars ([Linfield et al., 1984](#); [Mutel et al., 1986](#); [Ananthakrishnan et al., 1989](#)). For a more in-depth discussion about the developments of high-resolution radio astronomy the reader is referred to more extensive reviews by [K. I. Kellermann et al., 2001](#) and [B. G. Clark, 2003](#), for example.

Offline correlation is still employed today for global VLBI observations, such as those with the EHT for example, but the advent of high-speed internet connections across the world is enabling the move to more and more real-time correlation ([M. Garrett, 2007](#); [Paragi, 2015](#)). Finally, the already ambiguous term “very long” will only grow more ambiguous. What defines very long? pushing beyond the status quo of instruments? Physically long in terms of meters or long with respect to the wavelength? Historically the boundary between VLBI and regular “long baseline interferometry” seems to be the point at which data is no longer correlated in real-time, but as technology advances and interferometric arrays grow bigger this line continues to blur. One such array is the *low frequency array* (LOFAR).

1.4.3 LOFAR

At the start of the 1990s, results using VLA observations at 74 MHz demonstrated the feasibility of sensitive high-resolution observations at meter wavelengths ([Kassim et al., 1993](#)). This led to LOFAR being proposed to revolutionise low-frequency radio astronomy. It was realised about two decades later ([Haarlem et al., 2013](#)). The full telescope is now the *International LOFAR Telescope* (ILT), with stations throughout Europe. LOFAR stations are split into three groups: core stations, remote stations, and international stations. Stations are named with two letters followed by three digits, such as CS003HBA0, RS210HBA

¹As well as for low-frequency VLBI in general to my knowledge, at the moment of writing.

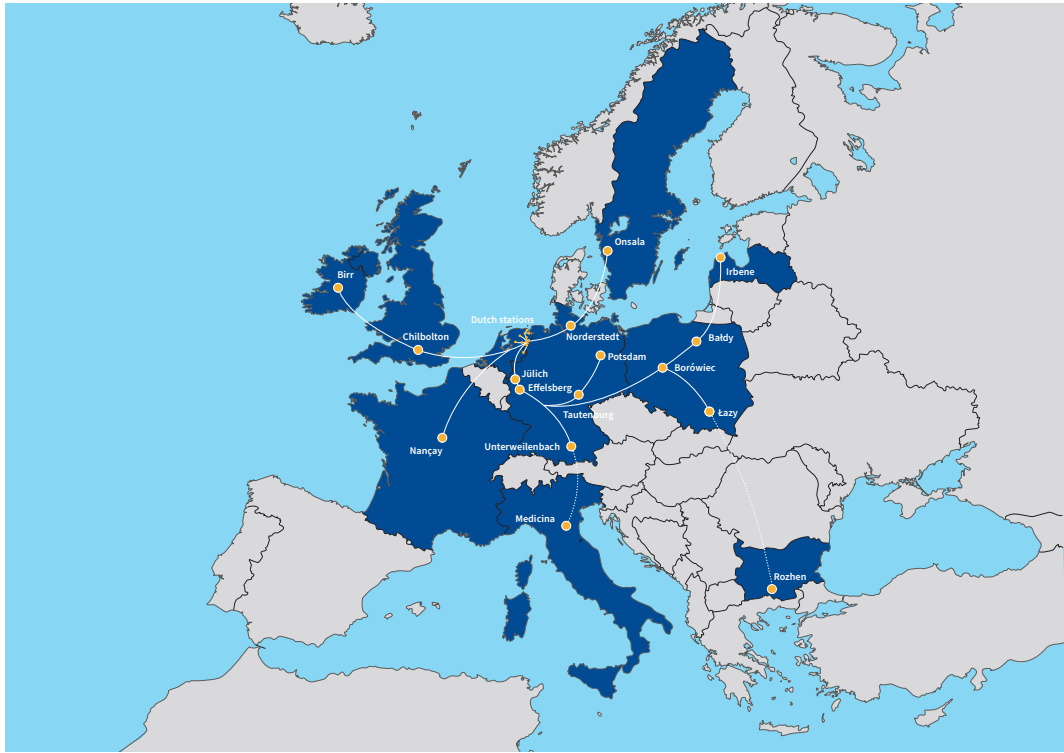


Figure 1.5: A schematic overview showing the locations of all current ILT stations in Europe. An interactive overlay on Google Earth can be found at <https://www.astron.nl/lofar-tools/lofarmap.html>.

and IE613HBA. The prefixes CS and RS indicate core and remote stations located in The Netherlands. International stations get their country code as a prefix, e.g. IE for Ireland. The first digit indicates the spiral arm of the originally envisioned log-spiral layout² of the stations (Röttgering, 2003) in which the station resides – 1: towards the south-east, 2: towards south, 3: towards south-west, 4: towards north-west, 5: towards north and international stations being designated 6. The two other digits indicate their distance from the superterp for Dutch stations (M. Brentjens, priv. comm.), and build order for international stations. Figure 1.5 shows a map of Europe with the locations of ILT stations indicated. At the moment of writing, there are 24 core stations, 14 remote stations and 14 international stations. The core and remote stations are strewn throughout the Dutch provinces of Friesland, Groningen and Drenthe, with the core being located in Exloo, Drenthe. Across Europe, there are 6 stations in Germany, 3 in Poland and one each in France, Ireland, Latvia, Sweden and the United Kingdom. New stations are now planned to be built in Italy³ and, most recently, Bulgaria⁴.

LOFAR is a so-called aperture array (e.g. Farhat et al., 2014): instead of a dish focussing radiation on

²For practical reasons, like available land, wet terrain, connectivity or RFI, this layout ultimately changed (M. Brentjens, M. Gerbers, priv. comm.).

³<https://www.astron.nl/lofar-crosses-the-alps-italy-joins/>

⁴<https://lofar.bg/what-is-lofar-bg/>

a receiver, a collection of numerous phased-array setups forms the aperture of the telescope. By inserting specific delays for each antenna, the direction from which signals arrive in phase can be altered. This allows one to electronically “point” the array and maximise sensitivity in a direction of interest. The array itself consists of two antenna systems: the *low band antennas* (LBAs) operating in the 10 – 90 MHz regime and the *high band antennas* (HBAs) operating in the 110 – 240 MHz regime. This thesis uses the HBAs. In this thesis, we use the HBAs. The typical observing setup for work such as presented here uses only the frequency range 120 – 168 MHz, providing a 48 MHz bandwidth. This range is where the HBAs are most sensitive and is also practical, allowing for two simultaneous equal-bandwidth beams on the sky per observation (Shimwell et al., 2017). These HBA stations consist of tiles that each contain 16 Vivaldi antennas in a 4×4 grid.

Dutch LOFAR

The HBA core stations are split in two “ears” of 24 tiles each, which are usually correlated separately. Remote stations consist of 48 tiles, but only the inner 24 are typically used to match the field of view of the core stations. This combination is the so-called HBA_DUAL_INNER mode. Together, LOFAR’s Dutch stations offer baselines up to approximately 120 km in length, allowing it to reach angular resolutions of the order of $\sim 6''$. LOFAR’s station field of view (FoV) is given by

$$\theta_{\text{FWHM}} = 1.02 \frac{\lambda}{D} \quad (1.2)$$

where λ is the observing wavelength and D the (effective) station diameter⁵. This gives the Dutch array in HBA_DUAL_INNER mode an FoV of 4.75° at 120 MHz down to 3.39° at 168 MHz.

For several years, the Dutch array has been carrying out the *LOFAR Two-metre Sky Survey* (LoTSS, Shimwell et al., 2017). This is a sensitive 144 MHz survey of the northern sky at an angular resolution of 6. In the second data release (Shimwell et al., 2022) the median sensitivity that is reached is $83 \mu\text{Jy beam}^{-1}$. With over 4.4 million sources detected, LoTSS DR2 is currently the largest radio catalogue in existence in terms of source counts.

International LOFAR

International stations use all 96 tiles and are therefore more sensitive. However, due to their larger diameter, they also have a smaller field of view. Their field of view ranges from 2.58° at 120 MHz down to 1.85° at 168 MHz. Expanding across the entire European continent has increased LOFAR’s maximum baseline over tenfold to almost 2000 km. In addition to enabling sub-arcsecond resolution imaging of the metrewave sky, the uv coverage remains dense and covers a wide range of scales. This allows the ILT to not only have exceptional angular resolution but also makes it retain its sensitivity to extended emission. Only in the $1 - 2''$ range is there a noticeable gap in uv -coverage left. Recent improvements in calibration strategies, pipelines and software have made it possible to start exploiting the ILT to its full capabilities. One is the *Long Baseline Calibrator Survey* (LBCS, Moldón et al., 2015; N. Jackson et al., 2016; N. J. Jackson et al., 2021), a snapshot survey of flat-spectrum sources in the Northern sky using quick 3-minute, 3 MHz observations to compile a list of candidate calibrator sources for the ILT. Other advancements are the development of a pipeline for easier processing of long baseline data (L. Morabito et al., 2021) and the expansion of the calibration to the full FoV (Sweijen et al., 2022a).

⁵<https://science.astron.nl/telescopes/lofar/lofar-system-overview/observing-modes/lofar-imaging-capabilities-and-sensitivity/>

1.5 In this thesis

This thesis explores both technical aspects and scientific aspects of low-frequency observations at high angular resolution. From the technical side, we focus on the calibration and imaging of the ILT's full field of view. Scientifically we employ the ILT to study radio AGNs.

Chapter 1 describes a single target study of the high-redshift radio galaxy 4C 43.15 to study the correlation between the steepening of the synchrotron spectral index and source redshift. ILT observations at 54 and 144 MHz are combined with VLA observations at 4,740 and 8,460 MHz. With matched-resolution images, we demonstrate, for the first time, spatially resolved spectral modeling of a high-redshift object using low-frequency radio data. Our findings support the idea that inverse-Compton losses may become the driving factor behind this correlation at higher redshifts or sources with weaker magnetic fields than 4C 43.15.

Chapter 2 expands on the calibration of and imaging with the ILT. Building on the strategies developed for single-target imaging we present an approach to calibrate and image the full 6.4 deg^2 international station field of view at sub-arcsecond resolution and $\sim 30 \mu\text{Jy beam}^{-1}$ (central) sensitivity. This strategy was employed on the Lockman Hole LOFAR deep field, producing a seven-gigapixel image of the central area.

Chapter 3 uses the results from Chapter 2 to study the population of hyperluminous infrared galaxies (HLIRGs) in the Lockman Hole region. The extreme IR luminosity of these objects suggests immense star formation rates of hundreds to thousands of solar masses per year if interpreted as pure star formation. Reproducing their observed number density under the interpretation of pure star-forming systems is challenging for current galaxy formation models. While there is consensus that there is likely an AGN component to this population, the extent of it remains uncertain. In this chapter we employ the high resolution of the ILT to identify AGNs among the HLIRGs in a dust-unobscured way using radio brightness temperature measurements, almost doubling the number of identified AGNs.

Chapter 4 pulls back for a broader view of the general population of radio AGNs. Combining images with angular resolutions of $6''$, $1.8''$ and $0.45''$, the full range of scales accessible to the ILT use used to attempt to measure the projected physical size distribution of $S_{150\text{MHz}} > 600 \mu\text{Jy}$ radio sources out to $z = 2.5$, in the Lockman Hole region down to the (sub-)arcsecond level. Our findings disagree with earlier gigahertz surveys, which we attribute to the lack of short baseline spacings in those, leading to reduced sensitivity to diffuse extended structure. Measured sizes are then compared to the derived radio powers. We find an increase of higher-power radio sources at redshifts $0.8 \leq z < 2.5$ compared to sources at $z < 0.8$. We speculate this may reflect more short-lived high accretion events in the Early Universe.

1.6 Outlook to the future

An all-sky survey and LOFAR 2.0

Advances in ILT data reduction both in terms of technical approaches are steadily progressing. A special issue in *Astronomy & Astrophysics* dedicated to sub-arcsecond imaging with the ILT emphasized single-target studies. Now the LOFAR Deep Fields are being processed to demonstrate the full capabilities of the instrument (Boötes, Escott et al. in prep.; ELAIS-N1, de Jong et al. in prep., Ye et al. subm.; Lockman Hole, Sweijen et al., 2022a). Furthermore, reprocessing of previous LoTSS observations that did not include the international stations in their data reduction has been started. These technical advances, combined with the general growth in computational power offered by modern large-scale compute infrastructure have brought a sub-arcsecond low-frequency northern sky survey on our horizon. With the HBA international station field of view being roughly twice smaller than that of the Dutch stations, the current distribution of LoTSS observations will have holes in its sky coverage. The proposed ILoTSS survey will aim to fill those gaps, as well as to reobserve fields that previously did not contain (enough) international stations.

One of the final frontiers for the ILT will be to exploit its international baselines at LBA frequencies. It offers the potential to reach angular resolutions at the arcsecond level at frequencies as low as 30 MHz. Full FoV calibration and imaging with the international stations in the LBA band is still actively being worked on, but first attempts at ILT imaging in the LBA band have already yielded enticing results (Leah K. Morabito et al., 2016; Groeneveld et al., 2022). Together with the coming upgrade to the array (see below), the planned *LBA LOFAR Community Sky Survey* (LLoCuSS⁶) will push the boundaries of radio astronomy once more by attempting to go to arcsecond resolution with the international stations.

To that extent, soon the LOFAR2.0⁷ upgrade will start. This upgrade will bring about two major changes. The first is that all Dutch stations will be synchronised by the same clock. Currently, only the core stations share the same clock. The remote and international stations have their own atomic clocks which are synchronised to GPS, but they can still drift by up to 20 ns per 20 min (Gasperin et al., 2019). Such drifts imprint a phase difference and will decorrelate the signal if not corrected for. By putting the entire Dutch array on a single clock, such phase errors will be eliminated for the Dutch stations.

The second upgrade will be an increase the computational capacity of stations, which will improve, for example, LBA performance through the *Digital Upgrade for Premier LOFAR Low-band Observing* (DUPLLO⁸) program. Currently, the system is limited to using only 48 out of the 96 antennas present for each LBA station. After the upgrade the full 96 antennas will be usable, boosting the LBA array's sensitivity and also providing a uniform station size between all of the core, remote and international stations, meaning one will not have to deal with different fields of view between them. This extra compute capacity doubles the bandwidth available for simultaneous beams on the sky. It will allow for simultaneous HBA+LBA observations, or double the survey speed in one band compared to the current system. The latter will be of great benefit to surveys such as the aforementioned ILoTSS.

Multi-wavelength synergies

With an angular resolution of $\sim 0.3 - 1''$ ILT surveys will be able to provide matched-resolution low-frequency radio images not only to higher-frequency radio images, but also to data at optical or infrared

⁶<https://sites.google.com/view/llocuss/>

⁷<https://www.lofar.eu/lofar2-0-documentation/>

⁸<https://www.nwo.nl/en/researchprogrammes/nwo-investment-grant-large/grants-awarded-2018>

wavelengths from current and coming state-of-the-art observatories in space, such as HST, Euclid (Euclid Collaboration et al., 2022) and *James Webb Space Telescope* (JWST), and on the ground such as *Vera C. Rubin Observatory* (LSST Science Collaboration et al., 2009) and the *Extremely Large Telescope* (ELT). On the radio side resolved spectral studies will be possible at a higher resolution than before. In the optical and infrared bands, it opens up the space for detailed multi-wavelength studies. Radio, optical and IR emission can be studied at similar physical scales, which will benefit, for example, the separation of RQ AGNs from SFGs or spatially resolved correlations between star formation and radio emission.

Final word

In a decade, radio astronomy will celebrate a century of discoveries. Major advancements in our understanding of the Universe have been tied to new instruments coming online that probe new parts of parameter space in terms of wavelength, sensitivity, angular resolution or both. For LOFAR that meant opening up the low-frequency sky at unprecedented sensitivity (both in absolute sense and in terms of angular scales) and resolution; being almost an order of magnitude more sensitive and having a resolution four times higher than TGSS, the leading low-frequency survey at the same frequency at the time. In the near future, the *Square Kilometre Array* (SKA) will start coming online on Earth's southern hemisphere. It is split into two systems: SKA-Low in Australia, which will observe in the 50 – 350 MHz range, and SKA-Mid in South Africa, set to observe in the 350 – 15,400 MHz range. On the northern hemisphere the ngVLA⁹ is being planned as the successor to the VLA. Aiming to observe in the 1 – 116 GHz range, with baselines out to 1000 km, it sets an ambitious goal for high-resolution radio interferometry at gigahertz frequencies. Amongst these, the ILT will remain a leading competitive instrument for low-frequency radio astronomy. Not only is it a premiere radio-astronomical facility in the northern hemisphere, but its unique combination of long ~ 2000 km baselines and dense uv -coverage on its multitude of angular scales offers a view on the low-frequency radio sky that will not be surpassed soon.

⁹<https://ngvla.nrao.edu/>

Bibliography

- Alfvén, H. and N. Herlofson (June 1950). “Cosmic Radiation and Radio Stars”. In: *Physical Review* 78.5, pp. 616–616. DOI: [10.1103/PhysRev.78.616](https://doi.org/10.1103/PhysRev.78.616). (Visited on 10/16/2023).
- Allen, L. R., H. P. Palmer, and B. Rowson (Nov. 1960). “New Limits to the Diameters of Some Radio Sources”. In: *Nature* 188.4752, pp. 731–732. ISSN: 1476-4687. DOI: [10.1038/188731a0](https://doi.org/10.1038/188731a0). (Visited on 09/19/2023).
- Allen, L. R. et al. (June 1962b). “Observations of 384 Radio Sources at a Frequency of 158 Mc/s with a Long Baseline Interferometer”. In: *Monthly Notices of the Royal Astronomical Society* 124.6, pp. 477–499. ISSN: 0035-8711. DOI: [10.1093/mnras/124.6.477](https://doi.org/10.1093/mnras/124.6.477). (Visited on 09/18/2023).
- Ananthakrishnan, S. et al. (Mar. 1989). “VLBI Observations of the Nuclei of a Mixed Sample of Bright Galaxies and Quasars at 327 MHz”. In: *Monthly Notices of the Royal Astronomical Society* 237.2, pp. 341–354. ISSN: 0035-8711. DOI: [10.1093/mnras/237.2.341](https://doi.org/10.1093/mnras/237.2.341). (Visited on 01/29/2020).
- Baade, W. (May 1956). “Polarization in the Jet of Messier 87.” In: *The Astrophysical Journal* 123, pp. 550–551. ISSN: 0004-637X. DOI: [10.1086/146194](https://doi.org/10.1086/146194). (Visited on 10/16/2023).
- Baade, W. and R. Minkowski (Jan. 1954a). “Identification of the Radio Sources in Cassiopeia, Cygnus A, and Puppis A.” In: *The Astrophysical Journal* 119, p. 206. ISSN: 0004-637X. DOI: [10.1086/145812](https://doi.org/10.1086/145812). (Visited on 09/06/2023).
- Baldi, Ranieri D., Alessandro Capetti, and Gabriele Giovannini (Apr. 2015). “Pilot Study of the Radio-Emitting AGN Population: The Emerging New Class of FR 0 Radio-Galaxies”. In: *Astronomy and Astrophysics* 576. ISSN: 14320746. DOI: [10.1051/0004-6361/201425426](https://doi.org/10.1051/0004-6361/201425426). arXiv: [1502.00427](https://arxiv.org/abs/1502.00427). (Visited on 09/14/2020).
- Baldwin, J. E. et al. (Dec. 1985). “The 6C Survey of Radio Sources – I. Declination Zone $\delta > +80^\circ$ ”. In: *Monthly Notices of the Royal Astronomical Society* 217.4, pp. 717–730. ISSN: 0035-8711. DOI: [10.1093/mnras/217.4.717](https://doi.org/10.1093/mnras/217.4.717). (Visited on 09/08/2023).
- Bare, C. et al. (July 1967). “Interferometer Experiment with Independent Local Oscillators”. In: *Science* 157.3785, pp. 189–191. DOI: [10.1126/science.157.3785.189](https://doi.org/10.1126/science.157.3785.189). (Visited on 09/18/2023).
- Bennett, A. S. and F. G. Simth (July 1962). “The Preparation of the Revised 3C Catalogue of Radio Sources”. In: *Monthly Notices of the Royal Astronomical Society* 125.1, pp. 75–86. ISSN: 0035-8711. DOI: [10.1093/mnras/125.1.75](https://doi.org/10.1093/mnras/125.1.75). (Visited on 09/07/2023).
- Best, P N et al. (Aug. 2023). “The LOFAR Two-metre Sky Survey: Deep Fields Data Release 1. V. Survey Description, Source Classifications, and Host Galaxy Properties”. In: *Monthly Notices of the Royal Astronomical Society* 523.2, pp. 1729–1755. ISSN: 0035-8711. DOI: [10.1093/mnras/stad1308](https://doi.org/10.1093/mnras/stad1308). (Visited on 06/07/2023).
- Bolton, J. G. (July 1948). “Discrete Sources of Galactic Radio Frequency Noise”. In: *Nature* 162.4108, pp. 141–142. ISSN: 1476-4687. DOI: [10.1038/162141a0](https://doi.org/10.1038/162141a0). (Visited on 09/05/2023).

- Bolton, J. G., F. F. Gardner, and M. B. Mackey (Sept. 1964). “The Parkes Catalogue of Radio Sources, Declination Zone -20° to -60° ”. In: *Australian Journal of Physics* 17, p. 340. ISSN: 0004-9506. DOI: [10. 1071/PH640340](https://doi.org/10.1071/PH640340). (Visited on 09/18/2023).
- Bolton, J. G. and G. J. Stanley (Mar. 1948a). “Observations on the Variable Source of Cosmic Radio Frequency Radiation in the Constellation of Cygnus”. In: *Australian Journal of Scientific Research A Physical Sciences* 1, p. 58. ISSN: 0004-9506. DOI: [10. 1071/CH9480058](https://doi.org/10.1071/CH9480058). (Visited on 09/05/2023).
- (Feb. 1948b). “Variable Source of Radio Frequency Radiation in the Constellation of Cygnus”. In: *Nature* 161.4087, pp. 312–313. ISSN: 1476-4687. DOI: [10. 1038/161312b0](https://doi.org/10.1038/161312b0). (Visited on 08/17/2023).
- (June 1949a). “The Position and Probable Identification of the Source of the Galactic Radio-Frequency Radiation Taurus-A”. In: *Australian Journal of Scientific Research A Physical Sciences* 2, p. 139. ISSN: 0004-9506. DOI: [10. 1071/CH9490139](https://doi.org/10.1071/CH9490139). (Visited on 09/06/2023).
- Bolton, J. G., G. J. Stanley, and O. B. Slee (July 1949b). “Positions of Three Discrete Sources of Galactic Radio-Frequency Radiation”. In: *Nature* 164.4159, pp. 101–102. ISSN: 1476-4687. DOI: [10. 1038/164101b0](https://doi.org/10.1038/164101b0). (Visited on 09/06/2023).
- Broten, N. W. et al. (1967a). “Long Base Line Interferometry: A New Technique”. In: *Science* 156.3782, pp. 1592–1593. ISSN: 0036-8075. JSTOR: [1721590](https://www.jstor.org/stable/1721590). (Visited on 09/19/2023).
- Broten, N. W. et al. (July 1967b). “Observations of Quasars Using Interferometer Baselines up to 3,074 Km”. In: *Nature* 215, p. 38. ISSN: 0028-0836. DOI: [10. 1038/215038a0](https://doi.org/10.1038/215038a0). (Visited on 09/19/2023).
- Brown, R. Hanbury and C. Hazard (Nov. 1950). “Radio-Frequency Radiation from the Great Nebula in Andromeda (M.31)”. In: *Nature* 166.4230, pp. 901–902. ISSN: 1476-4687. DOI: [10. 1038/166901a0](https://doi.org/10.1038/166901a0). (Visited on 11/29/2023).
- Brown, R. Hanbury and R.Q. Twiss (July 1954). “LXXIV. A New Type of Interferometer for Use in Radio Astronomy”. In: *The London, Edinburgh, and Dublin Philosophical Magazine and Journal of Science* 45.366, pp. 663–682. ISSN: 1941-5982. DOI: [10. 1080/14786440708520475](https://doi.org/10.1080/14786440708520475). (Visited on 09/19/2023).
- Burbidge, G. R. (Jan. 1970). “The Nuclei of Galaxies”. In: *Annual Review of Astronomy and Astrophysics* 8, p. 369. ISSN: 0066-4146. DOI: [10. 1146/annurev.aa.08.090170.002101](https://doi.org/10.1146/annurev.aa.08.090170.002101). (Visited on 10/16/2023).
- Burns, Russell W and Russell W Burns (2004). “Communications: an international history of the formative years”. In: IET.
- Capetti, A., F. Massaro, and R. D. Baldi (Feb. 2017a). “FRICAT: A FIRST Catalog of FR I Radio Galaxies”. In: *Astronomy & Astrophysics* 598, A49. ISSN: 0004-6361, 1432-0746. DOI: [10. 1051/0004-6361/201629287](https://doi.org/10.1051/0004-6361/201629287). (Visited on 10/23/2023).
- (May 2017b). “FRIICAT: A FIRST Catalog of FR II Radio Galaxies”. In: *Astronomy & Astrophysics* 601, A81. ISSN: 0004-6361, 1432-0746. DOI: [10. 1051/0004-6361/201630247](https://doi.org/10.1051/0004-6361/201630247). (Visited on 10/23/2023).
- Carr, T. D. et al. (1970). “Very Long Baseline Interferometry of Jupiter at 18 MHz”. In: *Radio Science* 5.10, pp. 1223–1226. ISSN: 1944-799X. DOI: [10. 1029/RS005i010p01223](https://doi.org/10.1029/RS005i010p01223). (Visited on 09/15/2023).
- Chiu, Hong-Yee (May 1964). “Gravitational Collapse”. In: *Physics Today* 17.5, pp. 21–34. ISSN: 0031-9228. DOI: [10. 1063/1.3051610](https://doi.org/10.1063/1.3051610). (Visited on 10/15/2023).
- Clark, B. (Jan. 1968). “Radio Interferometers of Intermediate Type”. In: *IEEE Transactions on Antennas and Propagation* 16.1, pp. 143–144. ISSN: 1558-2221. DOI: [10. 1109/TAP.1968.1139118](https://doi.org/10.1109/TAP.1968.1139118).
- Clark, B. G. (Jan. 2003). “A Review of the History of VLBI”. In: 300, p. 1. (Visited on 09/19/2023).
- Cohen, A. S. et al. (2006). “The VLA Low-frequency Sky Survey”. In: *Astronomische Nachrichten* 327.2-3, pp. 262–265. ISSN: 1521-3994. DOI: [10. 1002/asna.200510519](https://doi.org/10.1002/asna.200510519). (Visited on 09/21/2023).

BIBLIOGRAPHY

- Cohen, M. H., E. J. Gundermann, and D. E. Harris (Dec. 1967). “New Limits on the Diameters of Radio Sources”. In: *The Astrophysical Journal* 150, p. 767. ISSN: 0004-637X, 1538-4357. DOI: [10.1086/149380](https://doi.org/10.1086/149380). (Visited on 09/18/2023).
- Condon, J. J. (Jan. 1992). “Radio Emission from Normal Galaxies.” In: *Annual Review of Astronomy and Astrophysics* 30, pp. 575–611. ISSN: 0066-4146. DOI: [10.1146/annurev.aa.30.090192.003043](https://doi.org/10.1146/annurev.aa.30.090192.003043). (Visited on 08/18/2023).
- Davidson, W. (Nov. 1961). “The Cosmological Implications of the Recent Counts of Radio Sources: I. Analysis of the Results and Their Immediate Interpretation”. In: *Monthly Notices of the Royal Astronomical Society* 123.5, pp. 425–435. ISSN: 0035-8711. DOI: [10.1093/mnras/123.5.425](https://doi.org/10.1093/mnras/123.5.425). (Visited on 09/11/2023).
- Day, G. A. et al. (Feb. 1966). “The Parkes Catalogue of Radio Sources, Declination Zone 0° to +20°”. In: *Australian Journal of Physics* 19, p. 35. ISSN: 0004-9506. DOI: [10.1071/PH660035](https://doi.org/10.1071/PH660035). (Visited on 09/18/2023).
- De Breuck, C. et al. (Apr. 2000). “A Sample of 669 Ultra Steep Spectrum Radio Sources to Find High Redshift Radio Galaxies”. In: *Astronomy and Astrophysics Supplement Series* 143.2, pp. 303–333. ISSN: 0365-0138. DOI: [10.1051/aas:2000181](https://doi.org/10.1051/aas:2000181). (Visited on 09/11/2018).
- Dewhurst, D. W. (Jan. 1959). “The Optical Identification of Radio Sources”. In: *Symposium - International Astronomical Union* 9, pp. 507–513. ISSN: 0074-1809. DOI: [10.1017/S007418090005138X](https://doi.org/10.1017/S007418090005138X). (Visited on 10/05/2023).
- Douglas, James N. et al. (May 1996). “The Texas Survey of Radio Sources Covering -35.5 Degrees < Declination < 71.5 Degrees at 365 MHz”. In: *The Astronomical Journal* 111, p. 1945. ISSN: 0004-6256. DOI: [10.1086/117932](https://doi.org/10.1086/117932). (Visited on 09/13/2023).
- Edge, D. O., P. A. G. Scheuer, and J. R. Shakeshaft (Apr. 1958). “Evidence on the Spatial Distribution of Radio Sources Derived from a Survey at a Frequency of 159 Mc/s”. In: *Monthly Notices of the Royal Astronomical Society* 118.2, pp. 183–196. ISSN: 0035-8711. DOI: [10.1093/mnras/118.2.183](https://doi.org/10.1093/mnras/118.2.183). (Visited on 09/10/2023).
- Ekers, J. A. (Jan. 1969). “The Parkes Catalogue of Radio Sources, Declination Zone +20 to -90.” In: *Australian Journal of Physics Astrophysical Supplement* 7, pp. 3–75. (Visited on 09/18/2023).
- Elgaroy, O., D. Morris, and B. Rowson (Jan. 1962). “A Radio Interferometer for Use with Very Long Baselines”. In: *Monthly Notices of the Royal Astronomical Society* 124, p. 395. ISSN: 0035-8711. DOI: [10.1093/mnras/124.5.395](https://doi.org/10.1093/mnras/124.5.395). (Visited on 09/19/2023).
- Euclid Collaboration et al. (June 2022). “Euclid Preparation. I. The Euclid Wide Survey”. In: *Astronomy and Astrophysics* 662, A112. ISSN: 0004-6361. DOI: [10.1051/0004-6361/202141938](https://doi.org/10.1051/0004-6361/202141938). (Visited on 11/06/2023).
- Event Horizon Telescope Collaboration et al. (Apr. 2019). “First M87 Event Horizon Telescope Results. I. The Shadow of the Supermassive Black Hole”. In: *Apj* 875.1, L1, p. L1. DOI: [10.3847/2041-8213/ab0ec7](https://doi.org/10.3847/2041-8213/ab0ec7). arXiv: [1906.11238 \[astro-ph.GA\]](https://arxiv.org/abs/1906.11238).
- Fanaroff, B. L. and J. M. Riley (Apr. 1974). “The Morphology of Extragalactic Radio Sources of High and Low Luminosity”. In: *Monthly Notices of the Royal Astronomical Society* 167.1, 31P–36P. ISSN: 0035-8711. DOI: [10.1093/mnras/167.1.31P](https://doi.org/10.1093/mnras/167.1.31P). (Visited on 11/26/2018).
- Faraday, Michael (May 1846b). “LIV. Thoughts on Ray-Vibrations”. In: *The London, Edinburgh, and Dublin Philosophical Magazine and Journal of Science* 28.188, pp. 345–350. ISSN: 1941-5966. DOI: [10.1080/14786444608645431](https://doi.org/10.1080/14786444608645431). (Visited on 06/07/2023).

- Farhat, Eman O. et al. (2014). “Aperture arrays for radio astronomy”. In: *2014 International Conference on Electromagnetics in Advanced Applications (ICEAA)*, pp. 185–190. DOI: [10.1109/ICEAA.2014.6903852](https://doi.org/10.1109/ICEAA.2014.6903852).
- Garratt, Gerald Reginald Mansel (1994). *The early history of radio: from Faraday to Marconi*. 20. Iet.
- Garrett, M.A. (2007). “E-VLBI... a Wide-Field Imaging Instrument with Milliarcsecond Resolution & Microjy Sensitivity”. In: *Exploring the Cosmic Frontier*. Ed. by Andrei P. Lobanov et al. ESO Astrophysics Symposia European Southern Observatory. Berlin, Heidelberg: Springer, pp. 171–174. ISBN: 978-3-540-39756-4. DOI: [10.1007/978-3-540-39756-4_46](https://doi.org/10.1007/978-3-540-39756-4_46).
- Gasperin, F. de et al. (Feb. 2019). “Systematic Effects in LOFAR Data: A Unified Calibration Strategy”. In: *Astronomy & Astrophysics* 622, A5. ISSN: 0004-6361, 1432-0746. DOI: [10.1051/0004-6361/201833867](https://doi.org/10.1051/0004-6361/201833867). (Visited on 01/26/2022).
- Gopal-Krishna and P. J. Wiita (Nov. 2000). “Extragalactic Radio Sources with Hybrid Morphology: Implications for the Fanaroff-Riley Dichotomy”. In: *Astronomy and Astrophysics* 363, pp. 507–516. ISSN: 0004-6361. DOI: [10.48550/arXiv.astro-ph/0009441](https://doi.org/10.48550/arXiv.astro-ph/0009441). (Visited on 10/23/2023).
- Goss, W. M., Claire Hooker, and Ronald D. Ekers (2023). *Joe Pawsey and the Founding of Australian Radio Astronomy: Early Discoveries, from the Sun to the Cosmos*. Historical & Cultural Astronomy. Cham: Springer International Publishing. ISBN: 978-3-031-07915-3 978-3-031-07916-0. DOI: [10.1007/978-3-031-07916-0](https://doi.org/10.1007/978-3-031-07916-0). (Visited on 09/10/2023).
- Gower, J. F. R. (July 1966). “The Source Counts from the 4C Survey”. In: *Monthly Notices of the Royal Astronomical Society* 133.1, pp. 151–161. ISSN: 0035-8711. DOI: [10.1093/mnras/133.1.151](https://doi.org/10.1093/mnras/133.1.151). (Visited on 09/11/2023).
- Gower, J. F. R., P. F. Scott, and D. Wills (Jan. 1967). “A Survey of Radio Sources in the Declination Ranges -07° to 20° and 40° to 80° ”. In: *Memoirs of the Royal Astronomical Society* 71, p. 49. (Visited on 09/07/2023).
- Greenstein, Jesse L. and Thomas A. Matthews (Jan. 1963). “Redshift of the Radio Source 3C 48.” In: *The Astronomical Journal* 68, p. 279. ISSN: 0004-6256. DOI: [10.1086/109140](https://doi.org/10.1086/109140). (Visited on 10/15/2023).
- Groeneveld, C. et al. (Feb. 2022). “Pushing Sub-Arsecond Resolution Imaging down to 30 MHz with the Trans-European International LOFAR Telescope”. In: *Astronomy and Astrophysics* 658, A9. ISSN: 0004-6361. DOI: [10.1051/0004-6361/202141352](https://doi.org/10.1051/0004-6361/202141352). (Visited on 02/28/2024).
- Haarlem, M. P. van et al. (Aug. 2013). “LOFAR: The LOw-Frequency ARray”. In: *Astronomy & Astrophysics* 556, A2. ISSN: 0004-6361, 1432-0746. DOI: [10.1051/0004-6361/201220873](https://doi.org/10.1051/0004-6361/201220873). (Visited on 09/20/2023).
- Hale, Catherine L. et al. (Jan. 2021). “The Rapid ASKAP Continuum Survey Paper II: First Stokes I Source Catalogue Data Release”. In: *Publications of the Astronomical Society of Australia* 38, e058. ISSN: 1323-3580, 1448-6083. DOI: [10.1017/pasa.2021.47](https://doi.org/10.1017/pasa.2021.47). (Visited on 09/13/2023).
- Hales, S. E. G., J. E. Baldwin, and P. J. Warner (Oct. 1988). “The 6C Survey of Radio Sources – II. The Zone $30^{\circ} < \delta < 51^{\circ}$, $0^{\text{h}} < \alpha < 09^{\text{h}} 05^{\text{m}}$ and $22^{\text{h}} 35^{\text{m}} < \alpha < 24^{\text{h}}$ ”. In: *Monthly Notices of the Royal Astronomical Society* 234.4, pp. 919–936. ISSN: 0035-8711. DOI: [10.1093/mnras/234.4.919](https://doi.org/10.1093/mnras/234.4.919). (Visited on 09/08/2023).
- (July 1993b). “The 6C Survey of Radio Sources – VI. The Continuous Zone $30^{\circ} < \delta < 51^{\circ}$, $0^{\text{h}} < \alpha < 09^{\text{h}} 05^{\text{m}}$ and $22^{\text{h}} 35^{\text{m}} < \alpha < 24^{\text{h}}$ ”. In: *Monthly Notices of the Royal Astronomical Society* 263.1, pp. 25–30. ISSN: 0035-8711. DOI: [10.1093/mnras/263.1.25](https://doi.org/10.1093/mnras/263.1.25). (Visited on 09/08/2023).
- Hales, S. E. G. et al. (Sept. 1990). “The 6C Survey of Radio Sources - III. The Zone 48”. In: *Monthly Notices of the Royal Astronomical Society* 246, pp. 256–262. ISSN: 0035-8711. (Visited on 09/08/2023).

BIBLIOGRAPHY

- Hales, S. E. G. et al. (July 1991). “The 6C Survey of Radio Sources – IV. The Zone $67^{\circ} \leq \delta \leq 82^{\circ}, 0^{\circ} \leq \alpha \leq 24^{\circ}$ ”. In: *Monthly Notices of the Royal Astronomical Society* 251.1, pp. 46–53. ISSN: 0035-8711. DOI: [10.1093/mnras/251.1.46](https://doi.org/10.1093/mnras/251.1.46). (Visited on 09/08/2023).
- Hales, S. E. G. et al. (June 1993c). “The 6C Survey of Radio Sources – V. The Zones $6^{\circ} \leq \delta \leq 48^{\circ}, 0^{\circ} \leq \alpha \leq 68^{\circ}$, $0^{\circ} \leq \delta \leq 68^{\circ}, 17^{\circ} \leq \alpha \leq 20^{\circ}$ ”. In: *Monthly Notices of the Royal Astronomical Society* 262.4, pp. 1057–1061. ISSN: 0035-8711. DOI: [10.1093/mnras/262.4.1057](https://doi.org/10.1093/mnras/262.4.1057). (Visited on 09/08/2023).
- Hales, S. E. G. et al. (Dec. 2007). “A Final Non-Redundant Catalogue for the 7C 151-MHz Survey”. In: *Monthly Notices of the Royal Astronomical Society* 382.4, pp. 1639–1642. ISSN: 0035-8711. DOI: [10.1111/j.1365-2966.2007.12392.x](https://doi.org/10.1111/j.1365-2966.2007.12392.x). (Visited on 09/08/2023).
- Hanbury Brown, R. and C. Hazard (Apr. 1953b). “A Survey of 23 Localized Radio Sources in the Northern Hemisphere”. In: *Monthly Notices of the Royal Astronomical Society* 113.2, pp. 123–133. ISSN: 0035-8711. DOI: [10.1093/mnras/113.2.123](https://doi.org/10.1093/mnras/113.2.123). (Visited on 02/20/2023).
- Hanbury Brown, R., R. C. Jennison, and M. K. Das Gupta (Dec. 1952). “Apparent Angular Sizes of Discrete Radio Sources: Observations at Jodrell Bank, Manchester”. In: *Nature* 170.4338, pp. 1061–1063. ISSN: 1476-4687. DOI: [10.1038/1701061a0](https://doi.org/10.1038/1701061a0). (Visited on 09/19/2023).
- Hardcastle, M. J. and M. G. H. Krause (Mar. 2013). “Numerical Modelling of the Lobes of Radio Galaxies in Cluster Environments”. In: *Monthly Notices of the Royal Astronomical Society* 430, pp. 174–196. ISSN: 0035-8711. DOI: [10.1093/mnras/sts564](https://doi.org/10.1093/mnras/sts564). (Visited on 10/23/2023).
- Hardcastle, M. J. et al. (Feb. 2019). “Radio-Loud AGN in the First LoTSS Data Release”. In: *Astronomy & Astrophysics* 622, A12. ISSN: 0004-6361. DOI: [10.1051/0004-6361/201833893](https://doi.org/10.1051/0004-6361/201833893). (Visited on 01/24/2020).
- Harwood, Jeremy J, Tessa Vernstrom, and Andra Stroe (Jan. 2020). “Unveiling the Cause of Hybrid Morphology Radio Sources (HyMoRS)”. In: *Monthly Notices of the Royal Astronomical Society* 491.1, pp. 803–822. ISSN: 0035-8711. DOI: [10.1093/mnras/stz3069](https://doi.org/10.1093/mnras/stz3069). (Visited on 08/09/2023).
- Harwood, Jeremy J. et al. (Nov. 2013). “Spectral Ageing in the Lobes of FR-II Radio Galaxies: New Methods of Analysis for Broad-Band Radio Data”. In: *Monthly Notices of the Royal Astronomical Society* 435.4, pp. 3353–3375. ISSN: 00358711. DOI: [10.1093/mnras/stt1526](https://doi.org/10.1093/mnras/stt1526). arXiv: [1308.4137](https://arxiv.org/abs/1308.4137). (Visited on 07/31/2018).
- Hazard, C., M. B. Mackey, and A. J. Shimmins (Mar. 1963). “Investigation of the Radio Source 3C 273 By The Method of Lunar Occultations”. In: *Nature* 197.4872, pp. 1037–1039. ISSN: 1476-4687. DOI: [10.1038/1971037a0](https://doi.org/10.1038/1971037a0). (Visited on 02/01/2023).
- Heckman, Timothy M. and Philip N. Best (Aug. 2014). “The Coevolution of Galaxies and Supermassive Black Holes: Insights from Surveys of the Contemporary Universe”. In: *Annual Review of Astronomy and Astrophysics* 52, pp. 589–660. ISSN: 00664146. DOI: [10.1146/annurev-astro-081913-035722](https://doi.org/10.1146/annurev-astro-081913-035722). arXiv: [1403.4620](https://arxiv.org/abs/1403.4620). (Visited on 10/12/2020).
- Hey, J. S., S. J. Parsons, and J. W. Phillips (Aug. 1946a). “Fluctuations in Cosmic Radiation at Radio-Frequencies”. In: *Nature* 158.4007, pp. 234–234. ISSN: 1476-4687. DOI: [10.1038/158234a0](https://doi.org/10.1038/158234a0). (Visited on 09/10/2023).
- Hey, J. S., J. W. Phillips, and S. J. Parsons (Mar. 1946b). “Cosmic Radiations at 5 Metres Wave-length”. In: *Nature* 157.3984, pp. 296–297. ISSN: 1476-4687. DOI: [10.1038/157296c0](https://doi.org/10.1038/157296c0). (Visited on 08/17/2023).
- Hogbom, J. A. and W. N. Brouw (July 1974). “The Synthesis Radio Telescope at Westerbork. Principles of Operation, Performance and Data Reduction”. In: *Astronomy and Astrophysics* 33, p. 289. ISSN: 0004-6361. (Visited on 08/07/2023).

- Hoyle, F. and J. V. Narlikar (Aug. 1961). “On the Counting of Radio Sources in the Steady-state Cosmology”. In: *Monthly Notices of the Royal Astronomical Society* 123.2, pp. 133–166. ISSN: 0035-8711. DOI: [10.1093/mnras/123.2.133](https://doi.org/10.1093/mnras/123.2.133). (Visited on 09/11/2023).
- Hurley-Walker, N et al. (Jan. 2017). “GaLactic and Extragalactic All-sky Murchison Widefield Array (GLEAM) Survey – I. A Low-Frequency Extragalactic Catalogue”. In: *Monthly Notices of the Royal Astronomical Society* 464.1, pp. 1146–1167. ISSN: 0035-8711. DOI: [10.1093/mnras/stw2337](https://doi.org/10.1093/mnras/stw2337). (Visited on 09/13/2023).
- Intema, H. T. et al. (Feb. 2017). “The GMRT 150 MHz All-Sky Radio Survey - First Alternative Data Release TGSS ADR1”. In: *Astronomy & Astrophysics* 598, A78. ISSN: 0004-6361, 1432-0746. DOI: [10.1051/0004-6361/201628536](https://doi.org/10.1051/0004-6361/201628536). (Visited on 09/11/2023).
- Jackson, N. et al. (Nov. 2016). “LBCS: The LOFAR Long-Baseline Calibrator Survey”. In: *Astronomy & Astrophysics* 595, A86. ISSN: 0004-6361. DOI: [10.1051/0004-6361/201629016](https://doi.org/10.1051/0004-6361/201629016). arXiv: [1608.02133](https://arxiv.org/abs/1608.02133). (Visited on 05/23/2018).
- Jackson, N. J. et al. (May 2021). “Sub-Arcsecond Imaging with the International LOFAR Telescope. II. Completion of the LOFAR Long-Baseline Calibrator Survey”. In: *Astronomy & Astrophysics*. ISSN: 0004-6361. DOI: [10.1051/0004-6361/202140756](https://doi.org/10.1051/0004-6361/202140756). (Visited on 07/19/2021).
- Jaffe, W. J. and G. C. Perola (Aug. 1973). “Dynamical Models of Tailed Radio Sources in Clusters of Galaxies”. In: *Astronomy and Astrophysics* 26, p. 423. ISSN: 0004-6361. (Visited on 10/23/2023).
- Jansky, K.G. (Dec. 1932). “Directional Studies of Atmospheric at High Frequencies”. In: *Proceedings of the Institute of Radio Engineers* 20.12, pp. 1920–1932. ISSN: 2162-6626. DOI: [10.1109/JRPROC.1932.227477](https://doi.org/10.1109/JRPROC.1932.227477).
- Jansky, Karl G. (Dec. 1933a). “Electrical phenomena that apparently are of interstellar origin”. In: *Popular Astronomy* 41, pp. 548–555.
- (July 1933b). “Radio Waves from Outside the Solar System”. In: *Nature* 132.3323, p. 66. DOI: [10.1038/132066a0](https://doi.org/10.1038/132066a0).
- Jennison, R. C. and M. K. Das Gupta (Nov. 1953). “Fine Structure of the Extra-terrestrial Radio Source Cygnus I”. In: *Nature* 172.4387, pp. 996–997. ISSN: 1476-4687. DOI: [10.1038/172996a0](https://doi.org/10.1038/172996a0). (Visited on 03/01/2023).
- Jennison, R. C. and M. K. Das Gupta (Jan. 1956a). “V. The Measurement of the Angular Diameter of Two Intense Radio Sources. I: A Radio Interferometer Using Post-Detector Correlation”. In: *The Philosophical Magazine: A Journal of Theoretical Experimental and Applied Physics* 1.1, pp. 55–64. ISSN: 0031-8086. DOI: [10.1080/14786435608238076](https://doi.org/10.1080/14786435608238076). (Visited on 09/20/2023).
- (Jan. 1956b). “VI. The Measurement of the Angular Diameter of Two Intense Radio Sources-II: Diameter and Structural Measurements of the Radio Stars Cygnus a and Cassiopeia a”. In: *The Philosophical Magazine: A Journal of Theoretical Experimental and Applied Physics* 1.1, pp. 65–75. ISSN: 0031-8086. DOI: [10.1080/14786435608238077](https://doi.org/10.1080/14786435608238077). (Visited on 09/20/2023).
- Kardashev, N. S. (Jan. 1962). “Nonstationarity of Spectra of Young Sources of Nonthermal Radio Emission”. In: *Astronomicheskii Zhurnal* 39, p. 393. ISSN: 0004-6299. (Visited on 10/23/2023).
- Kardashev, N. S., A. D. Kuz'min, and S. I. Syrovatskii (Oct. 1962). “The Nature of the Emission from the Radio Galaxy Cygnus A”. In: *Soviet Astronomy* 6, p. 167. ISSN: 0038-5301. (Visited on 10/23/2023).
- Kassim, N. E. et al. (Dec. 1993). “Subarcminute Resolution Imaging of Radio Sources at 74 MHz with the Very Large Array”. In: *The Astronomical Journal* 106, p. 2218. ISSN: 00046256. DOI: [10.1086/116795](https://doi.org/10.1086/116795). (Visited on 09/21/2023).

BIBLIOGRAPHY

- Kellermann, K. I. and J. M. Moran (2001). “The Development of High-Resolution Imaging in Radio Astronomy”. In: *Annual Review of Astronomy and Astrophysics* 39.1, pp. 457–509. DOI: [10 . 1146 / annurev . astro . 39 . 1 . 457](https://doi.org/10.1146/annurev.astro.39.1.457). (Visited on 09/18/2023).
- Kellermann, K. I. et al. (Oct. 1989). “VLA Observations of Objects in the Palomar Bright Quasar Survey”. In: *The Astronomical Journal* 98, p. 1195. ISSN: 0004-6256. DOI: [10 . 1086 / 115207](https://doi.org/10.1086/115207). (Visited on 11/01/2023).
- Klein, U., U. Lisenfeld, and S. Verley (Mar. 2018). “Radio Synchrotron Spectra of Star-Forming Galaxies”. In: *Astronomy & Astrophysics* 611, A55. ISSN: 0004-6361, 1432-0746. DOI: [10 . 1051 / 0004 - 6361 / 201731673](https://doi.org/10.1051/0004-6361/201731673). (Visited on 10/30/2023).
- Lane, W. M. et al. (May 2014). “The Very Large Array Low-frequency Sky Survey Redux (VLSSr)”. In: *Monthly Notices of the Royal Astronomical Society* 440.1, pp. 327–338. ISSN: 0035-8711. DOI: [10 . 1093 / mnras / stu256](https://doi.org/10.1093/mnras/stu256). (Visited on 09/21/2023).
- Large, M. I. et al. (Mar. 1981). “The Molonglo Reference Catalogue of Radio Sources”. In: *Monthly Notices of the Royal Astronomical Society* 194.3, pp. 693–704. ISSN: 0035-8711. DOI: [10 . 1093 / mnras / 194 . 3 . 693](https://doi.org/10.1093/mnras/194.3.693). (Visited on 10/05/2023).
- Ledlow, Michael J. and Frazer N. Owen (July 1996). “20 CM VLA Survey of Abell Clusters of Galaxies. VI. Radio/Optical Luminosity Functions”. In: *The Astronomical Journal* 112, p. 9. ISSN: 0004-6256. DOI: [10 . 1086 / 117985](https://doi.org/10.1086/117985). (Visited on 10/23/2023).
- Linfield, R. and R. S. Simon (Dec. 1984). “High-Resolution Observations of Radio-Source Hot Spots at 329 MHz”. In: *The Astronomical Journal* 89, p. 1799. ISSN: 00046256. DOI: [10 . 1086 / 113688](https://doi.org/10.1086/113688). (Visited on 09/15/2023).
- Lodge, Oliver J. and James L. Howard (June 1888). “On Electric Radiation and Its Concentration by Lenses”. In: *Proceedings of the Physical Society of London* 10.1, p. 143. ISSN: 1478-7814. DOI: [10 . 1088 / 1478 - 7814 / 10 / 1 / 324](https://doi.org/10.1088/1478-7814/10/1/324). (Visited on 08/17/2023).
- LSST Science Collaboration et al. (Dec. 2009). “LSST Science Book, Version 2.0”. In: *arXiv e-prints*, arXiv:0912.0201, arXiv:0912.0201. DOI: [10 . 48550 / arXiv . 0912 . 0201](https://doi.org/10.48550/arXiv.0912.0201). arXiv: [0912 . 0201 \[astro-ph.IM\]](https://arxiv.org/abs/0912.0201).
- Lynden-Bell, D. (Aug. 1969). “Galactic Nuclei as Collapsed Old Quasars”. In: *Nature* 223.5207, pp. 690–694. ISSN: 1476-4687. DOI: [10 . 1038 / 223690a0](https://doi.org/10.1038/223690a0). (Visited on 08/28/2023).
- Matthews, Thomas A. and Allan R. Sandage (July 1963). “Optical Identification of 3C 48, 3C 196, and 3C 286 with Stellar Objects.” In: *The Astrophysical Journal* 138, p. 30. ISSN: 0004-637X. DOI: [10 . 1086 / 147615](https://doi.org/10.1086/147615). (Visited on 09/18/2023).
- Mauch, T. et al. (July 2003). “SUMSS: A Wide-Field Radio Imaging Survey of the Southern Sky – II. The Source Catalogue”. In: *Monthly Notices of the Royal Astronomical Society* 342.4, pp. 1117–1130. ISSN: 0035-8711. DOI: [10 . 1046 / j . 1365 - 8711 . 2003 . 06605 . x](https://doi.org/10.1046/j.1365-8711.2003.06605.x). (Visited on 09/13/2023).
- Maxwell, J. Clerk (1865). “A Dynamical Theory of the Electromagnetic Field”. In: *Philosophical Transactions of the Royal Society of London* 155, pp. 459–512. ISSN: 0261-0523. JSTOR: [108892](https://www.jstor.org/stable/108892). (Visited on 06/05/2023).
- McGilchrist, M. M. et al. (Sept. 1990). “The 7C Survey of Radio Sources at 151 MHz - Two Regions Centered at RA 10h 28m, Dec. 41 and RA 06h 28m, DEC 45.” In: *Monthly Notices of the Royal Astronomical Society* 246, pp. 110–122. ISSN: 0035-8711. (Visited on 09/15/2023).
- Mills, B. Y. (Dec. 1952a). “Apparent Angular Sizes of Discrete Radio Sources: Observations at Sydney”. In: *Nature* 170.4338, pp. 1063–1064. ISSN: 1476-4687. DOI: [10 . 1038 / 1701063a0](https://doi.org/10.1038/1701063a0). (Visited on 09/06/2023).

- Mills, B. Y. (June 1952b). “The Distribution of the Discrete Sources of Cosmic Radio Radiation”. In: *Australian Journal of Scientific Research A Physical Sciences* 5, p. 266. ISSN: 0004-9506. DOI: [10.1071/CH9520266](https://doi.org/10.1071/CH9520266). (Visited on 09/11/2023).
- (Jan. 1952c). “The Positions of Six Discrete Sources of Cosmic Radio Radiation”. In: *Australian Journal of Scientific Research A Physical Sciences* 5, p. 456. ISSN: 0004-9506. DOI: [10.1071/CH9520456](https://doi.org/10.1071/CH9520456). (Visited on 09/06/2023).
- Mills, B. Y., O. B. Slee, and E. R. Hill (Sept. 1958). “A Catalogue of Radio Sources between Declinations +10° and -20°”. In: *Australian Journal of Physics* 11, p. 360. ISSN: 0004-9506. DOI: [10.1071/PH580360](https://doi.org/10.1071/PH580360). (Visited on 10/15/2023).
- Mingo, B et al. (Sept. 2019). “Revisiting the Fanaroff–Riley Dichotomy and Radio-Galaxy Morphology with the LOFAR Two-Metre Sky Survey (LoTSS)”. In: *Monthly Notices of the Royal Astronomical Society* 488.2, pp. 2701–2721. ISSN: 0035-8711. DOI: [10.1093/mnras/stz1901](https://doi.org/10.1093/mnras/stz1901). (Visited on 08/09/2023).
- Mingo, B et al. (Apr. 2022). “Accretion Mode versus Radio Morphology in the LOFAR Deep Fields”. In: *Monthly Notices of the Royal Astronomical Society* 511.3, pp. 3250–3271. ISSN: 0035-8711. DOI: [10.1093/mnras/stac140](https://doi.org/10.1093/mnras/stac140). (Visited on 05/16/2022).
- Minkowski, R. (Nov. 1960). “A New Distant Cluster of Galaxies.” In: *The Astrophysical Journal* 132, pp. 908–910. ISSN: 0004-637X. DOI: [10.1086/146994](https://doi.org/10.1086/146994). (Visited on 10/20/2023).
- Moldón, J. et al. (2015). “The LOFAR Long Baseline Snapshot Calibrator Survey”. In: *Astronomy and Astrophysics* 574. ISSN: 14320746. DOI: [10.1051/0004-6361/201425042](https://doi.org/10.1051/0004-6361/201425042). arXiv: [1411.2743](https://arxiv.org/abs/1411.2743).
- Morabito, L. et al. (Apr. 2021). “Sub-Arcsecond Imaging with the International LOFAR Telescope. I. Foundational Calibration Strategy and Pipeline”. In: *Astronomy & Astrophysics*. ISSN: 0004-6361. DOI: [10.1051/0004-6361/202140649](https://doi.org/10.1051/0004-6361/202140649). (Visited on 07/19/2021).
- Morabito, Leah K. et al. (2016). “LOFAR VLBI Studies at 55MHz of 4C 43.15, a $z = 2.4$ Radio Galaxy”. In: *Monthly Notices of the Royal Astronomical Society* 461.3, pp. 2676–2687. ISSN: 13652966. DOI: [10.1093/mnras/stw1501](https://doi.org/10.1093/mnras/stw1501). arXiv: [1606.06741](https://arxiv.org/abs/1606.06741).
- Mutel, R. L. and M. W. Hodges (Aug. 1986). “The Structure of Compact Double Radio Sources - 610 MHz VLBI Observations of 1518 + 047 and 2050 + 364”. In: *The Astrophysical Journal* 307, p. 472. ISSN: 0004-637X, 1538-4357. DOI: [10.1086/164436](https://doi.org/10.1086/164436). (Visited on 09/15/2023).
- O’Dea, Christopher P. and D. J. Saikia (Mar. 2021). “Compact Steep-Spectrum and Peaked-Spectrum Radio Sources”. In: *The Astronomy and Astrophysics Review* 29.1, p. 3. ISSN: 1432-0754. DOI: [10.1007/s00159-021-00131-w](https://doi.org/10.1007/s00159-021-00131-w). (Visited on 08/08/2023).
- Oort, J. H. and Th. Walraven (May 1956). “Polarization and Composition of the Crab Nebula”. In: *Bulletin of the Astronomical Institutes of the Netherlands* 12, p. 285. ISSN: 0365-8910. (Visited on 10/16/2023).
- Pacholczyk, A.G. (1970). “Radio astrophysics : nonthermal processes in galactic and extragalactic sources”. eng. In: A series of books in astronomy and astrophysics.
- Padovani, P. et al. (Aug. 2017). “Active Galactic Nuclei: What’s in a Name?” In: *Astronomy and Astrophysics Review* 25.1, pp. 1–91. ISSN: 09354956. DOI: [10.1007/s00159-017-0102-9](https://doi.org/10.1007/s00159-017-0102-9). arXiv: [1707.07134](https://arxiv.org/abs/1707.07134). (Visited on 08/06/2021).
- Panessa, Francesca et al. (May 2019). “The Origin of Radio Emission from Radio-Quiet Active Galactic Nuclei”. In: *Nature Astronomy* 3.5, pp. 387–396. ISSN: 23973366. DOI: [10.1038/s41550-019-0765-4](https://doi.org/10.1038/s41550-019-0765-4). (Visited on 06/17/2021).
- Paragi, Zsolt (May 2015). “Real-Time Processing e-VLBI with the EVN and the SKA”. In: *2015 1st URSI Atlantic Radio Science Conference (URSI AT-RASC)*, pp. 1–1. DOI: [10.1109/URSI-AT-RASC.2015.7303170](https://doi.org/10.1109/URSI-AT-RASC.2015.7303170).

BIBLIOGRAPHY

- Pawsey, J. L. (Jan. 1955). “A Catalogue of Reliably Known Discrete Sources of Cosmic Radio Waves.” In: *The Astrophysical Journal* 121, p. 1. ISSN: 0004-637X, 1538-4357. DOI: [10.1086/145957](https://doi.org/10.1086/145957). (Visited on 09/06/2023).
- (Jan. 1957). “Preliminary Statistics of Discrete Sources Obtained with the ‘Mills Cross’”. In: 4, p. 228. (Visited on 09/11/2023).
- Pawsey, J. L., R. Payne-Soott, and L. L. McCREADY (Feb. 1946). “Radio-Frequency Energy from the Sun”. In: *Nature* 157.3980, pp. 158–159. ISSN: 1476-4687. DOI: [10.1038/157158a0](https://doi.org/10.1038/157158a0). (Visited on 08/17/2023).
- Peacock, J. A., L. Miller, and A. R. G. Mead (Jan. 1986). “The Radio Emission from Optically Selected Quasars”. In: 119, p. 103. (Visited on 10/30/2023).
- Pilkington, J. D. H. and J. F. Scott (Jan. 1965). “A Survey of Radio Sources between Declinations 20° and 40°”. In: *Memoirs of the Royal Astronomical Society* 69, p. 183. (Visited on 09/07/2023).
- Price, R. M. and D. K. Milne (Aug. 1965). “The Parkes Catalogue of Radio Sources, Declination Zone -60° to -90°”. In: *Australian Journal of Physics* 18, p. 329. ISSN: 0004-9506. DOI: [10.1071/PH650329](https://doi.org/10.1071/PH650329). (Visited on 09/18/2023).
- Ratner, M. I. (Jan. 1976). “Very-Long-Baseline Observations of Jupiter’s Millisecond Radio Bursts”. In: (visited on 09/15/2023).
- Readhead, A. C. S., P. N. Wilkinson, and G. H. Purcell (July 1977). “Very Long Baseline Interferometry Observations at 610 MHz of Sources Which Are Suspected of Showing Decimetric Flux Density Variations.” In: *The Astrophysical Journal* 215, pp. L13–L15. ISSN: 0004-637X. DOI: [10.1086/182466](https://doi.org/10.1086/182466). (Visited on 09/18/2023).
- Reber, Grote (June 1940). “Notes: Cosmic Static.” In: *ApJ* 91, pp. 621–624. DOI: [10.1086/144197](https://doi.org/10.1086/144197).
- Rees, M. J. (Jan. 1971). “New Interpretation of Extragalactic Radio Sources”. In: *Nature* 229.5283, pp. 312–317. ISSN: 1476-4687. DOI: [10.1038/229312a0](https://doi.org/10.1038/229312a0). (Visited on 10/16/2023).
- Rees, Nick (May 1990). “A Deep 38-MHz Radio Survey of the Area Delta >+60.” In: *Monthly Notices of the Royal Astronomical Society* 244, pp. 233–246. ISSN: 0035-8711. (Visited on 09/15/2023).
- Rengelink, R. B. et al. (Aug. 1997). “The Westerbork Northern Sky Survey (WENSS)”. In: *Astronomy and Astrophysics Supplement Series* 124.2, pp. 259–280. ISSN: 0365-0138. DOI: [10.1051/aas:1997358](https://doi.org/10.1051/aas:1997358). (Visited on 06/04/2020).
- Robertson, Peter, Wayne Orchiston, and Bruce Slee (Nov. 2014). “JOHN BOLTON AND THE DISCOVERY OF DISCRETE RADIO SOURCES”. In: *Journal of Astronomical History and Heritage* 17.03, pp. 283–306. ISSN: 1440-2807. DOI: [10.3724/SP.J.1440-2807.2014.03.04](https://doi.org/10.3724/SP.J.1440-2807.2014.03.04). (Visited on 09/05/2023).
- Roettgering, H. J. A. et al. (Nov. 1994). “Samples of Ultra-Steep Spectrum Radio Sources.” In: *Astronomy and Astrophysics Supplement Series* 108, pp. 79–141. ISSN: 0365-0138. (Visited on 10/24/2023).
- Röttgering, Huub (Sept. 2003). “LOFAR, a New Low Frequency Radio Telescope”. In: *New Astronomy Reviews. High-Redshift Radio Galaxies - Past, Present and Future* 47.4, pp. 405–409. ISSN: 1387-6473. DOI: [10.1016/S1387-6473\(03\)00057-5](https://doi.org/10.1016/S1387-6473(03)00057-5). (Visited on 09/21/2023).
- Ryle, M. (Jan. 1968). “The Evolution of Quasi-Stellar Sources and Radio Galaxies”. In: *Highlights of Astronomy* 1, pp. 380–383. ISSN: 1539-2996. DOI: [10.1017/S1539299600001490](https://doi.org/10.1017/S1539299600001490). (Visited on 10/15/2023).
- Ryle, M. and R. W. Clarke (Apr. 1961). “An Examination of the Steady-state Model in the Light of Some Recent Observations of Radio Sources”. In: *Monthly Notices of the Royal Astronomical Society* 122.4, pp. 349–362. ISSN: 0035-8711. DOI: [10.1093/mnras/122.4.349](https://doi.org/10.1093/mnras/122.4.349). (Visited on 09/11/2023).

- Ryle, M. and P. A. G. Scheuer (July 1955). “The Spatial Distribution and the Nature of Radio Stars”. In: *Proceedings of the Royal Society of London Series A* 230, pp. 448–462. ISSN: 0080-4630/1364-5021. DOI: [10.1098/rspa.1955.0146](https://doi.org/10.1098/rspa.1955.0146). (Visited on 09/11/2023).
- Ryle, M. and D. D. Vonberg (Sept. 1946). “Solar Radiation on 175 Mc./s”. In: *Nature* 158.4010, pp. 339–340. ISSN: 1476-4687. DOI: [10.1038/158339b0](https://doi.org/10.1038/158339b0). (Visited on 08/06/2023).
- Ryle, Martin and M. S. Longair (June 1967). “A Possible Method for Investigating the Evolution of Radio Galaxies”. In: *Monthly Notices of the Royal Astronomical Society* 136.2, pp. 123–140. ISSN: 0035-8711. DOI: [10.1093/mnras/136.2.123](https://doi.org/10.1093/mnras/136.2.123). (Visited on 10/15/2023).
- Schmidt, M. (Mar. 1963). “3C 273 : A Star-Like Object with Large Red-Shift”. In: *Nature* 197.4872, pp. 1040–1040. ISSN: 1476-4687. DOI: [10.1038/1971040a0](https://doi.org/10.1038/1971040a0). (Visited on 08/28/2023).
- Schmidt, Maarten (Nov. 1970). “Space Distribution and Luminosity Functions of Quasars”. In: *The Astrophysical Journal* 162, p. 371. ISSN: 0004-637X. DOI: [10.1086/150668](https://doi.org/10.1086/150668). (Visited on 11/01/2023).
- Sciama, D. W. (Apr. 1963). “On the Interpretation of Radio Source Counts”. In: *Monthly Notices of the Royal Astronomical Society* 126.2, pp. 195–201. ISSN: 0035-8711. DOI: [10.1093/mnras/126.2.195](https://doi.org/10.1093/mnras/126.2.195). (Visited on 09/11/2023).
- Science., British Association for the Advancement of (1889). *Report of the British Association for the Advancement of Science*. Vol. 58th meeting (1888). London, p. 1254.
- Scott, P. F. and M. Ryle (May 1961). “The Number–Flux Density Relation for Radio Sources Away from the Galactic Plane”. In: *Monthly Notices of the Royal Astronomical Society* 122.5, pp. 389–397. ISSN: 0035-8711. DOI: [10.1093/mnras/122.5.389](https://doi.org/10.1093/mnras/122.5.389). (Visited on 09/10/2023).
- Seyfert, Carl K. (Jan. 1943). “Nuclear Emission in Spiral Nebulae.” In: *The Astrophysical Journal* 97, p. 28. ISSN: 0004-637X. DOI: [10.1086/144488](https://doi.org/10.1086/144488). (Visited on 10/23/2023).
- Shakeshaft, J. R. et al. (Jan. 1955). “A Survey of Radio Sources between Declinations —38° and +83°.” In: *Memoirs of the Royal Astronomical Society* 67, p. 106. (Visited on 09/11/2023).
- Shimmins, A. J. and G. A. Day (June 1968). “The Parkes Catalogue of Radio Sources, Declination Zone +20° to +27°”. In: *Australian Journal of Physics* 21, p. 377. ISSN: 0004-9506. DOI: [10.1071/PH680377](https://doi.org/10.1071/PH680377). (Visited on 09/18/2023).
- Shimmins, A. J. et al. (Dec. 1966). “The Parkes Catalogue of Radio Sources, Declination Zone 0° to -20°”. In: *Australian Journal of Physics* 19, p. 837. ISSN: 0004-9506. DOI: [10.1071/PH660837](https://doi.org/10.1071/PH660837). (Visited on 09/18/2023).
- Shimwell, T. W. et al. (Feb. 2017). “The LOFAR Two-metre Sky Survey”. In: *Astronomy & Astrophysics* 598, A104. ISSN: 0004-6361. DOI: [10.1051/0004-6361/201629313](https://doi.org/10.1051/0004-6361/201629313). (Visited on 11/30/2018).
- Shimwell, T. W. et al. (Feb. 2019). “The LOFAR Two-metre Sky Survey - II. First Data Release”. In: *Astronomy & Astrophysics* 622, A1. ISSN: 0004-6361, 1432-0746. DOI: [10.1051/0004-6361/201833559](https://doi.org/10.1051/0004-6361/201833559). (Visited on 02/01/2022).
- Shimwell, T. W. et al. (Mar. 2022). “The LOFAR Two-metre Sky Survey - V. Second Data Release”. In: *Astronomy & Astrophysics* 659, A1. ISSN: 0004-6361, 1432-0746. DOI: [10.1051/0004-6361/202142484](https://doi.org/10.1051/0004-6361/202142484). (Visited on 06/30/2023).
- Shklovsky, Joseph (1953). In: *Proc. Acad. Sci. USSR* 90, p. 983.
- (Feb. 1964). “Nature of Sources of Cosmic Synchrotron Radiation”. In: *Nature* 201.4919, pp. 588–588. ISSN: 1476-4687. DOI: [10.1038/201588a0](https://doi.org/10.1038/201588a0). (Visited on 10/16/2023).
- Smith, F. G. (Sept. 1951). “An Accurate Determination of the Positions of Four Radio Stars”. In: *Nature* 168.4274, pp. 555–555. ISSN: 1476-4687. DOI: [10.1038/168555a0](https://doi.org/10.1038/168555a0). (Visited on 10/05/2023).
- Susskind, Charles (1964). “Observations of Electromagnetic-Wave Radiation before Hertz”. In: *Isis* 55.1, pp. 32–42. ISSN: 0021-1753. JSTOR: [227753](https://www.jstor.org/stable/227753). (Visited on 08/17/2023).

BIBLIOGRAPHY

- Sweijen, F. et al. (Jan. 2022a). “Deep Sub-Arcsecond Wide-Field Imaging of the Lockman Hole Field at 144 MHz”. In: *Nature Astronomy*, pp. 1–7. ISSN: 2397-3366. DOI: [10.1038/s41550-021-01573-z](https://doi.org/10.1038/s41550-021-01573-z). (Visited on 01/28/2022).
- Terashima, Yuichi and Andrew S. Wilson (Jan. 2003). “Chandra Snapshot Observations of Low-Luminosity Active Galactic Nuclei with a Compact Radio Source”. In: *The Astrophysical Journal* 583, pp. 145–158. ISSN: 0004-637X. DOI: [10.1086/345339](https://doi.org/10.1086/345339). (Visited on 11/01/2023).
- Véron, M. P. and P. Véron (Dec. 1974). “A Catalogue of Extragalactic Radio Source Identifications”. In: *Astronomy and Astrophysics Supplement Series* 18, p. 309. ISSN: 0365-0138. (Visited on 09/07/2023).
- Visser, A. E. et al. (May 1995). “The 7C Survey of Radio Sources at 151 MHz - a 418-Square-Degree Region Centred at RA 17h, Dec. 65deg.” In: *Astronomy and Astrophysics Supplement Series* 110, p. 419. ISSN: 0365-0138. (Visited on 09/15/2023).
- White, Richard L. et al. (Feb. 1997). “A Catalog of 1.4 GHz Radio Sources from the FIRST Survey”. In: *The Astrophysical Journal* 475.2, pp. 479–493. ISSN: 0004-637X. DOI: [10.1086/303564](https://doi.org/10.1086/303564). (Visited on 06/04/2020).
- Wilkinson, P. N. et al. (Sept. 1979). “VLBI Observations of Compact Radio Sources at 609 Megahertz.” In: *The Astrophysical Journal* 232, pp. 365–381. ISSN: 0004-637X. DOI: [10.1086/157296](https://doi.org/10.1086/157296). (Visited on 09/15/2023).
- Williams, P. J. S., S. Kenderdine, and J. E. Baldwin (Jan. 1966). “A Survey of Radio Sources and Background Radiation at 38 Mc/s”. In: *Memoirs of the Royal Astronomical Society* 70, pp. 53–110. (Visited on 09/21/2023).

BIBLIOGRAPHY

CHAPTER 2

Technical primer

[Radio] images are square, because imagers make square images.

– R. J. van Weeren; LOFAR SKSP Meeting, Turin 2019

2.1 Interferometric imaging

Radio telescopes operate differently from what we are used to. While telescopes operating in the optical spectrum, or any telescope using some form of camera for that matter, record a signal that is a direct reflection of the intensity of the sky, radio telescopes operate in the Fourier domain. Electromagnetic waves fall on the receiver and one can record the voltage or power resulting from that. Turning these values into an image is a non-trivial task. We must first understand how an interferometer samples the radio sky.

Young’s double slit experiment demonstrates how a plane wave falling on two apertures projects a sinusoidal fringe pattern on a screen. Conceptually, a two-element interferometer can be seen as performing a double slit experiment on the incoming wavefront with the antennas being the “slits”. Via the reciprocity theorem, we can turn this around and state that the instrument will cast an identical fringe pattern on the sky. This is the pattern seen in the left diagram of Fig. 1.3. Through these fringes, Equation 1.1 now can be split into two parts as

$$\theta_{\text{pb}} \propto \frac{\lambda}{D} \quad (2.1)$$

$$\theta_{\text{syn}} \propto \frac{\lambda}{b} \quad (2.2)$$

where θ_{pb} is the field of view expressed as the FWHM of the “*primary beam*” set by the antenna diameter D ; b denotes the largest separation between two antennas, also known as the longest baseline and θ_{syn} indicates the FWHM of the “*synthesised beam*”, indicating the angular resolution. For a sinusoidal sensitivity pattern, the latter manifests as the spacing of the fringes. The former is a global attenuation caused by the individual antenna’s reception pattern. Conceptually, one way of interpreting Equation 1.4 is that it tells you the distance between two points after which you can no longer (accurately) measure a difference in arrival time at each antenna.

A major problem of interferometers now arises: an individual fringe pattern is most sensitive to scales corresponding to its fringe spacing. In other words, baselines in interferometers act as spatial filters. Each

angular scale of interest on the sky needs to be represented by a baseline on the ground. The longest baseline thus limits the smallest angular scale the instrument can probe. Conversely, the shortest baseline dictates the largest angular scale that the instrument is sensitive to. The placement of antennas needs to be carefully considered when observing sources with radio emission on various angular scales. One solution is to simply build a dense array that samples all scales (relatively) well. The other solution is to have movable antennas, such as the VLA, and to regularly rotate through configurations to allow observations tailored to the observer's needs. Finally, to make up for the typically extremely sparse sampling provided by a limited number of antennas used, the Earth's rotation is exploited by long integration times, where the changing projection of the baselines on the sky slowly fills the synthetic aperture as the Earth rotates.

With a very basic understanding of how interferometers sample the sky, we can finally discuss imaging. Interferometric data lives in the Fourier domain, so we need a way to transform that back to the normal intensity domain in order to make an image. At the heart of this transformation lies the *van Cittert–Zernike theorem*. Mathematically this theorem states

$$\mathcal{V}_v(u, v, w) = \iint \mathcal{I}_v(l, m) e^{-2\pi i(ul+vm+wn)} dl dm \quad (2.3)$$

where $\mathcal{V}_v(u, v, w)$ is the so-called *visibility function* sampled at the coordinates (u, v, w) . These coordinates are expressed as multiples of the observing wavelength. \vec{u} points east and \vec{v} points towards the north celestial pole. \vec{w} points towards the delay centre of the observation and its magnitude w represents a delay in arrival time of the signal between two antennas. For any source in the field, we then define a direction vector $\vec{s} = (l, m, n)$ by projecting it onto \vec{u} , \vec{v} and \vec{w} . The visibility function results from integrating over the sky intensity distribution \mathcal{I} . The latter is only a function of l and m since \vec{s} is a unit vector and thus two components automatically set the third. If we assume that $wn \ll un + vm$, we see that \mathcal{V} becomes the 2D Fourier Transform of \mathcal{I} :

$$\mathcal{V}_v(u, v) = \iint \mathcal{I}_v(l, m) e^{-2\pi i(ul+vm)} dl dm \quad (2.4)$$

or conversely

$$\mathcal{I}_v(l, m) = \iint \mathcal{V}_v(u, v) e^{2\pi i(ul+vm)} du dv \quad (2.5)$$

For a small patch of the sky where the “ w -term” is negligible, the sky brightness distribution can thus be recovered by taking the Fourier Transform of the measured visibilities. To first order this w -term can be eliminated by so-called “fringe-stopping”. This is achieved by introducing an extra factor $e^{2\pi iw}$. Multiplying Eqn. 2.3 with this factor it turns into:

$$\mathcal{V}_v(u, v, w) = \iint \mathcal{I}_v(l, m) e^{-2\pi i(ul+vm+w(n-1))} \frac{dl dm}{\sqrt{1-l^2-m^2}} \quad (2.6)$$

The assumption of a small w -term now turns into the criterion of $w(n-1) = w(\sqrt{1-l^2-m^2}-1) \ll 1$. Unfortunately, this assumption breaks down for non-co-planar arrays or large images. In the early 1990s [T. J. Cornwell et al., 1992](#) already devised two ways to deal with this. One approach is to extend 2.6 to a full 3d Fourier transform. Another approach is to divide the sky into small patches where locally the variation of w is negligible or acceptably small. This is often called “facetting”. These ideas eventually evolved into the modern adaptations that are used today in the form of w -projection ([Tim J. Cornwell et al., 2008](#)), w -stacking ([Offringa et al., 2014](#)) or improvements thereon ([Ye et al., 2020](#); [Arras et al., 2021](#))

2.1.1 Gridding

Direct Fourier Transforms are expensive to calculate, notwithstanding the millions to billions of visibilities one needs to transform for modern interferometers. One would thus prefer to use Fast Fourier Transforms (FFTs) where possible. Such algorithms come at a cost as well: they operate a regular grid. This is problematic since the measured visibilities do not form a regularly sampled grid. The process of converting the irregularly sampled uv plane to a regularly sampled grid is called “gridding”. Analogous to pixels in an image, this grid consists of cells $\Delta u \times \Delta v$ in size, within which visibilities are grouped to a single value. How exactly one does that grouping is of importance for the resulting image quality. In one of its simplest forms, one would choose a Δu and Δv and simply sum or average all the visibilities nearest to each cell’s centre (J. Jackson et al., 1991). As it turns out, this is not the optimal way of gridding. It was shown by O’Sullivan, 1985 a convolution with

$$C(x) = \frac{\sin x\pi}{x\pi} \quad (2.7)$$

is the ideal approach to use during gridding. This function is also known as the sinc $x\pi$ function. It extends infinitely, however, which is undesirable from the point of view of computational cost. Unfortunately, truncating or otherwise limiting the sinc function’s extent can reintroduce artifacts in the image plane after Fourier-Transforming the gridded data. The existence of the w term makes gridding ultimately a three-dimensional problem. In reality, $C(x)$ is thus a function of the entire Fourier plane: $C(u, v, w)$. As such, gridding has been and still is an area that is actively studied in order to find methods that are fast, accurate and well-behaved. This led to the development of, for example, the aforementioned w -gridded or the image domain gridded (IDG, Tol et al., 2018; Bram Veenboer et al., 2019) which have both played an important role in realising this work. A detailed exploration of all these methods is beyond the scope of this thesis to discuss, but essentially all aim to minimise aliasing, account for the w -term and bring the problem back to the realm of FFTs. Especially the development of fast algorithms such as IDG and w gridded played an important role in making the work of this thesis possible.

2.1.2 Deconvolution

After gridding the data can finally be inverted to from the uv plane to the image plane. Of course, the complications don’t stop there. Interferometric observations sample the uv plane incompletely, thus leaving holes in the uv coverage. This can be due to finite observation time, limited bandwidth or a limited number of baselines, for example, but it ultimately means that the point spread function (psf) will be degraded. The initial image created from gridded data will be contaminated by sidelobe structures of the psf. This first image is referred to as a “dirty image” and the degraded psf as the “dirty psf” (or “dirty beam”). In a 2D case, the simplest form of the dirty psf is obtained by considering a sampling function

$$\mathcal{S}(u, v) = \begin{cases} 1, & \text{if } \exists \mathcal{V}^{\text{obs}}(u, v) \in \mathbb{C} \\ 0, & \text{otherwise} \end{cases} \quad (2.8)$$

where $\mathcal{V}_v^{\text{obs}}(u, v)$ are the observed samples of the visibility function \mathcal{V} and \mathbb{C} indicates the set of complex numbers. Equation 2.5 can then be rewritten as

$$\mathcal{I}_v^{\text{dirty}}(l, m) = \iint \mathcal{S}(u, v) \mathcal{V}_v(u, v) \exp^{2\pi i(ul+vm)} \mathrm{d}u \mathrm{d}v \quad (2.9)$$

where $\mathcal{I}^{\text{dirty}}(l, m)$ is the observed sky intensity distribution in the dirty image. By the convolution theorem, we can write the Fourier transform of a product as the convolution of their respective Fourier transforms:

$$\mathcal{I}_v^{\text{dirty}}(l, m) = \left(\int \mathcal{S}(u, v) e^{2\pi i(ul+vm)} du dv \right) * \left(\int \mathcal{V}_v(u, v) e^{2\pi i(ul+vm)} du dv \right) \quad (2.10)$$

where $*$ indicates a convolution. Per Eqn. 2.5 the right term is just the sky intensity distribution $\mathcal{I}_v(u, v)$ again. The left term is what yields the dirty psf, allowing us finally to describe the dirty image as the sky brightness distribution convolved with the dirty psf:

$$\mathcal{I}_v^{\text{dirty}}(l, m) = \mathcal{P}_v^{\text{dirty}}(l, m) * \mathcal{I}_v(l, m) \quad (2.11)$$

For a perfectly sampled uv plane with $\mathcal{S}(u, v) = 1$ we see that $\mathcal{I}_v^{\text{dirty}}(u, v) = \mathcal{I}_v^{\text{dirty}}(u, v)$. Any sparseness or undesirable features \mathcal{S} introduces in the Fourier domain (intentionally or unintentionally) will, however, reflect in $\mathcal{P}_v^{\text{dirty}}$ and worsen image fidelity.

To tackle this issue, a technique called “deconvolution” was invented. It aims to remove the sidelobe structures introduced by $\mathcal{P}_v^{\text{dirty}}$. A simple, and still the most widely used approach in radio interferometry, is the CLEAN algorithm first published by Högbom, 1974. After making the dirty image, the idea is to iteratively subtract a scaled version of the dirty psf to build up a model of the sky, which can then be “restored” using the “restoring psf”¹ $\mathcal{V}_v^{\text{clean}}$. The procedure can be summarised as follows:

1. Create the dirty image and dirty psf.
2. Find the brightest peak $I_v^{\text{dirty, peak}}$ at location (x, y) in the image².
3. Subtract a scaled version of the dirty psf $g\mathcal{P}_v^{\text{dirty}}$ from the entire map, centred at (x, y) . Here g is the so-called “loop gain”.
4. Add $g \cdot \delta(x, y)$ to the model \mathcal{M} .
5. Repeat 1 and 2 on the residual image \mathcal{R}_v , until all real emission is CLEANed.
6. Estimate the clean psf.
7. Create the CLEAN image by first convolving the model components with the clean psf and subsequently adding them back to the final residual image.

Mathematically, we can thus describe the CLEAN image as

$$I_v^{\text{clean}} = \mathcal{R}_v + \left(\mathcal{P}_v^{\text{clean}} * \mathcal{M} \right) \quad (2.12)$$

It was later mathematically proven by Schwarz, 1978 that clean represents a least-squares fit of sine functions to the visibility function. B. G. Clark, 1980 expanded on this algorithm with the introduction of major and minor cycles, among other improvements. In the minor cycle a classic hogböm clean is performed for several iterations. A major cycle is then triggered which subtracts a Fourier transform of the model from the

¹also called the “restoring beam” or the “clean beam”.

²Technically one wants to search for the location of maximum correlation between $\mathcal{P}_v^{\text{dirty}}$ and $I_v^{\text{dirty, peak}}$

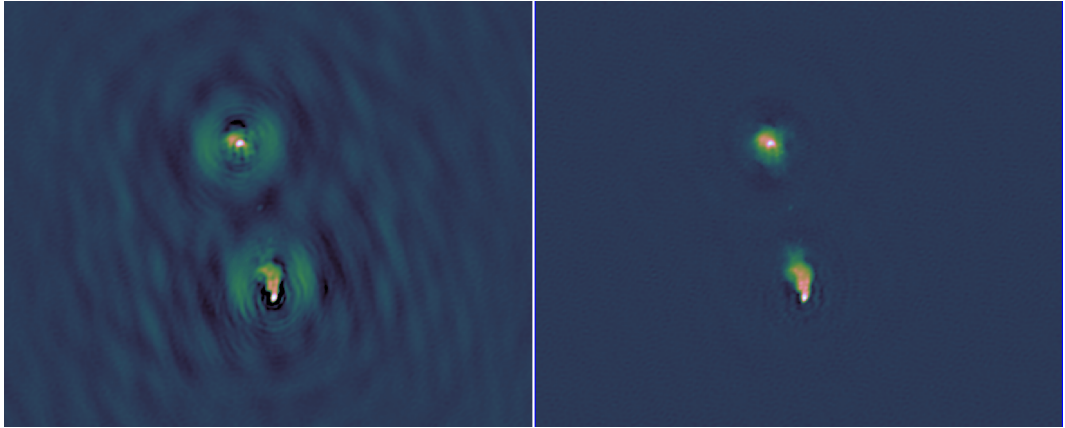


Figure 2.1: A comparison between a dirty image and a clean image of 4C 43.15. The side lobe patterns contaminate the image notably, making identification of real emission harder and also affecting the rest of the field should one be interested in imaging and/or calibrating other nearby sources.

gridded uv data. A second improvement was that only a limited area of the dirty psf was considered and that only peaks brighter than the first side lobe would be considered for the minor cycles. This enabled the deconvolution of large images that could not fit entirely in memory. A few years later, Schwab, 1984 described an updated algorithm to accommodate direction-dependent effects, where the difference was that in the major cycle, model components were now subtracted from the ungridded visibilities with the corrections for that specific direction. Multiscale clean (Tim J. Cornwell et al., 2008) is one of the more recent extensions to the classic algorithm. Originally it worked by means of δ functions, which become numerous when dealing with diffuse emission. This makes it both computationally intensive in terms of the number of model components and arguably less suited to describe such emission. Multiscale clean therefore allows 2D Gaussian profiles to be fit on various scales as well. Other forms of deconvolution have been or are being explored as well, such as the maximum entropy method (MEM) (Gull et al., 1978; Narayan et al., 1986), compressed sensing methods like MORESANE (Dabbech et al., 2015) or Bayesian approaches like resolve (Junklewitz et al., 2016). Nonetheless, clean remains the most widespread deconvolution algorithm in use today. Figure 2.1 demonstrates the difference CLEAN makes to image fidelity.

2.2 Interferometric calibration

Perhaps the most important chapter of this thesis focuses on the calibration of the ILT. In this section, we will therefore give the reader a crash course in radio-interferometric calibration to provide some technical background to the subsequent chapters.

As astronomers grew more ambitious and instruments became more capable, the need for proper calibration became increasingly important. This required a formal mathematical framework that allows one to take into account the polarisation nature of light and also the imperfection of the instrument in a well-defined way. That framework is what we call the *radio interferometric measurement equation*, or RIME. It was introduced by Hamaker et al., 1996a as the first of a series of publications about radio polarimetry.

Together with [Sault et al., 1996](#), a matrix formulation of the calibration was presented by using the idea of Mueller and Jones calculus from optical polarimetry ([Jones, 1941](#)). Originally derived through 4×4 Mueller matrices that operate on the Stokes vector

$$\vec{S} = \begin{pmatrix} I \\ Q \\ U \\ V \end{pmatrix} = \begin{pmatrix} E_X E_X^\dagger + E_Y E_Y^\dagger \\ E_X E_X^\dagger - E_Y E_Y^\dagger \\ E_X E_Y^\dagger + E_Y E_X^\dagger \\ -i(E_X E_Y^\dagger - E_Y E_X^\dagger) \end{pmatrix} \quad (2.13)$$

where the \dagger symbol denotes the conjugate transpose operation, [Hamaker, 2000](#) reformulated it in terms of 2×2 Jones matrices that operate on the Jones vector

$$\vec{E} = \begin{pmatrix} E_x e^{i\phi_x} \\ E_y e^{i\phi_y} \end{pmatrix} \quad (2.14)$$

where E and ϕ denote the amplitude and phase of the two orthogonal components of the electric field vector. He finally demonstrated a practical example a few years later ([Hamaker, 2006](#))³. A rigorous discussion of the rime in the modern day context can be found in [Smirnov, 2011a](#); [Smirnov, 2011b](#); [Smirnov, 2011c](#); [Smirnov, 2011d](#), for example. The Mueller and Jones formulations of the RIME are mathematically equivalent, but the 2×2 Jones formulation is, in my opinion, intuitively easier to understand and hence the one I will introduce in this section. In the RIME, $\mathcal{V}(u, v)$ will represent the visibility *matrix* containing the correlations between two measured polarisations. For linear polarisation, such as measured by the ILT, this will be X and Y. For instruments that measure circular polarisations, like the VLA, this will be R and L. Following [Smirnov, 2011a](#) and [Thompson et al., 2017](#), the voltage measured by an antenna is proportional to the electric field, allowing us to write the observed visibility matrix for a pair of antennas p and q at a frequency ν , and eventually the Stokes parameters, as

$$\begin{aligned} \mathcal{V}_{p,q,\nu} &\propto \begin{pmatrix} E_X e^{i\phi_X} \\ E_Y e^{i\phi_Y} \end{pmatrix}_{p,\nu} \begin{pmatrix} E_X e^{i\phi_X} & E_Y e^{i\phi_Y} \end{pmatrix}_{q,\nu}^\dagger \\ &= \begin{pmatrix} \mathcal{V}_{X_p X_q} & \mathcal{V}_{X_p Y_q} \\ \mathcal{V}_{Y_p X_q} & \mathcal{V}_{Y_p Y_q} \end{pmatrix}_\nu \\ &= \begin{pmatrix} I + Q & U - iV \\ U - iV & I - Q \end{pmatrix}_\nu \end{aligned} \quad (2.15)$$

Following equations 3-8 from [Smirnov, 2011a](#), the observed visibilities can be described as the true visibilities distorted by some unknown “gain” \mathcal{G} :

$$\mathcal{V}_{pq}^{\text{obs}} = \mathcal{G}_p \mathcal{V}_{pq}^{\text{true}} \mathcal{G}_q^\dagger \quad (2.16)$$

or inversely:

$$\mathcal{V}_{pq}^{\text{true}} = \mathcal{G}_p^\dagger \mathcal{V}_{pq}^{\text{obs}} \mathcal{G}_q \quad (2.17)$$

³for completeness we also refer the interested reader to the discussion by [Hamaker et al., 1996a](#) about the definition of the stokes parameters.

As $\mathcal{V}_{pq}^{\text{true}}$ is of course unknown in practise, one searches for a model \mathcal{M} such that

$$\mathcal{V}_{pq}^{\text{obs}} = \mathcal{G}_p \mathcal{M}_{pq} \mathcal{G}_q^\dagger \quad (2.18)$$

In a worst-case scenario of solving the full Jones matrix, one tries to solve

$$\begin{pmatrix} \mathcal{V}_{X_p X_q} & \mathcal{V}_{X_p Y_q} \\ \mathcal{V}_{Y_p X_q} & \mathcal{V}_{Y_p Y_q} \end{pmatrix} = \begin{pmatrix} A_{XX} e^{i\phi_{XX}} & A_{XY} e^{i\phi_{XY}} \\ A_{YX} e^{i\phi_{YX}} & A_{YY} e^{i\phi_{YY}} \end{pmatrix}_p \begin{pmatrix} \mathcal{M}_{X_p X_q} & \mathcal{M}_{X_p Y_q} \\ \mathcal{M}_{Y_p X_q} & \mathcal{M}_{Y_p Y_q} \end{pmatrix} \begin{pmatrix} A_{XX} e^{i\phi_{XX}} & A_{XY} e^{i\phi_{XY}} \\ A_{YX} e^{i\phi_{YX}} & A_{YY} e^{i\phi_{YY}} \end{pmatrix}_q^\dagger \quad (2.19)$$

Calibration thus centres around finding the inverse gain to correct for \mathcal{G} that minimises the difference with respect to a model of the sky. The beauty of the RIME lies in \mathcal{G} . Successive gain matrices can capture successive corruptions in the signal chain. Calibration is now elegantly expressed as a set of perturbations to be solved for, in a physically motivated order, where the perturbation that occurs *last* in the chain is corrected for *first*. Physical elegance aside, the order should be treated with care. Since we are dealing with matrix multiplications, certain commutation rules apply:

1. Scalar matrices always commute.
2. Diagonal matrices commute amongst themselves.
3. 2×2 rotation matrices commute amongst themselves.

Scalar terms $\mathcal{G} = \begin{pmatrix} g & g \\ g & g \end{pmatrix}$ are independent of polarisation. Diagonal terms $\mathcal{G} = \begin{pmatrix} g_{XX} & 0 \\ 0 & g_{YY} \end{pmatrix}$ affect only the parallel hands. Terms $\mathcal{G} = \begin{pmatrix} g_{XX} & g_{XY} \\ g_{YX} & g_{YY} \end{pmatrix}$ that affect all correlations we shall refer to as “fulljones” terms. These do not commute and are thus crucial to apply at the correct time in the calibration process, lest one will introduce subtle inconsistencies.

2.2.1 Systematic effects

Telescopes are at the end of the signal chain in astronomical observations. The first corrupting effects that need to be corrected are thus those introduced by the system. This is achieved by observing bright calibrator sources whose flux density, spatial structure and polarisation properties (if applicable or required) are well known. Typically these will be referred to with names such as “flux density calibrators” or “bandpass calibrators”. The instrumental effects can include:

- instrumental polarisation \mathcal{D} : often called “leakage” this describes the polarised response of the instrument to an unpolarised source.
- bandpass response \mathcal{B} : translates between arbitrary system units and physical units (e.g. Jy). It describes the frequency response of the system.
- parallactic angle \mathcal{P} : a source rotates in the field of view as it moves across the sky.
- elevation effects \mathcal{E} : the effective area and sensitivity of the telescope change as a function of elevation.
- average time delays \mathcal{C} : individual station clocks can drift with respect to each other.

In the RIME formalism, this becomes

$$\mathcal{V}_{pq}^{\text{obs}} = \mathcal{B}_p \mathcal{C}_p \mathcal{E}_p \mathcal{D}_p \mathcal{P}_p \mathcal{V}_{pq}^{\text{true}} \mathcal{P}_q^\dagger a_q^\dagger \mathcal{E}_q^\dagger \mathcal{D}_q^\dagger \mathcal{C}_q^\dagger \mathcal{B}_q^\dagger \quad (2.20)$$

As an example to illustrate the non-commutative nature of gains, these matrices take the form

$$\begin{aligned} \mathcal{B} &= \begin{pmatrix} A_{XX} & 0 \\ 0 & A_{YY} \end{pmatrix} & \mathcal{C} &= \begin{pmatrix} e^{i\phi} & 0 \\ 0 & e^{i\phi} \end{pmatrix} & \mathcal{D} &= \begin{pmatrix} 1 & A_{XY} \\ A_{YX} & 1 \end{pmatrix} \\ \mathcal{E} &= \begin{pmatrix} A_{XX} e^{i\phi_{XX}} & A_{XY} e^{i\phi_{XY}} \\ A_{YX} e^{i\phi_{YX}} & A_{YY} e^{i\phi_{YY}} \end{pmatrix} & \mathcal{P} &= \begin{pmatrix} \cos \theta & \sin \theta \\ -\sin \theta & \cos \theta \end{pmatrix}, \end{aligned} \quad (2.21)$$

where A and ϕ indicate arbitrary amplitude and phase corrections.

2.2.2 Telluric effects

Before cosmic radio waves reach the telescope they are already distorted by telluric effects. At gigahertz radio frequencies this is mainly absorption from water vapour, while at lower frequencies effects from the ionosphere become the dominating effects (Sramek, 1990). Correcting for these effects is done through so-called *phase referencing*: a source with a known structure, ideally a point source, that is near the target of interest is used to calibrate the visibility phases. For mechanical telescopes such as the VLA, this means occasionally pointing at that nearby source. For telescopes such as the ILT, the field of view is so large that the phase reference easily fits within the primary beam. However, the idea of a single phase reference also breaks down in this case. We will come back to that section 1.4.3. First, we will focus on the ionosphere, as that is the most important for low-frequency telescopes such as the ILT (Intema et al., 2009; F. de Gasperin et al., 2018; F. de Gasperin et al., 2019).

The ionosphere's refractive nature introduces an additional dispersive delay on top that caused by the path length difference between the antennas (Mangum et al., 2015). As the ionosphere is a plasma, these are driven by the electron column density between the observer and the source. Following Datta-Barua et al., 2008 and Petit et al., 2010⁴, we can write the extra path length Δl a signal traverses as

$$\Delta l = \int_{\vec{r}_{\text{source}}}^{\vec{r}_{\text{telescope}}} (n - 1) dl \quad (2.22)$$

where n is the refractive index. Delays in signal arrival time encode the position that the signal came from. Changes in it will thus make sources dance across the sky. If this was a single offset, it would be straightforward to deal with. The problematic part is, of course, that these effects vary both temporally and spatially across the sky. Solar activity, geomagnetic activity, the seasons and diurnal changes will all affect the ionosphere and the distortions it induces. It can be anything from a slow waltz to a cosmic mosh pit. In the case of exceptional ionospheric violence, such as during a solar storm, its corruption can be severe enough to wipe out any usable signal.

Per equation 9.19 in Petit et al., 2010, grouping the last two terms, the refractive index n of eqn. 2.22 can be expanded in the form

$$n = 1 - \frac{q^2}{8\pi^2 m_e \epsilon_0} \frac{n_e}{v^2} - \frac{q^3 B \cos \theta}{16\pi^3 m_e^2 \epsilon_0} \frac{n_e}{v^3} - \left(\frac{q^4 n_e}{128\pi^4 m_e^2 \epsilon_0^2} + \frac{q^4 B^2 (1 + \cos^2 \theta)}{64\pi^4 m_e^3 \epsilon_0} \right) \frac{n_e}{v^4} \quad (2.23)$$

⁴specifically equation 9.14

which leads to a path length difference of

$$\begin{aligned}\Delta l = & -\frac{1}{\nu^2} \int_{\vec{r}_{\text{source}}}^{\vec{r}_{\text{telescope}}} \frac{q^2 n_e}{8\pi^2 m_e \epsilon_0} dl \\ & -\frac{1}{\nu^3} \int_{\vec{r}_{\text{source}}}^{\vec{r}_{\text{telescope}}} \frac{q^3 n_e B \cos \theta}{16\pi^3 m_e^2 \epsilon_0} dl \\ & -\frac{1}{\nu^4} \int_{\vec{r}_{\text{source}}}^{\vec{r}_{\text{telescope}}} \left(\frac{q^4 n_e^2}{128\pi^4 m_e^2 \epsilon_0^2} + \frac{q^4 n_e B^2 (1 + \cos^2 \theta)}{64\pi^4 m_e^3 \epsilon_0} \right) dl\end{aligned}$$

where terms have been rearranged to emphasize the frequency dependency. Finally, dividing by the speed of light, we get the time delay $\Delta\tau = \Delta l/c$. Which can be translated to a phase difference $\Delta\phi$ in the signal of

$$\Delta\phi = 2\pi\nu\Delta\tau \quad (2.24)$$

or

$$\begin{aligned}\Delta\phi = & -\frac{2\pi}{c\nu} \int_{\vec{r}_{\text{source}}}^{\vec{r}_{\text{telescope}}} \frac{q^2 n_e}{8\pi^2 m_e \epsilon_0} dl \\ & -\frac{2\pi}{c\nu^2} \int_{\vec{r}_{\text{source}}}^{\vec{r}_{\text{telescope}}} \frac{q^3 n_e B \cos \theta}{16\pi^3 m_e^2 \epsilon_0} dl \\ & -\frac{2\pi}{c\nu^3} \int_{\vec{r}_{\text{source}}}^{\vec{r}_{\text{telescope}}} \left(\frac{q^4 n_e^2}{128\pi^4 m_e^2 \epsilon_0^2} + \frac{q^4 n_e B (1 + \cos^2 \theta)}{64\pi^4 m_e^3 \epsilon_0} \right) dl\end{aligned}$$

Ionospheric distortions thus manifest as first, second and third-order phase effects that scale inversely with frequency. The third order term can usually be ignored at frequencies $\nu \gtrsim 40$ MHz (F. de Gasperin et al., 2018). Now we define the *total electron content* (TEC) as the integral over n_e :

$$\text{TEC} \equiv \int_{\vec{r}_{\text{source}}}^{\vec{r}_{\text{telescope}}} n_e dl \quad (2.25)$$

which is a column density with its corresponding unit being the *TEC unit* (TECU). It has been defined as $1 \text{ TECU} \equiv 10^{16} \text{ m}^{-2}$.

The first order term describes a dispersive delay, that can then be rewritten as a function of TEC:

$$\begin{aligned}\Delta\phi_1 = & -\frac{q^2}{4\pi m_e \epsilon_0 c} \left(\frac{\mathcal{I}}{10^{-16} \text{ TECU}} \right) \left(\frac{\nu}{\text{Hz}} \right)^{-1} \\ = & -8.44797256 \times 10^9 \times \frac{\mathcal{I}}{\nu} \frac{\text{Hz}}{\text{TECU}}\end{aligned} \quad (2.26)$$

The second order term describes the phenomenon known as *Faraday rotation*:

$$\begin{aligned}\Delta\phi_2 &= \frac{1}{v^2} \frac{q^3}{8\pi^2 m_e^2 \epsilon_0 c} \int_{\vec{r}_{\text{source}}}^{\vec{r}_{\text{telescope}}} n_e B \cos\theta dl \\ &= \frac{c^2}{v^2} \frac{q^3}{8\pi^2 m_e^2 \epsilon_0 c^3} \int_{\vec{r}_{\text{source}}}^{\vec{r}_{\text{telescope}}} n_e B \cos\theta dl \\ &= \lambda^2 \frac{\text{RM}}{\text{m}^{-2}}\end{aligned}\quad (2.27)$$

Here, RM indicates the *rotation measure*, which is typically expressed in rad m^{-2} . The effect was first reported by [Faraday, 1846a](#), observing the angle of the polarisation plane changing as light passed through a magnetic field. In the earth's ionosphere, a magnetoplasma, it originates from the circular birefringent nature of plasmas [Guéroult et al., 2023](#). It imparts a phase difference specifically between left and right *circular* polarisations of light. This is a devilish effect for telescopes using linear feeds, such as the ILT. In circular polarisation, it means moving intensity from RR to LL; the Stokes I intensity is conserved. In linear polarisation, however, it translates to moving intensity *out* of XX and YY into the cross hands XY and YX. The killing aspect for linear feeds is the *differential* Faraday rotation across the field of view and between antennas. This means the polarisation is rotated by different amounts for each receiver between a pair of telescopes and hence the Stokes I intensity is *not* conserved if not corrected for.

The third order term depends on the spatial structure and uniformity of the ionosphere. As this term only becomes relevant at frequencies below our range of interest, we ignore this term for the rest of this thesis.

2.2.3 Direction-dependent effects and self-calibration

Thus far we have assumed mostly direction-independent effects and that we are using a well-known source for calibration. While the latter is usually true for the flux density calibrators (at least, for the most part), for the phase reference and target source it is generally not. Secondly, as we mentioned earlier, the ionosphere varies temporally and spatially across the sky. Corrections derived at one time in a certain direction are thus not fully valid at another time or in another direction, leading to incomplete corrections. This necessitates corrections in multiple directions.

Halfway through the 1980s, [Schwab, 1984](#) noted the profound effect ionospheric distortions would have on radio frequencies < 300 MHz and how the self-calibration procedure up till then would fall short. Allowing the antenna phase to be a free parameter was the initial solution to this problem. While (self-)calibration has evolved to more advanced techniques and approaches (e.g. [Weeren et al. 2016](#); [Tasse 2014](#); [Weeren et al. 2021](#)), the basic principle of treating antenna phases and amplitudes as free parameters has remained the same. [T. J. Cornwell et al., 1992](#) generalised the facet approach of [Schwab, 1984](#) for widefield imaging and noted its potential power for calibration since each facet can be treated independently. One self-calibrates on sources inside the facet to obtain corrections in that direction. During imaging one then grids the visibilities multiple times using the corrections for each facet to create facet images, which can eventually be glued together into one large mosaic. Direction-dependent phase effects are predominantly ionospheric in nature at VHF frequencies. Direction-dependent amplitude corrections mostly capture errors in the primary beam corrections.

The issue of incomplete source models and corrections can be solved through the process known as “self-calibration”, assuming that the signal-to-noise ratio (SNR) is high enough. As its name implies, this tries to use the source itself to bootstrap the calibration. Discussed by [Pearson et al., 1984](#) and [T. Cornwell et al., 1989](#), for example, the basic premise is that we can use the information given to us by the data to make plausible assumptions about source structure. These assumptions can then be fed back into the calibration with the ultimate aim of obtaining a better result than before. It can be summarised in an iterative scheme:

1. Create an initial model, either from a first image or other constraints.
2. Calibrate the data against this model.
3. Image the corrected data and create a new model.
4. Repeat 2-4 until satisfied.

It is imperative that the degrees of freedom are kept limited and the system remains overdetermined, lest one starts “cooking”. In the presence of too many degrees of freedom, overfitting can occur where the data is artificially made to fit the model and (fake) source structure is calibrated into existence. The requirements are set by the number of parameters one intends to solve for (e.g. amplitudes or phases, polarisation dependent or independent) and by the number of independent measurements available (i.e. the visibilities). This can be achieved in multiple ways by

- Restricting the problem to be antenna-based instead of baseline-based. This reduces the degrees of freedom from $N(N - 1)/2$ to just N .
- Restricting the number of parameters being solved for. A scalar phase correction has only 2 phases to fit for, while a fulljones correction has 32 independent parameters: four amplitudes and four phases for each of the two antennas forming a baseline.
- Choosing a sufficiently large time or frequency interval such that many data points constrain the fit.
- Exploiting known functional or smooth behaviour, for example, the effect of the ionosphere as a function of frequency.

For arrays with a large number of antennas, these conditions tend to be relatively easily met. For $N \geq 5$ one already has 10 measurements to fit 8 parameters. For many- N interferometers such as the VLA (27 dishes) or the ILT (72 stations) the number of baselines rapidly outnumbers the number of parameters. The real challenge is achieving a sufficiently high SNR to be able to accurately fit the desired parameters on the relevant angular, time and frequency scales. For VLBI arrays (for example, the VLBA or EHT), however, antennas tend to be few and far between⁵ and great(er) care must be taken for their calibration.

While self-calibration still has not yet been formally proven to work or converge, it still pervades radio astronomy as a highly successful approach.

2.2.4 LOFAR calibration

Closing off this brief introduction about calibration, we will describe the procedure used to calibrate LOFAR’s HBA antennas. HBA observations first spend 15-minutes on a flux density calibrator, then 8-hours⁶ on the target field and finally 15-minutes on a flux density calibrator again for redundancy.

⁵If there was ever a moment for this expression, this is it. Pun intended.

⁶Or less, depending on the target’s elevation.

The direction-independent calibration strategy is described by [F. de Gasperin et al., 2019](#). It is currently implemented in the *LOFAR Initial Calibration* (LINC) pipeline⁷. The first part, dubbed LINC Calibrator, runs on the observation of the flux density calibrator. After averaging the data to a resolution of 4 s and 48.82 kHz, four main systematic effects are corrected for:

1. A phase offset between XX and YY; referred to as `polalign`.
2. Faraday rotation, such that more accurate bandpasses can be derived.
3. Bandpasses that give the translation between instrument units and physical units; referred to as `bandpass`.
4. Clock offsets between stations; referred to as `clock`.

The corrupting signal chain for LOFAR is as follows: the ionosphere imparts a dispersive delay and Faraday rotation as per the previous section, the signal is attenuated by the primary beam response, then is corrupted by the instrumental response like the bandpass and polarisation response and finally any drifts of the station clocks are imprinted when the time of measurement is recorded. Calibration is done with DP3 ([van Diepen et al., 2018a](#); [Dijkema et al., 2023](#)). Various effects are extracted using the *LOFAR Solution Tool* (LoSoTo)⁸. The first two effects are extracted from solutions derived with a special `rotation+diagonal` mode in DP3 ([F. de Gasperin et al., 2019](#)). This constrains the solutions to the form

$$\mathcal{G} = \begin{pmatrix} A_{XX} e^{i\psi_{XX}} & 0 \\ 0 & A_{YY} e^{i\psi_{YY}} \end{pmatrix} \begin{pmatrix} \cos \theta & -\sin \theta \\ \sin \theta & \cos \theta \end{pmatrix} \quad (2.28)$$

where $\theta \in \left[-\frac{\pi}{2}, \frac{\pi}{2}\right)$. This allows the fit to capture effects like Faraday rotation in the rotation matrix while capturing other effects in the diagonal matrix. For an unpolarised source, one expects no difference between the XX and YY correlations. Therefore, the `polalign` correction is obtained as $\psi_{PA} = \psi_{XX} - \psi_{YY}$. The solutions and derived correction are shown in [Fig. 2.2](#). An identical solve is now done to obtain the amount of Faraday rotation, providing an RM correction. These solutions and derived correction are shown in [Fig. 2.3](#). For the bandpass, the amplitude solutions shown in [Fig. 2.3](#) are used to estimate the diagonal matrix \mathcal{B} from [Eqn. 2.21](#) using LoSoTo's `BANDPASS` task. A median over time is taken to derive a time-independent bandpass correction. These solutions and derived correction are shown in [Fig. 2.4](#).

A bandpass correction translates instrumental units to physical units. One thus needs to have accurate knowledge of the calibrator source with which these corrections are derived. LOFAR's most commonly used flux density calibrators are a set of bright 3C sources: 3C 48, 3C 147, 3C 196, 3C 295 and 3C 380. They all have flux densities $S_\nu > 50$ Jy, but their structure varies significantly. 3C 48 and 3C 147 are the most point-like, but even they are extended at the 0.5 – 1'' scale. The others are up to 30'' in size. The ILT's longest baselines can reach an angular resolution of approximately 0.3'' (or slightly higher depending on the weighting scheme used), making these sources well resolved on international baselines and even moderately resolved on Dutch baselines already. The existing model of 3C 295 was insufficient for ILT work, for example. A more detailed model was therefore created as part of this thesis, shown in [Fig. 2.5](#), which is now included in LINC.

⁷<https://git.astron.nl/RD/LINC>; previously known as `prefactor`

⁸<https://github.com/revoltek/losoto>

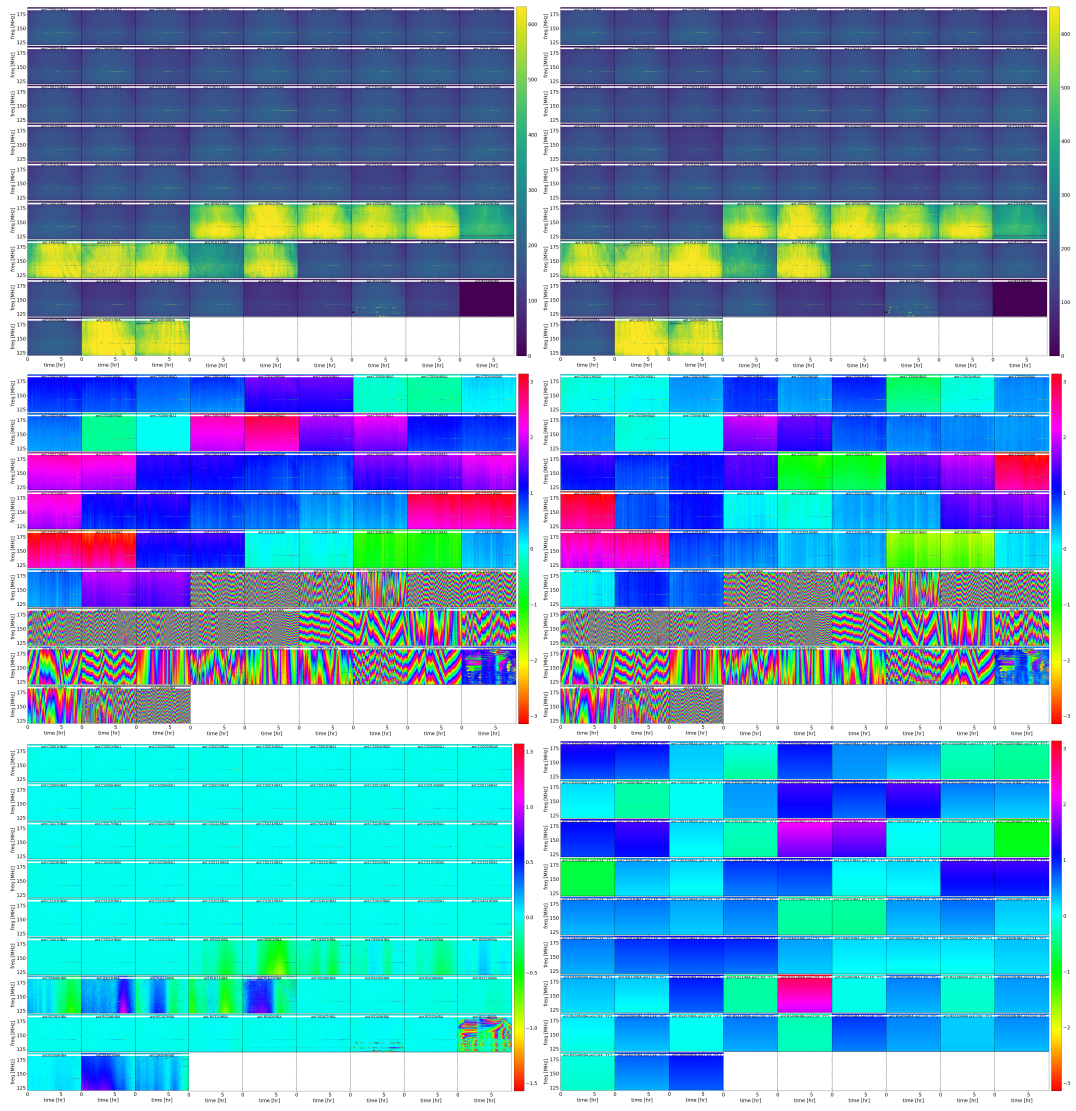


Figure 2.2: Solution plots for the polalign solve on an 8 hour scan of 3C 295. Top to bottom, left to right: XX amplitude, YY amplitude, XX phase, YY phase, rotation angle and derived correction.

2. TECHNICAL PRIMER

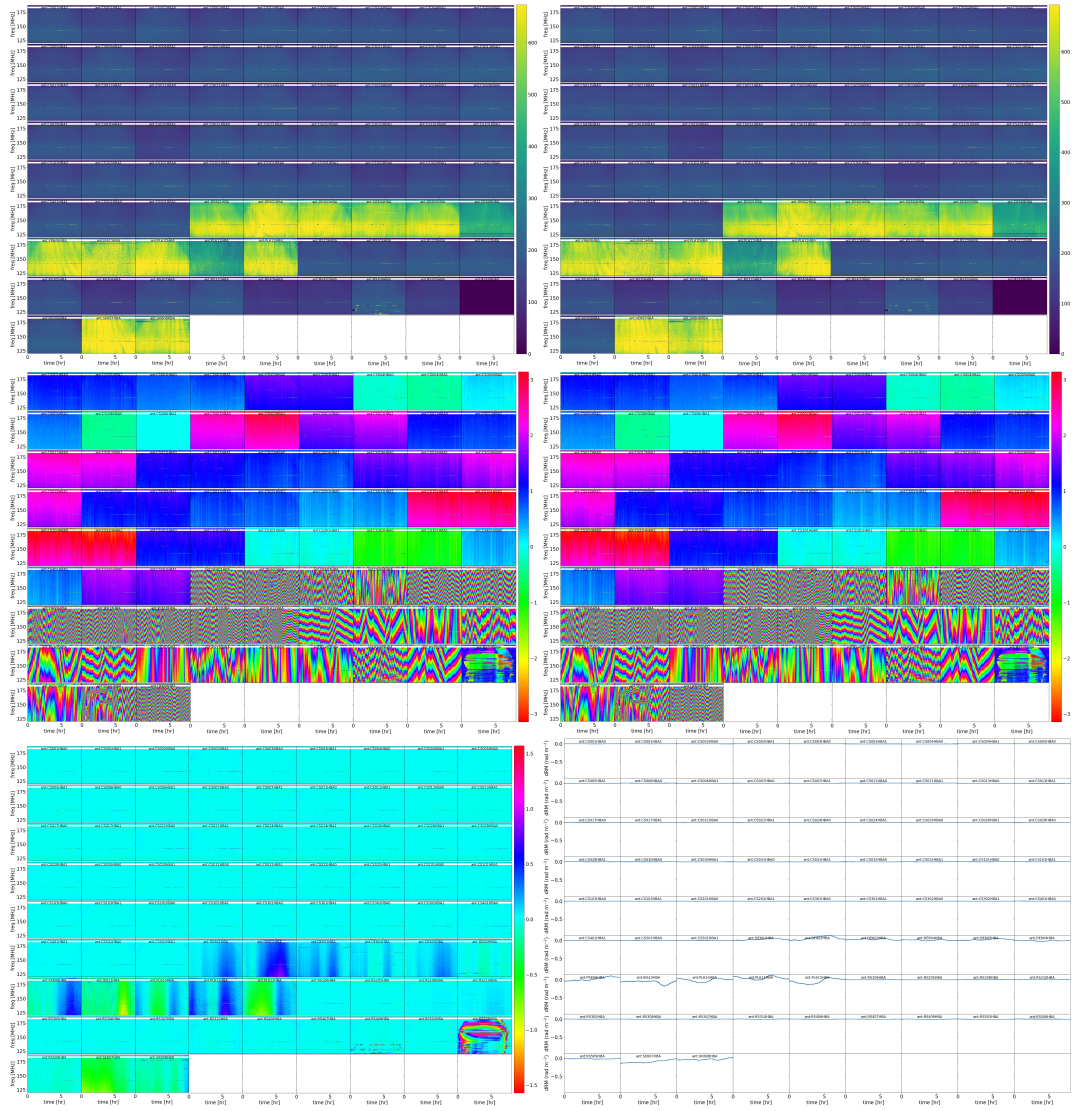


Figure 2.3: Solution plots for the Faraday rotation solve on an 8-hour scan of 3C 295. Top to bottom, left to right: XX amplitude, YY amplitude, XX phase, YY phase, rotation angle and derived correction.

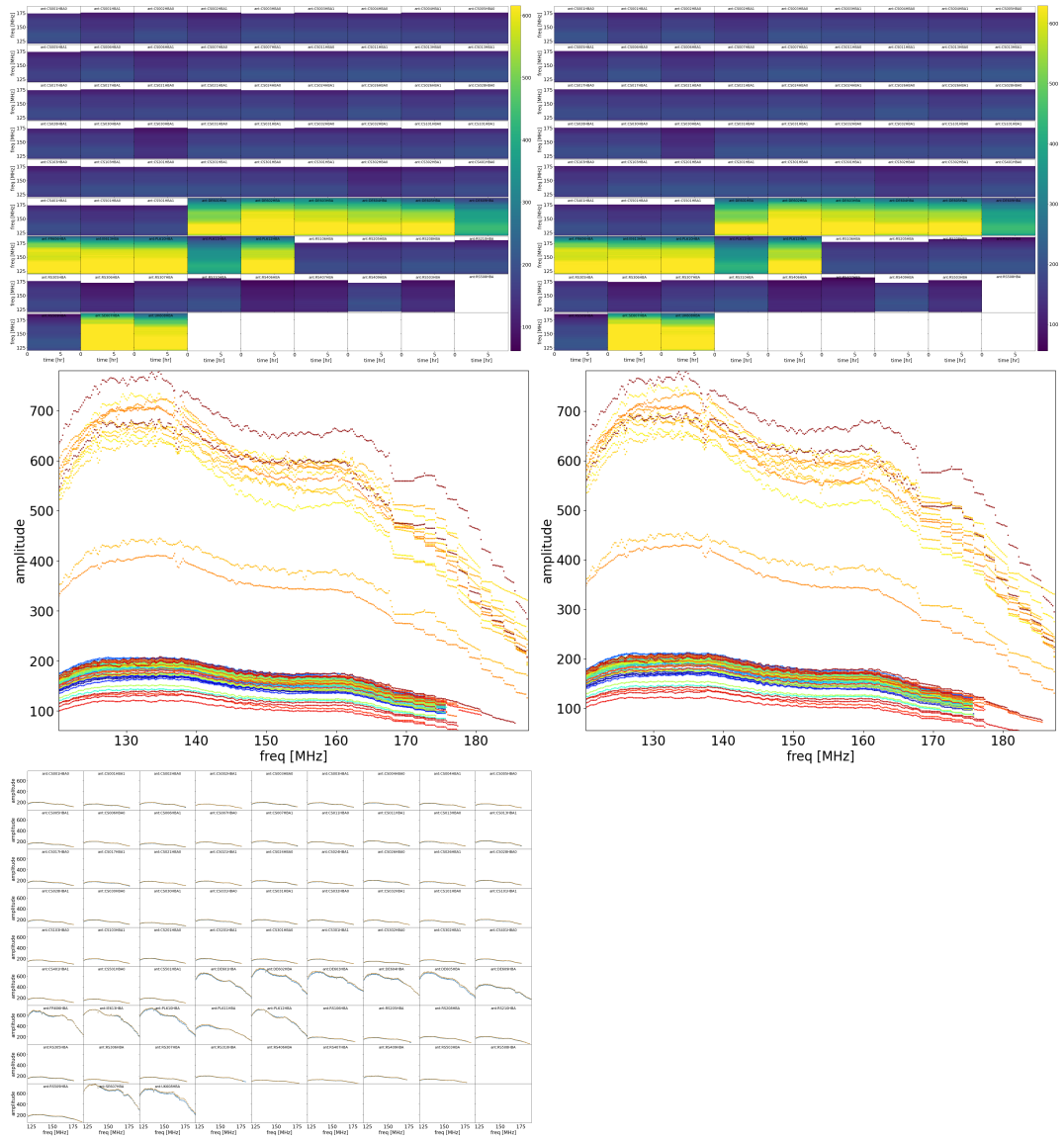


Figure 2.4: Solution plots for the bandpass on an 8-hour scan of 3C 295. Top to bottom, left to right: 2D plots of derived bandpasses for XX and YY, the median bandpass over time for XX and YY, and time-median bandpasses for individual stations.

Finally, each of ψ_{PA} , the RM correction and B are applied before doing a final scalar phase solve to solve ionospheric effects. This solves for a polarisation-independent phase:

$$\mathcal{G} = e^{i\psi} \begin{pmatrix} 1 & 0 \\ 0 & 1 \end{pmatrix} \quad (2.29)$$

Exploiting the known phase structure of a time delay (Eqn. 2.24) and ionospheric delay (Eqn. 2.26), so-called “clock-TEC separation” (Weeren et al., 2016; F. de Gasperin et al., 2018) is employed to separate phase changes due to offsets between station clocks from phase changes induced by the ionospheric delay. These are separated because the clock offsets are direction-independent and can thus be used to correct the target observation. The solutions and derived corrections are shown in fig. 2.6

With systematic corrections in hand, LINC Target derives direction-independent phase corrections for the target field, for the *Dutch* stations. First, the corrections from LINC Calibrator are applied. RMextract⁹ is then used to obtain RM corrections using satellite data, after which the data is averaged to a resolution of 8 s and 97.64 kHz (two channels per subband). A starting model is generated from the TGSS survey, from which diagonal phase solutions are derived:

$$\mathcal{G} = \begin{pmatrix} e^{i\psi_{XX}} & 0 \\ 0 & e^{i\psi_{YY}} \end{pmatrix} \quad (2.30)$$

The solutions from this step are shown in Fig. 2.7.

International stations require a different calibration approach. The systematic effects derived by LINC Calibrator are also derived for international stations. The international stations are calibrated using the lofar-vlbi pipeline¹⁰. The strategy is described by L. K. Morabito et al., 2022. This calibration was extended to the ILL’s full field of view in chapter 4 of this thesis (Sweijen et al., 2022a).

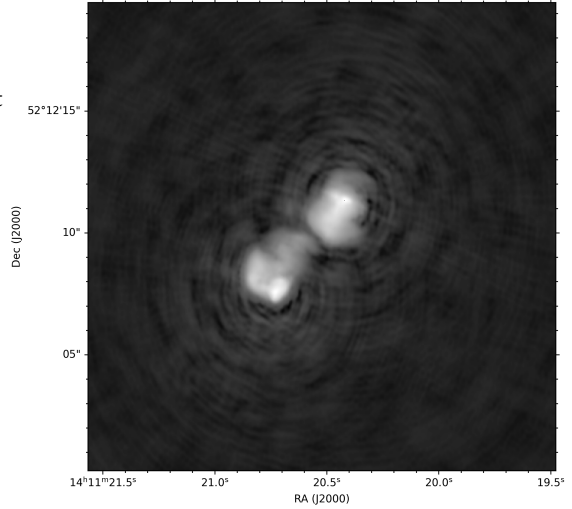


Figure 2.5: The final image of 3C 295 at 144 MHz and 0.3'' resolution, from which the clean-component model was used for bandpass calibration.

⁹<https://github.com/lofar-astron/RMextract>

¹⁰<https://github.com/lmorabit/lofar-vlbi>

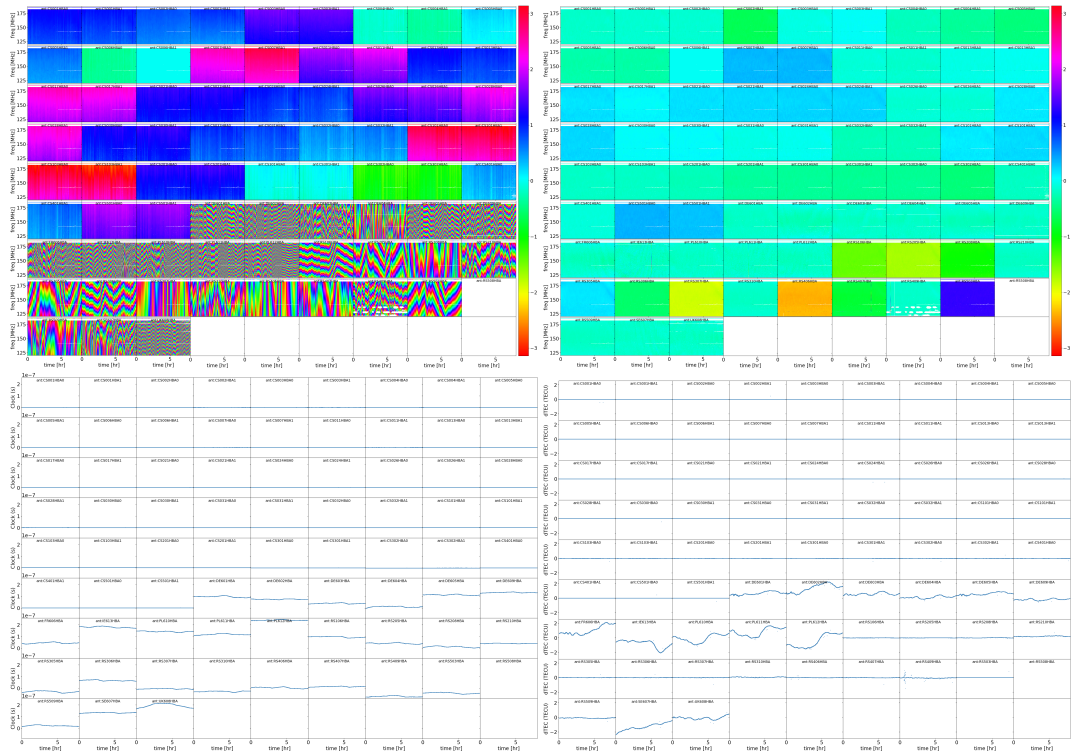


Figure 2.6: Solution plots for the final solve to correct for clock and ionospheric delays. Top to bottom, left to right: polarisation-independent phase solutions, the residuals after subtracting all derived corrections thus far, clock offsets and derived dTEC values.

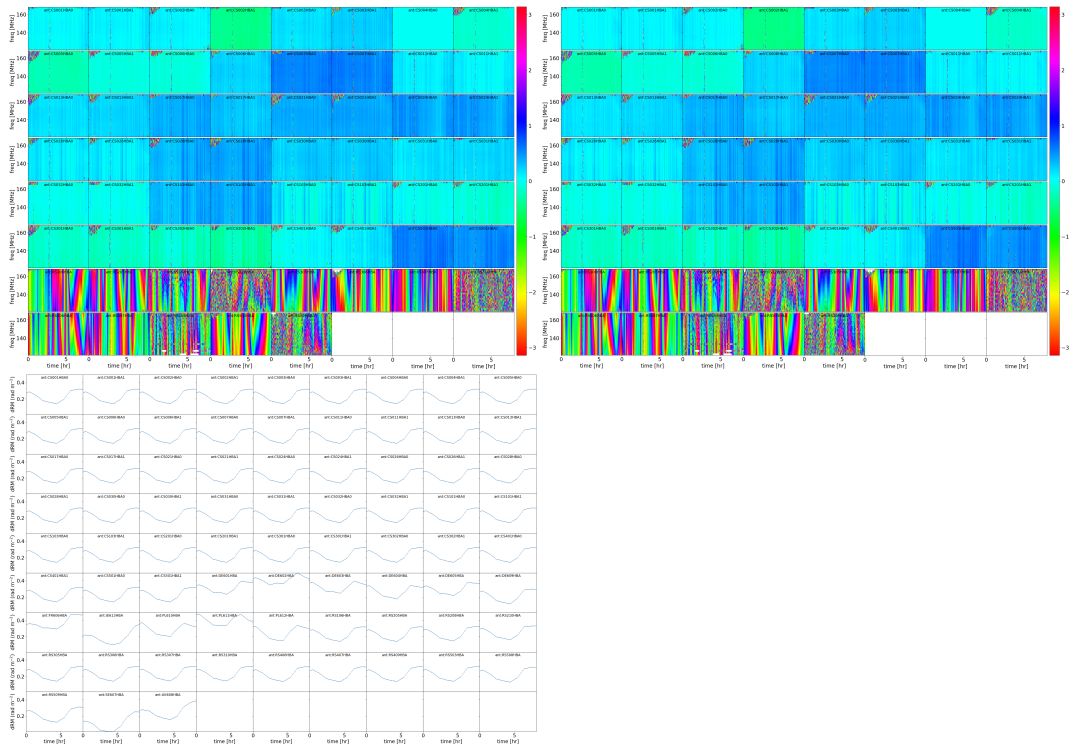


Figure 2.7: Phase solutions derived by LINC target after solving against a TGSS sky model.

Bibliography

- Arras, Philipp et al. (Feb. 2021). “Efficient Wide-Field Radio Interferometry Response”. In: *Astronomy & Astrophysics* 646, A58. ISSN: 0004-6361, 1432-0746. DOI: [10.1051/0004-6361/202039723](https://doi.org/10.1051/0004-6361/202039723). (Visited on 08/24/2023).
- Clark, B. G. (Sept. 1980). “An Efficient Implementation of the Algorithm ‘CLEAN’”. In: *Astronomy and Astrophysics* 89, p. 377. ISSN: 0004-6361. (Visited on 08/25/2023).
- Cornwell, T. J. and R. A. Perley (July 1992). “Radio-Interferometric Imaging of Very Large Fields. The Problem of Non-Coplanar Arrays.” In: *Astronomy and Astrophysics* 261, pp. 353–364. ISSN: 0004-6361. (Visited on 08/24/2023).
- Cornwell, Tim and Edward B. Fomalont (Jan. 1989). “Self-Calibration”. In: 6, p. 185. (Visited on 08/30/2023).
- Cornwell, Tim J., Kumar Golap, and Sanjay Bhatnagar (Oct. 2008). “The Noncoplanar Baselines Effect in Radio Interferometry: The W-Projection Algorithm”. In: *IEEE Journal of Selected Topics in Signal Processing* 2.5, pp. 647–657. ISSN: 1941-0484. DOI: [10.1109/JSTSP.2008.2005290](https://doi.org/10.1109/JSTSP.2008.2005290).
- Dabbech, A. et al. (Apr. 2015). “MORESANE: MODEL REconstruction by Synthesis-ANalysis Estimators - A Sparse Deconvolution Algorithm for Radio Interferometric Imaging”. In: *Astronomy & Astrophysics* 576, A7. ISSN: 0004-6361, 1432-0746. DOI: [10.1051/0004-6361/201424602](https://doi.org/10.1051/0004-6361/201424602). (Visited on 08/26/2023).
- Datta-Barua, S. et al. (2008). “Bounding Higher-Order Ionosphere Errors for the Dual-Frequency GPS User”. In: *Radio Science* 43.5. ISSN: 1944-799X. DOI: [10.1029/2007RS003772](https://doi.org/10.1029/2007RS003772). (Visited on 08/28/2023).
- de Gasperin, F. et al. (Aug. 2018). “The effect of the ionosphere on ultra-low-frequency radio-interferometric observations”. In: *A&A* 615, A179, A179. DOI: [10.1051/0004-6361/201833012](https://doi.org/10.1051/0004-6361/201833012). arXiv: [1804.07947](https://arxiv.org/abs/1804.07947) [astro-ph. IM].
- de Gasperin, F. et al. (Feb. 2019). “Systematic effects in LOFAR data: A unified calibration strategy”. In: *A&A* 622, A5, A5. DOI: [10.1051/0004-6361/201833867](https://doi.org/10.1051/0004-6361/201833867). arXiv: [1811.07954](https://arxiv.org/abs/1811.07954) [astro-ph. IM].
- Dijkema, T. J. et al. (May 2023). *DP3: Streaming processing pipeline for radio interferometric data*. Astrophysics Source Code Library, record ascl:2305.014. ascl: [2305.014](https://ascl.net/2305.014).
- Faraday, Michael (Dec. 1846a). “I. Experimental Researches in Electricity.—Nineteenth Series”. In: *Philosophical Transactions of the Royal Society of London* 136, pp. 1–20. DOI: [10.1098/rstl.1846.0001](https://doi.org/10.1098/rstl.1846.0001). (Visited on 08/30/2023).
- Gueroult, Renaud, Jean-Marcel Rax, and Nathaniel J. Fisch (Feb. 2023). “Wave Propagation in Rotating Magnetised Plasmas”. In: *Plasma Physics and Controlled Fusion* 65.3, p. 034006. ISSN: 0741-3335. DOI: [10.1088/1361-6587/acb1d4](https://doi.org/10.1088/1361-6587/acb1d4). (Visited on 08/30/2023).
- Gull, S. F. and G. J. Daniell (Apr. 1978). “Image Reconstruction from Incomplete and Noisy Data”. In: *Nature* 272.5655, pp. 686–690. ISSN: 1476-4687. DOI: [10.1038/272686a0](https://doi.org/10.1038/272686a0). (Visited on 08/26/2023).

- Hamaker, J. P. (May 2000). “Understanding Radio Polarimetry - IV. The Full-Coherency Analogue of Scalar Self-Calibration: Self-alignment, Dynamic Range and Polarimetric Fidelity”. In: *Astronomy and Astrophysics Supplement Series* 143.3, pp. 515–534. ISSN: 0365-0138, 1286-4846. DOI: [10.1051/aas:2000337](https://doi.org/10.1051/aas:2000337). (Visited on 08/26/2023).
- (Sept. 2006). “Understanding Radio Polarimetry - V. Making Matrix Self-Calibration Work: Processing of a Simulated Observation”. In: *Astronomy & Astrophysics* 456.1, pp. 395–404. ISSN: 0004-6361, 1432-0746. DOI: [10.1051/0004-6361:20065145](https://doi.org/10.1051/0004-6361:20065145). (Visited on 08/26/2023).
- Hamaker, J. P. and J. D. Bregman (May 1996a). “Understanding Radio Polarimetry. III. Interpreting the IAU/IEEE Definitions of the Stokes Parameters.” In: *Astronomy and Astrophysics Supplement Series* 117, pp. 161–165. ISSN: 0365-0138. (Visited on 08/26/2023).
- Högbom, J. A. (June 1974). “Aperture Synthesis with a Non-Regular Distribution of Interferometer Baselines”. In: *Astronomy and Astrophysics Supplement Series* 15, p. 417. ISSN: 0365-01380004-6361. (Visited on 08/24/2023).
- Intema, H. T. et al. (July 2009). “Ionospheric Calibration of Low Frequency Radio Interferometric Observations Using the Peeling Scheme - I. Method Description and First Results”. In: *Astronomy & Astrophysics* 501.3, pp. 1185–1205. ISSN: 0004-6361, 1432-0746. DOI: [10.1051/0004-6361/200811094](https://doi.org/10.1051/0004-6361/200811094). (Visited on 08/28/2023).
- Jackson, J.I. et al. (Sept. 1991). “Selection of a convolution function for Fourier inversion using gridding (computerised tomography application)”. In: *IEEE Transactions on Medical Imaging* 10.3, pp. 473–478. ISSN: 1558-254X. DOI: [10.1109/42.97598](https://doi.org/10.1109/42.97598).
- Jones, R. Clark (July 1941). “New Calculus for the Treatment of Optical Systems. I. Description and Discussion of the Calculus”. In: *Journal of the Optical Society of America (1917-1983)* 31, p. 488. ISSN: 0030-3941. (Visited on 11/10/2023).
- Junklewitz, H. et al. (Feb. 2016). “RESOLVE: A New Algorithm for Aperture Synthesis Imaging of Extended Emission in Radio Astronomy”. In: *Astronomy & Astrophysics* 586, A76. ISSN: 0004-6361, 1432-0746. DOI: [10.1051/0004-6361/201323094](https://doi.org/10.1051/0004-6361/201323094). (Visited on 08/26/2023).
- Mangum, Jeffrey G. and Patrick Wallace (Jan. 2015). “Atmospheric Refractive Electromagnetic Wave Bending and Propagation Delay”. In: *Publications of the Astronomical Society of the Pacific* 127.947, p. 74. ISSN: 1538-3873. DOI: [10.1086/679582](https://doi.org/10.1086/679582). (Visited on 08/28/2023).
- Morabito, L. K. et al. (Feb. 2022). “Sub-arcsecond imaging with the International LOFAR Telescope. I. Foundational calibration strategy and pipeline”. In: *A&A* 658, A1, A1. DOI: [10.1051/0004-6361/202140649](https://doi.org/10.1051/0004-6361/202140649). arXiv: [2108.07283 \[astro-ph.IM\]](https://arxiv.org/abs/2108.07283).
- Narayan, Ramesh and Rajaram Nityananda (Jan. 1986). “Maximum Entropy Image Restoration in Astronomy.” In: *Annual Review of Astronomy and Astrophysics* 24, pp. 127–170. ISSN: 0066-4146. DOI: [10.1146/annurev.aa.24.090186.001015](https://doi.org/10.1146/annurev.aa.24.090186.001015). (Visited on 08/26/2023).
- O’Sullivan, J. D. (1985). “A Fast Sinc Function Gridding Algorithm for Fourier Inversion in Computer Tomography”. In: *IEEE transactions on medical imaging* 4.4, pp. 200–207. ISSN: 0278-0062. DOI: [10.1109/TMI.1985.4307723](https://doi.org/10.1109/TMI.1985.4307723).
- Offringa, A. R. et al. (2014). “Wsclean: An Implementation of a Fast, Generic Wide-Field Imager for Radio Astronomy”. In: *Monthly Notices of the Royal Astronomical Society* 444.1, pp. 606–619. ISSN: 13652966. DOI: [10.1093/mnras/stu1368](https://doi.org/10.1093/mnras/stu1368). arXiv: [1407.1943](https://arxiv.org/abs/1407.1943).
- Pearson, T. J. and A. C. S. Readhead (Jan. 1984). “Image Formation by Self-Calibration in Radio Astronomy”. In: *Annual Review of Astronomy and Astrophysics* 22, pp. 97–130. ISSN: 0066-4146. DOI: [10.1146/annurev.aa.22.090184.000525](https://doi.org/10.1146/annurev.aa.22.090184.000525). (Visited on 08/30/2023).
- Petit, Gérard and Brian Luzum (Jan. 2010). “IERS Conventions (2010)”. In: *IERS Technical Note* 36, p. 1.

- Sault, R. J., J. P. Hamaker, and J. D. Bregman (May 1996). “Understanding Radio Polarimetry. II. Instrumental Calibration of an Interferometer Array.” In: *Astronomy and Astrophysics Supplement Series* 117, pp. 149–159. ISSN: 0365-0138. (Visited on 08/26/2023).
- Schwab, F. R. (July 1984). “Relaxing the Isoplanatism Assumption in Self-Calibration; Applications to Low-Frequency Radio Interferometry”. In: *The Astronomical Journal* 89, p. 1076. ISSN: 00046256. DOI: [10.1086/113605](https://doi.org/10.1086/113605). (Visited on 08/25/2023).
- Schwarz, U. J. (Apr. 1978). “Mathematical-Statistical Description of the Iterative Beam Removing Technique (Method CLEAN)”. In: *Astronomy and Astrophysics* 65, p. 345. ISSN: 0004-6361. (Visited on 08/25/2023).
- Smirnov, O. M. (Mar. 2011a). “Revisiting the Radio Interferometer Measurement Equation - I. A Full-Sky Jones Formalism”. In: *Astronomy & Astrophysics* 527, A106. ISSN: 0004-6361, 1432-0746. DOI: [10.1051/0004-6361/201016082](https://doi.org/10.1051/0004-6361/201016082). (Visited on 03/13/2023).
- (Mar. 2011b). “Revisiting the Radio Interferometer Measurement Equation: II. Calibration and Direction-Dependent Effects”. In: *Astronomy & Astrophysics* 527, A107. ISSN: 0004-6361, 1432-0746. DOI: [10.1051/0004-6361/201116434](https://doi.org/10.1051/0004-6361/201116434). (Visited on 03/13/2023).
- (Mar. 2011c). “Revisiting the Radio Interferometer Measurement Equation: III. Addressing Direction-Dependent Effects in 21 Cm WSRT Observations of 3C 147”. In: *Astronomy & Astrophysics* 527, A108. ISSN: 0004-6361, 1432-0746. DOI: [10.1051/0004-6361/201116435](https://doi.org/10.1051/0004-6361/201116435). (Visited on 03/13/2023).
- (July 2011d). “Revisiting the Radio Interferometer Measurement Equation: IV. A Generalized Tensor Formalism”. In: *Astronomy & Astrophysics* 531, A159. ISSN: 0004-6361, 1432-0746. DOI: [10.1051/0004-6361/201116764](https://doi.org/10.1051/0004-6361/201116764). (Visited on 03/13/2023).
- Sramek, Richard A. (Jan. 1990). “Atmospheric phase stability at the VLA.” In: *URSI/IAU Symposium on Radio Astronomical Seeing*. Ed. by J. E. Baldwin and Shouguan Wang, pp. 21–30.
- Sweijen, F. et al. (Jan. 2022a). “Deep Sub-Arcsecond Wide-Field Imaging of the Lockman Hole Field at 144 MHz”. In: *Nature Astronomy*, pp. 1–7. ISSN: 2397-3366. DOI: [10.1038/s41550-021-01573-z](https://doi.org/10.1038/s41550-021-01573-z). (Visited on 01/28/2022).
- Tasse, C. (June 2014). “Nonlinear Kalman Filters for Calibration in Radio Interferometry”. In: *Astronomy & Astrophysics* 566, A127. ISSN: 0004-6361, 1432-0746. DOI: [10.1051/0004-6361/201423503](https://doi.org/10.1051/0004-6361/201423503). (Visited on 08/30/2023).
- Thompson, A. Richard, James M. Moran, and George W. Swenson (2017). *Interferometry and Synthesis in Radio Astronomy*. Astronomy and Astrophysics Library. Cham: Springer International Publishing. ISBN: 978-3-319-44429-1 978-3-319-44431-4. DOI: [10.1007/978-3-319-44431-4](https://doi.org/10.1007/978-3-319-44431-4). (Visited on 08/31/2023).
- Tol, Sebastiaan van der, Bram Veenboer, and André R. Offringa (Aug. 2018). “Image Domain Gridding: A Fast Method for Convolutional Resampling of Visibilities”. In: *Astronomy & Astrophysics* 616, A27. ISSN: 0004-6361, 1432-0746. DOI: [10.1051/0004-6361/201832858](https://doi.org/10.1051/0004-6361/201832858). (Visited on 08/24/2023).
- van Diepen, Ger, Tammo Jan Dijkema, and André Offringa (Apr. 2018a). *DPPP: Default Pre-Processing Pipeline*. Astrophysics Source Code Library, record ascl:1804.003. ascl: [1804.003](https://www.astronomy.swin.edu.au/ascl/1804.003).
- Veenboer, Bram et al. (Nov. 2019). “IDG: Image Domain Gridding”. In: *Astrophysics Source Code Library*, ascl:1911.011. (Visited on 08/24/2023).
- Weeren, R. J. van et al. (Mar. 2016). “LOFAR FACET CALIBRATION”. In: *The Astrophysical Journal Supplement Series* 223.1, p. 2. ISSN: 0067-0049. DOI: [10.3847/0067-0049/223/1/2](https://doi.org/10.3847/0067-0049/223/1/2). (Visited on 08/30/2023).

- Weeren, R. J. van et al. (July 2021). “LOFAR Observations of Galaxy Clusters in HETDEX - Extraction and Self-Calibration of Individual LOFAR Targets”. In: *Astronomy & Astrophysics* 651, A115. ISSN: 0004-6361, 1432-0746. DOI: [10.1051/0004-6361/202039826](https://doi.org/10.1051/0004-6361/202039826). (Visited on 08/30/2023).
- Ye, Haoyang et al. (Jan. 2020). “Optimal Gridding and Degriding in Radio Interferometry Imaging”. In: *Monthly Notices of the Royal Astronomical Society* 491.1, pp. 1146–1159. ISSN: 0035-8711. DOI: [10.1093/mnras/stz2970](https://doi.org/10.1093/mnras/stz2970). (Visited on 08/22/2023).

CHAPTER 3

High-resolution international LOFAR observations of 4C 43.15 – Spectral ages and injection indices in a high- z radio galaxy

Based on the publication: *Astronomy & Astrophysics, Volume 658, id.A3, 13pp.*

Abstract

It has long been known that radio sources with the steepest spectra are preferentially associated with the most distant galaxies, the $\alpha - z$ relation, but the reason for this relation is an open question. The spatial distribution of spectra in high- z radio sources can be used to study this relation, and low-frequency observations are particularly important in understanding the particle acceleration and injection mechanisms. However, the small angular sizes of high- z sources together with the inherently low resolution of low-frequency radio telescopes until now have prevented high angular resolution low-frequency observations of distant objects. Here we present subarcsecond observations of a $z = 2.4$ radio galaxy at frequencies between 121 MHz and 166 MHz. We measure the spatial distribution of spectra and discuss the implications for models of the $\alpha - z$ relation. We targeted 4C 43.15 with the High Band Antennas (HBAs) of the *International LOFAR Telescope* (ILT) with a range of baselines up to 1300 km. At the central frequency of 143 MHz, we achieve an angular resolution of $\sim 0.3''$. By complementing our data with archival *Very Large Array* (VLA) data we study the spectral index distribution across 4C 43.15 between 55 MHz and 8.4 GHz at resolutions of $0.4''$ and $0.9''$. With a magnetic field strength of $B = 5.2$ nT and fitted injection indices of $\alpha_{\text{inj}}^{\text{north}} = -0.8$ and $\alpha_{\text{inj}}^{\text{south}} = -0.6$, fitting a Tribble spectral ageing model results in a spectral age of $\tau_{\text{spec}} = 1.1 \pm 0.1$ Myr. We conclude that our data on 4C 43.15 indicates that inverse Compton losses could become comparable to or exceed synchrotron losses at higher redshifts and that inverse Compton losses could be a viable explanation for the $\alpha - z$ relation. Statistical studies of these objects will become possible in the future when wide-area subarcsecond surveys start.

3.1 Introduction

High-redshift radio galaxies are important probes of galaxy evolution as they allow the study of the (co)evolution of black holes and their host galaxies over cosmic time. A correlation that has frequently been used to search for high-redshift radio galaxies, but is still under debate, is the $\alpha - z$ relation, where radio sources with steeper spectra appear to be preferentially associated with higher redshift sources (Tielens et al., 1979; De Breuck et al., 2000; G. Miley et al., 2008). One of the mechanisms that has been suggested to explain this

relation is that this is the result of the increased inverse Compton (ic) losses at higher redshifts, due to the higher energy density of the cosmic microwave background (CMB) (e.g. Ghisellini et al. 2014 or Klamer et al. 2006). Recently, Leah K Morabito et al., 2018 found that ic losses could indeed be the primary driver behind the $\alpha - z$ relation, by modelling a large number of sources over a wide range of redshifts using the *Broadband Radio Astronomy Tools* (BRATS) software package¹ (Jeremy J. Harwood et al., 2013; Jeremy J. Harwood et al., 2015). There are two other scenarios that could result in this relation, one connected with observational biases and the other related to the environment of the galaxy. Blundell et al., 1999 studied the correlations between radio luminosity, linear size, spectral index, and redshift for flux-density-limited surveys, and propose that the observed $\alpha - z$ relation follows from a $p - \alpha$ relation, where p is the radio power. The Malmquist bias will then naturally drive an $\alpha - z$ correlation as the most powerful sources are the easiest to detect. Klamer et al., 2006 suggest that an increased ambient density around radio sources in the early universe could be an important factor in steepening the spectrum. A denser medium at high redshift would keep the radio lobes more confined and would result in a higher surface brightness for older radio emission coming from the low-energy electron populations. If at higher redshifts radio galaxies preferentially lie in denser environments, these effects could lead to the observed relation. Another effect of an increased ambient density is related to the acceleration of electrons in or near the hotspot. Based on the findings by Kirk et al., 1987, among others, that the spectral index is sensitive to properties of the shock front near the hotspot, R. Athreya et al., 1998 proposed that a radio jet working against higher ambient densities would already have a steeper initial spectrum of electrons being produced before flowing back into the lobes and steepening more due to further energy losses. Gopal-Krishna et al., 2012 argue against steeper injection indices based on the absence of a correlation between the spectral index and rotation measure (which probes the density) in a sample of compact steep spectrum (CSS) sources from Murgia et al., 2002 which have a median injection index of $\alpha = -0.63$.

Studying the spatial distribution of spectra over as wide a frequency range as possible is crucial in disentangling the various processes that produce the radio emission, such as synchrotron ageing, IC losses, and evolution. The rate at which energy is lost depends on the energy of the radiating or scattering electrons. These energy losses over time cause the spectrum to deviate from a power law and introduce curvature that becomes more pronounced at higher frequencies. This curving of the spectrum is referred to as the spectral ageing of the source. It is for this reason that measurements over a large frequency bandwidth are required to properly characterise the spectrum. For decades work has been done using measurements across the radio spectrum to study the evolution of radio galaxies (e.g. Myers et al., 1985; P. Alexander et al., 1987; Carilli et al., 1991; Jamrozy et al., 2008; Jeremy J. Harwood et al., 2013; Jeremy J. Harwood et al., 2016; Mahatma et al., 2019). With multiple measurements, it is possible to fit a spectral ageing model to the spectrum to obtain an estimate of the spectral age of the plasma. Low-frequency data plays a crucial role in such modelling because it constrains the injection index α_{inj} , which is the spectral index of the young electrons in hotspots, recently (re)accelerated through the interaction of the jet with the surrounding medium. This part of the spectrum will be closer to the original power law, while at higher frequencies the spectrum will steepen due to the ageing of the electrons.

To fully understand the evolution of these sources, spatially resolved studies spanning the entire radio spectrum over a range of redshifts are required. Until recently, high angular resolution observations of these high-redshift objects have been limited to gigahertz frequencies or higher, using facilities such as the Very Large Array (VLA), or the technique of very long baseline interferometry (VLBI). Large nearby sources such as Cygnus A are easily resolved at most frequencies (see e.g. McKean et al. 2016 or Perley et al. 1984

¹<http://www.askanastronomer.co.uk/brats/>

in the case of Cygnus A at megahertz and gigahertz frequencies, respectively). However, the typically poor angular resolution of low-frequency radio telescopes prevents such detailed views of their higher-redshift brethren and has, therefore, limited spectral studies of distant AGNs to numerical models (e.g. [Huarte-Espinosa et al., 2011](#); [Cielo et al., 2017](#)). [Jeremy J. Harwood, 2017](#) shows that modelling sources using only their integrated spectrum is unreliable and cannot recover the correct value for properties such as the injection index and robust spectral ages, highlighting the need for high angular resolution observations. The low-frequency array (LOFAR; [Haarlem et al. 2013](#)) is a low-frequency interferometer. It can observe between 10 and 90 MHz with the low band antennas (LBAs) and between 110 and 240 MHz with the high band antennas (HBAs). With its international stations, it is possible to venture into subarcsecond territory at frequencies below 240 MHz. This opens up the window for (highly) spatially resolved studies of objects at low frequencies (e.g. [Leah K. Morabito et al., 2016](#); [Varenius et al., 2014](#); [Varenius et al., 2016](#); [Ramírez-Olivencia et al., 2018](#); [D. E. Harris et al., 2019](#)).

This paper is a follow-up study at 143 MHz of the 55 MHz study presented in [Leah K. Morabito et al., 2016](#). 4C 43.15 is part of a small sample of high-redshift radio galaxies to be studied in detail at low frequencies. These sources were selected to investigate the $\alpha - z$ relation because of their (apparent) ultra-steep spectra. 4C 43.15 is a high-redshift radio galaxy (HzRG) with a redshift of $z = 2.429$ ([McCarthy, 1991](#)). It has an integrated spectral index between 365 MHz and 1.4 GHz of $\alpha = -1.1$. [Leah K. Morabito et al., 2016](#) showed that for 4C 43.15 this ultra-steep spectral index is the result of a break in the spectrum at intermediate frequencies and steepening at higher frequencies. Here we add 143 MHz LOFAR data and, combined with archival VLA data, present a spatially resolved spectral study of a high-redshift galaxy, from 55 MHz to 8.46 GHz. We use the LOFAR LBA data presented by [Leah K. Morabito et al., 2016](#).

In this paper we try to assess whether IC losses can be a main contributor to the steepness of the spectrum of 4C 43.15, using high spatial resolution low-frequency observations. Section 2 describes the observations that were used. In Section 3 the data reduction and spectral modelling are described. Section 4 describes the results that were obtained. Finally, sections 5 and 6 discuss the results in the context of the $\alpha - z$ relation and present the conclusions.

The assumed cosmology is that of the 2015 Planck results ([Ade et al., 2016](#)), with $H_0 = 67.8 \text{ km s}^{-1} \text{ Mpc}^{-1}$, $\Omega_m = 0.308$, and $\Omega_\Lambda = 0.692$. At the redshift of 4C 43.15, $1''$ corresponds to 8.3 kpc. Furthermore, the spectral index α is defined as $S_\nu \propto \nu^\alpha$ and S_ν is the flux density at a given frequency ν .

3.2 Observations

The LOFAR HBA observations of 4C 43.15 presented in this paper were carried out on 21 January 2016, starting at 19:16 UT (PI: Morabito, LT5_006, L427100). The phase centre of the beam was pointed at J2000 $\alpha = 7\text{h}35\text{m}22.44\text{s}$, $\delta = 43^\circ44'24.72''$, and the target was observed with a standard eight-hour pointing. The HBA_DUAL_INNER configuration was used, including international stations. In total 47 stations participated in the observation: 24 core stations and 14 remote stations, hereafter referred to as the Dutch array, and 9 international stations in Germany, France, Sweden, and the UK. The international stations were DE601, DE602, DE603, DE604, DE605, DE609, FR606, SE607, and UK608. This provides a longest projected baseline of 1292 km, giving a synthesised beam size of the order of $\sim 0.3''$ at 151 MHz. Data were recorded at 1 s, 3.051 kHz resolution and averaged to 2 s, 12.207 kHz resolution before being uploaded to the long-term archive (LTA). A total bandwidth of 47.1 MHz covered the frequency range from 120.3 MHz to 167.4 MHz.

Observations of two compact flux density calibrators, 3C 147 and 3C 48, bookended the target observation of 4C 43.15. The calibrator scans were 15 minutes long and had the same configuration as the target observations.

Archival VLA observations in C band (4535.1 MHz and 4885.1 MHz) and X band (8414.9 MHz) were used: project codes AC0374 (Carilli et al., 1997) and AK0410, respectively. Each spectral window had 50 MHz of bandwidth. Both projects had data taken with the VLA in A configuration. Observations were carried out on 19 March 1994 (AC0374) and 31 August 1995 (AK0410). The total on-source time was 28 minutes for AC0374 and 40 minutes for AK0410.

3.3 Data reduction

The LOFAR HBA raw data (L427100) were fully reduced using the LOFAR data reduction software, and the VLA data (projects AC0374 and AK0410) were retrieved from the archive and reduced again with the *Common Astronomy Software Applications* (CASA) package. The LBA data were already reduced and we used the radio map obtained by Leah K. Morabito et al. (2016). This image is shown in Fig. 3.7.

Data reduction of the HBA data consisted of three stages. First, the shorter baselines from the Dutch array were calibrated using the prefactor pipeline². Subsequently, a beta version of the long baseline pipeline³ was used to calibrate the international stations. Finally, self-calibration was performed on the complete data set. The prefactor pipeline was run with version 2.19 of the LOFAR software.

The prefactor pipeline consists of two parts: the calibrator and the target. First the calibrators were processed using the calibrator part of the pipeline, solving for a diagonal gain and the common rotation angle. This was followed by clock-TEC separation, which separates the phase effects due to clock drifts from those due to the ionosphere (TEC) (see e.g. Weeren et al. 2016). Additionally, the phase offset between X and Y polarisations was determined. Both the 3C 48 and 3C 147 scan were processed. The phase solutions for 3C 48 showed inexplicable shifts in time, which 3C 147 did not. Hence the solutions obtained from 3C 147 were used. It is important to note that the calibrator pipeline derived solutions for all the stations (i.e. Dutch and international stations).

3.3.1 Dutch LOFAR calibration

Following the calibrator reduction, the target field was processed with the target part of the pipeline. This first corrects the clock offsets and applies gain and primary beam solutions. Finally, a correction for the rotation angle was determined and applied. The data were then averaged to 4 s time resolution and 48.82 kHz frequency resolution (four channels per sub-band) before a phase-only calibration on the target was carried out using a sky model from the Tata Institute of Fundamental Research (TIFR) *Giant Metre Wave Radio Telescope* (GMRT) Sky Survey (TGSS) (Intema et al., 2017) for the target field. This time and frequency resolution is a balance between keeping data size down and retaining the ability to apply or find corrections with the required precision. From the TGSS sky model, phase solutions for only the core and remote stations are obtained.

²<https://github.com/lofar-astron/prefactor>

³https://github.com/lmorabit/long_baseline_pipeline

3.3.2 International LOFAR calibration

The LOFAR international stations were calibrated using a beta version of the long-baseline pipeline being developed by Morabito et al. (in prep.), using version 2.20 of the LOFAR software. In this section, we describe the calibration strategy used in this version of the pipeline and the subsequent self-calibration that was carried out by hand. The starting point for the pipeline is the gain solutions from the calibrator part of prefactor, the phase solutions from the target part, and a user-supplied list of potential in-field calibrators selected from the Long Baseline Calibrator Survey (LBCS, Moldón et al., 2015; N. Jackson et al., 2016). We started with the raw uncalibrated data as input, with its original temporal and spectral resolution.

Apply prefactor solutions

As a first step, the input data were matched against the available solutions produced by calibrating the Dutch array. This ensured that the best available solutions were applied to each sub-band, and that sub-bands for which there were no matching solutions were excluded from further processing. The matching sub-bands were then copied to the working directory. The international station DE603, ~ 400 km from the core, was flagged because its signal was unusable. This resulted in a slightly diminished uv-coverage at the shorter international baselines.

Next, the amplitude and clock solutions derived from the calibrator data were interpolated to each individual sub-band and stored in a separate calibration table. Solutions were derived for all stations.

Finally, the *New Default Pre-Processing Pipeline* (NDPPP; van Diepen et al. 2018b) was used to apply all initial corrections to the data. At this stage the data had been corrected for station clock offsets, gain corrections, beam corrections, and phase corrections, in this order.

In-field calibrator selection

Before running this version of the pipeline, however, one or more potentially suitable calibrator(s) within the 4C 43.15 field needed to be determined. These calibrators were selected manually using a Python script that queries the LBCS database and presents potential calibrator sources, as shown in Fig. 3.1. Using this plot, the sources indicated with observation IDs L394813, L394815, and L394817 were selected to be used in the pipeline. This is only an initial selection. The pipeline will decide on the best calibrator by means of closure phases.

When the initial corrections were applied, a new data set for each selected calibrator was created by phase shifting to their respective positions. After the data were phase-shifted to each calibrator, data from all core stations were added coherently to create a new station ST001, which is temporarily equivalent to an additional more sensitive station, and finally, the data were averaged to 8 s time resolution and one channel per sub-band (195.312 kHz) frequency resolution. ST001 was not used in the final imaging process because of its small field of view. The final data sets for each calibrator contain the full bandwidth and span the entire observation. By means of the closure phase, the relative quality of the calibrators to each other was assessed. The benefit of closure phases is that the sum of phases on a triangle of telescopes is independent of atmospheric errors (Jennison, 1958).

Calculated closure phases were then unwrapped and the mean value of the squared gradient was calculated. The best calibrator candidate was then selected as the source with the lowest mean value. For 4C43.15 the best in-field calibrator candidate turned out to be L394815. It is located at $\alpha = 7\text{h}32\text{m}43.72\text{s}$ and $\delta = 43^\circ35'40.50''$, about half a degree away from the phase centre. Stations DE601, DE605, and ST001

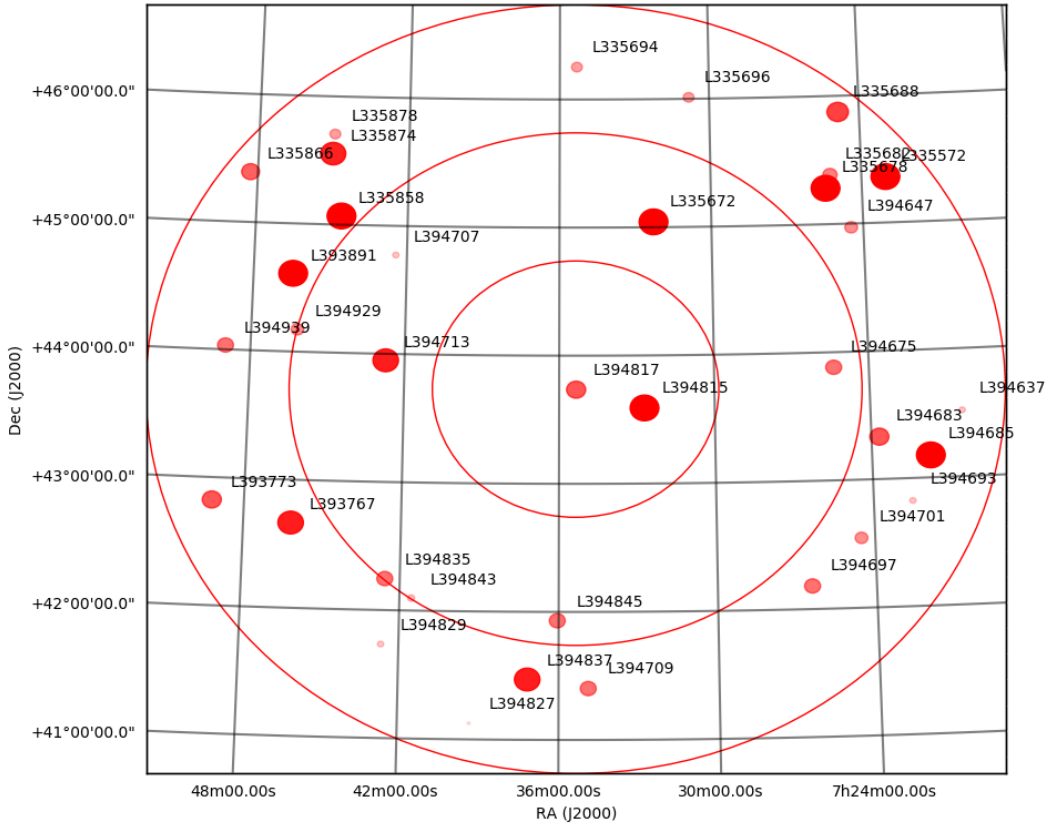


Figure 3.1: Overview of potential calibrators within 3° of the target’s coordinates. The red circles are drawn at 1°, 2°, and 3° radii. Three of the closest calibrators were chosen to be used during calibration: L394813, L394815, and L394817. Bigger, redder dots mean more stations have coherent phases on the calibrator in question.

formed the triangle on which the closure phase was measured. The statistic as measured by the process described earlier was 0.23. For L394813 and L394817 the values were 1.55 and 0.42, respectively.

Phase reference calibration

In the next step, the in-field calibrator is calibrated against a model to obtain gain solutions. The initial model for the calibrator was a circular Gaussian point source, 0.1'' in size. Solution intervals were chosen equal to the resolution of the data, 8 s and 1 channel or 195.312 kHz (i.e. a single time and frequency slot).

After this calibration, the gains are applied to the target data, where all core stations are calibrated with the solutions for the phased-up station, ST001. Solutions were inspected by eye and found to smoothly vary in both time and frequency. The phase slope with respect to frequency is the delay (e.g. 306 ns on the

remote station RS306 and $1.2 \mu\text{s}$ on the international station UK608). The following calibration solutions were then applied to the raw data, in the listed order:

1. Phase offsets as a function of time and frequency, obtained from the clock offsets between the stations, determined by the prefactor calibrator pipeline;
2. Amplitude solutions for all stations from the prefactor calibrator pipeline to set the global flux density scale. We use the flux scale by [Scaife et al., 2012](#);
3. Primary beam corrections to take into account the attenuating effect of the primary beam as a function of distance to the field phase centre;
4. The common rotation angle found by RMextract⁴ ([Mevius, 2018](#)), which corrects for Faraday rotation;
5. Direction-independent phase solutions from the prefactor target pipeline, obtained by calibrating against a TGSS sky model;
6. Gain solutions obtained from the in-field calibrator.

Finally, the data were averaged to 16 s and 195.312 kHz (1 channel per sub-band), and were compressed using Dysco ([Offringa, 2016](#)) into 65 GB of calibrated data compared to 7 TB of raw data.

3.3.3 LOFAR self-calibration

Before self-calibrating the target, the phase solutions found on the infield calibrator were applied. Several iterations of self-calibration were subsequently performed in order to obtain the final calibrated data set. These consisted of phase-only self-calibration, followed by amplitude-and-phase self-calibration. Both were repeated until no significant improvement in terms of signal-to-noise ratio was obtained. This occurred after four phase-only and seven amplitude-and-phase iterations. After each calibration cycle, a new image with a corresponding model was created with WSClean ([Offringa et al., 2014](#)) using a robust weighting with a robust parameter of -1 , multi-scale clean, and multi-frequency synthesis (MFS) deconvolution.

For an objective measure of whether or not the image quality had increased, after a cycle of self-calibration we used the absolute ratio of the maximum and minimum pixel value in the image. The maximum value is the peak flux of the target source. The minimum value is most likely due to artefacts around the source from residual errors. An increase in the ratio between the two indicates that there are likely fewer artefacts.

The solution interval was gradually reduced during phase-only calibration, starting with a solution for every time slot for the full bandwidth, down to a solution for every two time slots and four sub-bands. Gradually tracking faster changes in phase was made possible due to increasing model quality after each iteration. During amplitude-and-phase calibration the solution intervals were kept constant at ~ 10 min. and ten sub-bands, which was found to be short enough to allow for time-varying corrections, but not so short as to cause overfitting. The amplitude calibration had an inner uv-cut applied, which was set at 100 km. This improved stability and produced the best results. We show the progress and final image in [Fig. 3.2](#). An angular resolution of $0.28'' \times 0.22''$ is obtained. [Figure 3.3](#) shows a comparison between an image with only the Dutch array, with a resolution of the order of $\sim 6''$ and an image with the international stations.

⁴<https://github.com/lofar-astron/RMextract>

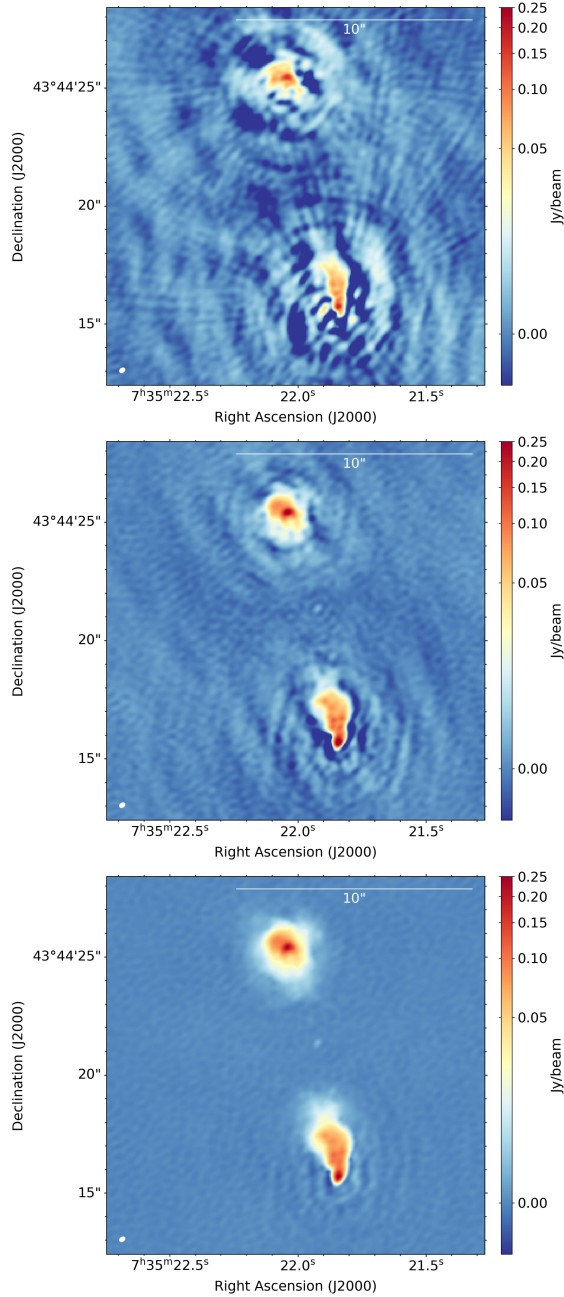


Figure 3.2: Comparison between the pipeline-calibrated (*top*), phase-only self-calibrated (*middle*), and amplitude-and-phase self-calibrated (*bottom*) images of the 143 MHz data. The colour scale is shown in an inverse hyperbolic sine (arcsinh) stretch, with the same scale for each image. For each image, the pixel scale is $0.05''$. In the bottom left corner, the restoring beam is shown (white ellipse), $0.28'' \times 0.22''$ in size. The RMS noise is $172 \mu\text{Jy beam}^{-1}$ in the final image. North is up and east is to the left.

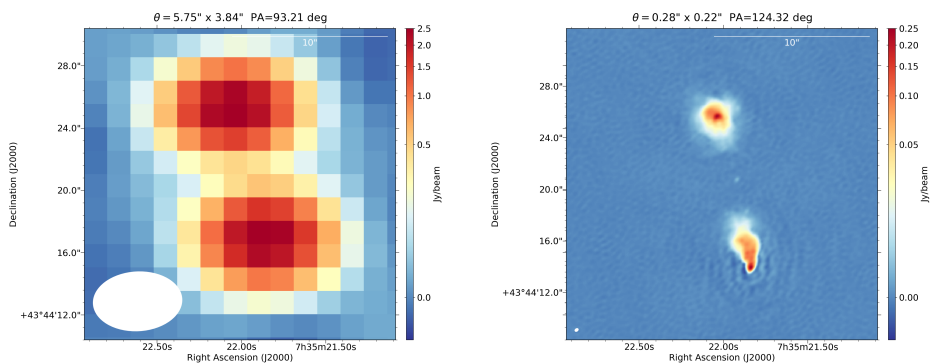


Figure 3.3: Difference in resolving power at 143 MHz between using only the Dutch array vs using the full international array. The white ellipse in the bottom left corner shows the beam size, which in each image is $5.8'' \times 3.8''$ with a position angle of 93.2° (*left*) and $0.28'' \times 0.22''$ with a position angle of 124.3° (*right*). In the top right corner, a scale bar shows a $10''$ (83 kpc) reference. North is up and east is to the left. The colour bar indicates intensity and is shown with a square root stretch.

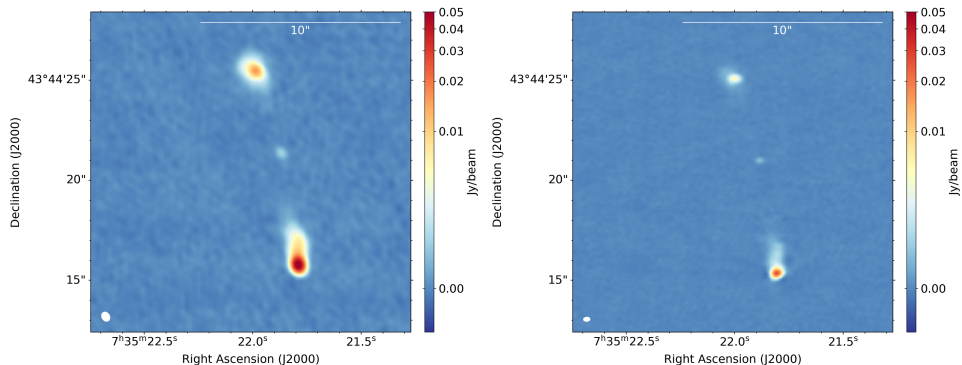


Figure 3.4: Natural weighted radio maps showing the re-reduced VLA 4.7 GHz (*left*) and 8.44 GHz (*right*) data. The colour scale is shown on an inverse hyperbolic sine (arcsinh) stretch from -0.001 to $0.05 \text{ Jy beam}^{-1}$. In the bottom left corner, the restoring beam is shown as a white ellipse. This is $0.52'' \times 0.42''$ with a position angle of 32.2° and $0.36'' \times 0.25''$ with a position angle of -86.1° , for the 4.7 and 8.44 GHz maps, respectively.

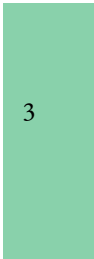


Table 3.1: Final reimaging parameters for each data set for the $0.9''$ resolution maps.

Data set	Frequency	Weighting	UV range
LOFAR LBA	55 MHz	robust -1.5	$> 1.4 \text{ k}\lambda$
LOFAR HBA	143.26 MHz	robust -1	$20 - 230 \text{ k}\lambda$
VLA (A conf.)	4.74 GHz	natural	$20 - 230 \text{ k}\lambda$
VLA (A conf.)	8.46 GHz	natural	$20 - 230 \text{ k}\lambda$

3.3.4 Archival VLA recalibration

To obtain radio maps at higher frequencies, the archival VLA data were recalibrated using CASA 5.3.0 (McMullin et al., 2007). The data used here from the old vla, so before reprocessing the data were imported into the casa image format using `importvla`.

First, the calibrator was determined and its model applied, with `setjy`, using the Perley et al., 2017 flux scale. For the X-band this was 3C 48 and for the C-band this was 3C 286. We then solved for phase-only gains on a one-minute solution interval, followed by an amplitude-and-phase calibration over the entire observation. This was done for both the flux density calibrator and the phase reference using the `gaincal` task.

Next, the phase reference was put on the correct flux density scale using the `fluxscale` task, transferring the information from the flux density calibrator. We then solved for the gains of the phase reference in the same way as described above. Finally, the corrections were applied to the data, and the data were imaged using `clean`. Subsequent amplitude-and-phase self-calibration concludes the reduction of the archival VLA data. Figure 3.4 shows the resulting radio maps.

3.3.5 Resolution matching and astrometric corrections

For spectral comparison, the maps of 4C 43.15 at different frequencies need to be matched in terms of resolution, uv-coverage, and astrometry. The highest resolution that can be obtained is set by the frequency with the lowest native resolution, in this case, the LBA data. Excluding the LBA data, the lowest resolution is set by the HBA data. Table 3.1 summarises the reimaging parameters. To match the uv-coverage of LOFAR and VLA an inner cut of $20 \text{ k}\lambda$ was used. This limit is set by the X-band data. Outer cuts of $230 \text{ k}\lambda$ and $589 \text{ k}\lambda$ were used to get close to the target resolutions of $0.9''$ and $0.38''$, respectively, after which the images were further smoothed to the desired resolution using a Gaussian kernel. The CASA `imsmooth` task was used for smoothing. Finally, the image was rebinned to the desired pixel scale with `imrebin`. Regridding was needed for the VLA C-band image, from B1950 to J2000. The final products are images with a $0.9''$ circular beam and a $0.2''$ pixel scale, and images with a $0.38''$ circular beam and a $0.05''$ pixel scale.

Except for the LBA map, we aligned the images relative to each other using the compact radio core. In the LOFAR HBA and the VLA data, the core can clearly be seen. Therefore, we corrected the astrometry of these images, using the K-band continuum image of Motohara et al., 2000. First, a Gaussian fit was made to the K-band image to determine the host galaxy's position. This gave us a position of $\alpha_k = 7\text{h}35\text{m}21.92\text{s}$, $\delta_k = 43^\circ44'20.70''$. The uncertainties on the fit are 1 mas in both right ascension and declination. The core was then fitted with a Gaussian in all the other images. The centroids of the Gaussians were then subtracted from the centroid of the k band to determine the astrometric offsets, which are summarised in

Table 3.2: Offsets in right ascension and declination for the astrometric correction of the LOFAR HBA data and VLA C- and X-band data, with respect to the K-band position.

Frequency	Δ RA [arcsec]	Δ DEC [arcsec]
143.26 MHz	0.06	-0.6
4.71 GHz	1.8	-0.45
8.44 GHz	0.5	-0.3

table 3.2. Using these offsets the images were then aligned in pixel space to the K-band image, using the `geom` task in `aips`⁵.

This procedure could not be used for the LBA image because the radio core was not detected in the LBA map. Hence, the alignment between LBA and HBA images was done assuming a Gaussian shape for the lobes.

3.3.6 Spectral modelling

Here we describe the procedure that was used for the spectral modelling. Section 4.3 presents the results. We used the BRATS software package to produce spectral index maps and to perform the spectral modelling. The northern and southern lobes were modelled separately because of their apparent difference, but the procedure was the same for both.

The four radio maps were loaded into BRATS together with DS9 region files defining the two lobes and an empty sky region for measuring the RMS noise. The flux density uncertainties for the VLA were set to 11% to be consistent with the measurements of [Carilli et al., 1997](#), and set to 20% for the lba ([Leah K. Morabito et al., 2016](#)) and HBA frequencies.

The HBA uncertainties are dominated by uncertain beam models that affect the transfer of amplitudes from the flux density calibrator to the target source and uncertainties in the flux density of the calibrator source. An initial cut of $5\sigma_{\text{RMS}}$ was then made to determine the pixels to use during modelling. The `signaltonoise` parameter in BRATS allows for an additional constraint in the signal-to-noise ratio when deciding what pixels to keep. This parameter was set to 3 for the northern lobe and 6 for the southern lobe. Values lower than this resulted in BRATS rejecting the model fits. Its values were determined manually and balanced the number of pixels used versus the goodness of fit. A detailed explanation of this parameter can be found in [Jeremy J. Harwood et al., 2013](#). Spectral index maps were made using a weighted linear least-squares fit to the data that remained after the above signal-to-noise criteria were applied.

An estimate of the magnetic field is required before any further fitting of spectral models can be done. This estimate is based on the revised equipartition field strength presented in [Beck et al., 2005](#), who present an alternative formulation of the equipartition formula in terms of a constant proton-electron ratio k_0 (which is 0 for FRIIs; see e.g. The results from [Hardcastle et al. 2002](#); [Croston et al. 2004](#), and [Croston et al. 2005](#)), the intensity of the synchrotron radiation and the spectral index. Over the years evidence has been found that the magnetic field can be significantly weaker than that estimated from equipartition. [Perley et al., 1991](#) found a factor of three difference in 3C 295 when comparing the equipartition field strength with the field strength required to match the hotspot advance speed with the speed at which the lobe and core were moving apart. Similarly, [Wellman et al., 1997](#) found that a ratio of $b/b_{\text{eq}} = 0.25$ was required for

⁵*astronomical image processing system*, <http://www.aips.nrao.edu/index.shtml>

consistent interpretation of their data and that the general scatter around this value in their sample was small ($\sim 15\%$). [Croston et al., 2005](#) used X-ray observations of 33 radio galaxies and quasars and found that it is common for magnetic field strengths to be different from those calculated via equipartition, and [Jeremy J. Harwood et al., 2016](#) confirmed a departure of equipartition for 3C 452 and 3C 223 showing that it may be the cause of discrepancies between the spectral and dynamical ages. Recently, [Ineson et al., 2017](#) studied a sample of 47 radio galaxies at both x-ray and radio wavelengths, and [Turner et al., 2018](#) studied sources in the third Cambridge catalogue of radio sources (3C). Both authors find a median magnetic field strength of $b = 0.4b_{\text{eq}}$. [Mahatma et al., 2019](#) also identify the range $b = 0.1 - 0.5b_{\text{eq}}$ as plausible. We therefore scale our equipartition magnetic field strength by 0.4.

A search for the best fitting injection index was then performed using the `findinject` task in `BRATS`, and finally, a spectral ageing model was fitted to the data. `BRATS` allows different models to be fitted: Kardashev-Pacholczyk (KP; [Kardashev 1962](#)), Jaffe-Perola (JP; [Jaffe et al. 1973](#)), or Tribble ([Tribble 1993](#)). The difference between the KP and JP model is that in the JP model, the electron pitch angle is an average value over its radiative lifetime instead of a constant value. The Tribble model describes the magnetic field as a Gaussian random field instead of a constant value. 4C 43.15 was fitted with a JP+Tribble model, which is thought to be the most realistic of the three because it allows the magnetic field to vary across the source ([Hardcastle et al., 2013](#); [Jeremy J. Harwood et al., 2013](#)). First, the injection index α_{inj} was determined through a coarse search between -0.5 and -1.0 , with steps of 0.05 . This yields a best fit in an interval $\delta\alpha_{\text{inj}} = 0.05$ wide. Another finer search was then done in this interval, with a step size of 0.01 . Finally, the `fitjptribble` task was used to fit the ageing model.

3.4 Results

3.4.1 A GHz steep-spectrum core

With the core detected at 143 MHz, 4.71 GHz, and 8.44 GHz, its overall spectral shape can be determined. Typically, radio galaxy cores have flat spectra in the GHz regime. It has been shown, for example by [R. M. Athreya et al., 1997](#) and [Carilli et al., 1997](#), that the cores of high-redshift radio galaxies can have spectral indices $\alpha < -0.5$, between 4.7 GHz and 8.3 GHz, including the core of 4C 43.15.

Flux densities were measured, using $0.38''$ matched resolution maps, using the same aperture for all three images, based on the $3\sigma_{\text{RMS}}$ contours of the HBA map, where σ_{RMS} is the RMS map noise. The measured flux densities are listed in [Table 3.3](#).

The spectral indices between these frequencies are $\alpha_{4.71 \text{ GHz}}^{8.44 \text{ GHz}} = -0.83 \pm 0.04$, $\alpha_{8.44 \text{ GHz}}^{143 \text{ MHz}} = -0.35 \pm 0.05$, and $\alpha_{4.71 \text{ GHz}}^{143 \text{ MHz}} = -0.27 \pm 0.06$. Uncertainties were derived using Gaussian error propagation, neglecting the uncertainty in the effective frequency at which the measurements were taken.

3.4.2 ILT radio morphology and measurements

From the intensity map, it is clear that the two lobes are different. The northern lobe has a more circular morphology as projected on the plane of the sky. It does not show a sharp termination of the hotspot where it meets the surrounding medium. Instead, its hotspot appears to be embedded in a region of diffuse emission. The southern lobe has a more conical shape with a clear termination between the hotspot and its surrounding medium, showing no diffuse emission past this point. The bridge of emission seen at 55 MHz is not seen at 143 MHz or higher frequencies. No jet emission is identified either, although a small patch

Table 3.3: Flux densities of the radio core, measured using the same aperture, in $0.38''$ matched resolution maps. Uncertainties are taken to be 20% for the HBA and 2% for the VLA, the same as for the spectral modelling.

Frequency	S_{int} [mJy]
143 MHz	3.0 ± 0.6
4.71 GHz	1.2 ± 0.02
8.44 GHz	0.72 ± 0.01

of emission just slightly northeast of the core can be identified at the $3 - 5\sigma_{\text{RMS}}$ level. Table 3.4 presents the flux densities of both lobes, measured from the HBA and reprocessed VLA maps. The reprocessed VLA maps are on average 30% brighter than the flux densities reported by Leah K. Morabito et al., 2016, but are within 11% of the values reported by Carilli et al., 1997 in terms of total flux density. The flux densities of the northern and southern lobes are equal within the uncertainties at 143 MHz. Imaging the source with only the Dutch array yields an integrated flux density of $S = 6.2 \pm 1.2$ Jy (assuming a 20% uncertainty). This is consistent with scaling the 6C value of 5.9 Jy (S. E. G. Hales et al., 1993a) from 151 MHz to 143.26 MHz using the measured spectral index of $\alpha = -0.83$ (Leah K. Morabito et al., 2016). The total integrated flux density presented in table 3.4 (measured inside $5\sigma_{\text{rms}}$ contours) is lower than the measurement from the low-resolution map but is consistent within the uncertainties. When using the same aperture as for the low-resolution map, however, an integrated flux density of $s = 6.3 \pm 1.3$ Jy (assuming a 20% uncertainty) was found. This likely indicates that some of the flux density is still contained in the artefacts such as those around the southern lobe.

The 143 MHz flux density of 4C 43.15 corresponds to a luminosity of $L_{143\text{MHz}} = 2.3 \times 10^{29} \text{ W Hz}^{-1}$; the luminosity is given by

$$L_{\nu} = 4\pi D_L^2 S_{\nu} (1+z)^{-(1+\alpha)}, \quad (3.1)$$

where D_L is the luminosity distance, S_{ν} is the flux density, z is the redshift, and α is the spectral index. The integrated spectral index of $\alpha = -0.83$, for frequencies below 500 MHz (see Leah K. Morabito et al. 2016), was used to calculate L_{ν} .

In the 143 MHz map the angular size of the source from the northern hotspot to the southern hotspot is $9.9''$ on the sky, corresponding to a linear size of 82 kpc. The positions of each hotspot and the core were determined by fitting Gaussian functions using the CASA viewer. These positions were then used to determine the parameters listed in Table 3.4. Here the jet angle is defined as the angle anti-clockwise with respect to the nearest vertical at the position of the radio core.

3.4.3 Spectral index maps and model fitting

Figure 3.5 shows the spectral index maps obtained. The map including the LBA data has a resolution of $0.9''$; the map excluding the LBA map has a resolution of $0.38''$. As expected, the spectra become steeper in directions away from the hotspots and towards the lobes. In the northern lobe, the spectral index ranges from -1.0 ± 0.2 to -1.3 ± 0.4 and in the southern lobe from -0.6 ± 0.2 to -1.3 ± 0.3 . For the high-resolution map at $0.38''$, the spectral index ranges from -1.0 to -1.4 in the northern lobe and up to -1.5 in the southern lobe.

Table 3.4: Flux densities of the northern and southern lobes, measured from native resolution maps. All are measured within $3\sigma_{\text{RMS}}$ contours, except for LOFAR, which was measured within $5\sigma_{\text{RMS}}$. Quoted errors in flux density are the combination of calibration uncertainty and the RMS noise in the map: $\sqrt{\sigma_{\text{map}}^2 + \sigma_{\text{cal}}^2}$. The errors in core distance and jet angle come from uncertainties from fitting and uncertainty propagation. Reported jet angles are taken as east of north, modulo 90° (i.e. with respect to their closest vertical).

	Frequency	S_{int} [mJy]	RMS [mJy beam $^{-1}$]	Core distance [kpc]	Jet angle [$^\circ$]
N	143.26 MHz	$(3.0 \pm 0.6) \times 10^3$	0.17	35.4 ± 0.2	$17.4 \pm 6.5 \cdot 10^{-2}$
	4.71 GHz	39.6 ± 4.4	0.072	35.9 ± 0.2	$17.8 \pm 6.0 \cdot 10^{-2}$
	8.44 GHz	15.4 ± 1.7	0.034	35.6 ± 0.1	$17.3 \pm 4.5 \cdot 10^{-2}$
S	143.26 MHz	$(3.0 \pm 0.6) \times 10^3$	0.17	47.2 ± 0.1	$9.0 \pm 1.5 \cdot 10^{-2}$
	4.71 GHz	113.2 ± 12.5	0.072	46.6 ± 0.1	$8.6 \pm 1.3 \cdot 10^{-2}$
	8.44 GHz	56.1 ± 6.2	0.034	47.2 ± 0.1	$8.6 \pm 1.5 \cdot 10^{-2}$

The high-resolution map shows a steep drop in the spectral index in the southwestern corner of the southern lobe, which is likely due to the remaining negative artefact around the source. This prevents a reliable lower value of the spectral index from being determined. The core has an average spectral index of -0.3 , consistent with earlier calculations of its integrated spectral index.

The spectral index map clearly shows a difference between the northern and southern lobes of 4C43.15. The southern lobe shows a wide range of spectral indices ($\Delta\alpha = 0.85$) between the flattest and steepest parts. The northern lobe shows a narrower spread in spectral indices ($\Delta\alpha = 0.39$) and is steeper on average.

Assuming equipartition, a magnetic field strength of $B_{\text{eq}} = 13.1$ nT was estimated. Scaled by the previously discussed factor of 0.4, this translates to an actual magnetic field strength of $B = 5.2$ nT for the lobes. Because of their different injection indices, the northern and southern lobes were modelled separately. The best fit for the injection index of $\alpha_{\text{inj}}^{\text{north}} = -0.8$ and $\alpha_{\text{inj}}^{\text{south}} = -0.6$ was found for the northern and southern lobes, respectively. Figure 3.8 shows the χ^2 landscape of the explored injection indices. In Fig. 3.6 we present the spectral age maps, obtained by fitting a JP+Tribble model to the $0.9''$ data. For the northern lobe the model could not be rejected at the 90% significance level, and spectral ages in the range $\tau_{\text{spec}}^{\text{min}} = 0.36_{-0.06}^{+0.04}$ Myr to $\tau_{\text{spec}}^{\text{max}} = 0.81_{-0.06}^{+0.05}$ Myr were found. For the southern lobe, the model could not be rejected at the 90% significance level, and spectral ages in the range $\tau_{\text{spec}}^{\text{min}} = 0.0_{-0.0}^{+0.02}$ Myr to $\tau_{\text{spec}}^{\text{max}} = 1.08_{-0.05}^{+0.07}$ Myr were found. These ages result in hotspot advance speeds of $0.15c$ and $0.14c$, respectively, for the northern and southern hotspots. Here c is the speed of light. Figure 3.9 shows model fits to the youngest, oldest, and best-fitting regions of each lobe.

3.5 Discussion

With the high angular resolution of the ILT, spectral studies can now be done on distant objects. For example, D. E. Harris et al., 2019 studied jet knots in 4C 41.19 and they favour an intrinsically curved particle energy distribution as the cause behind the observed spectral curvature in the knots. The spectral mod-

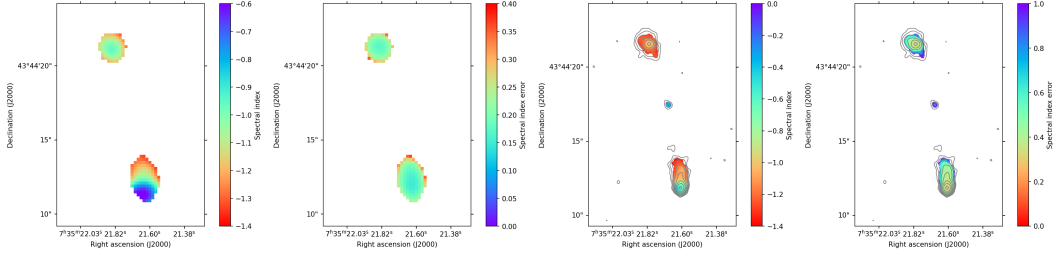


Figure 3.5: Spectral index maps of 4C43.15 obtained from BRATS and considering only pixels with values $> 5\sigma_{\text{RMS}}$. *Left*: $0.9''$ resolution map made from the LBA, HBA, and VLA data. The same additional signal-to-noise constraint as when fitting the ageing model was used. *Right*: $0.38''$ pixel-by-pixel map made from the HBA and VLA data. No additional signal-to-noise constraint was used in BRATS. The grey contours are drawn based on the 4.71 GHz map, starting at $0.29 \text{ mJy beam}^{-1}$ and $0.38 \text{ mJy beam}^{-1}$ for the left and right images, respectively. Each contour represents a factor of two increase in intensity.

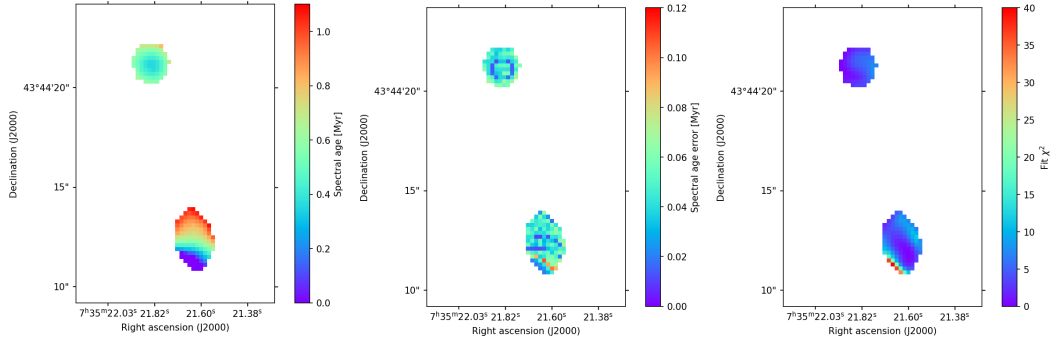
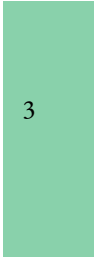


Figure 3.6: Spectral age maps of the fitted regions in 4C 43.15 after fitting a JP+Tribble model to the LBA, HBA, and VLA data. From left to right the panels show the spectral age of the plasma, its positive uncertainty, and the χ^2 value of the regions. The maps are shown at a $0.9''$ resolution. The grey contours are drawn based on the 4.71 GHz map, starting at 0.29 mJy/beam . Each contour represents a factor of $\sqrt{2}$ increase in intensity.



elling presented in this work focuses on lobes and is similar to the recent modelling in [Jeremy J. Harwood et al., 2016](#); [Jeremy J. Harwood et al., 2017](#).

The northern lobe has a rounder shape and the hotspot is embedded in the lobe, while the southern lobe is more elongated with the hotspot sitting at the edge. This could be a consequence of the ambient density being almost a factor of two lower for the northern lobe, as determined by [Motohara et al. \(2000\)](#) from observations of the $H\alpha$ emission line. This would allow the lobe to expand more easily into its surroundings. The southern lobe is facing a higher ambient density. Material here will thus have a harder time expanding into its surroundings, taking on a more cylindrical shape. It could also be more simply an orientation effect. There is no estimate of the inclination of the source available, which can complicate morphological analysis, but overall the morphology of 4C 43.15 is that of a typical FR II radio galaxy.

The closest example of such an object is the well-studied radio galaxy Cygnus A (e.g. [Carilli et al. 1991](#); [Steenbrugge et al. 2010](#); [McKean et al. 2016](#); [Vries et al. 2018](#); hereafter Cyg A). We therefore first compare our findings for 4C 43.15 with it and two other nearby sources studied in [Jeremy J. Harwood et al., 2016](#) and [Jeremy J. Harwood et al., 2017](#): 3C 223 and 3C 452, $z = 0.137$ and $z = 0.081$, respectively. We see the expected morphological similarities between the two sources, but differences are also seen. In Cyg A, two hotspots are identified in each lobe, which may be attributed to the jet changing direction over time ([Carilli et al., 1999](#)). In 4C 43.15 there is a smaller extent of diffuse emission from material flowing back to the core compared to the other sources. It reaches about midway between the hotspot and the core, whereas the nearby sources have diffuse emission close to the core. This could indicate that the material has not had the time to flow back yet, reflected by the two orders of magnitude difference in spectral age.

The hotspots in 4C 43.15 are advancing faster than those in these local sources. Estimates for Cyg A range from $0.005c$ to $0.05c$ ([Muxlow et al., 1988](#); [Paul Alexander et al., 1996](#)) and for 3C 223 and 3C 452 they are between $0.01c - 0.02c$, which is an order of magnitude slower. 4C 43.15 has a significantly higher radio luminosity than these local sources, and hence a more powerful jet. The kinetic power of the jets increases with radio luminosity ([Hardcastle et al., 2019](#)). A more powerful jet could thus produce faster-moving hotspots, being less affected by the environmental density, due to a larger driving force pushing material out.

These are only three local sources, however. To put 4C 43.15 in a broader context, we compare its advanced speeds and injection indices with other radio galaxies in the literature. [P. Alexander et al., 1987](#), [Liu et al., 1992](#), and [C. P. O’Dea et al., 2009](#) measured spectral indices for a number of sources over a range of redshifts, and estimated advance speeds and spectral ages based on their estimated break frequencies. These ages depend on the adopted ratio b/b_{eq} , but are between $\sim 10^6$ and a few times 10^7 Myr, comparable to what we find for this source. The corresponding advance speeds range up to $0.4c$. They find injection indices between -0.65 and -1.11 . We consider our values to be consistent with those found in the literature.

Finally, the spectral index and spectral age maps show the same characteristics for all sources: relatively young and flat emission at the hot spots, steepening and growing older towards the core. For 3C 223 and 3C 452, the spectral index ranges from $\alpha \approx -0.5$ in the hotspots to $\alpha \approx -1$ in the oldest regions near the core. What makes 4C 43.15 different is a steeper spectrum in general, and the difference between the two lobes. This asymmetry between the lobes is discussed next.

3.5.1 What drives the lobe difference?

The intensity map and spectral index map both show the lobes to be different. The northern lobe has a more diffuse circular shape and has steeper spectra. Here we revisit this difference.

We rule out that the difference in steepness is caused by Doppler boosting. [Humphrey et al., 2007](#) calculated the expected spectral index asymmetries from Doppler boosting for various hotspot advance speeds. An advance speed of $0.2c$ would only imply a 0.12 asymmetry in the spectral index of the hotspots for an inclination angle of 50° , much less than the observed difference.

This brings us back to the question of whether the environment it resides in has an effect on steepening the spectrum, specifically the scenario where a higher ambient density would cause a steeper spectrum. The two arguments for this scenario introduced earlier are longer confinement of the lobes increasing surface brightness of the oldest emission, and slower speeds of the plasma near the hotspot leading to a steeper injection index. Estimates of the environmental density are available from [Motohara et al. \(2000\)](#), who measure the medium surrounding the northern lobe to only have 55% the density of that surrounding the southern lobe. If the steep spectrum of 4C 43.15 indeed comes from these environmental effects, we expect the steepest spectral index in the southern lobe and the steepest hotspot spectral index in the southern lobe.

For the first case, we measure no difference between the steepest spectral indices in each lobe. The lobe in the less dense environment is also the steepest on average, opposite to what was expected if confinement by a dense medium drove the steepening. The second case provides a stronger argument. A jet working against a denser medium is proposed to have a steeper injection index. In this work, we estimated the spectral index near the hotspot directly from the data and fitted for the injection index. Both measurements show the northern hotspot to have the steepest spectral index, even though it resides in the lower-density environment. For the southern lobe, the hotspot spectral index and fitted injection index are consistent with the range of measurements in the literature. They are also close to the theoretical lower limit of $\alpha_{\text{inj}} = -0.5$ ([R. Athreya et al., 1998](#)). We rule out the environment as the cause for a steeper spectral index based on the new information about the spatial distribution of spectra in this source.

Having ruled out Doppler boosting based on the estimated advance speeds, and ruled out the effects on the particle acceleration due to the environmental density based on the spatial distribution of spectra, we remain at the original conclusion by [Leah K. Morabito et al., 2016](#). It is likely that the difference between the lobes is caused by adiabatic expansion having a stronger effect on the northern lobe due to its lower ambient density. The expansion will lower the surface brightness of the lobe, as is observed. Furthermore, adiabatic expansion will shift the emission by equal amounts in intensity and frequency ([Katz-Stone et al., 1997](#)). As the intensity lowers due to expansion, the emission is shifted to lower frequencies. The spectrum will therefore be artificially steepened by this effect, but it is difficult to quantify how much it has been steepened.

3.5.2 Core spectral index

The spectral index of the core between 4.71 GHz and 8.42 GHz that we find is a factor of two less steep than originally found in [Carilli et al., 1997](#), for this source and for their sample. It was mentioned, however, that in this case, the identification of the core was uncertain due to source confusion, a low signal-to-noise ratio, or a core with $\alpha \leq -1$. Our results seem to exclude the last. Our measured spectral index of -0.8 is broadly in line with the values reported by [R. M. Athreya et al., 1997](#).

3.5.3 Magnetic field strength

The uncorrected equipartition magnetic field strength of 13.1 nT found for 4C 43.15 appears to be higher than its local counterparts, even when scaled by 0.4. A typical field strength for local counterparts is ~ 1 nT. [Krolik et al., 1991](#) show that the equipartition magnetic field in the lobes scales as $b \propto (1+z)^{0.8}$, assuming

synchrotron radiation as the dominant energy loss process and that the distributions of lobe volume and the time electrons spend here do not scale with redshift. At $z = 2.429$, this scaling could increase the magnetic field strength by a factor of 2.68. Locally Cygnus A has an equipartition field strength of 4 nT (Vries et al., 2018) and the nearby radio galaxy 3C 277.3 (coma a, $z = 0.0857$, Bridle et al. 1981) has a magnetic field strength of 3–5 nT in its southern lobe when assuming equipartition. Scaling both of these nearby galaxies according to the above relation yields similar field strengths to what is observed here. Chambers et al., 1990 also derived similarly high magnetic field strengths for components in the $z = 3.8$ radio galaxy 4C 41.17. The field strength values reported by Liu et al., 1992 and C. P. O’Dea et al., 2009 are similar. Therefore, the strong magnetic field in 4C 43.15 appears to be in line with expectations.

What does its magnetic field strength imply? The equivalent magnetic field strength of the CMB is 3.7 nT at this redshift ($B_{\text{CMB}} = 0.318(1+z)^2$; Jeremy J. Harwood et al. 2013). This is close to the scaled magnetic field strength value of 5.2 nT found for 4C 43.15. In this case, synchrotron cooling appears to still be the dominant effect of energy losses in the lobe plasma, but only by a factor of 1.4. At redshifts $z \gtrsim 3$, the CMB’s equivalent magnetic field strength becomes 5.2 nT. Given its luminosity, 4C 43.15 is one of the rare powerful radio-loud AGNs over a range of redshifts up to $z = 5$ (Hardcastle et al., 2019). For the assumed scaling of $b = 0.4b_{\text{eq}}$, we would therefore expect a significant fraction of sources above redshift 3 to be dominated by IC losses. Closer sources will still be dominated by synchrotron losses, depending on their magnetic field strength. The proportionality constant between the equipartition magnetic field strength and the actual magnetic field strength spans a wide range of values. A larger sample of sources with an estimate of their magnetic field strength is needed over a wide range of redshifts for any strong conclusions to be drawn.

3.5.4 The $\alpha - z$ correlation

The first question we address here, in the context of the $\alpha - z$ correlation, is whether or not 4C 43.15 is a true ultra-steep spectrum source, which is typically said to have $\alpha < -1$. The key question is whether the 4C 43.15 spectrum is intrinsically steep, or if it is just observed to be. Leah K. Morabito et al., 2016 already pointed out that its integrated spectral index below 1.4 GHz (i.e. 4.8 GHz rest frame) would no longer classify as ultra-steep because of a break in the spectrum. This is reflected by the values of the injection index for both lobes as well. The injection index probes the low-frequency power-law part of the spectrum and does not show ultra-steep values for either lobe. Hence, although it fits the ultra-steep spectrum criteria of De Breuck et al., 2000 ($\alpha_{1.4\text{GHz}}^{325\text{MHz}} < -1.3$), the spectral index is not ultra-steep across the entire spectrum. Most importantly, the estimated injection indices are in agreement with typical values found for this kind of source in the literature. This rules out that the spectrum is intrinsically steep, and means instead that it has steepened because of spectral ageing effects.

What does 4C 43.15 therefore tell us about the $\alpha - z$ correlation? The goal was to see if this source could tell us something about the main driving force behind this correlation. Earlier, three possible causes for this relation were introduced: environmental effects, observational bias, and IC losses. Klammer et al., 2006 discuss how a higher density environment could lead to steeper spectra. Based on the scenarios there, if the steep spectral indices found in this source were driven by environmental density effects, they would be expected in or near the southern hotspot where the ambient density is highest. However, in this case, we find that the steeper spectrum belongs to the lobe residing in the lower-density environment. Environmental effects are certainly at play. The northern lobe will be more strongly affected by adiabatic expansion because of the significantly lower density around it compared to the southern lobe.

Secondly, could we be affected by an observational bias? As explored by Ker et al., 2012 and other

authors, observational biases should be considered carefully and make interpreting correlations such as $\alpha - z$ difficult. From the luminosity of 4C 43.15, it is clear that we are looking at one of the rarer bright sources in the radio sky. The radio luminosity and jet power of a source are related to each other. Work by [Ineson et al., 2017](#) and [Hardcastle et al., 2019](#), among others, show increasing jet powers for increasing 150 MHz luminosities, and these relations put 4C 43.15 at high jet powers. [Blundell et al., 1999](#) presented arguments for a relation between jet power and spectral index, where more powerful jets can create a stronger magnetic field in the hotspots. As a consequence, more powerful radio sources with stronger magnetic fields age more rapidly, producing steeper spectra. If a stronger jet also means a stronger lobe magnetic field strength, we could be affected by the Malmquist bias here, possibly looking at one of the more luminous members of the high-redshift population. A single source is not enough to draw any conclusions in this regard, but this is not an unreasonable assumption: 3C and 4C sources are powerful radio galaxies. Results for 3C sources from [Vaddi et al., 2019](#) support this; in their sample, the highest redshift sources also show the highest magnetic field strength.

Finally, we suggest that there is an interaction with CMB photons. Inverse Compton losses become increasingly important at higher redshifts. As the energy density of the CMB increases, the CMB photons will more efficiently scatter electrons, contributing more to cooling the plasma. The cooling in 4C 43.15 is still mainly through synchrotron losses, as $B_{\text{lobe}} > B_{\text{CMB}}$, but the difference is only a factor of 1.5. This makes both synchrotron and IC losses important mechanisms for energy loss. The magnetic field strengths reported in [Vaddi et al., 2019](#) increase with redshift and reach $\sim 90\%$ of that found in 4C43.15, but also show a wide range of values. If the magnetic field strength of 4C 43.15 is not representative for the average magnetic field strength in HzRGs, then IC losses could be a significant contributor or start to dominate at higher redshifts or for sources with weaker magnetic fields in their lobes. Such a scenario, that increased IC losses can explain the observed correlation, is also consistent with the findings of [Leah K Morabito et al., 2018](#).

3.6 Conclusion

The aim of this paper was to investigate whether increased IC losses, Malmquist bias, or environmental effects are the possible drivers behind the $\alpha - z$ relation. For the first time, we demonstrate spatially resolved spectral modelling of a high-redshift object using low-frequency observations by combining high angular resolution ILT and VLA data from 55 MHz to 8.4 GHz. We used the BRATS software package to fit a spectral ageing model to the data. A magnetic field strength of $B = 5.2$ nT was estimated and best fitting injection indices of $\alpha_{\text{inj}}^{\text{north}} = -0.8$ and $\alpha_{\text{inj}}^{\text{south}} = -0.7$ were determined. Using these to fit a JP Tribble ageing model, we measure a young spectral age compared to local sources, with values of $\tau_{\text{spec}} = 0.8 \pm 0.1$ Myr and $\tau_{\text{spec}} = 0.9 \pm 0.1$ Myr for the northern and southern lobes.

Although no strong conclusions about the origins of the $\alpha - z$ correlation can be drawn from this source alone, our data supports the possibility that the increasing IC losses at higher redshifts is one of the drivers behind it. The strong magnetic field of 4C 43.15 seems plausible. In this case, synchrotron losses still dominate over IC losses, but a magnetic field that is half the strength would already reverse this. Assuming that the jet power, radio luminosity and magnetic field strength all scale with each other, the general high-redshift population may well be dominated by IC losses, gradually switching dominant mechanisms as redshift increases. Given the high luminosity of 4C 43.15 and the lack of data on a larger sample, we cannot rule out that the $\alpha - z$ relation is partially driven by Malmquist bias. Finally, we have ruled out that an

increased density of the environment steepens the spectrum.

A handful of studies have now demonstrated LOFAR's unique capabilities for high-resolution imaging. In the future, high-resolution imaging will become routine. When combined with LOFAR's wide field of view, a large sample of spatially resolved high-redshift objects will become available. This will allow us to extend analyses such as the one in this paper to a statistically significant sample and investigate the low-frequency structure and spectra of the general high-redshift population. Finally, the Low Band Antennas of the ILT will further push the boundaries, providing subarcsecond resolution at frequencies well below 100 MHz.

3.7 Acknowledgements

We thank Sean Mooney, Raffaella Morganti and Raymond Oonk for their valuable input on early drafts of this manuscript. This paper is based (in part) on data obtained with the International LOFAR Telescope (ILT) under project code LT5_006. LOFAR (van Haarlem et al. 2013) is the Low Frequency Array designed and constructed by ASTRON. It has observing, data processing, and data storage facilities in several countries, that are owned by various parties (each with their own funding sources), and that are collectively operated by the ILT foundation under a joint scientific policy. The ILT resources have benefited from the following recent major funding sources: CNRS-INSU, Observatoire de Paris and Université d'Orléans, France; BMBF, MIWF-NRW, MPG, Germany; Science Foundation Ireland (SFI), Department of Business, Enterprise and Innovation (DBEI), Ireland; NWO, The Netherlands; The Science and Technology Facilities Council, UK; Ministry of Science and Higher Education, Poland. RJvW acknowledges support from the ERC Starting Grant ClusterWeb 804208. This work has made use of the Dutch national e-infrastructure with the support of SURF Cooperative through grant e-infra 180169. JM acknowledges financial support from the State Agency for Research of the Spanish MCIU through the "Center of Excellence Severo Ochoa" award to the Instituto de Astrofísica de Andalucía (SEV-2017-0709) and from the grant RTI2018-096228-B-C31 (MICIU/FEDER, EU)

Appendix

LOFAR LBA 55 MHz map

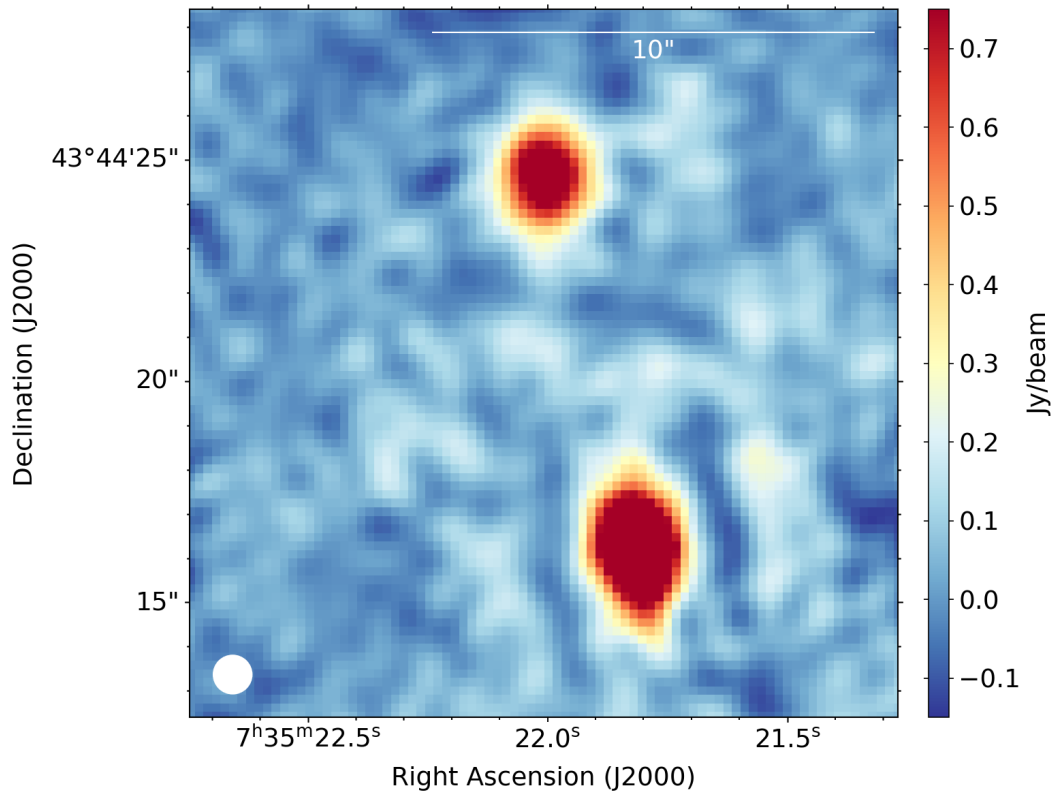


Figure 3.7: LOFAR LBA map at 55 MHz from Leah K. Morabito et al. (2016). The colour scale is shown on a linear stretch and ranges from -0.15 to $0.75 \text{ Jy beam}^{-1}$. In the bottom left corner, a white circle illustrates the restoring beam of $0.9''$ to which the image was smoothed. North is up and east is to the left.

Injection index and model fits

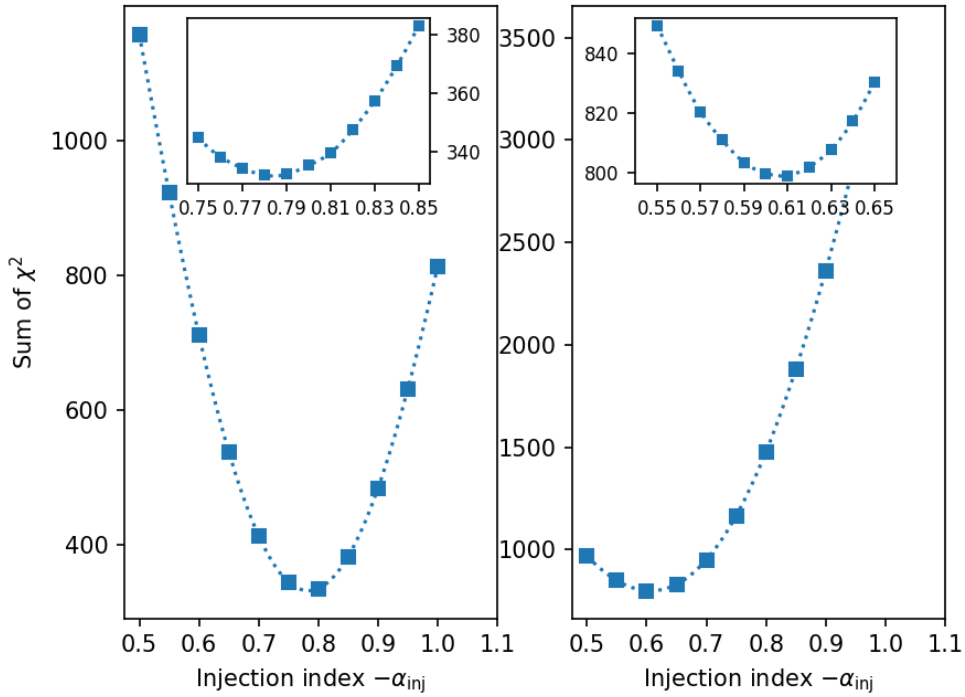


Figure 3.8: χ^2 landscape of the initial broad search for the injection index α_{inj} . *Left:* Northern lobe. *Right:* Southern lobe. Squares indicate the explored values. The dotted lines are cubic spline fits for illustrative purposes. The large panels show the χ^2 values for the broad search from 0.5 to 1.0. The insets show the χ^2 values for the detailed search in a narrower range of 0.75 – 0.85 (left) and 0.55 – 0.65 (right).

3.7. ACKNOWLEDGEMENTS

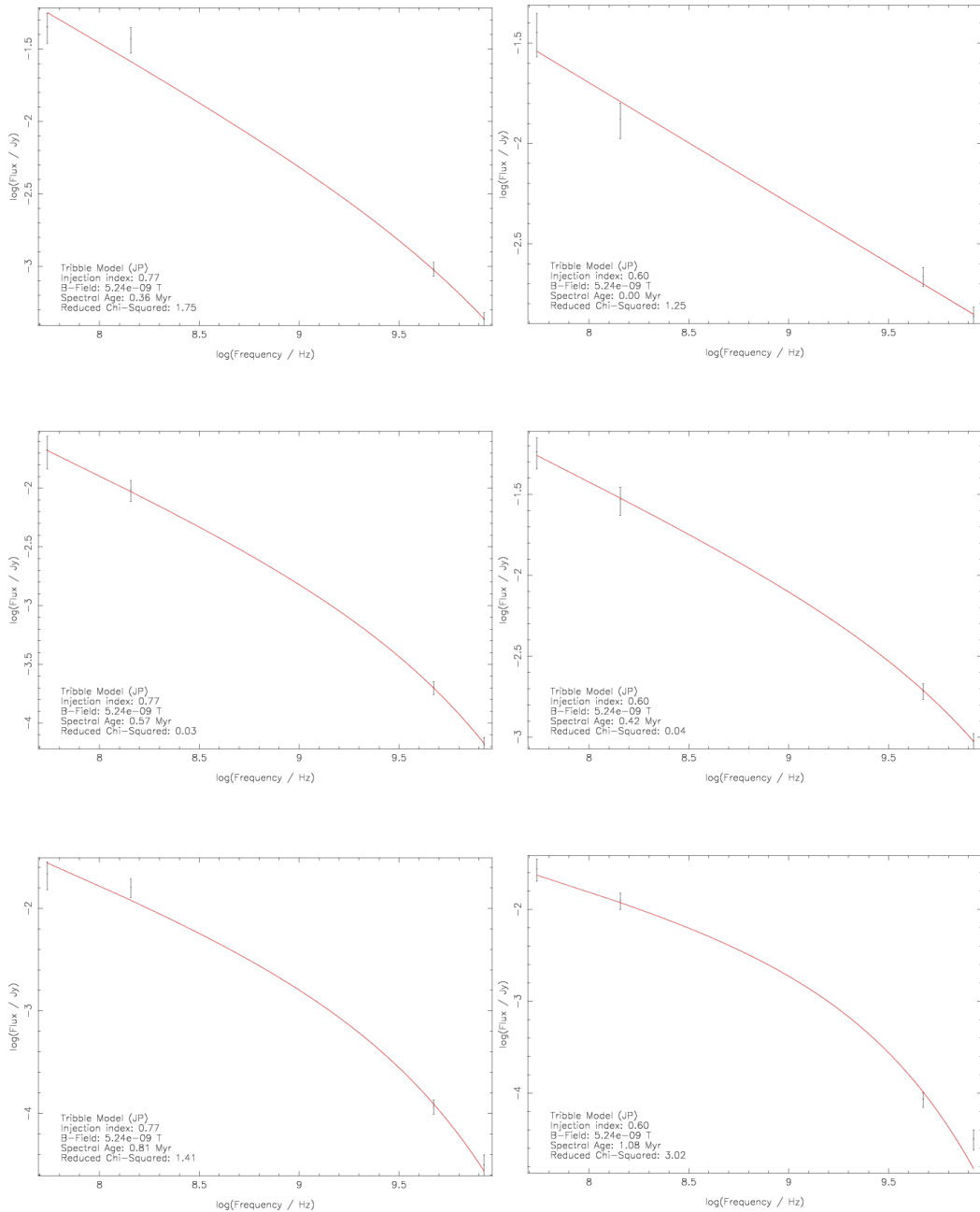


Figure 3.9: Model fits of the JP Tribble spectral ageing model for the northern (*left*) and southern (*right*) lobes. Fits in a region with the youngest spectral age (*top*), lowest reduced χ^2 (*middle*), and oldest spectral age (*bottom*) are shown. The black points with error bars indicate the flux density data points in that region and the red line shows the model fit. In the lower left corner of each panel the fitted model, best fitting injection index, magnetic field strength and spectral age in that region, and the reduced χ^2 values are listed.

Bibliography

- Ade, P. A. R. et al. (Oct. 2016). “Planck 2015 Results”. In: *Astronomy & Astrophysics* 594, A13. ISSN: 0004-6361. DOI: [10.1051/0004-6361/201525830](https://doi.org/10.1051/0004-6361/201525830). (Visited on 11/07/2018).
- Alexander, P. and J. P. Leahy (Mar. 1987). “Ageing and speeds in a representative sample of 21 classical double radio sources.” In: *MNRAS* 225, pp. 1–26. DOI: [10.1093/mnras/225.1.1](https://doi.org/10.1093/mnras/225.1.1).
- Alexander, Paul and G. G. Pooley (1996). “The large-scale structure, dynamics and thermodynamics of Cygnus A”. In: *Cygnus A – Study of a Radio Galaxy, Proceedings of the Greenbank Workshop, held in Greenbank, West Virginia, 1-4 May, 1995. Edited by C.L. Carilli and D.E. Harris. ISBN 0521553431, Cambridge University Press, 1996., p.149*. Ed. by Christopher L. Carilli and Daniel E. Harris, p. 149.
- Athreya, R. M. et al. (Aug. 1997). “Steep-spectrum radio cores in high-redshift galaxies”. In: *Monthly Notices of the Royal Astronomical Society* 289.3, pp. 525–534. ISSN: 0035-8711. DOI: [10.1093/mnras/289.3.525](https://doi.org/10.1093/mnras/289.3.525). URL: <https://academic.oup.com/mnras/article-lookup/doi/10.1093/mnras/289.3.525>.
- Athreya, R.~M. and V.~K. Kapahi (Dec. 1998). “The Redshift Dependence of Spectral Index in Powerful Radio Galaxies.” In: *Journal of Astrophysics and Astronomy* 19, pp. 63–77. DOI: [10.1007/BF02714911](https://doi.org/10.1007/BF02714911).
- Beck, R. and M. Krause (July 2005). “Revised equipartition and minimum energy formula for magnetic field strength estimates from radio synchrotron observations”. In: *Astronomische Nachrichten* 326.6, pp. 414–427. ISSN: 0004-6337. DOI: [10.1002/asna.200510366](https://doi.org/10.1002/asna.200510366). URL: <http://doi.wiley.com/10.1002/asna.200510366>.
- Blundell, Katherine M., Steve Rawlings, and Chris J. Willott (Feb. 1999). “The Nature and Evolution of Classical Double Radio Sources from Complete Samples”. In: *The Astronomical Journal* 117.2, pp. 677–706. ISSN: 00046256. DOI: [10.1086/300721](https://doi.org/10.1086/300721). arXiv: [9810197](https://arxiv.org/abs/9810197) [astro-ph]. URL: <http://stacks.iop.org/1538-3881/117/i=2/a=677>.
- Bridle, A. H. et al. (Sept. 1981). “VLA observation of radio/optical knots in 3C 277.3 = Coma A”. In: *ApJ* 248, pp. 499–503. DOI: [10.1086/159174](https://doi.org/10.1086/159174).
- Carilli, C. L. et al. (Dec. 1991). “Multifrequency Radio Observations of Cygnus A: Spectral Aging in Powerful Radio Galaxies”. In: *ApJ* 383, p. 554. DOI: [10.1086/170813](https://doi.org/10.1086/170813).
- Carilli, C. L. et al. (Mar. 1997). “Radio Continuum Imaging of High-Redshift Radio Galaxies”. In: *The Astrophysical Journal Supplement Series* 109.1, pp. 1–44. ISSN: 0067-0049. DOI: [10.1086/312973](https://doi.org/10.1086/312973). URL: <http://stacks.iop.org/0067-0049/109/i=1/a=1>.
- Carilli, C. L. et al. (Dec. 1999). “High-Resolution Millimeter and Infrared Observations of the Hot Spots of Cygnus A”. In: *AJ* 118.6, pp. 2581–2591. DOI: [10.1086/301137](https://doi.org/10.1086/301137).
- Chambers, K. C., G. K. Miley, and W. J. M. van Breugel (Nov. 1990). “4C 41.17: A Radio Galaxy at a Redshift of 3.8”. In: *ApJ* 363, p. 21. DOI: [10.1086/169316](https://doi.org/10.1086/169316).

- Cielo, Salvatore et al. (June 2017). “AGN Feedback Compared: Jets versus Radiation”. In: *Monthly Notices of the Royal Astronomical Society* 477.1, pp. 1336–1355. ISSN: 1365-2966. DOI: 10.1093/mnras/sty708. arXiv: 1712.03955. URL: <https://academic.oup.com/mnras/article/477/1/1336/4937823> http://arxiv.org/abs/1712.03955%7B%5C%7D0Ahttp://dx.doi.org/10.1093/mnras/sty708.
- Croston, J. H. et al. (Sept. 2004). “X-ray emission from the nuclei, lobes and hot-gas environments of two FR II radio galaxies”. In: *Monthly Notices of the Royal Astronomical Society* 353.3, pp. 879–889. ISSN: 00358711. DOI: 10.1111/j.1365-2966.2004.08118.x. URL: <https://academic.oup.com/mnras/article-lookup/doi/10.1111/j.1365-2966.2004.08118.x>.
- Croston, J. H. et al. (June 2005). “An X-Ray Study of Magnetic Field Strengths and Particle Content in the Lobes of FR II Radio Sources”. In: *The Astrophysical Journal* 626.2, pp. 733–747. ISSN: 0004-637X. DOI: 10.1086/430170. URL: <http://stacks.iop.org/0004-637X/626/i=2/a=733>.
- De Breuck, C. et al. (Apr. 2000). “A Sample of 669 Ultra Steep Spectrum Radio Sources to Find High Redshift Radio Galaxies”. In: *Astronomy and Astrophysics Supplement Series* 143.2, pp. 303–333. ISSN: 0365-0138. DOI: 10.1051/aas:2000181. (Visited on 09/11/2018).
- Ghisellini, G. et al. (Mar. 2014). “Radio-loud active galactic nuclei at high redshifts and the cosmic microwave background”. In: *Monthly Notices of the Royal Astronomical Society* 438.3, pp. 2694–2700. ISSN: 00358711. DOI: 10.1093/mnras/stt2394. arXiv: 1311.7147. URL: <http://academic.oup.com/mnras/article/438/3/2694/973903/Radioloud-active-galactic-nuclei-at-high-redshifts>.
- Gopal-Krishna, Mukul Mhaskey, and A. Mangalam (Jan. 2012). “On the Injection Spectrum of Relativistic Electrons in High-redshift Radio Galaxies”. In: *ApJ* 744.1, 31, p. 31. DOI: 10.1088/0004-637X/744/1/31. arXiv: 1110.3884 [astro-ph.CO].
- Haarlem, M. P. van et al. (Aug. 2013). “LOFAR: The LOw-Frequency ARray”. In: *Astronomy & Astrophysics* 556, A2. ISSN: 0004-6361, 1432-0746. DOI: 10.1051/0004-6361/201220873. (Visited on 09/20/2023).
- Hales, S. E. G., J. E. Baldwin, and P. J. Warner (July 1993a). “The 6C Survey of Radio Sources - VI. The Continuous Zone 30 < < 51, 0h < < 09h 05m and 22h 35m < < 24h”. In: *Monthly Notices of the Royal Astronomical Society* 263.1, pp. 25–30. ISSN: 0035-8711. DOI: 10.1093/mnras/263.1.25. (Visited on 12/14/2018).
- Hardcastle, M. J. and M. G. H. Krause (Mar. 2013). “Numerical Modelling of the Lobes of Radio Galaxies in Cluster Environments”. In: *Monthly Notices of the Royal Astronomical Society* 430, pp. 174–196. ISSN: 0035-8711. DOI: 10.1093/mnras/sts564. (Visited on 10/23/2023).
- Hardcastle, M. J. et al. (Dec. 2002). “Magnetic Field Strengths in the Hot Spots and Lobes of Three Powerful Fanaroff-Riley Type II Radio Sources”. In: *The Astrophysical Journal* 581.2, pp. 948–973. ISSN: 0004-637X. DOI: 10.1086/344409.
- Hardcastle, M. J. et al. (Feb. 2019). “Radio-Loud AGN in the First LoTSS Data Release”. In: *Astronomy & Astrophysics* 622, A12. ISSN: 0004-6361. DOI: 10.1051/0004-6361/201833893. (Visited on 01/24/2020).
- Harris, D. E. et al. (Feb. 2019). “LOFAR Observations of 4C+19.44: On the Discovery of Low-frequency Spectral Curvature in Relativistic Jet Knots”. In: *The Astrophysical Journal* 873.1, p. 21. ISSN: 1538-4357. DOI: 10.3847/1538-4357/ab01ff. arXiv: 1903.06824.
- Harwood, Jeremy J. (2017). “Spectral ageing in the era of big data: Integrated versus resolved models”. In: *Monthly Notices of the Royal Astronomical Society* 466.3, pp. 2888–2894. ISSN: 13652966. DOI: 10.1093/mnras/stw3318. arXiv: 1612.04390.

- Harwood, Jeremy J., Martin J. Hardcastle, and Judith H. Croston (Dec. 2015). “Spectral ageing in the lobes of cluster-centre FR II radio galaxies”. In: *Monthly Notices of the Royal Astronomical Society* 454.4, pp. 3403–3422. ISSN: 13652966. DOI: 10.1093/mnras/stv2194. arXiv: 1509.06757. URL: <https://academic.oup.com/mnras/article-lookup/doi/10.1093/mnras/stv2194>.
- Harwood, Jeremy J. et al. (Nov. 2013). “Spectral Ageing in the Lobes of FR-II Radio Galaxies: New Methods of Analysis for Broad-Band Radio Data”. In: *Monthly Notices of the Royal Astronomical Society* 435.4, pp. 3353–3375. ISSN: 00358711. DOI: 10.1093/mnras/stt1526. arXiv: 1308.4137. (Visited on 07/31/2018).
- Harwood, Jeremy J. et al. (June 2016). “FR II radio galaxies at low frequencies – I. Morphology, magnetic field strength and energetics”. In: *Monthly Notices of the Royal Astronomical Society* 458.4, pp. 4443–4455. ISSN: 0035-8711. DOI: 10.1093/mnras/stw638. URL: <https://academic.oup.com/mnras/article-lookup/doi/10.1093/mnras/stw638>.
- Harwood, Jeremy J. et al. (Apr. 2017). “FR-II radio galaxies at low frequencies II: spectral ageing and source dynamics”. In: *MNRAS* 469, pp. 1–18. ISSN: 0021-8812. DOI: 10.1093/mnras/stx820. arXiv: arXiv:1704.01576v1. URL: <http://arxiv.org/abs/1704.01576> <http://dx.doi.org/10.1093/mnras/stx820> <https://arxiv.org/pdf/1704.01576.pdf>.
- Huarte-Espinosa, Martín, Martin Krause, and Paul Alexander (Oct. 2011). “3D-MHD simulations of the evolution of magnetic fields in FR II radio sources”. In: *Monthly Notices of the Royal Astronomical Society* 417, pp. 382–399. ISSN: 17439213. DOI: 10.1017/S1743921310015899. arXiv: 1106.4586 [astro-ph.CO]. URL: <https://academic.oup.com/mnras/article-lookup/doi/10.1111/j.1365-2966.2011.19271.x>.
- Humphrey, A. et al. (Feb. 2007). “Giant Ly nebulae around $z > 2$ radio galaxies: evidence for infall”. In: *Monthly Notices of the Royal Astronomical Society* 375.2, pp. 705–714. ISSN: 0035-8711. DOI: 10.1111/j.1365-2966.2006.11344.x. URL: <https://academic.oup.com/mnras/article-lookup/doi/10.1111/j.1365-2966.2006.11344.x>.
- Ineson, J. et al. (Jan. 2017). “A representative survey of the dynamics and energetics of FR II radio galaxies”. In: *Monthly Notices of the Royal Astronomical Society* 467.2, pp. 1586–1607. ISSN: 13652966. DOI: 10.1093/mnras/stx189. arXiv: 1701.05612. URL: <https://academic.oup.com/mnras/article-lookup/doi/10.1093/mnras/stx189>.
- Intema, H. T. et al. (Feb. 2017). “The GMRT 150 MHz All-Sky Radio Survey - First Alternative Data Release TGSS ADR1”. In: *Astronomy & Astrophysics* 598, A78. ISSN: 0004-6361, 1432-0746. DOI: 10.1051/0004-6361/201628536. (Visited on 09/11/2023).
- Jackson, N. et al. (Nov. 2016). “LBCS: The LOFAR Long-Baseline Calibrator Survey”. In: *Astronomy & Astrophysics* 595, A86. ISSN: 0004-6361. DOI: 10.1051/0004-6361/201629016. arXiv: 1608.02133. (Visited on 05/23/2018).
- Jaffe, W. J. and G. C. Perola (Aug. 1973). “Dynamical Models of Tailed Radio Sources in Clusters of Galaxies”. In: *Astronomy and Astrophysics* 26, p. 423. ISSN: 0004-6361. (Visited on 10/23/2023).
- Jamrozy, M. et al. (Apr. 2008). “A multifrequency study of giant radio sources - II. Spectral ageing analysis of the lobes of selected sources”. In: *MNRAS* 385.3, pp. 1286–1296. DOI: 10.1111/j.1365-2966.2007.12772.x. arXiv: 0712.0162 [astro-ph].
- Jennison, R. C. (Jan. 1958). “A phase sensitive interferometer technique for the measurement of the Fourier transforms of spatial brightness distributions of small angular extent”. In: *MNRAS* 118, p. 276. DOI: 10.1093/mnras/118.3.276.
- Kardashev, N. S. (Jan. 1962). “Nonstationarity of Spectra of Young Sources of Nonthermal Radio Emission”. In: *Astronomicheskii Zhurnal* 39, p. 393. ISSN: 0004-6299. (Visited on 10/23/2023).

- Katz-Stone, D. M. and L. Rudnick (Oct. 1997). “An Analysis of the Synchrotron Spectrum in the Fanaroff-Riley Type I Galaxy 3C 449”. In: *ApJ* 488.1, pp. 146–154. DOI: 10.1086/304661.
- Ker, L. M. et al. (Mar. 2012). “New insights on the z - α correlation from complete radio samples”. In: *Monthly Notices of the Royal Astronomical Society* 420.3, pp. 2644–2661. ISSN: 00358711. DOI: 10.1111/j.1365-2966.2011.20235.x. arXiv: arXiv:1111.5244v1. URL: <https://academic.oup.com/mnras/article-lookup/doi/10.1111/j.1365-2966.2011.20235.x>.
- Kirk, J.-G. and P Schneider (Apr. 1987). “On the Acceleration of Charged Particles at Relativistic Shock Fronts”. In: *apj* 315, p. 425. DOI: 10.1086/165147.
- Klamer, I. J. et al. (Sept. 2006). “A search for distant radio galaxies from SUMSS and NVSS - III. Radio spectral energy distributions and the z -correlation”. In: *Monthly Notices of the Royal Astronomical Society* 371.2, pp. 852–866. ISSN: 0035-8711. DOI: 10.1111/j.1365-2966.2006.10714.x. URL: <https://academic.oup.com/mnras/article-lookup/doi/10.1111/j.1365-2966.2006.10714.x>.
- Krolik, Julian H. and Wan Chen (Nov. 1991). “Steep radio spectra in high-redshift radio galaxies”. In: *AJ* 102, p. 1659. ISSN: 00046256. URL: <http://adsabs.harvard.edu/cgi-bin/bib%7B%5C%7Dquery?1991AJ....102.1659K>.
- Liu, Ronghui, Guy Pooley, and Julia M. Riley (1992). “Spectral ageing in a sample of 14 high-luminosity double radio sources”. In: *Monthly Notices of the Royal Astronomical Society* 257.4, pp. 545–571. ISSN: 13652966. DOI: 10.1093/mnras/257.4.545.
- Mahatma, Vijay H et al. (2019). “Investigating the spectral age problem with powerful radio galaxies”. In: *Monthly Notices of the Royal Astronomical Society* 491.4, pp. 5015–5034. ISSN: 0035-8711. DOI: 10.1093/mnras/stz3396. arXiv: 1912.01028.
- McCarthy, P. J. (Aug. 1991). “High redshift radio galaxies from the Third Bologna Catalogue.” In: *AJ* 102, pp. 518–521. DOI: 10.1086/115890.
- McKean, J. P. et al. (Dec. 2016). “LOFAR imaging of Cygnus A – direct detection of a turnover in the hotspot radio spectra”. In: *Monthly Notices of the Royal Astronomical Society* 463.3, pp. 3143–3150. ISSN: 0035-8711. DOI: 10.1093/mnras/stw2105. URL: <https://academic.oup.com/mnras/article-lookup/doi/10.1093/mnras/stw2105>.
- McMullin, J. P. et al. (2007). “CASA Architecture and Applications”. In: *Astronomical Data Analysis Software and Systems XVI*. Ed. by R. A. Shaw, F. Hill, and D. J. Bell. Vol. 376. Astronomical Society of the Pacific Conference Series, p. 127.
- Mevius, Maaijke (June 2018). *RMextract: Ionospheric Faraday Rotation calculator*. ascl: 1806.024.
- Miley, George and Carlos De Breuck (2008). “Distant radio galaxies and their environments”. In: *Astronomy and Astrophysics Review* 15.2, pp. 67–144. ISSN: 09354956. DOI: 10.1007/s00159-007-0008-z. arXiv: 0802.2770.
- Moldón, J. et al. (2015). “The LOFAR Long Baseline Snapshot Calibrator Survey”. In: *Astronomy and Astrophysics* 574. ISSN: 14320746. DOI: 10.1051/0004-6361/201425042. arXiv: 1411.2743.
- Morabito, Leah K and Jeremy J Harwood (Oct. 2018). “Investigating the Cause of the α - z Relation”. In: *Monthly Notices of the Royal Astronomical Society* 480.2, pp. 2726–2732. ISSN: 13652966. DOI: 10.1093/MNRAS/STY2019. arXiv: 1807.09793. (Visited on 11/26/2018).
- Morabito, Leah K. et al. (2016). “LOFAR VLBI Studies at 55MHz of 4C 43.15, a $z = 2.4$ Radio Galaxy”. In: *Monthly Notices of the Royal Astronomical Society* 461.3, pp. 2676–2687. ISSN: 13652966. DOI: 10.1093/mnras/stw1501. arXiv: 1606.06741.

- Motohara, Kentaro et al. (Feb. 2000). “Infrared Imaging of $z = 2.43$ Radio Galaxy B3 0731+438 with the Subaru Telescope — Detection of H α Ionization Cones of a Powerful Radio Galaxy”. In: *Publications of the Astronomical Society of Japan* 52.1, pp. 33–41. ISSN: 0004-6264. DOI: 10.1093/pasj/52.1.33. URL: <https://academic.oup.com/pasj/article-lookup/doi/10.1093/pasj/52.1.33>.
- Murgia, M. et al. (May 2002). “Synchrotron spectra and ages of compact steep spectrum radio sources”. In: *New A Rev.* 46.2-7, pp. 307–311. DOI: 10.1016/S1387-6473(01)00200-7. arXiv: astro-ph/9904141 [astro-ph].
- Muxlow, T. W. B., G. Pelletier, and J. Roland (Nov. 1988). “Cygnus A : hot SPOT spectra and the condition of classical hydrodynamics.” In: *A&A* 206, pp. 237–244.
- Myers, S. T. and S. R. Spangler (Apr. 1985). “Synchrotron aging in the lobes of luminous radio galaxies.” In: *ApJ* 291, pp. 52–62. DOI: 10.1086/163040.
- O’Dea, C. P. et al. (Feb. 2009). “Physical properties of very powerful FR II radio galaxies”. In: *Astronomy & Astrophysics* 494.2, pp. 471–488. ISSN: 0004-6361. DOI: 10.1051/0004-6361:200809416. URL: <http://www.aanda.org/10.1051/0004-6361:200809416>.
- Offringa, A. R. (Nov. 2016). “Compression of interferometric radio-astronomical data”. In: *Astronomy & Astrophysics* 595, A99. ISSN: 0004-6361. DOI: 10.1051/0004-6361/201629565. arXiv: 1609.02019. URL: <http://www.aanda.org/10.1051/0004-6361/201629565%20http://arxiv.org/abs/1609.02019%7B%5C%7D0Ahttp://dx.doi.org/10.1051/0004-6361/201629565>.
- Offringa, A. R. et al. (2014). “Wsclean: An Implementation of a Fast, Generic Wide-Field Imager for Radio Astronomy”. In: *Monthly Notices of the Royal Astronomical Society* 444.1, pp. 606–619. ISSN: 13652966. DOI: 10.1093/mnras/stu1368. arXiv: 1407.1943.
- Perley, R. A. and B. J. Butler (May 2017). “An Accurate Flux Density Scale from 50 MHz to 50 GHz”. In: *ApJS* 230.1, 7, p. 7. DOI: 10.3847/1538-4365/aa6df9. arXiv: 1609.05940 [astro-ph.IM].
- Perley, R. A., J. W. Dreher, and J. J. Cowan (Oct. 1984). “The jet and filaments in Cygnus A”. In: *ApJ* 285, pp. L35–L38. DOI: 10.1086/184360.
- Perley, R. A. and G. B. Taylor (May 1991). “VLA Observations of 3C 295—A Young Radio Galaxy?” In: *AJ* 101, p. 1623. DOI: 10.1086/115792.
- Ramírez-Olivencia, N. et al. (2018). “Sub-arcsecond imaging of Arp 299-A at 150 MHz with LOFAR: Evidence for a starburst-driven outflow”. In: *Astronomy and Astrophysics* 610. ISSN: 14320746. DOI: 10.1051/0004-6361/201732543.
- Scaife, Anna M. M. and George H. Heald (June 2012). “A broad-band flux scale for low-frequency radio telescopes”. In: *Monthly Notices of the Royal Astronomical Society: Letters* 423.1, pp. L30–L34. ISSN: 17453925. DOI: 10.1111/j.1745-3933.2012.01251.x. URL: <https://academic.oup.com/mnrasl/article/423/1/L30-L34/1074398>.
- Steenbrugge, Katrien C., Ian Heywood, and Katherine M. Blundell (Jan. 2010). “Multiwavelength study of Cygnus A - III. Evidence for relic lobe plasma”. In: *MNRAS* 401.1, pp. 67–76. DOI: 10.1111/j.1365-2966.2009.15663.x. arXiv: 0909.1073 [astro-ph.CO].
- Tielens, A. G. G. M., G. K. Miley, and A. G. Willis (Feb. 1979). “Westerbork Observations of 4C Sources with Steep Radio Spectra”. In: *Astronomy and Astrophysics Supplement Series* 35, p. 153. ISSN: 0365-0138. (Visited on 10/24/2023).
- Tribble, Peter C. (Mar. 1993). “Radio spectral ageing in a random magnetic field”. In: *Monthly Notices of the Royal Astronomical Society* 261.1, pp. 57–62. ISSN: 0035-8711. DOI: 10.1093/mnras/261.1.57.

URL: <https://academic.oup.com/mnras/article-lookup/doi/10.1093/mnras/261.1.57>.

- Turner, Ross J, Stanislav S Shabala, and Martin G H Krause (Mar. 2018). “RAiSE III: 3C radio AGN energetics and composition”. In: *Monthly Notices of the Royal Astronomical Society* 474.3, pp. 3361–3379. ISSN: 0035-8711. DOI: [10.1093/mnras/stx2947](https://doi.org/10.1093/mnras/stx2947). URL: <http://academic.oup.com/mnras/article/474/3/3361/4631166>.
- Vaddi, Set al. (Mar. 2019). “A VLA–GMRT Look at 11 Powerful FR <sc>ii</Sc> Quasars”. In: *Monthly Notices of the Royal Astronomical Society* 484.1, pp. 385–408. ISSN: 0035-8711. DOI: [10.1093/mnras/sty3494](https://doi.org/10.1093/mnras/sty3494). (Visited on 02/06/2019).
- van Diepen, Ger, Tammo Jan Dijkema, and André Offringa (Apr. 2018b). *DPPP: Default Pre-Processing Pipeline*. ascl: [1804.003](https://ascl.net/1804.003).
- Varenius, E. et al. (2014). “Subarcsecond international LOFAR radio images of the M82 nucleus at 118 MHz and 154 MHz”. In: 114, pp. 1–15. ISSN: 14320746. DOI: [10.1051/0004-6361/201425089](https://doi.org/10.1051/0004-6361/201425089). arXiv: [1411.7680](https://arxiv.org/abs/1411.7680). URL: <http://arxiv.org/abs/1411.7680%7B%5C%7D0Ahttp://dx.doi.org/10.1051/0004-6361/201425089>.
- Varenius, E. et al. (2016). “Subarcsecond international LOFAR radio images of Arp 220 at 150 MHz: A kpc-scale star forming disk surrounding nuclei with shocked outflows”. In: 86, pp. 1–18. ISSN: 0004-6361. DOI: [10.1051/0004-6361/201628702](https://doi.org/10.1051/0004-6361/201628702). arXiv: [1607.02761](https://arxiv.org/abs/1607.02761). URL: <http://arxiv.org/abs/1607.02761%7B%5C%7D0Ahttp://dx.doi.org/10.1051/0004-6361/201628702>.
- Vries, M N de et al. (Aug. 2018). “Detection of non-thermal X-ray emission in the lobes and jets of Cygnus A”. In: *Monthly Notices of the Royal Astronomical Society* 478.3, pp. 4010–4029. ISSN: 0035-8711. DOI: [10.1093/mnras/sty1232](https://doi.org/10.1093/mnras/sty1232). URL: <https://academic.oup.com/mnras/article/478/3/4010/5026631>.
- Weeren, R. J. van et al. (Mar. 2016). “LOFAR FACET CALIBRATION”. In: *The Astrophysical Journal Supplement Series* 223.1, p. 2. ISSN: 0067-0049. DOI: [10.3847/0067-0049/223/1/2](https://doi.org/10.3847/0067-0049/223/1/2). (Visited on 08/30/2023).
- Wellman, Greg F., Ruth A. Daly, and Lin Wan (May 1997). “The Gaseous Environments of Powerful Extended Radio Sources”. In: *The Astrophysical Journal* 480.1, pp. 96–114. ISSN: 0004-637X. DOI: [10.1086/303962](https://doi.org/10.1086/303962).

CHAPTER 4

Deep sub-arcsecond widefield imaging of the Lockman Hole field at 144 MHz using the International LOFAR Telescope

The history of research does not necessarily follow the logic of plans by expert committees or central administration [...] Radio astronomy is a technique-oriented science. Starting with Karl Jansky, the major discoveries discussed in previous chapters were made primarily by skilled scientists who often built, or at least understood, their instruments. They were able to recognize and interpret their results, which were often unexpected and unrelated to what they were looking for.

Bouton & Kellerman, 2023

Based on the publication: *Nature Astronomy*, Volume 6, p. 350-356

High-quality low-frequency radio surveys have the promise of advancing our understanding of important topics in astrophysics, including the life cycle of active galactic nuclei (AGNs), jet particle acceleration processes, star formation and exoplanet magnetospheres [Vedantham et al., 2020](#). Recent results show that the vast majority of 144 MHz detected sources are unresolved at the typical resolution of a few arcseconds [Shimwell et al., 2019](#). This makes sub-arcsecond surveys essential for detailed studies of the radio sky. At low radio frequencies the biggest challenge is dealing with the ionosphere and the propagation delay of radio waves it induces [F. de Gasperin et al., 2018](#). If not adequately corrected for, this blurs the images to arcsecond or even arcminute scales. Additionally, the required image size to map the degree-scale field of view of low-frequency radio telescopes at sub-arcsecond resolution is far greater than what typical soft- and hardware are currently capable of handling. Here we present for the first time deep degree-scale sub-arcsecond imaging at low radio frequencies. We derive ionospheric corrections in 44 directions on individual sources with compact sub-arcsecond structures. This has yielded a sensitive 6.6 deg^2 144 MHz map with a resolution of $0.38'' \times 0.30''$ and a sensitivity of $30 \mu\text{Jy beam}^{-1}$, near the phase centre. This breakthrough will allow mapping of the entire northern low-frequency sky at sub-arcsecond resolution.

Endeavours in expanding sub-arcsecond resolution observations to both go deeper and wider have had successes at both 300 MHz [Lenc et al., 2008](#) and GHz [Morgan et al., 2011](#); [Chi et al., 2013](#); [Middelberg et al., 2013](#); [Radcliffe et al., 2019](#); [Muxlow et al., 2020](#) frequencies using *very long baseline interferometry* (VLBI). However, producing contiguous images spanning degrees on the sky at sub-arcsecond resolution has not been done at these low frequencies and is still tedious at higher frequencies due to the limited field of view. A combination of a lack of known compact sources (limiting available calibrators and blind

surveying), the long observing times required (limiting survey speed) or the amount of resources required to produce such images further complicates this.

An ideal instrument for low-frequency sub-arcsecond surveying is the ILT. It is most sensitive at frequencies between 120 and 168 MHz and has baselines ranging from 68 m up to approximately 2000 km. This provides a theoretical angular resolution of approximately $0.2''$ at 144 MHz. The exact resolution varies depending on the visibility weighting scheme. The international station's size sets the field of view at 2.1° full width at half maximum at 144 MHz. Over the past decade innovative algorithms have been developed to overcome the ionospheric blurring sufficiently to allow high quality $6''$ resolution imaging and novel computer science approaches have been designed to efficiently process data on large-scale parallel-compute infrastructure [F. de Gasperin et al., 2019](#). Recently developed pipelines have demonstrated the ability to produce low-frequency sub-arcsecond resolution images of individual sources spanning regions of a few arcminutes [L. Morabito et al., 2021](#). Following this achievement, two major outstanding questions become: (i) can calibration of $\sim 10^3$ km baselines be reliably extended to many sources, correcting for ionospheric effects at a sub-arcsecond level across the full field of view and (ii) can we subsequently image the entire field of view at full resolution?

To address these questions, we use an eight-hour ILT observation of the Lockman Hole field, centred at $\alpha = 10\text{h}45\text{m}00\text{s}$, $\delta = +58\text{d}05\text{m}00\text{s}$, where there is a wealth of available ancillary data (e.g. deep optical, near and far-infrared data). The ionospheric conditions during this observation were typical, based on the $6''$ image quality [F. de Gasperin et al., 2018](#). We demonstrate calibrating and imaging of the ILT's full international station field of view at sub-arcsecond resolution. [Figure 4.1](#) illustrates the result. This provides a general strategy for widefield high-resolution imaging at low radio frequencies for dense interferometers such as the ILT.

This strategy begins with a direction-independent calibration on a known calibrator source (ILTJ 104940 +583529) from the *Long Baseline Calibrator Survey* (LBCS) [N. J. Jackson et al., 2021](#). This direction-independent (DI) calibration is not sufficient to fully calibrate the FoV, however, and direction-dependent effects (DDEs) remain. These mainly come from the ionosphere, which varies strongly over time and across the sky. Successfully correcting for these DDEs hinges on two conditions: the DI calibration needs to be approximately valid over the area that is to be calibrated and there need to be enough bright sources with a sufficient compact structure to allow self-calibration to succeed. The former depends on the isoplanatic patch size and suitable calibrators within them while the latter depends on the amount of compact emission in sources.

Judging the amount of compact emission at sub-arcsecond scales in sources is difficult at a resolution of $6''$. To facilitate the selection of DDE calibrator candidates, an intermediate resolution image with an angular resolution of approximately $1''$ was created. If calibration is poor or of insufficient quality on the intermediate and longer baselines, image quality will be poor or the image will appear unfocused, giving a rough indication of the validity of the direction-independent calibration across the field. Sources that appear as compact at this resolution are also more likely to retain compact emission at sub-arcsecond resolution compared to sources that appear compact at a resolution of $6''$. We selected sources that had a peak intensity of 25 mJy beam^{-1} or higher in the $1''$ image, resulting in a sample of 46 potential calibrators. The data were then phaseshifted to these sources, creating individual datasets, and self-calibrated.

In the direction-dependent self-calibration process, we leverage the fact that the dominant remaining effects are the ionosphere and slowly varying effects, such as errors in the primary beam model. A starting model was automatically generated for each source by imaging it before the first iteration started. Subsequent self-calibration is an iterative process where in each iteration calibration solutions are obtained that provide an updated model, which can in turn provide better calibration solutions. Dominated by the iono-

sphere, we can constrain the “phase-only” self-calibration iterations to calibrate for differential Total Electron Content (dTEC), reducing the degrees of freedom by introducing the known frequency dependence of the ionospheric delay as the functional constraint given by Equation 4.1.

$$\phi = -8.44797245 \times 10^9 \times \frac{\text{dTEC}}{\nu}, \quad (4.1)$$

Here ϕ is the phase in radian and ν is the frequency in Hz. For every source, now only a single dTEC value per time interval is determined, instead of frequency-dependent phases. This reduces the degrees of freedom 48 times compared to, solving for scalar phases at a frequency interval of at 1 MHz (a typical solution interval for 6'' calibration), significantly increasing the effective signal-to-noise ratio (SNR). This leaves 46 degrees of freedom: one for each calibrator. Following this, long-timescale amplitude corrections were determined to correct the remaining amplitude effects. For the ILT an imperfect primary beam model is one of the dominant causes of residual amplitude errors.

Manual inspection of the 46 DDE calibrators concluded that 44 had converged after the dTEC iterations and 41 allowed for subsequent amplitude corrections. The remaining 2 sources did not have sufficient compact flux for successful self-calibration and were discarded. Figure 4.2 shows the progression of self-calibration on three sources of varying complexity and distance from the initial LBCS calibrator. The fact that self-calibration converged for 44 directions across the entire 6.6 deg² area confirms that the density of compact sources is high enough to correct direction-dependent effects across the field of view. Furthermore, the fact that a sufficiently accurate starting model for self-calibration could be obtained from a DI-calibrated dataset indicates that for similar ionospheric conditions, a single correction is likely to be approximately valid over the entire field of view. Finally, the solutions were interpolated into a 2D map of corrections using radial basis function interpolation. This provides spatially smooth “screens” with calibration solutions for every location in the field.

Imaging the entire field of view is another challenge due to the amount of pixels required. We chose a pixel scale of 0.11''px⁻¹. Covering the ILT’s field of view then requires a total of 6 – 7 × 10⁹ pixels. For comparison, the entire *Very Large Array (VLA) Faint Images of the Radio Sky at Twenty-cm* (FIRST) survey covers 10⁴ deg² using roughly 4 × 10⁹ pixels R. L. White et al., 1997.

At the time of writing it is not feasible to make a single image at the required size. Therefore, the field was split into 25 facets that were imaged individually. Each facet image covered a 0.69° × 0.69° area that could be imaged at a manageable 22700 × 22700 pixels. For each facet, the 1'' resolution image was used to subtract sources outside of a central 0.55° × 0.55° region. This suppresses imaging artifacts that would arise from undeconvolved emission outside the image boundary. The imaged area extends beyond this subtraction border to account for the remaining source structure due to imperfect subtraction. Lastly, the inner 0.55° × 0.55° regions of the facets overlap each other to avoid gaps in the mosaic. The final mosaic has approximately 83 950 × 83 500 pixels covering 6.6 deg² on the sky.

Imaging was done using WSClean in combination with the newly developed Image Domain Gridding (IDG) Offringa et al., 2014; Tol et al., 2018; Bram Veenboer et al., 2019. Multi-frequency synthesis was used to account for the large bandwidth and multi-scale CLEAN was used to account for both extended and compact emission. One of the bottlenecks for imaging is the need to place visibilities measured by a radio telescope on a regular grid in a computationally expensive process called gridding. IDG is a novel approach to gridding that is computationally efficient as it circumvents the need to calculate expensive convolution functions during this process. It simultaneously allows for on-the-fly application of primary beam corrections and other direction-dependent corrections at little extra cost. Each of the facets took between 5 and 7 days of wall clock time to image. Using both local (ALICE at Leiden Observatory) and

national (Spider at SURFsara) compute resources imaging ran in parallel and the effective wall time was significantly reduced.

A total of approximately 250 000 core hours were required for the data reduction process in order to arrive at the final image. This was split between calibration and imaging as 34% and 76%, respectively. For the imaging of this dataset, this translates to 458 corehour/Gvis. During calibration data sizes vary greatly, hence a general number for that is hard to give. The image covers a 6.6 deg^2 sky area at a central angular resolution of $0.38'' \times 0.30''$ and a central rms noise level of $30 \mu\text{Jy beam}^{-1}$. This equates to a 1.4 GHz sensitivity of $7 \mu\text{Jy beam}^{-1}$, assuming a spectral index of $\alpha = -0.7$. This depth is comparable to the deepest 1.4 GHz VLA image of the field [Iverson et al., 2002](#).

In the $6''$ resolution image, 6103 sources are detected in the ILT covered area using the same 8-hour observation, with a noise level of $\sigma_{\text{rms}}^{\text{central}} = 70 \mu\text{Jy beam}^{-1}$. 5650 (93%) of these are unresolved and 453 (7%) are resolved, using the same criterion as LoTSS [Shimwell et al., 2019](#). Of the $6''$ -unresolved sources, 2483 (43%) had a high resolution counterpart detected at a $\text{snr} := i_{\nu}^{\text{peak}}/\sigma_{\text{rms}}^{\text{local}} > 5$, of which 291 are multi-gaussian (12%) and 2192 remain single-gaussian (88%). The final catalogue was created by cross-matching to the $6''$ resolution catalogue of the LOFAR deep fields survey [Kondapally et al., 2021](#); [Tasse et al., 2021](#)

Wide-field, low-frequency, sub-arcsecond resolution imaging with the ILT opens up important new scientific parameter space with its ability to conduct a blind all-sky sub-arcsecond survey. At this resolution, the ILT is also well matched to other telescopes such as e-MERLIN or the VLA. Over the past years the *LOFAR Two-Metre Sky Survey* (LoTSS) has been conducting a sensitive $6''$ survey of the northern sky [Shimwell et al., 2019](#). The data recorded for this survey holds incredible legacy value for a future sub-arcsecond survey. Over 75% of the sky has already been observed for LoTSS, using the same duration, bandwidth and averaging as the data presented here. Weighted by integration time, per hour of observing, 97% of this data contains international stations. 54% has ≥ 12 international stations and 84% has ≥ 10 . A significant amount of data is thus already present in the archive, ready to be processed. Relatively little extra or repeat observing will thus be necessary. The work presented here demonstrates a general strategy for widefield low-frequency sub-arcsecond imaging and paves the road towards easier, pipelined data processing for a new sub-arcsecond low-frequency survey of the northern sky.

4.1 Methods

4.1.1 Observation

For this work, we used an observation of the Lockman Hole field located at $\alpha = 10\text{h}47\text{m}00\text{s}$, $\delta = 58^\circ05'00''$. This pointing was observed on July 12, 2018, from 11:08:10 to 19:08:10 UTC. In total 8 hours were spent on the target field, which was bookended by two 15-minute calibrator scans of 3C 196 and 3C 295, respectively. The observing setup was the standard LoTSS HBA setup with 48 MHz of bandwidth spanning a frequency range of 120-168 MHz. With the exception of DE609, all 12 other international stations partook in the observation. We will use the term *Dutch LOFAR Telescope* (DLT) to refer to the core and remote stations.

4.1.2 Calibration and imaging

Calibration of the radio data started from the raw data stored in the Long Term Archive (LTA). First, the data was processed using the de facto pipelines for calibrating the Dutch stations: PREFACTOR and DDF-PIPELINE (F. de Gasperin et al., 2019; Shimwell et al., 2019; Tasse et al., 2021). Subsequently, a suitable infield *Long Baseline Calibrator Survey* (LBCS) calibrator was selected. From thereon no dedicated pipeline existed. The first direction-independent calibration of the international stations was carried out. An intermediate resolution image at $\sim 1''$ was used to select sources for direction-dependent calibration, which were subsequently self-calibrated. Finally, the field was split up in “facets” and imaged at the full native resolution.

Direction independent calibration of the DLT

The PREFACTOR pipeline consists of two workflows for the calibrator scan and target scan respectively. A detailed overview of the calibration strategy is given by (F. de Gasperin et al., 2019). A short overview of these workflows will be given next.

First, the calibrator workflow determined the following corrections for both Dutch and international stations: a phase offset to align XX and YY polarisations (based on the assumption that the calibrator is unpolarised), a bandpass translating correlator units to physical units and a clock offset in nanoseconds to synchronize the clocks of each station to the same reference. These solutions were determined on a 4 s time interval and a 48.82 kHz frequency interval. Finally, they were transferred to the target dataset and the target workflow determined XX and YY phase solutions for the Dutch stations by calibrating against a skymodel from the TFIR GMRT Sky Survey (TGSS, Intema et al., 2017) on an 8 s time interval and a 195.28 kHz frequency interval.

Direction dependent calibration of the DLT

Next, the DDF-PIPELINE was run for direction-dependent calibration of the Dutch stations. See (Shimwell et al., 2019; Tasse et al., 2018; Tasse et al., 2021) for a detailed description of this pipeline. First, the direction-independent calibration was refined by means of self-calibration of the entire Dutch station field of view. Following this, both phase and amplitude calibration solutions were determined in 45 directions across the Dutch field of view, following a facet-based approach. This provided a high-quality $6''$ resolution image of the target field covering the field of view of the Dutch stations.

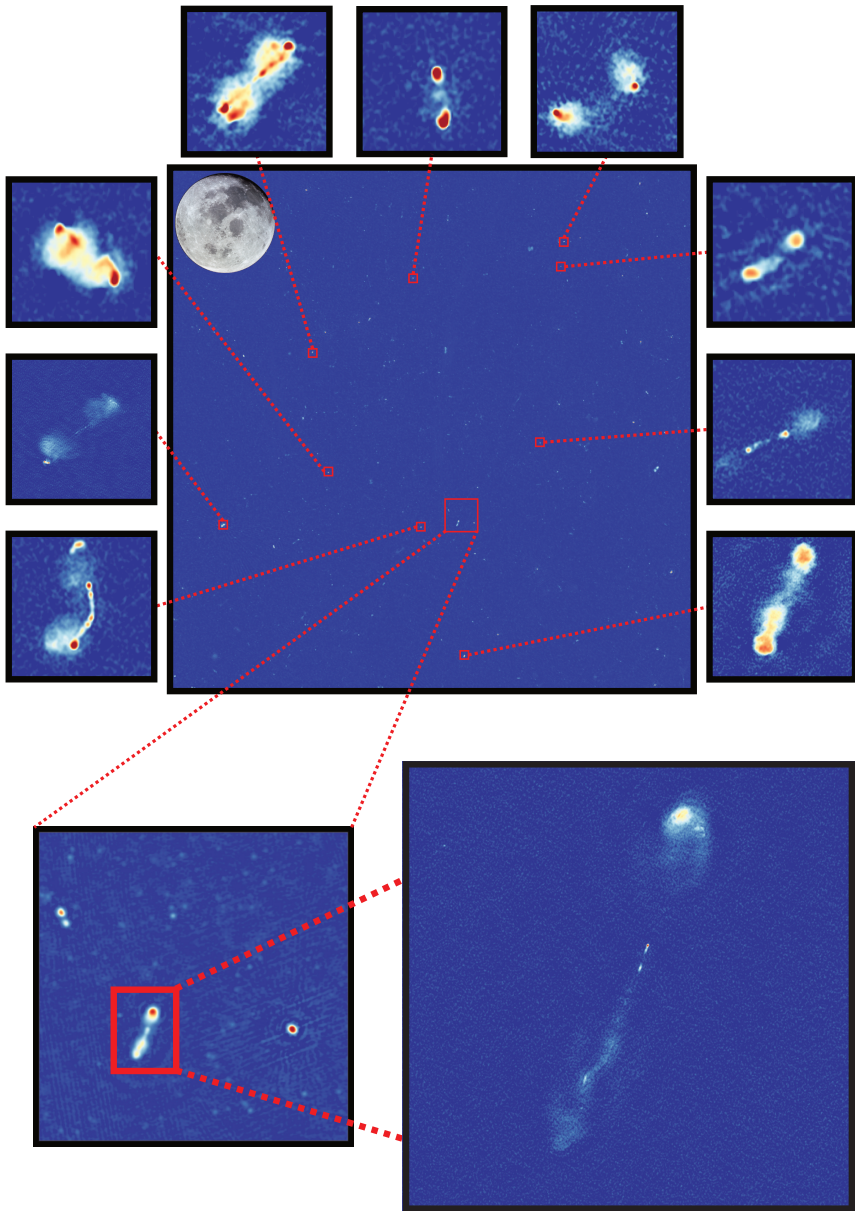


Figure 4.1: An overview of the field illustrating both the widefield and high-resolution aspects. The central image shows a 6'' image of the covered part of the field. The bottom two panels zoom in on a small portion of the field at 6'' and a particular source at 0.3'' in the bottom left and right, respectively. Surrounding the central image are highlights of various other sources detected in the 0.3'' resolution map. Moon image credit: NASA.

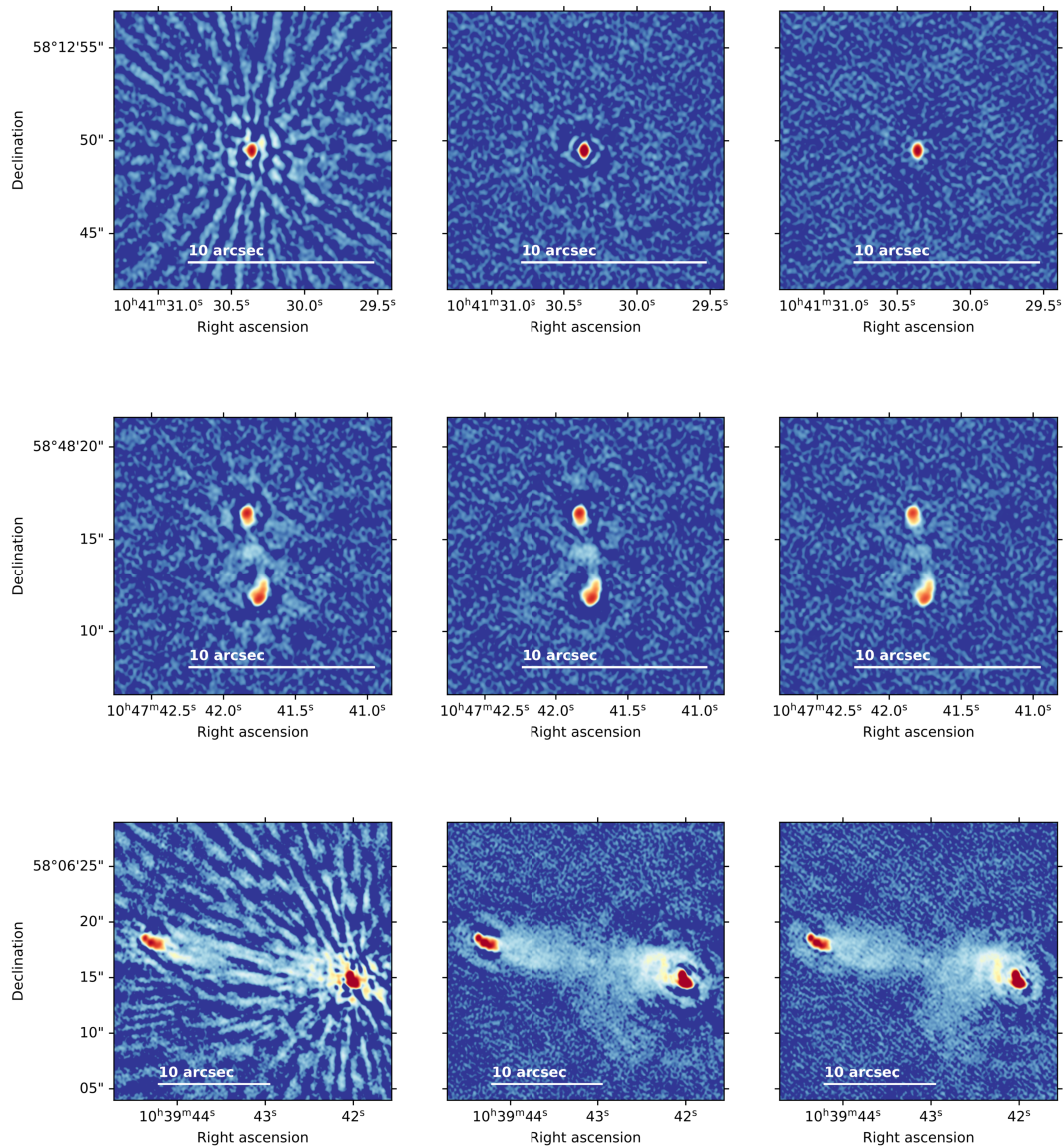


Figure 4.2: Illustration of the direction-dependent self-calibration process for different sources across the field and various degrees of extendedness. From left to right: the initial image with only direction-independent corrections applied, the image after dTEC corrections have been applied and finally the image after amplitude corrections have been applied. A significant improvement is seen after correcting ionospheric errors, while the amplitude corrections provide a more subtle improvement. The top and middle images cover a $15'' \times 15''$ area and the bottom image covers $25'' \times 25''$. A scale bar is shown for size.

Direction independent calibration of the ILT

To start calibration of the international stations, we followed the strategy as the LOFAR-VLBI pipeline (L. Morabito et al., 2021). Calibration solutions from PREFACTOR and DDF-PIPELINE were applied, data was combined into 24 manageable 2 MHz chunks of 32 gb and finally a suitable lbcS calibrator was selected within the international station field of view (N. J. Jackson et al., 2021). This calibrator source was then split off from the main dataset by phase shifting the visibilities towards this source. After phase shifting, the core stations were all combined into a single “super station”, `st001`. The dataset was also averaged down to a 16 s time interval and a 195.28 kHz frequency interval. This heavy averaging causes a $\sim 50\%$ intensity loss due to smearing at a distance of $\sim 4'$ from the phase centre, which considerably reduces the influence of other sources. ST001 has a field of view of the order of $\sim 4'$ as well, further significantly suppressing the effects of other sources on every baseline with this station. Self-calibration was performed using the routine described in Weeren et al., 2021. This uses DPPP (van Diepen et al., 2018a) to determine calibration solutions and `wsclean` (Offringa et al., 2014) for imaging. First, 9 “fast” iterations to solve for rapid phase variations were performed. The solution interval was 16 s (the resolution of the data) and the solution type was `scalarphase`, i.e. a phase as a function of time and frequency, but independent of polarisation. Then 7 more iterations were performed where in addition to the fast solves, a “slow” solve using DPPP’s `complexgain` mode was done. This determined time, frequency and polarisation-dependent amplitude and phase solutions on a 15 min timescale and a 195.28 kHz frequency interval, for the XX and YY polarisations. The starting model for the first phase-only iteration was a point source, due to the lack of more information, with the flux density taken from the low-resolution $6''$ image. While such a starting model is likely naive and possibly incorrect, after each iteration the model was updated and the self-calibration cycle converged to a believable double-lobed source structure. These solutions were then applied to the target field dataset as initial direction-independent calibration for the international stations and refined direction-independent calibration solutions for the remote and core stations. The core stations were corrected with the solutions for ST001.

Intermediate resolution imaging and faceting

Due to its sheer size, the full field of view could not be covered with a single image at the ILT’s native resolution. Therefore the field was split into 25 facets that were imaged separately. To help suppress interference from undeconvolved sources outside of each facet and to determine suitable candidate sources for direction-dependent calibration, an intermediate resolution image at approximately $1''$ was made by tapering the data with a Gaussian taper. The resulting image was 25000×25000 pixels in size and covered the full field of view.

In preparation for high-resolution imaging, 25 datasets (“facets”) were then split out with their phase centres spread over the field of view in a 5×5 grid, with each facet spanning $0.55 \times 0.55 \text{ deg}^2$ on the sky, separated by 0.5 deg. For each facet, the intermediate resolution map was subtracted outside this $0.55 \times 0.55 \text{ deg}^2$ area. The 0.05 deg on each side ensured some overlap between the facets to not have gaps in the sky coverage. The data were then phase shifted to each of these phase centres and averaged to 4 s and 48.82 kHz time and frequency resolution. These were the final 25 datasets that would be imaged at high resolution. The data for each facet were about 250 GB in total size.

Direction dependent calibration of the ILT

Sources that remain bright and compact at $1''$ resolution have a better chance of remaining compact down to $0.3''$ compared to a selection at $6''$. From the intermediate resolution image sources with a peak intensity above 25 mJy/beam were selected as candidate DDE calibrators. These were then split off into separate datasets similarly to the LBCS calibrator, but averaged more in time to a 1 min interval. For the brightest sources, this balanced well the signal-to-noise ratio while still retaining the time resolution to correct most of the residual ionospheric distortions properly. The calibration solutions derived on the LBCS calibrator were pre-applied and a similar self-calibration routine as for the LBCS calibrator was subsequently used to self-calibrate these sources, outlined below.

First, an initial image was made from which a starting model was derived. As the majority of phase-related errors had been corrected on the infield calibrator, it was assumed that the remaining direction-dependent effects were dominated by ionospheric differences. Therefore in the fast iterations, DPPP's `tec` mode was used to determine dTEC values rather than phases. In the slow iterations, DPPP's `complexgain` mode was used to solve for remaining amplitude errors due to the slowly varying station beams. Solution intervals for both solves were calculated automatically based on the intensity detected on 800 km baselines [Weeren et al., 2021](#).

The TEC iterations converged for 44 sources and the `complexgain` iterations for 41 sources. So-called “jumps”, manifesting as solutions that are offset by a multiple of a specific “jump” value, were present in the TEC solutions. These jumps are a consequence of local χ^2 minima in the TEC-fitting ([Weeren et al., 2016](#)). This jump value was subtracted from the offending solution blocks iteratively until no jumps remained. The dTEC values were then spatially interpolated to a smooth screen over *ra* and *dec*. A simple approach to convert discrete directions into screens would be a Voronoi tessellation based on the calibrator locations. This would, however, introduce sharp transitions, which would negatively impact IDG imaging later on. Therefore the solutions were interpolated with a multiquadric radial basis function instead, using `scipy's interpolate.rbf` function. Interpolation was constrained such that at the location of a calibrator source the screen solutions matched with the original solutions. Similarly, the `complexgain` solutions were also interpolated to a screen. These two screens were used to apply direction-dependent calibration solutions during the final imaging.

Final imaging

Final high-resolution imaging of the data was done using WSClean in combination with IDG in CPU mode. Since the IDG algorithm can leverage a GPU for the gridding calculations, this amount can likely be significantly reduced ([B. Veenboer et al., 2020](#)). A 22500×22500 image of a similar dataset finished four times faster on a 22-core Intel Xeon Gold 6226 system with an Nvidia Tesla V100 compared to an identical system without one. Each of the facets was imaged separately with robust -1 weighting, a $0.11''$ pixel size and a 22700×22700 pixel image size. Multiscale multi-frequency synthesis clean was used together with spectral fitting using a second-order polynomial (through `fit-spectral-pol 3`). Differential primary beam, dTEC and gain corrections were all applied on the fly during imaging. The beam corrections were applied every 10 min, dTEC solutions were applied every minute and gain solutions every hour. This could be done efficiently through the use of IDG. The data was imaged using hardware on the Spider platform at surfSARA and the ALICE cluster in Leiden. Imaging took 5 – 7 days wall clock time per facet on average using 24 cores on a node with two 12-core Xeon Gold 6126 running at 2.6GHz and 384 GB of RAM. Effective wall clock time was significantly reduced however due to the availability of many compute nodes,

allowing imaging to run in parallel where each compute node imaged a facet independently. From start to finish the entire data reduction procedure consumed approximately 250,000 core hours.

4.1.3 Source detection and catalogues

After imaging source detection was done using PyBDSF (Mohan et al., 2015b). Because source detection was done on each facet separately, there will be duplicate detections. Therefore the catalogues were first merged and then cleaned of duplicate detections. The compact sources and extended sources were treated separately for this. First, we processed the compact sources, starting with a cross-match to the 6'' resolution catalogue of the LOFAR deep fields survey with key optical host properties (Kondapally et al., 2021; Tasse et al., 2021). Next duplicate detections were removed using an internal cross-match within a radius of 0.15'' of the fitted high-resolution position (i.e. approximately within the restoring beam of the high-resolution map). The match closest to its facet centre was kept, while the others were discarded. Next a size constraint was introduced. Sources with fitted major or minor axes that were larger than 6'' were discarded as poor fits as by definition the unresolved sources cannot be larger than the low-resolution restoring beam. Next, a signal-to-noise ratio cut was made, constraining the peak intensity to be $\geq 5\sigma_{\text{rms}}$, where σ_{rms} is the rms noise around the source as measured by PyBDSF. Finally, the compact and extended source catalogues were combined into a single catalogue and a final duplicate removal was done. The final catalogue contains 2483 sources.

4.1.4 Astrometric corrections

As phases hold information about source positions, the self-calibration process may have shifted the astrometry away from a well-defined reference. During calibration of the LBCS calibrator, we noted self-calibration had “recentered” the image near one of the lobes, due to the use of a point-source starting model, introducing a noticeable offset that needs correcting. Therefore the final image needs to be realigned to a reference. As our reference, we used the final calibrated and aligned radio catalogue of Lockman Hole from the LOFAR Deep Fields survey.

Offsets to align the high-resolution image to the low-resolution image were determined for each facet separately. First, point sources with $\text{SNR} := I_{\text{peak}}/\sigma_{\text{rms}}^{\text{local}} > 5$ were selected. Secondly, an isolation constraint for no other sources to be present within 30'' was applied. Astrometric offsets were then determined by the median value of the difference with the 6'' position for right ascension and declination, respectively. Figure 4.4 shows the offsets for each facet. There is a roughly systematic offset due to the aforementioned recentering behaviour during the calibration of the LBCS source. The remaining differences are due to additional offsets in those facets but are small and of the order of one resolution element or less.

A single offset using only $\text{SNR} > 25$ sources was also determined as a check. The median values obtained from this agree with the median of all individual facets combined. Therefore the facet-based offsets are adopted to allow for inter-facet variations.

4.1.5 Smearing

A variety of effects can degrade the effective resolution in the image, referred to as the “smearing” of sources. This results in a reduction of peak intensity and artificial broadening of sources. These effects include time and bandwidth smearing, ionospheric disturbances and interstellar or interplanetary scattering (ISS/IPS). Time and bandwidth smearing is an “instrumental” effect that occurs when averaging the data. It artificially

broadens sources in the image radially (bandwidth smearing) and azimuthally (time smearing). Figure 4.3 illustrates the smearing losses on the longest baseline (Bridle et al., 1999). Ionospheric disturbances are mostly corrected for in both the direction-independent and direction-dependent calibration process but are difficult to perfectly remove as they are limited by the density of DD calibrators, available SNR, solution intervals and source complexity. The result is similar to atmospheric seeing. Finally, interstellar and interplanetary scattering scramble astronomical radio signals before they even reach the ionosphere and hence imprint an inherent, uncorrectable smearing on the data (Rickett, 1990). While the former can technically be resolved with better calibration, the latter sets a fundamental limit to the effective resolution that can be achieved. The combination of ionospheric seeing and interstellar and -planetary scattering manifests itself as the broadening of sources near the phase centre, where time and bandwidth smearing is non-existent.

If smearing is not accounted for, peak intensity and intrinsic size measurements will be off due to a wrong assumed PSF. Measuring the most compact sources in the centre of the field, where time and bandwidth smearing are negligible, will indicate whether broadening from ISS/IPS is an issue for this observation. The estimated PSF from WSClean is $0.38'' \times 0.30''$, while the smallest measured source in the central facet is $0.39'' \times 0.31''$. The expected broadening from ISS/IPS is ~ 50 msec (M. H. Cohen et al., 1974). We thus conclude that we achieve the theoretical angular resolution with possible minor broadening from ISS/IPS.

Broadening from time and bandwidth smearing will vary across the field. The net effect is a combination of the local PSF and smearing. We give the theoretical reduction in peak intensity as a measure of how severe the smearing is in Figure 4.3. For accurate deconvolved source sizes the smearing would need to be taken into account. A significant reduction in time smearing can be achieved by processing the data at its archived 1 s time resolution.

4.1.6 Flux scale corrections

A correction to the flux scale was necessary, as the reference bandpasses that were used were not tied to any particular flux density scale. For a reliable flux scale correction sources with the same flux density at low and high resolution were needed. A selection was made based on high-significance sources in the high-resolution image. Compact single-gaussian sources with $\text{SNR} > 25$ were selected and the median ratio $S_{\text{ILT}}/S_{\text{DLT}}$ was determined. The selection of bright high-SNR and compact sources ensures no flux density is lost. Smearing effects are mitigated by using the flux density, which should be conserved, instead of peak intensity. The correction factor was determined to be 1.21 ± 0.19 from the median flux density ratio. After scaling, the mean ratio is $S_{\text{ILT}}/S_{\text{DLT}} = 0.99^{+0.26}_{-0.34}$ and the median ratio is $S_{\text{ILT}}/S_{\text{DLT}} = 1.00^{+0.14}_{-0.18}$ (0.82 – 1.14). Both the uncertainty and the values in parentheses reflect the 16th and 84th percentiles, respectively. The distribution of the ratios over all facets after scaling can be seen in Fig. 4.4. A small number of sources is seen to have a ratio significantly smaller than unity. These are most likely sources that have extended emission below the detection threshold. This is a small number of outlying sources, however, and has not affected the scaling in a significant way.

The uncertainty on measured flux densities is compounded by two main effects: an uncertainty in the general flux density scale (σ_{cal}) and an uncertainty in our scaling factor (σ_{scale}). For the former, we assume a conservative error of 20% (Shimwell et al., 2019). This was added in quadrature with the other uncertainty to arrive at the total uncertainty on the flux density of $\sigma_{\text{total}} = \sqrt{\sigma_{\text{cal}}^2 + \sigma_{\text{scale}}^2} = 30\%$.

Acknowledgements

We thank the (anonymous) reviewers for their comments. FS would like to thank SURFsara for beta access to the Spider platform. This paper is based (in part) on data obtained with the International LOFAR Telescope (ILT) under project code LT10_012. LOFAR (van Haarlem et al. 2013) is the Low Frequency Array designed and constructed by ASTRON. It has observing, data processing, and data storage facilities in several countries, that are owned by various parties (each with their own funding sources), and that are collectively operated by the ILT foundation under a joint scientific policy. The ILT resources have benefited from the following recent major funding sources: CNRS-INSU, Observatoire de Paris and Université d'Orléans, France; BMBF, MIWF-NRW, MPG, Germany; Science Foundation Ireland (SFI), Department of Business, Enterprise and Innovation (DBEI), Ireland; NWO, The Netherlands; The Science and Technology Facilities Council, UK[7]. RJvW acknowledges support from the ERC Starting Grant ClusterWeb 804208. This work was supported by the Medical Research Council [grant MR/T042842/1]. This work made use of the Dutch national e-infrastructure with the support of the SURF Cooperative using grant no. EINF-251. PNB is grateful for support from the UK STFC via grants ST/R000972/1 and ST/V000594/1. This work was performed using the compute resources from the Academic Leiden Interdisciplinary Cluster Environment (ALICE) provided by Leiden University. This work also made use of SciPy, NumPy, Matplotlib and TOPCAT.

Author contribution statements

FS led the paper, reduced the data and produced the images. RJvW developed the self-calibration routine and helped expand it to international baselines. HJAR helped scope and write the paper. LKM and NJ conducted the LBCS survey and developed the LOFAR-VLBI pipeline which served as the foundation for this work. ARO, SvdT and BV maintain WSClean, and IDG and were of great help in fixing problems and adding features to the software. JBRO helped secure resources on SURFsara and provided support for our data reduction on their Spider platform. PNB led the proposal that obtained the data and contributed to the editing of the paper. MB is a member of the long-baseline working group and contributed to the editing of the paper. TWS contributed towards some of the various data processing pipelines used in this work and produced the deep Lockman 6" image. CT developed the DDFacet software used and produced the deep Lockman Hole 6" image. APT is a member of the long-baseline working group and helped determine the flux scale.

Competing interest statement

The authors declare no competing interests.

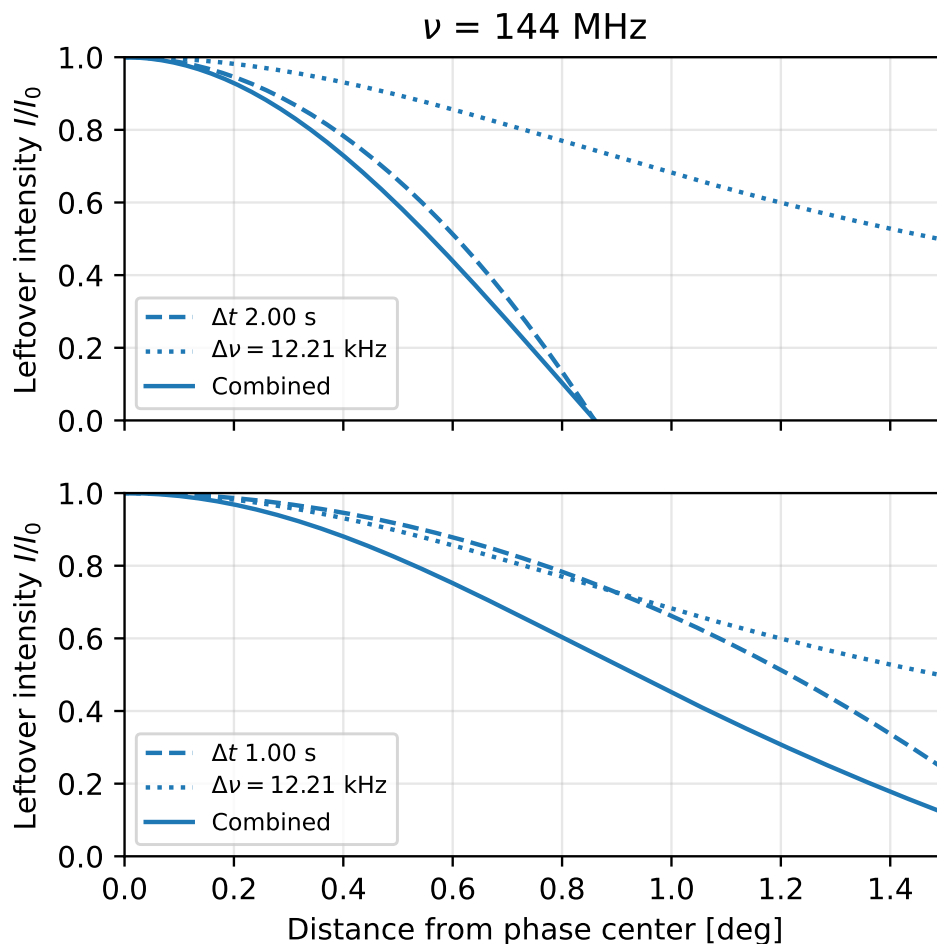


Figure 4.3: Time and bandwidth smearing losses on the longest baseline (1986 km, $\theta = 0.2''$ at 144 MHz), for the central frequency, as a function of distance to the phase centre. Losses are expressed as the remaining peak intensity I as a fraction of the original peak intensity I_0 . The dotted line indicates the reduction in peak intensity from bandwidth smearing, the dashed line is the reduction from time smearing and the solid line is the total reduction from both effects. The top panel shows smearing at the averaging of this dataset, while the bottom panel shows the smearing at the archived averaging parameters.

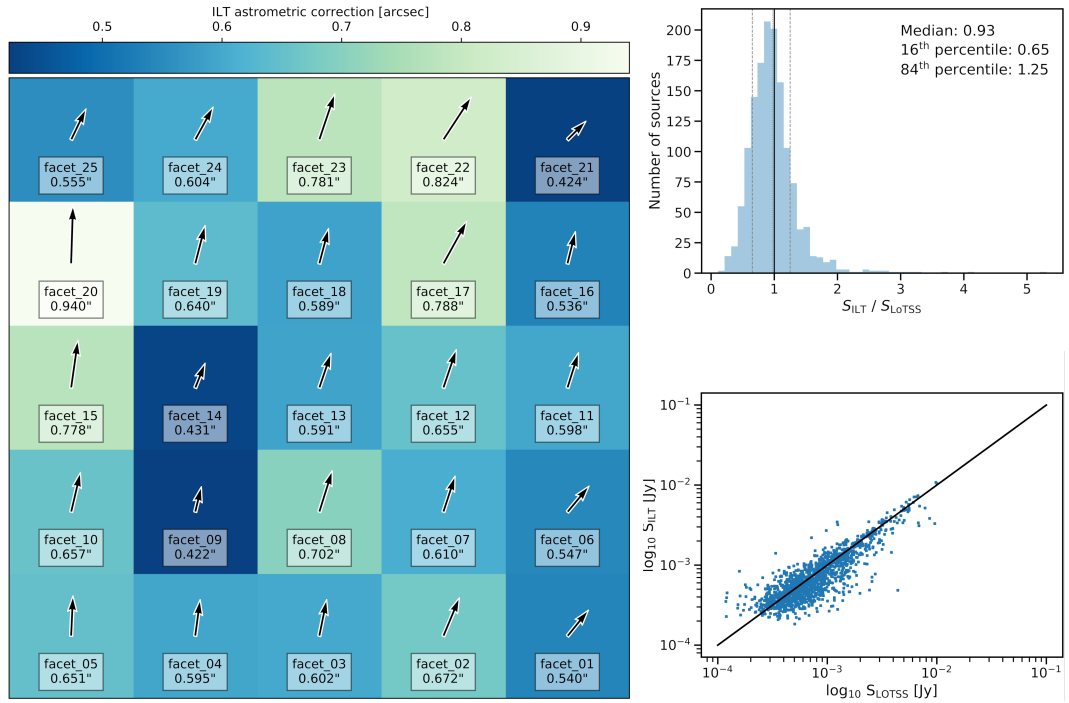


Figure 4.4: Astrometric offsets per facet and flux density distributions after setting the absolute flux scale. *Left:* Offsets in arcsecond to align the high-resolution catalogue with the 6'' catalogue. Each square is one facet. The black arrows are to scale with respect to each other and indicate the magnitude and direction of the applied offset. *Top right:* The distribution of flux density ratios of compact SNR > 5 sources, after scaling. The median, 16th and 84th percentiles are indicated by the dotted and dashed grey lines, respectively. The black line indicates unity. *Bottom right:* Flux densities measured with the international array versus those measured with the Dutch array. The black line indicates unity.

Data Availability

A source catalogue and the full-resolution images are accessible through the LOFAR Surveys Key Science Project webpage: <https://www.lofar-surveys.org/hdfields.html>

Code Availability

The various software and pipelines used in this work are publicly available at <https://github.com/lofar-astron/prefactor> (PREFACTOR), <https://github.com/cyriltasse/DDFacet> (DDFACET), <https://github.com/lmorabit/lofar-vlbi> (LOFAR-VLBI), <https://github.com/mhardcastle/ddf-pipeline> (DDF-PIPELINE) and <https://gitlab.com/astron-idg/idg> (IDG). Code from other parts not using these pipelines is not directly available, because it is not part of a complete pipeline, but is available upon reasonable request to the authors.

Bibliography

- Bridle, A. H. and F. R. Schwab (Jan. 1999). “Bandwidth and Time-Average Smearing”. In: *Synthesis Imaging in Radio Astronomy II*. Ed. by G. B. Taylor, C. L. Carilli, and R. A. Perley. Vol. 180. Astronomical Society of the Pacific Conference Series, p. 371.
- Chi, S., P. D. Barthel, and M. A. Garrett (Feb. 2013). “Deep, Wide-Field, Global VLBI Observations of the *Hubble* Deep Field North (HDF-N) and Flanking Fields (HFF)”. In: *Astronomy & Astrophysics* 550, A68. ISSN: 0004-6361. DOI: [10.1051/0004-6361/201220783](https://doi.org/10.1051/0004-6361/201220783). (Visited on 02/18/2020).
- Cohen, M. H. and W. M. Cronyn (Aug. 1974). “Scintillation and Apparent Angular Diameter”. In: *ApJ* 192, pp. 193–197. DOI: [10.1086/153050](https://doi.org/10.1086/153050).
- de Gasperin, F. et al. (Aug. 2018). “The effect of the ionosphere on ultra-low-frequency radio-interferometric observations”. In: *A&A* 615, A179, A179. DOI: [10.1051/0004-6361/201833012](https://doi.org/10.1051/0004-6361/201833012). arXiv: [1804.07947](https://arxiv.org/abs/1804.07947) [astro-ph. IM].
- de Gasperin, F. et al. (Feb. 2019). “Systematic effects in LOFAR data: A unified calibration strategy”. In: *A&A* 622, A5, A5. DOI: [10.1051/0004-6361/201833867](https://doi.org/10.1051/0004-6361/201833867). arXiv: [1811.07954](https://arxiv.org/abs/1811.07954) [astro-ph. IM].
- Intema, H. T. et al. (Feb. 2017). “The GMRT 150 MHz All-Sky Radio Survey - First Alternative Data Release TGSS ADR1”. In: *Astronomy & Astrophysics* 598, A78. ISSN: 0004-6361, 1432-0746. DOI: [10.1051/0004-6361/201628536](https://doi.org/10.1051/0004-6361/201628536). (Visited on 09/11/2023).
- Iverson, R. J. et al. (Nov. 2002). “Deep radio imaging of the SCUBA 8-mJy survey fields: submillimetre source identifications and redshift distribution”. In: *MNRAS* 337.1, pp. 1–25. DOI: [10.1046/j.1365-8711.2002.05900.x](https://doi.org/10.1046/j.1365-8711.2002.05900.x). arXiv: [astro-ph/0206432](https://arxiv.org/abs/astro-ph/0206432) [astro-ph].
- Jackson, N. J. et al. (May 2021). “Sub-Arcsecond Imaging with the International LOFAR Telescope. II. Completion of the LOFAR Long-Baseline Calibrator Survey”. In: *Astronomy & Astrophysics*. ISSN: 0004-6361. DOI: [10.1051/0004-6361/202140756](https://doi.org/10.1051/0004-6361/202140756). (Visited on 07/19/2021).
- Kondapally, R. et al. (Apr. 2021). “The LOFAR Two-meter Sky Survey: Deep Fields Data Release 1. III. Host-galaxy identifications and value added catalogues”. In: *A&A* 648, A3, A3. DOI: [10.1051/0004-6361/202038813](https://doi.org/10.1051/0004-6361/202038813). arXiv: [2011.08201](https://arxiv.org/abs/2011.08201) [astro-ph. GA].
- Lenc, E. et al. (Jan. 2008). “A Deep, High-Resolution Survey of the Low-Frequency Radio Sky”. In: *The Astrophysical Journal* 673.1, pp. 78–95. ISSN: 0004-637X. DOI: [10.1086/524295](https://doi.org/10.1086/524295). arXiv: [0710.1946](https://arxiv.org/abs/0710.1946).
- Middelberg, E. et al. (2013). “Mosaiced wide-field VLBI observations of the Lockman Hole/XMM”. In: *Astronomy and Astrophysics* 551. ISSN: 00046361. DOI: [10.1051/0004-6361/201220374](https://doi.org/10.1051/0004-6361/201220374). arXiv: [1212.4605](https://arxiv.org/abs/1212.4605).
- Mohan, Niruj and David Rafferty (Feb. 2015b). *PyBDSF: Python Blob Detection and Source Finder*. ascl: [1502.007](https://ascl.net/1502.007).

- Morabito, L. et al. (Apr. 2021). “Sub-Arcsecond Imaging with the International LOFAR Telescope. I. Foundational Calibration Strategy and Pipeline”. In: *Astronomy & Astrophysics*. ISSN: 0004-6361. DOI: [10.1051/0004-6361/202140649](https://doi.org/10.1051/0004-6361/202140649). (Visited on 07/19/2021).
- Morgan, J. S. et al. (Feb. 2011). “VLBI imaging throughout the primary beam using accurate UV shifting”. In: *Astronomy and Astrophysics* 526.17. ISSN: 00046361. DOI: [10.1051/0004-6361/201015775](https://doi.org/10.1051/0004-6361/201015775).
- Muxlow, T. W. B. et al. (June 2020). “The e-MERGE Survey (e-MERLIN Galaxy Evolution Survey): overview and survey description”. In: *MNRAS* 495.1, pp. 1188–1208. DOI: [10.1093/mnras/staa1279](https://doi.org/10.1093/mnras/staa1279). arXiv: [2005.02407 \[astro-ph.GA\]](https://arxiv.org/abs/2005.02407).
- Offringa, A. R. et al. (2014). “Wsclean: An Implementation of a Fast, Generic Wide-Field Imager for Radio Astronomy”. In: *Monthly Notices of the Royal Astronomical Society* 444.1, pp. 606–619. ISSN: 13652966. DOI: [10.1093/mnras/stu1368](https://doi.org/10.1093/mnras/stu1368). arXiv: [1407.1943](https://arxiv.org/abs/1407.1943).
- Radcliffe, J. F. et al. (May 2019). “Nowhere to Hide: Radio-faint AGN in GOODS-N field. I. Initial catalogue and radio properties (Corrigendum)”. In: *A&A* 625, C1, p. C1. DOI: [10.1051/0004-6361/201833399e](https://doi.org/10.1051/0004-6361/201833399e).
- Rickett, B. J. (Sept. 1990). “Radio Propagation Through the Turbulent Interstellar Plasma”. In: *Annual Review of Astronomy and Astrophysics* 28.1, pp. 561–605. ISSN: 0066-4146. DOI: [10.1146/annurev.aa.28.090190.003021](https://doi.org/10.1146/annurev.aa.28.090190.003021). URL: <http://www.annualreviews.org/doi/10.1146/annurev.aa.28.090190.003021>.
- Shimwell, T. W. et al. (Feb. 2019). “The LOFAR Two-metre Sky Survey - II. First Data Release”. In: *Astronomy & Astrophysics* 622, A1. ISSN: 0004-6361, 1432-0746. DOI: [10.1051/0004-6361/201833559](https://doi.org/10.1051/0004-6361/201833559). (Visited on 02/01/2022).
- Tasse, C. et al. (Apr. 2018). “Faceting for direction-dependent spectral deconvolution”. In: *A&A* 611, A87, A87. DOI: [10.1051/0004-6361/201731474](https://doi.org/10.1051/0004-6361/201731474). arXiv: [1712.02078 \[astro-ph.IM\]](https://arxiv.org/abs/1712.02078).
- Tasse, C. et al. (Apr. 2021). “The LOFAR Two-meter Sky Survey: Deep Fields Data Release 1. I. Direction-dependent calibration and imaging”. In: *A&A* 648, A1, A1. DOI: [10.1051/0004-6361/202038804](https://doi.org/10.1051/0004-6361/202038804). arXiv: [2011.08328 \[astro-ph.IM\]](https://arxiv.org/abs/2011.08328).
- Tol, Sebastiaan van der, Bram Veenboer, and André R. Offringa (Aug. 2018). “Image Domain Gridding: A Fast Method for Convolutional Resampling of Visibilities”. In: *Astronomy & Astrophysics* 616, A27. ISSN: 0004-6361, 1432-0746. DOI: [10.1051/0004-6361/201832858](https://doi.org/10.1051/0004-6361/201832858). (Visited on 08/24/2023).
- van Diepen, Ger, Tammo Jan Dijkema, and André Offringa (Apr. 2018a). *DPPP: Default Pre-Processing Pipeline*. Astrophysics Source Code Library, record ascl:1804.003. ascl: [1804.003](https://www.ascl.net/1804.003).
- Vedantham, H. K. et al. (Feb. 2020). “Coherent radio emission from a quiescent red dwarf indicative of star-planet interaction”. In: *Nature Astronomy* 4, pp. 577–583. DOI: [10.1038/s41550-020-1011-9](https://doi.org/10.1038/s41550-020-1011-9). arXiv: [2002.08727 \[astro-ph.EP\]](https://arxiv.org/abs/2002.08727).
- Veenboer, B. and J.W. Romein (2020). “Radio-astronomical imaging on graphics processors”. In: *Astronomy and Computing* 32, p. 100386. ISSN: 2213-1337. DOI: <https://doi.org/10.1016/j.ascom.2020.100386>. URL: <https://www.sciencedirect.com/science/article/pii/S2213133720300408>.
- Veenboer, Bram et al. (Nov. 2019). “IDG: Image Domain Gridding”. In: *Astrophysics Source Code Library*, ascl:1911.011. (Visited on 08/24/2023).
- Weeren, R. J. van et al. (Mar. 2016). “LOFAR FACET CALIBRATION”. In: *The Astrophysical Journal Supplement Series* 223.1, p. 2. ISSN: 0067-0049. DOI: [10.3847/0067-0049/223/1/2](https://doi.org/10.3847/0067-0049/223/1/2). (Visited on 08/30/2023).

- Weeren, R. J. van et al. (July 2021). “LOFAR Observations of Galaxy Clusters in HETDEX - Extraction and Self-Calibration of Individual LOFAR Targets”. In: *Astronomy & Astrophysics* 651, A115. ISSN: 0004-6361, 1432-0746. DOI: [10.1051/0004-6361/202039826](https://doi.org/10.1051/0004-6361/202039826). (Visited on 08/30/2023).
- White, Richard L. et al. (Feb. 1997). “A Catalog of 1.4 GHz Radio Sources from the FIRST Survey”. In: *The Astrophysical Journal* 475.2, pp. 479–493. ISSN: 0004-637X. DOI: [10.1086/303564](https://doi.org/10.1086/303564). (Visited on 06/04/2020).

CHAPTER 5

Piercing the dusty veil of hyper-luminous infrared galaxies: Sub-arcsecond 144MHz ILT observations of HLIRGs in the Lockman Hole

Based on the publication: *Astronomy & Astrophysics, Volume 671, id.A85, 18 pp.*

Abstract

Hyper-luminous infrared galaxies (HLIRGs) are among the most extreme systems in the Universe. With infrared (IR) luminosities of $L_{\text{IR}} > 10^{13} L_{\odot}$ they can have IR-derived star formation rates (SFRs) exceeding $10^3 M_{\odot} \text{ yr}^{-1}$. Theoretical models have a hard time reproducing the observed number densities of such extreme star-forming systems. It is known that at least part of the population harbours active galactic nuclei (AGNs), but their prevalence and relative contribution to the IR output is still debated. Assessing this is further complicated by the heavy dust obscuration. We aim to investigate the HLIRG population in the Lockman Hole field to assess whether they are truly highly star-bursting systems or whether notable AGN activity is present. A substantial AGN population could help resolve the tension between the HLIRG number densities obtained from observations and predicted by galaxy-formation models by lowering the amount of truly extremely star-forming galaxies. Starting from a highly complete *Herschel*-selected sample, we make use of recent wide-field sub-arcsecond 144 MHz *International LOFAR Telescope* (ILT) observations of the Lockman Hole field to probe AGN activity in HLIRGs in a dust-unobscured way. Brightness temperature (T_{b}) measurements are made to determine the fraction of HLIRGs harbouring a radio-AGN. This identification is then compared to the SED-fitting-based classification from the LOFAR Deep Fields project, the radio-excess q and IRAC infrared colours. We detect 33% of previously identified HLIRGs at sub-arcsecond resolution. All but one of the detected sources is found to exceed the T_{b} threshold for pure star formation, showing 98% of detections to contain a radio-AGN even though lower-resolution observations had classified them as SFGs. The remaining source is concluded to be consistent with having no AGN activity. Combining this T_{b} criterion with existing methods doubles the fraction of AGNs in the total population from 16% to 32%. 98% of our detected sources are found to likely host radio-AGNs, raising the number of identified AGNs among the HLIRG population in this field from 16% to 32%. This increased number of AGNs is not sufficient to bring observations and predictions of HLIRG number densities in agreement, however. Even at cosmic noon around $z \sim 2$, where the tension is lowest, it remains at a factor few. The identification of radio-AGN in supposed SFGs highlights the value of high-resolution radio observations in studying dusty objects such as HLIRGs. Broad consistency is seen between T_{b} and the other AGN indicators, and the observed relation between SFR and T_{b} is seen as indicative of co-evolution between stellar mass build-up and black hole growth.

5.1 Introduction

Observations at radio wavelengths offer a unique perspective on astronomical objects. They probe particle-acceleration processes such as free-free and synchrotron emission, tracing star-formation activity or activity from super-massive black holes (SMBHs), while their long wavelengths make them free from the effects of dust attenuation that hinder other shorter wavelengths. This allows observations at radio wavelengths to provide information about the source of emission in areas where optical and infrared (IR) observations can not penetrate. The non-thermal behaviour of synchrotron emission makes it such that radio sources are generally brighter at lower frequencies. This makes low-frequency radio telescopes a prime choice for studying the radio-source population.

For that purpose, the *Low-Frequency Array* (LOFAR; Haarlem et al. 2013) has been conducting the *LO-FAR Two-metre Sky Survey* (LoTSS; Shimwell et al. 2017; Shimwell et al. 2019): a sensitive low-frequency survey of the Northern sky between 120 and 168 MHz. It reaches a median sensitivity of $71 \mu\text{Jy beam}^{-1}$ with 8 hours observing time per pointing. In addition to covering the full Northern sky using 8 hour pointings, select areas of the sky are being observed for long times, aiming for multiple hundreds of hours. These fields, colloquially called LOFAR’s “Deep Fields”, are the Lockman Hole (Lockman et al. 1986), Boötes (part of the *NOAO Deep Wide-Field Survey*; Jannuzi et al. 1999), ELAIS-N1 (*European Large Area Infrared Space Observatory Survey-North 1*; Oliver et al. 2000) and NEP (*North Equatorial Pole*) fields. They were chosen for their wealth of available ancillary data from X-ray to infrared. The first three of these fields have had ~ 100 hours of data reduced, currently, reaching sensitivities $\leq 30 \mu\text{Jy beam}^{-1}$ Tasse et al., 2021.

The bulk of luminous radio-emitting objects consists of objects whose activity is driven by a central SMBH, the so-called active galactic nuclei (AGNs). The dominant population here are the radio-loud (RL) AGNs (Paolo Padovani, 2016). These typically launch powerful jets, readily giving away the presence of an AGN by their morphology in spatially resolved observations. Spatially unresolved observations can still find them, however, as they are also characterised by an excess of non-thermal radio emission compared to what would be expected from its star formation rate (if available), or a radio luminosity high compared to its luminosity in other bands such as optical or infrared (IR) (Hardcastle et al., 2019). At faint flux densities around $S_{1.4 \text{ GHz}} \sim 1 \text{ mJy}$ (corresponding to $S_{144 \text{ MHz}} \sim 6 \text{ mJy}$ at $\alpha = -0.8$) the population composition starts to change from being dominated by RL AGNs to being dominated by star-forming galaxies (SFGs), where instead of being driven by AGN activity, the emission is driven by supernova remnants (Paolo Padovani, 2016). Among this faint radio population, there are still AGNs that do not show large scale jets or a notable excess of radio emission, making them easily mistakable for SFGs in radio observations that do not spatially resolve the galaxy. As such, it is important for our understanding of this population to be able to confidently separate AGN activity from star formation.

Inferring the presence of an AGN can be tricky, and is best done by leveraging broad multi-wavelength spectral coverage. Extensive work has therefore been put into classifying the sources detected in the Deep Fields, using the available ancillary data. The multi-wavelength cross-identification and catalogues are described by Kondapally et al., 2021. Best et al. (in prep.) then employed four different spectral-energy distribution (SED) fitting codes to arrive at “consensus” values for stellar mass and star formation rate. Galaxies were then classified as SFGs, radio-quiet (RQ) AGNs, low-excitation radio galaxies (LERGs) or high-excitation radio galaxies (HERGs) based on their SED fits, radio excess compared to what is expected from star formation and other indicators such as IR colours. Sources for which the classification was not clear were designated unclassified. This provides a rich new dataset to further our understanding of the properties of radio galaxies and the various relations between them.

A particular class of objects for which the distinction between star formation and AGN activity is particularly important is that of the luminous infrared galaxies. Discovered by the *Infrared Astronomical Satellite* (IRAS, Neugebauer et al., 1984), luminous infrared galaxies emit the majority of their energy at infrared (IR) wavelengths. They come in four luminosity-based flavours: luminous IR galaxies ($L_{\text{IR}} > 10^{11} L_{\odot}$), ultra-luminous IR galaxies (ULIRGs, $L_{\text{IR}} > 10^{12} L_{\odot}$, Cutri et al., 1994), hyper luminous IR galaxies (HLIRGs, $L_{\text{IR}} > 10^{13} L_{\odot}$, Rowan-Robinson, 2000) and extremely luminous IR galaxies (ELIRGs, $L_{\text{IR}} > 10^{14} L_{\odot}$, Tsai et al., 2015) and are believed to be powered by a combination of (merger-induced) star formation and black hole accretion (Armus et al., 1987; H. E. Smith et al., 1998; Rowan-Robinson et al., 2018) (see also the introduction of Wang et al., 2021 and references therein). Based on their IR and sub-millimetre luminosities LIRGs appear to reach star formation rates (SFRs) in excess of $10^3 M_{\odot} \text{ yr}^{-1}$ (e.g. Rowan-Robinson et al., 2018).

The extreme nature of these objects poses a problem for our current understanding of galaxy formation. One problem is that reproducing their extreme SFRs is difficult (e.g. Davé et al., 2010; Narayanan et al., 2015). Furthermore, the predicted number densities from simulations are difficult to reconcile with observations (e.g. Hayward et al., 2013; Lovell et al., 2021; Wang et al., 2021). Their association with massive galaxies ($M_{*}^{\text{median}} \sim 10^{12} M_{\odot}$; Gao et al., 2021) further complicates the situation. How do such massive systems form so early on in the universe? although a shared contribution between star-formation activity and AGN activity seems likely, the relative contributions of intense star formation and AGN activity to the emission of these objects is still under debate (D. Farrah et al., 2002; Ruiz et al., 2013; Gao et al., 2021). Finally, their often heavy obscuration makes them difficult to detect at shorter wavelengths such as optical light. To determine the origin of the observed emission, one thus has to rely on a variety of selection techniques such as colour-colour cuts or luminosity ratios, depending on the data available, resulting in notable discourse about the origin mechanism in the literature, as succinctly summarised in the introduction of Duncan Farrah et al., 2017.

In this paper, we hope to address part of the tension with galaxy formation models found by Wang et al., 2021. To do so, we investigate AGN activity in the HLIRG population in the lockman hole field from a high-resolution low-frequency radio perspective. Unaffected by dust this should offer a clear view into the central engine of these sources. This allows radio observations to be used to infer the presence of an AGN in two ways. If star formation rate estimates are available, one can look for excess radio emission compared to what is expected from pure star formation. Best et al. (in prep.) used this criterion to identify radio-AGN. The second method uses the measured brightness temperature T_{b} . There exists a (frequency-dependent) upper limit that pure star formation can reach (Condon et al., 1991). Emission from a source exceeding this limit can therefore not originate purely from star formation and it has been used to successfully identify AGN using very long baseline interferometry (VLBI; e.g. Radcliffe et al. 2021).

The almost 2000 km long baselines of the *International LOFAR Telescope* (ILT) offer an angular resolution of $\theta \sim 0.3''$ at the central frequency of 144 MHz. Recent developments have made it possible to calibrate the ILT at its native resolution (N. Jackson et al., 2022; L. K. Morabito et al., 2022) and to exploit its full field of view (Sweijen et al., 2022a). This now allows us to investigate a sample of HLIRGs from a low-frequency high-resolution perspective, adding this brightness temperature criterion as an additional AGN classifier. Using the classification by Best et al. (in prep.) We can remove any known AGNs. From the remaining sfgs and unclassified sources, their brightness temperature will be used to look for AGN-related emission, which can then tell us how many are truly sfgs and how many harbour an AGN after all, refining their earlier classification. In this paper, we focus on a particular type of source. See Leah K Morabito et al., 2022 for an example of AGN identification in a wider population of radio sources detected in the LOFAR Deep Fields.

Section 5.2 outlines the data used. In Section 5.3 we outline the methods used to analyse this data. Section 5.4 presents our findings, which are discussed in Section 5.5. Finally, Section 5.6 covers the conclusions.

The assumed cosmology is that of the 2015 Planck results (Ade et al., 2016), with $H_0 = 67.8 \text{ km s}^{-1} \text{ Mpc}^{-1}$, $\Omega_m = 0.308$ and $\Omega_\Lambda = 0.692$. Additionally, the spectral index α is defined as $S_\nu \propto \nu^\alpha$, where S_ν is the flux density at a given frequency ν .

5.2 Data

5.2.1 Radio data

We used 144 MHz radio data from Lockman Hole observations taken as part of the LOFAR Two-metre Sky Survey Deep Fields program. The pointing centre of this field is J2000 $10^{\text{h}}47^{\text{m}}00^{\text{s}} +58^{\text{d}}05^{\text{m}}00^{\text{s}}$ (LT10_012, L659948; PI: Best). Low-resolution $6''$ data is provided by a catalogue created from ~ 100 hours of data combined (Tasse et al., 2021; Kondapally et al., 2021). For the high-resolution data we use the eight-hour $0.3'' \times 0.4''$ image from Sweijen et al., 2022a. The point-source sensitivity at the pointing centre of both images is comparable at $23 \mu\text{Jy beam}^{-1}$ and $25 \mu\text{Jy beam}^{-1}$, respectively. As the sub-arcsecond image was smaller, only the central 6.6 deg^2 covered by the high-resolution image was considered for the low-resolution data, using the multi-order coverage (MOC) map of the LoTSS-Deep-HD (LDHD hereafter) observation.

5.2.2 HLIRG sample

The HLIRG sample was first selected in Wang et al. (2021) and then further studied in Gao et al. (2021). In Wang et al. (2021) a parent sample of IR luminous galaxies was identified based on *Herschel* blind catalogues. They cross-matched *Herschel* sources with the LoTSS Deep Fields first data release (Duncan et al., 2021; Kondapally et al., 2021; Sabater et al., 2021; Tasse et al., 2021) in order to obtain multiwavelength counterparts for these *herschel* sources. Thanks to the tight correlation between fir and radio (e.g., Calistro Rivera et al., 2017b; Wang et al., 2021) and the superb quality of lofar imaging, they successfully matched lofar sources for $> 90\%$ *herschel* sources with $250 \mu\text{m}$ flux density above 40 mJy in the lockman hole field. The optical-radio cross-identification for lofar sources can be found in Kondapally et al. (2021) and their redshifts are determined in Duncan et al. (2021). After adopting sed fitting code cigale (Burgarella et al., 2005; Noll et al., 2009) to derive galaxy properties, they selected 164 HLIRGs in the lockman hole field that have IR luminosity due to star-formation activity above $10^{13} L_\odot$. The number of HLIRGs increased to 259 in Gao et al. (2021) when they required total IR luminosity that is contributed by both star-formation activity and AGN activity above $10^{13} L_\odot$. In Gao et al. (2021) they used two different sed fitting codes (CYGNUS and CIGALE) and three different AGN models (Efsthathiou et al. (1995, hereafter E95), Fritz et al., 2006, hereafter F06 and Stalevski et al., 2012, hereafter S12) in order to study the properties of HLIRGs, the correlation between AGN fraction and SFR, their contribution to the cosmic stellar mass and SFR density, and so on. We refer to Wang et al. (2021) and Gao et al. (2021) for a detailed description of this HLIRG sample. For conciseness, we only show quantities obtained from CYGNUS with the Efsthathiou et al., 1995 AGN model (hereafter CyE95) and CIGALE with the Stalevski et al., 2012 model (hereafter CiS12) in the main text. These will show the largest differences in fitting results. The results from the Fritz et al., 2006 model and other combinations are shown in ??.

The HLIRG catalogue was cross-matched with the LDHD catalogue by matching their respective parent sources, which come from the LoTSS-Deep catalogue. The MOC was then again used to trim the sample to the common sky area, leaving 154 sources. Figure 5.1 illustrates the sky distribution of the full HLIRG sample, those that fall inside the LDHD footprint and those that are detected at the $5\sigma_{\text{rms}}$ confidence level. The redshift distribution of the sample is shown in Fig. 5.2.

5.3 Methods

To determine whether a source is a radio-AGN we make use of the brightness temperature T_b . Following Condon et al., 1991, a starburst galaxy will satisfy

$$T_b = T_e (1 - e^{-\tau_{\text{ff}}}) \left(1 + 10 \left(\frac{\nu}{1 \text{ GHz}} \right)^{0.1+\alpha} \right), \quad (5.1)$$

where $T_e \sim 10^4 \text{ K}$ is the electron temperature, τ_{ff} is the free-free optical depth, ν is the observing frequency and α is the synchrotron spectral index (note the change in sign with respect to Condon et al., 1991 due to our definition of α). For $\nu = 144 \text{ MHz}$, $T_e = 10^4 \text{ k}$, $\alpha = -0.8$ and $\tau_{\text{ff}} \rightarrow \infty$ this gives a maximum brightness temperature of $T_b^{\text{max}} = 4 \times 10^5 \text{ k}$, or $\log_{10} T_b^{\text{max}} = 5.6$. An HLIRG exceeding this threshold must have something besides star formation powering its emission. Equation 5.1's dependence on α makes it sensitive to changes in the source's spectral index. Varying this changes the threshold to $\log_{10} T_b^{\text{max}} = 5.5$ for $\alpha = -0.7$ and $\log_{10} T_b^{\text{max}} = 5.7$ for $\alpha = -0.9$.

The sample was cross-matched with the deep 1.4 GHz observation of Prandoni et al., 2018. This yields a sub-sample of 39 sources for which a spectral index can be determined with respect to LoTSS-Deep. A Gaussian fit to data binned in $\delta\alpha = 0.05$ wide bins yields a mean spectral index of $\alpha_{144\text{MHz}}^{1.4\text{GHz}} = -0.68 \pm 0.12$, where the uncertainty is the standard deviation of the fitted gaussian. Only 5 sources (13%) are steeper than -0.8 . Without spectral information for all sources, we, therefore, take the T_b threshold for $\alpha = -0.8$ as a reasonably conservative assumption for this sample.

We calculate the brightness temperatures of our sources by assuming their intensity profiles to be two-dimensional Gaussians. Furthermore, the intensity I is calculated using its definition S/Ω , where S is the source flux density and Ω is the source solid angle, rather than the measured values because time and bandwidth smearing will have artificially reduced them. The rest-frame brightness temperature can then be expressed as:

$$T_b = 1.22 \times 10^6 \times (1+z) \times \left(\frac{\nu}{1 \text{ GHz}} \right)^{-2} \times \left(\frac{\theta_{\text{maj}} \theta_{\text{min}}}{1 \text{ arcsec}^2} \right)^{-1} \times \frac{S_{\nu}^{\text{ILT}}}{1 \text{ Jy}} \text{ K}, \quad (5.2)$$

where ν is the observing frequency, z is the source redshift, θ_{maj} and θ_{min} are the fitted major and minor axes and S_{ν}^{ILT} is the measured high-resolution flux density. The uncertainty on T_b is propagated from the 30% uncertainty on S_{ν}^{ILT} measured in the LDHD image (Sweijen et al., 2022a). Uncertainties on s_{ν} measured in the LoTSS-Deep image (where applicable) are taken conservatively at 20% (the uncertainty on LoTSS; see Shimwell et al. 2019).

5.3.1 Radio excess

We probe the radio excess compared to a pure star-formation-driven source via the so-called q -value. This value is calculated using the total rest-frame IR luminosity L_{IR} determined from SED fitting by Gao et al., 2021 and the measured 144 MHz rest-frame luminosity

$$L_{144\text{MHz}} = 4\pi D_L^2 S_{144\text{MHz}} (1+z)^{-(1-\alpha)} \quad (5.3)$$

as

$$q_{150} = \log_{10} \frac{L_{\text{IR}}}{3.75 \times 10^{12} \text{ Hz} \times L_{144\text{MHz}}} \quad (5.4)$$

where L_{IR} is the total IR 8–1000 μm rest-frame luminosity and $L_{144\text{MHz}}$ the radio luminosity at 144 MHz. Using Gaussian uncertainty propagation the uncertainties $\sigma_{144\text{MHz}}$ and σ_q can be expressed as

$$\sigma_{144\text{MHz}} = 4\pi D_L^2 \sigma_S (1+z)^{-(1-\alpha)} \quad (5.5)$$

$$\sigma_q = \frac{1}{\ln 10} \times \sqrt{\left(\frac{\sigma_{\text{IR}}}{L_{\text{IR}}}\right)^2 + \left(\frac{\sigma_{144\text{MHz}}}{L_{144\text{MHz}}}\right)^2} \quad (5.6)$$

where $\sigma_{144\text{MHz}}$ and σ_{IR} indicate the uncertainties in their respective luminosities. No error in z and α are assumed.

5.4 Results

5.4.1 Fraction of radio detections, brightness temperature

51 out of 154 sources are detected at a $I_{\text{peak}} > 5\sigma_{\text{rms}}^{\text{local}}$ level, where $\sigma_{\text{rms}}^{\text{local}}$ is the local root-mean-square noise around the source as estimated by PyBDSF. Figure 5.3 compares the low-resolution flux density and peak intensity distributions between high-resolution detected and undetected sources. The mean and median values of LDHD-undetected HLRGs lie close to or below the estimated limit (see Section 5.5). Since these values are still at an overall $> 5\sigma$ level, we interpret the non-detections as probably being extended sources with no significant compact emission. An intermediate $\sim 1''$ resolution image would be able to confirm this.

The brightness temperature distribution for the sample is shown in Fig. 5.4. Also indicated are the theoretical upper limits from Condon et al., 1991 for starburst activity, for several synchrotron spectral indices. Conservatively, we find that 40 out of 51 sources (78%) have $\log_{10} T_b > 5.6$ if we assume a spectral index of $\alpha = -0.8$. These sources are likely hosting an AGN. With a less-conservative spectral index of $\alpha = -0.7$ this fraction rises to 98%. Out of these 51 sources, 24 are known AGN from Best et al. (in prep.). From the remaining 27 sources 18 exceed $\log_{10} T_b = 5.6$ and 26 exceed $\log_{10} T_b = 5.5$, leaving only 9 and 1 below the AGN threshold, respectively. Of the full sample, 17% are known AGNs following the criteria of Best et al. (in prep.). This can be increased to 32%, by additionally including a brightness temperature cut.

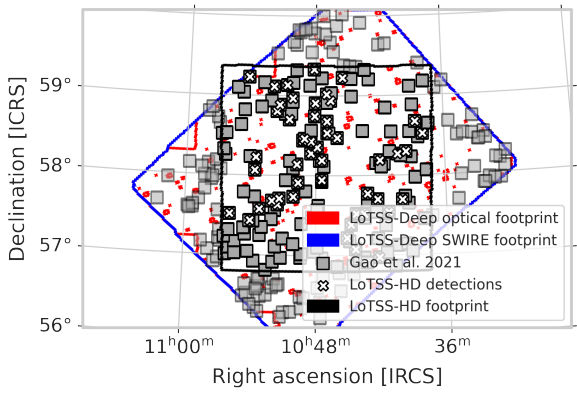


Figure 5.1: A map showing the distribution of HLRGs and, respectively, all sources in the sample (squares), the LoTSS-Deep-HD footprint (black line), sources that fall inside this footprint (opaque squares) and sources with a $\sigma_{\text{rms}}^{\text{local}} > 5$ detection in the LoTSS-Deep-HD image (white crosses).

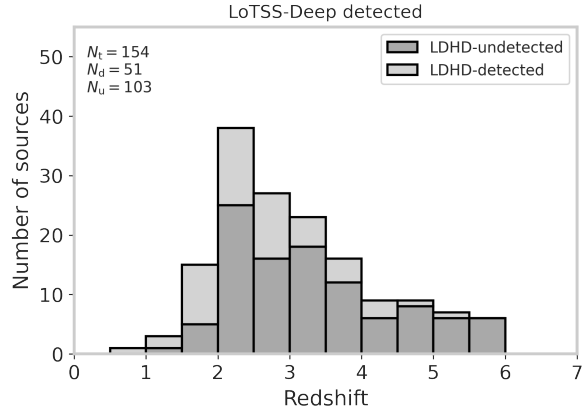


Figure 5.2: Redshift distributions for the full sample (N_t , solid lines), LDHD-detected (N_d , dashed lines) and LDHD-undetected (N_u , dotted lines) sources. The majority are photometric estimates by Duncan et al., 2021, but some have spectroscopically confirmed redshifts. No significant difference is seen between detected and undetected sources.

Table 5.1: HLIRG detections for $z \geq 2$ by redshift bins of $\Delta z = 0.5$. Column 1 indicates the detection fraction, columns 2 and 3 indicate the number of sources exceeding the respective T_b thresholds.

Redshift	$N_{\text{det.}} / N_{\text{tot.}}$	$\# T_b \geq 10^{5.6}$	$\# T_b \geq 10^{5.5}$
$2.0 \leq z < 2.5$	7/22	4	6
$2.5 \leq z < 3.0$	9/25	9	9
$3.0 \leq z < 3.5$	5/23	4	5
$3.5 \leq z < 4.0$	4/16	3	4
$4.0 \leq z < 4.5$	3/9	3	3
$4.5 \leq z$	2/22	2	2
All $z \geq 2.0$	30/117	25	29

5.4.2 Brightness temperature compared to SED fitting

AGN fraction

Figure 5.5 shows the estimated AGN fraction versus brightness temperature. A general correlation can be identified where the brightness temperature rises with increasing AGN fraction, but the estimated AGN fraction varies notably between the different models and fitting codes. The data hints at the existence of potentially two populations: sources with a high AGN fraction, but a low brightness temperature and conversely sources with a low AGN fraction, but a high brightness temperature.

The full redshift distribution of the sample can be seen in Fig. 5.2. A Kolmogorov-Smirnov (KS) test was performed to test the null hypothesis of the redshift distributions of detected and undetected sources being equal, using SciPy's `scipy.stats.ks_2samp`. This resulted in a KS-statistic of $KS = 0.28$ and a p -value of $p = 0.007$. We, therefore, do not reject the null hypothesis and consider there to be no significant difference between the two. In Tab. 5.1 we summarise the detection fraction of HLIRGs (i.e. $L_{\text{IR}} \geq 10^{13}$) in from $z = 2$ (where the tension with models found by Wang et al., 2021 starts), in bins of $\Delta z = 0.5$. We see a 20 – 35% ratio of detected to undetected HLIRGs in each bin, except for $z > 4.5$ where only 10% is detected.

Star-formation rate

All of the 103 sources below the detection threshold are classified as SFGs by Best et al. (in prep.). A minor fraction of 9 sources has a possible detection in the $3 - 5\sigma_{\text{rms}}$ range, but these were left out in favour of reliability. Figure 5.6 shows, for detected sources, the star formation rate derived from SED fitting by Gao et al., 2021 versus the measured brightness temperature. The colour and shape of the points indicate their classification by Best et al. (in prep.). Finally the theoretical brightness temperature limits for star formation from Condon et al., 1991 are indicated for values of the synchrotron spectral index of -0.7 , -0.8 and -0.9 , respectively.

Table 5.2 summarises the classification of the detected HLIRGs in the first two columns. The number of sources within that classification exceeding the two brightness temperature limits for $\alpha_{\text{syn}} = -0.8$ and -0.7 are reported in the third and fourth columns, respectively. After removing the known AGNs, we are left with 27 sources that are either SFGs or unclassified. Subsequently removing all sources whose

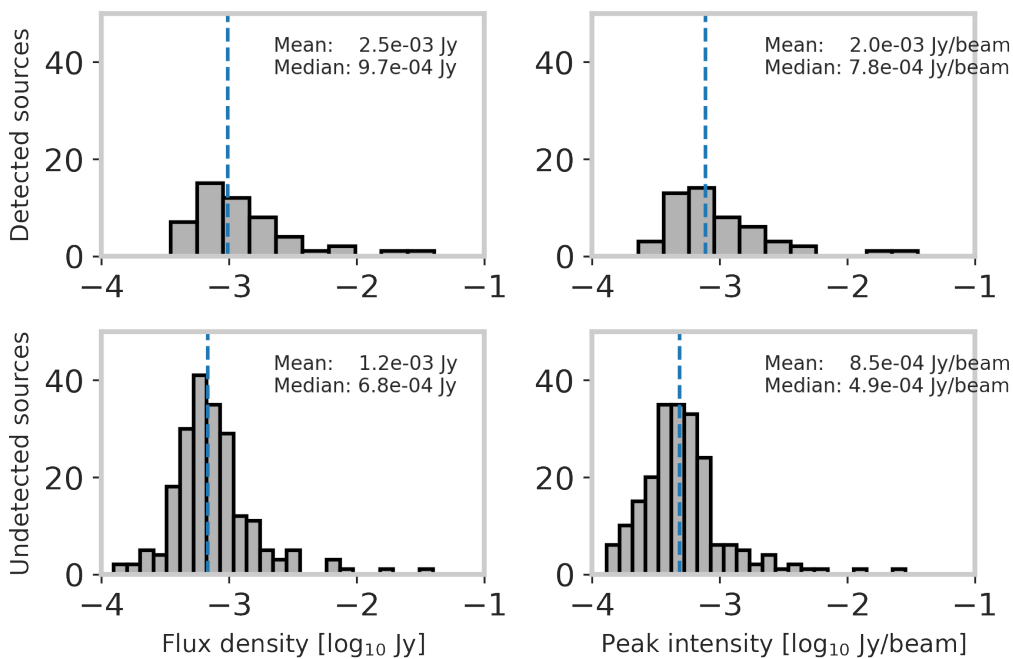


Figure 5.3: LoTSS-Deep 6'' flux density (*left*) and peak intensity (*right*) distributions for LoTSS-Deep-HD detected (*top*) and undetected (*bottom*) sources. The blue dashed line indicates the median. LoTSS-Deep-HD-undetected sources have systematically lower values that are close to or below the 5σ surface brightness limit of the high-resolution image.

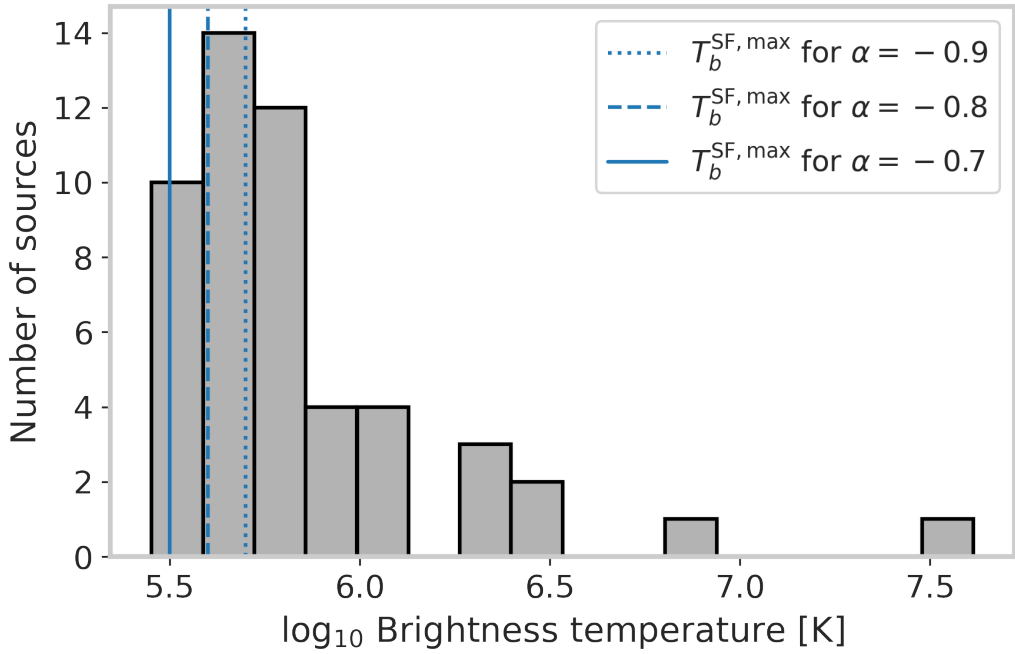


Figure 5.4: Distribution of brightness temperatures in the LoTSS-Deep-HD detected sources. The solid, dashed and dotted blue lines indicate the maximum brightness temperature from starbursts for a synchrotron spectral index α of -0.7 , -0.8 and -0.9 , respectively, as per by [Condon et al., 1991](#). Values to the right of this line cannot be driven by pure star formation.

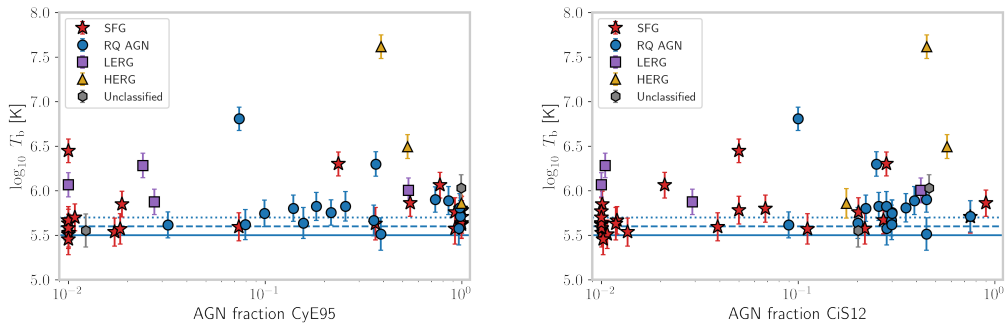


Figure 5.5: Brightness temperature versus AGN fraction. *Left*: AGN fraction derived from the CyE95 fit. *Right*: AGN fraction derived from the CiS12 fit.

Table 5.2: Classification of detected HLIRGs. Column 1 states the number of objects in the given class, and columns 2 and 3 indicate the number of sources exceeding the respective T_b thresholds. Numbers in parentheses indicate LDHD-undetected sources.

Class	# objects	# $\log_{10} T_b > 5.6$	# $\log_{10} T_b > 5.5$
SFG	25 (103)	17	24
RQ AGN	17	15	17
LERG	4	4	4
HERG	3	3	3
Unclassified	2	1	2
Total	51 (103)	40	50

brightness temperature exceeds $10^{5.6}$ K leaves 9 sources. Removing all sources whose brightness temperature exceeds $10^{5.5}$ K leaves 1 SFG. The sources in our sample appear to systematically avoid the high- T_b , low-SFR region.

Distance to the main sequence

The idea of a star-forming main sequence results from the observed correlation between the stellar mass and SFR of galaxies. We compared the difference between the estimated SFRs to their respective “main-sequence” SFRs, i.e. The distance to the main sequence $\Delta MS = SFR - SFR_{MS}$, for our LDHD-detected sample, using the relation of [Speagle et al., 2014](#). An anti-correlation between the AGN fraction derived from their sed fitting and the distance to the main sequence was found by [Gao et al., 2021](#). Figure 5.7 plots the distance to the main sequence versus the measured brightness temperature. The distance to the main sequence is calculated according to [Speagle et al., 2014](#). A slight anti-correlation is seen for SFGs and RQ AGNs. Below the main sequence sources with higher brightness temperatures are found and as brightness temperatures decrease, sources are seen to move towards and above their associated main sequence SFR.

5.4.3 Brightness temperature compared to radio excess

Figure 5.8 shows the 144 MHz radio excess q_{150} , as calculated by Eqn. 5.4, versus the brightness temperature of each detected HLIRG. A clear anti-correlation between T_b and q_{144} is seen. The radio excess increases with increasing brightness temperature, lowering q_{144} .

5.4.4 Brightness temperature compared to IRAC detections

Figure 5.9 displays a colour-colour diagram of the HLIRG sample using the four IRAC channels: $3.5 \mu\text{m}$, $4.5 \mu\text{m}$, $5.7 \mu\text{m}$ and $8.0 \mu\text{m}$, respectively. The [Donley et al., 2012](#) criteria constrain a region of this colour space that is inhabited by AGN. If this IR-based AGN indicator correlates with e.g. brightness temperature, a preference for sources to lie within the AGN region of this colour space would be expected. We will refer to sources within this region as IRAC AGN and sources outside this region as IRAC non-AGN. 22 out

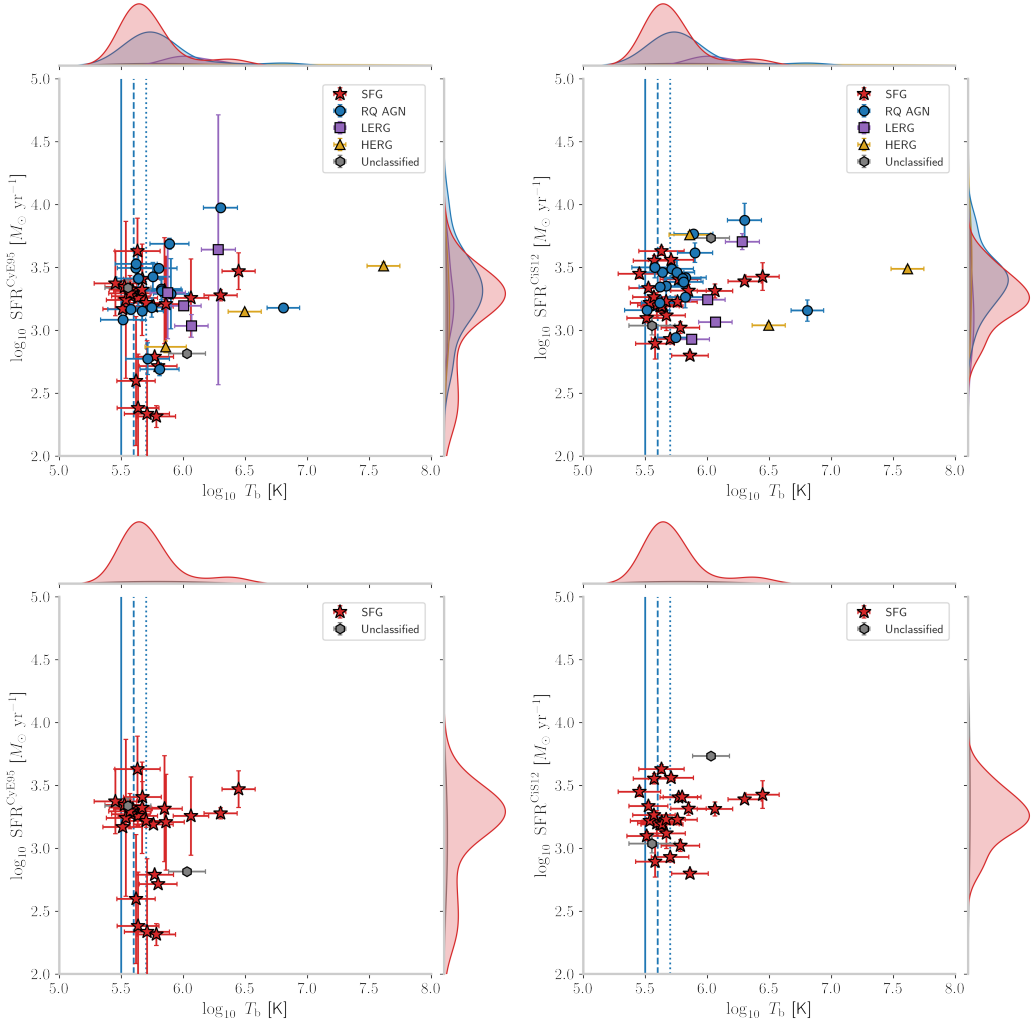


Figure 5.6: Star formation rate versus brightness temperature of the 51 HLRGs detected in LDHD image at the $5\sigma_{\text{rms}}$ level. *Top*: full sample, coloured by the classification of Best et al. (in prep.). *Bottom*: sample with the 24 AGN identified by Best et al. Removed, leaving 27 sources. *Left*: the SFR as estimated from the CyE95 model. *Right*: the SFR estimated from the CiS12 model. Marginalised distributions over the SFR and brightness temperature are shown on top and to the right of each panel.

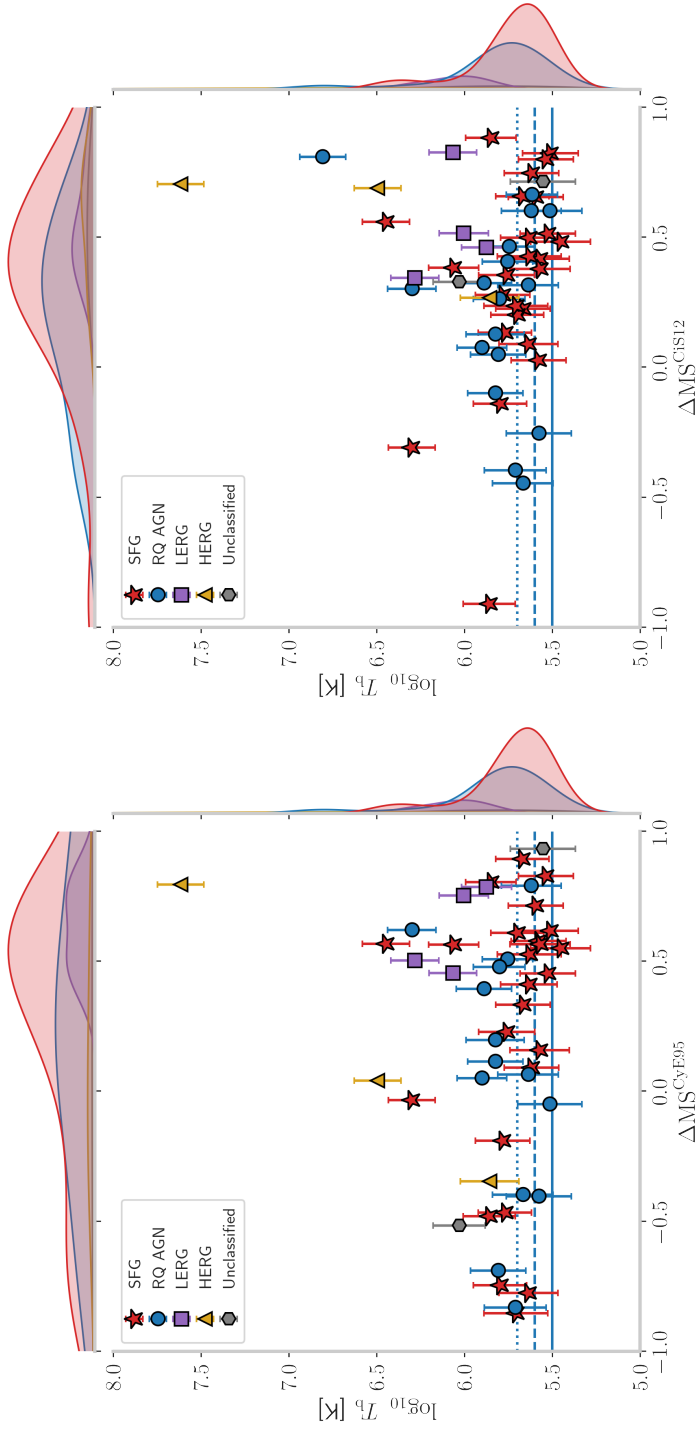


Figure 5.7: Brightness temperature T_b versus distance to the main sequence ΔMS for HLIRGs above the LDHD detection threshold. ΔMS is shown for the CyE95 (*left*) and CiS12 (*right*) models. Points are coloured by their classification according to Best et al. (in prep.). The solid, dashed and dotted blue lines indicate the maximum brightness temperature from starbursts for a synchrotron spectral index α of -0.7 , -0.8 and -0.9 , respectively, as per Condon et al., 1991. Points to the right of these lines cannot be driven by pure star formation.

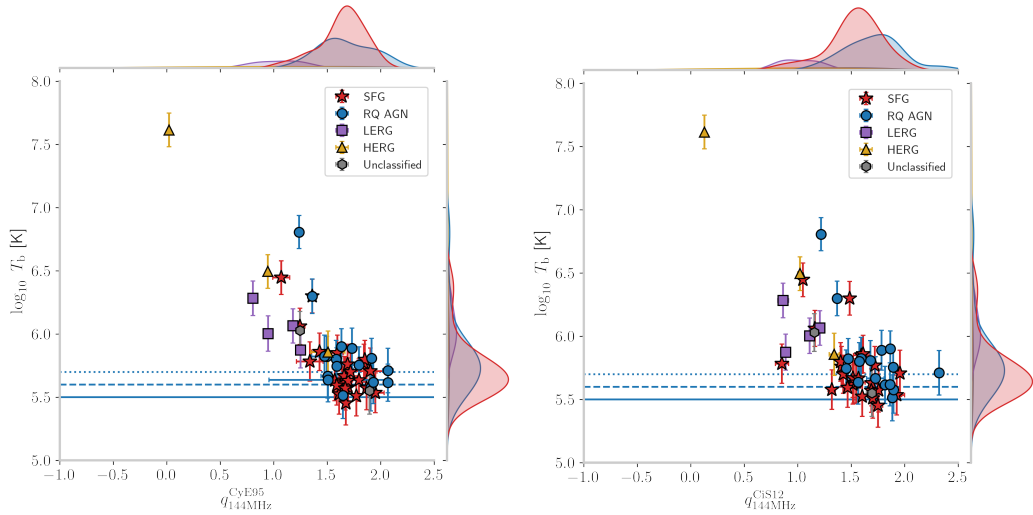


Figure 5.8: Brightness temperature versus radio excess. q was determined using IR luminosities from the CyE95 (*left*) and CiS12 (*right*) models. The solid, dashed and dotted blue lines indicate the maximum brightness temperature from starbursts for a synchrotron spectral index α of -0.7 , -0.8 and -0.9 , respectively, as per Condon et al., 1991. Points to the right of these lines cannot be driven by pure star formation.

of 51 LoTSS-Deep-HD detections (43%) can be classified as IRAC AGN. Of the non-detections, 35% (36 out of 103 sources) are IRAC AGN. Of the full HLIRG sample within the LDHD footprint, 38% (58 out of 154) are IRAC AGN. HLIRGs above the detection threshold in the LDHD data show no direct preference to also be IRAC AGN. Compared to HLIRGs below the LDHD detection threshold, however, they do appear more likely to be IRAC AGN. Finally, it is clear that the IRAC colours do well separating the AGN population from the supposed SFG population, but cannot successfully identify the AGN activity in those that we identified through brightness measurements.

Figure 5.10 shows the fraction of IRAC AGN in sources that exceed a given limiting brightness temperature. The fraction of IRAC AGN is seen to increase with limiting brightness temperature, as shown in black. In red and blue the fraction of, respectively, IRAC AGNs and IRAC non-AGNs exceeding this limit is shown. Two aspects become apparent. Firstly, the fraction of sources exceeding the threshold decreases as it increases. This is expected as there are simply fewer sources with higher brightness temperatures. Secondly, the IRAC AGNs show a systematically higher fraction of sources exceeding the limit compared to IRAC non-AGNs. This is most prominent between $5.6 < \log_{10} T_b < 5.9$, but remains for $\log_{10} T_b > 5.9$.

5.5 Discussion

One of the caveats of high-resolution observations is the decreased surface brightness sensitivity. This will affect the detection of extended source structure and thus completeness. Here we discuss this effect. We also put our high-resolution radio observations in context with other AGN indicators and the general idea

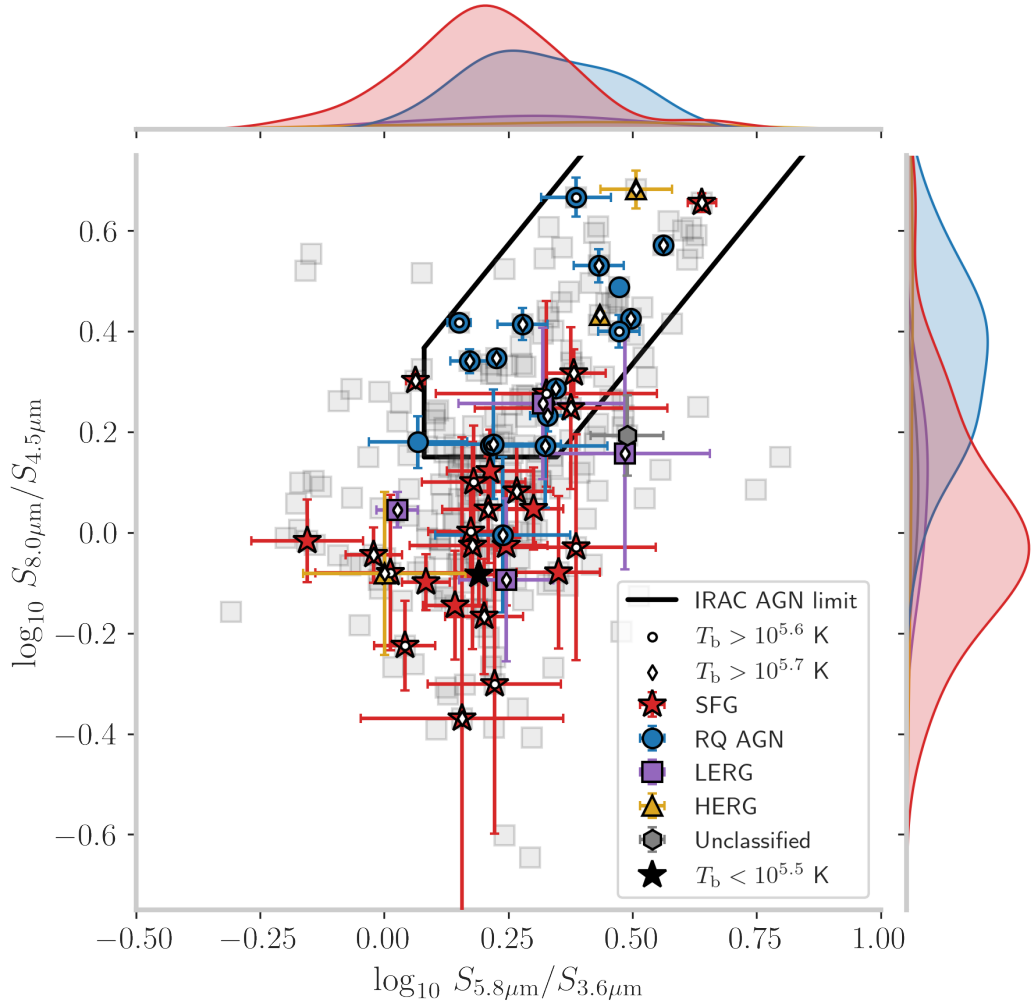


Figure 5.9: IRAC colour-colour diagram for LoTSS-Deep-HD detected (*left*) and undetected (*right*) sources. The black line denotes the region in which IRAC AGN are expected, as per the [Donley et al., 2012](#) criteria. Faded grey squares indicate the LDHD-undetected sample, while the coloured symbols indicate sources satisfying the full IRAC AGN selection criteria (colour region and a monotonically increasing far infrared flux density). Of the LDHD detections 43% (22/51) can be classified as IRAC AGN. For the non-detections this is 27% (56/208). In total 28% (22 / 78) of IRAC AGN are detected.

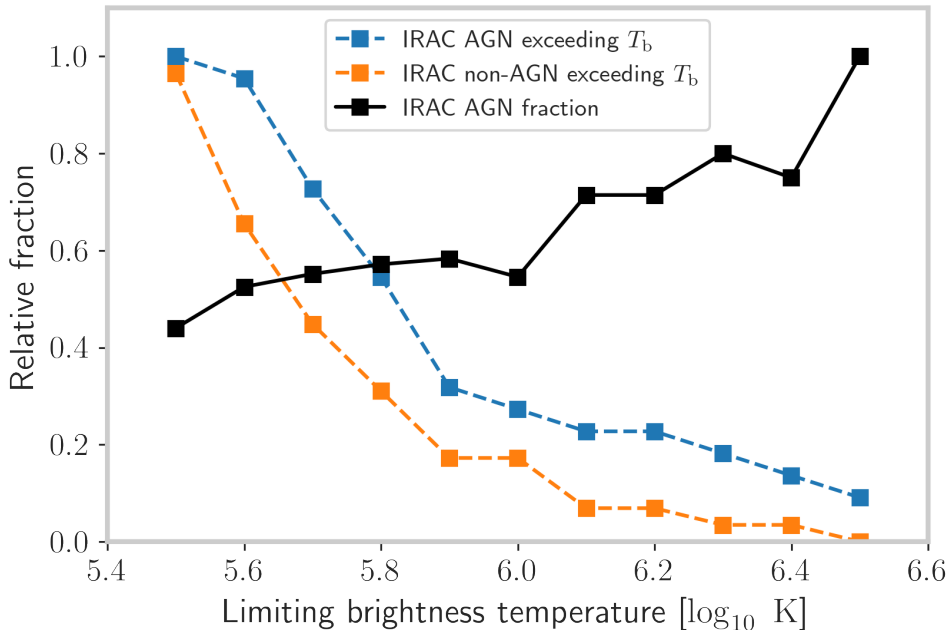


Figure 5.10: The fraction of IRAC sources as a function of certain brightness temperature limit. The black solid line indicates the fraction of IRAC AGN in sources that exceed the limiting brightness temperature. The red and blue dashed lines indicate the fraction of IRAC AGN and IRAC non-AGN, respectively, that exceed this limit.

of co-evolution of black holes and star formation.

5.5.1 Sensitivity to extended source structure and completeness and detection bias

At the given sensitivities per beam, the LoTSS-Deep-HD image will be ~ 326 times less sensitive to diffuse emission compared to the LoTSS-Deep image. A back-of-the-envelope estimate of this limiting surface brightness can be made as follows. For a patch of extended emission to be detected at the 5σ level, in the $0.3'' \times 0.4''$ resolution image, it would need an intensity of $125 \mu\text{Jy beam}^{-1}$. A 1 arcsec^2 area would consist of 7.1 beam elements, implying a flux density limit of roughly 0.9 mJy for a uniform patch of emission (and thus an identical peak intensity for a $6''$ -unresolved source).

Only a third of the HLIRGs is recovered above the detection limit, making it clear that the full LDHD sample is incomplete with respect to the LoTSS detections. A completeness of 81% at $S_{\nu}^{\text{ILT}} \geq 2 \text{ mJy}$ is estimated by determining the fraction of LDHD detected sources as a function of limiting LoTSS flux density. This is shown in Fig. 5.17. A steep drop in completeness starts between 0.7 and 0.8 mJy. This is close to the $\sim 6 \text{ mJy}$ turning point where the source population starts to become increasingly dominated by SFGs, which tend to be larger and more diffuse. We therefore interpret the non-detections as being closer to SFGs than to AGNs.

Finally, the reduced sensitivity to extended structure introduces an obvious, but important bias towards compact sources. This biases the sample to inherently prefer the detection of compact nuclear components such as AGNs and distant unresolved or barely resolved star-bursting galaxies.

5.5.2 Addressing the tension between HLIRGs and galaxy formation models

To relieve the tension between the GALFORM galaxy formation model (which assumes all the IR emission is reprocessed stellar emission; Gutcke et al. 2015) and the number densities of extreme star-forming systems found by Wang et al., 2021, those densities would have to come down by orders of magnitude. Here we discuss our findings in this context.

Our results show that even conservatively the majority of the remaining HLIRGs classified as SFGs are likely to contain AGNs. This is in contrast with Leah K Morabito et al., 2022, where only 12% of the more general SFG population was found to have a high brightness temperature, but consistent with other literature studies finding that a substantial fraction of HLIRGs display signs of AGN activity; e.g. D. Farrah et al., 2002, Ruiz et al., 2013, Gao et al., 2021. However, Rowan-Robinson et al., 2018, for example, conclude the majority of IR emission from their sample is dominated by star formation, while M. Symeonidis et al., 2018 propose that AGN can explain the full IR luminosity at $L_{\text{IR}} > 10^{13.5} L_{\odot}$. We see a similar “threshold” in Fig. 5.16, where all HLIRGs with $L_{\text{IR}} > 10^{13.5} L_{\odot}$ exceed our most conservative threshold of $\log_{10} T_{\text{b}} > 5.7$ for every model, except in the case of CyE95 where one falls below it, and have substantial estimated AGN fractions as well. A difference is that in our sample these sources lie at $z > 3$, while M. Symeonidis et al., 2018 studied sources in the range of $z = 1 - 2$. A substantial AGN fraction in combination with a brightness temperature in excess of our most conservative threshold supports the AGNs in high- z high- L_{IR} population of HLIRGs contributing substantially to the IR output.

To see if the tension can be resolved, we can, as a logical extreme, consider sources that exceed the brightness temperature threshold to be 100% powered by an AGN. The sole source falling below all thresholds we consider to be a “pure SFG” for this argument and it has an estimated redshift of $z \approx 2.1$. This falls in

the $z = 2.0 - 2.2$ bin of Fig. 10 of Wang et al., 2021. The tension here is still relatively small at only a factor of a few. Four LDHD-detected sources and nine LDHD-undetected sources fall in this redshift range. Only the aforementioned SFG falls below all brightness temperature thresholds. It also has an estimated AGN fraction consistent with zero for both the CyE95 and CiS12 sed-fitting models. Of the undetected HLIRGs, two have notable AGN fractions of 59% and 20% (CiS12) or 28% and 44% (CyE95). If for argument's sake, we assume all three of the high- T_b sources to be “pure AGNs”, the number of “pure sfgs” in this bin would drop from 13 to 10; a factor 1.3 or 23%. In the aforementioned Fig. 10 it can be seen that this is insufficient to reconcile the number counts with the predictions from the GALFORM model. In higher redshift bins this reduction can be of the order of a factor 2, but by $z = 3$ the discrepancy is already two orders of magnitude and increasing. Furthermore, realistically only the brightest HLIRGs may be *fully* powered by AGNs, lessening this “correcting factor” again. The tension between models and observations cannot be resolved, even if we assume all our detections to be completely AGN-driven.

5.5.3 Brightness temperature as a dust-unobscured tracer of AGN activity

To broadly assess the use of brightness temperatures as an AGN indicator, they were compared to three other indicators. A subtle point worth noting is that the *convolved* source sizes (i.e. The intrinsic source size convolved with the point spread function) were used to estimate brightness temperatures. *Deconvolved* sizes were not used, because time and bandwidth smearing made accurate deconvolved size measurements complicated. This does not affect the results presented here in a meaningful way, other than technically turning the measured brightness temperatures into lower limits.

SED fitting P N Best et al., 2023 used SED-fitting to classify sources into either SFGs, RQ AGNs, LERGs and HERGs. The SED-fitting from Gao et al., 2021 provides estimates of various parameters such as L_{IR} and f_{AGN} for various combinations of SED-fitting codes and models. Here we compare these classifications and quantities with our brightness temperature measurements.

Those objects classified as radio-loud AGNs (i.e. HERGs and LERGs) are recovered as high- T_b objects well exceeding even threshold value for AGN activity. Additionally, of the two unclassified sources, one clearly exceeds the threshold and the other marginally exceeds the least conservative threshold. For SFGs and RQ AGNs, the story differs, as both types of sources have objects exceeding the thresholds to various degrees. In the case of RQ AGNs, this illustrates that these (relatively) faint objects can still be recovered as AGNs through their compactness. In the case of SFGs, the label given when it was neither a radiative-mode AGN (identified with emission lines and IR colours) nor a radio-excess source (identified through a cut in the $L_{150\text{MHz}} - \text{SFR}$ plane), it demonstrates how high-resolution radio observations can both complement existing classification and act as an independent tracer of AGN activity.

Comparing T_b with L_{IR} and f_{AGN} , the estimated AGN fractions and IR luminosities estimated by CYGNUS and CIGALE both show general correlation with brightness temperature. Fig. 5.19 plots brightness temperature and the estimated AGN fraction versus this difference. As the difference $L_{\text{IR}}^{\text{CYGNUS}} - L_{\text{IR}}^{\text{CIGALE}}$ increases (that is, moves towards positive values), an increase in T_b for SFGs is seen (top panel). At the same time, f_{AGN} strongly decreases as this difference increases (middle and bottom panel). This may be related to the assumptions made in the fitting codes and to the difficulty of disentangling low-level AGN activity from e.g. star-formation activity. A detailed analysis of these trends and their significance is beyond the scope of this paper, but we note that Buat et al., 2019, for example, find that energy balance is not a good assumption for their sample of star-bursting sources. This highlights the importance of model assumptions.

Radio excess The existence of a correlation between radio emission and IR emission from star-forming galaxies has long been known (de Jong et al., 1985; Helou et al., 1985). This has since been used as a way to trace star formation through the radio-to-IR ratio q (Bell, 2003; Calistro Rivera et al., 2017b; Delvecchio et al., 2021). At the same time, this ratio can be used to search for AGNs, by looking for an excessive q -value (e.g. Donley et al., 2005). A lower value of q_{144} indicates a higher 144 MHz luminosity compared to a given IR luminosity. A higher brightness temperature is the result of a brighter and/or more compact radio source. One would thus expect a correlation between q_{144} and T_b if both trace AGN activity well. Figure 5.8 shows the measured brightness temperature versus the calculated q -value for the CyE95 and CiS12 SED fits. A clear correlation between the two quantities, as expected. This supports our brightness temperatures to be a sensible tracer of AGN activity and reaffirms either’s ability to be used for AGN identification.

IRAC AGN In Fig. 5.9 it was seen that LDHD-detected sources show an increased preference to be IRAC AGN compared to the full HLIRG sample. This is consistent with the literature in that a substantial amount of these sources are thought to harbour AGNs e.g. D. Farrah et al., 2002; Rowan-Robinson et al., 2018; Gao et al., 2021 and that they could be a substantial driver behind the IR emission e.g. M. Symeonidis et al., 2018; Symeonidis et al., 2021. Figure 5.10 shows an increasing fraction of IRAC AGN with brightness temperature. This correlation between the IR and radio activity is also seen in Figures 5.16 and 5.13, where L_{IR} is seen to increase with T_b . A preference for IRAC AGN to exceed the brightness temperature threshold more often than IRAC non-AGN is seen. Notably, the majority are RQ AGN which would indeed not be identified as AGN by low-resolution radio observations. This makes brightness temperatures especially useful to pinpoint relatively weak AGNs that would escape cuts based on radio excess, for example, for these obscured sources.

5.5.4 Co-evolution of black hole growth and star formation

The growth of black holes and the build-up of stellar populations over cosmic time are remarkably alike see e.g. the review of Heckman et al., 2014. This is not completely unexpected. After all, they have a common fuel source: the gas reserves of the galaxy.

In the top panel of Fig. 5.6 two source populations can potentially be identified. One concentrates around low brightness temperatures and SFRs on the high end, and one with a wider range of SFRs and brightness temperatures. Broadly speaking the higher brightness temperature HLIRGs also seem to be associated with higher SFRs. Furthermore, the detected HLIRGs seemingly avoid the region of parameter space corresponding to a high brightness temperature, but a low SFR. Figure 5.18 shows the SFR versus brightness temperature for the full sample. From this, it becomes clear that this region is predominantly inhabited by LERGs and HERGs. Of interest here is that this is not a general avoidance zone, but a radio-loud AGN-dominated region. This raises the question of why the HLIRGs in our sample seem to avoid this particular combination of parameters. To sustain the incredibly high SFR in HLIRGs, these galaxies should have a large reservoir of gas to draw from. This could naturally supply the central engine with fuel from that same supply, leading to a simultaneous increase in both star formation activity and AGN activity. We, therefore, speculate that the tentative trend of brightness temperature with star formation rate supports the idea of co-evolution in these massive galaxies.

5.6 Conclusion

HLIRGs are difficult to reproduce in simulations, both in terms of their extreme SFR and observed number density. In this work, we studied the HLIRG population in the Lockman Hole field from a sub-arcsecond perspective at 144 MHz using the ILT. This high-resolution radio data was used to assess AGN activity in HLIRGs by means of brightness temperature measurements, in order to see if the tension between observations and current galaxy formation models could be reduced. We conclude our findings as follows:

- The low-frequency brightness temperature T_b is an effective tool for revealing AGN activity in dusty objects such as HLIRGs. Not only are known radio-loud AGNs among the sample recovered, clearly exceeding the upper limit for pure star formation determined by Condon et al., 1991, but additional AGNs not readily picked up by the other methods discussed in this paper were identified.
- The total number of HLIRGs in this field harbouring an AGN could be increased from 16% to 26–32% (depending on how conservative one takes the threshold). All of these were initially classified as SFGs. One of the LDHD-detected sources remains consistent with pure star formation. A notable amount of HLIRGs may thus harbour a radio AGN that is not picked up on when using UV to IR or low-resolution radio observations.
- The additional AGNs identified here cannot relieve the tension between the observed number density of HLIRGs and predictions from the GALFORM theoretical model. The number density of extreme star-forming systems can only be reduced by a factor $\sim 1 - 1.5$ at cosmic noon using this additional information and assuming AGN dominance for all detected sources.
- Brightness temperature is seen to broadly correlate with AGN dominance probed by other indicators such as the radio excess, SED-fitted AGN fractions and IR colours. Additionally, it is seen to scale with estimated star-formation rates. We see this as an indication of co-evolution between star formation and AGN activity.

In this work we have given a tasting of what high-resolution radio observations could offer in terms of population studies of HLIRGs, but the sample size is still small, therefore limiting the robust identification of trends. Future sub-arcsecond surveys over large areas of the sky will provide detailed radio data for a large number of these extremely IR-luminous objects, penetrating the dusty curtain that enshrouds them, allowing us to peer deeper into the engine powering their high infrared luminosities.

Acknowledgements

This paper is based (in part) on data obtained with the International LOFAR Telescope (ILT) under project code LT10_012. LOFAR (van Haarlem et al. 2013) is the Low Frequency Array designed and constructed by ASTRON. It has observing, data processing, and data storage facilities in several countries, that are owned by various parties (each with their own funding sources), and that are collectively operated by the ILT foundation under a joint scientific policy. The ILT resources have benefited from the following recent major funding sources: CNRS-INSU, Observatoire de Paris and Université d’Orléans, France; BMBF, MIWF-NRW, MPG, Germany; Science Foundation Ireland (SFI), Department of Business, Enterprise

5.6. CONCLUSION

and Innovation (DBEI), Ireland; NWO, The Netherlands; The Science and Technology Facilities Council, UK; Ministry of Science and Higher Education, Poland. RJvW acknowledges support from the ERC Starting Grant ClusterWeb 804208. This work has made use of the Dutch national e-infrastructure with the support of SURF Cooperative through grant e-infra 180169.

5.7 Other code-model combinations

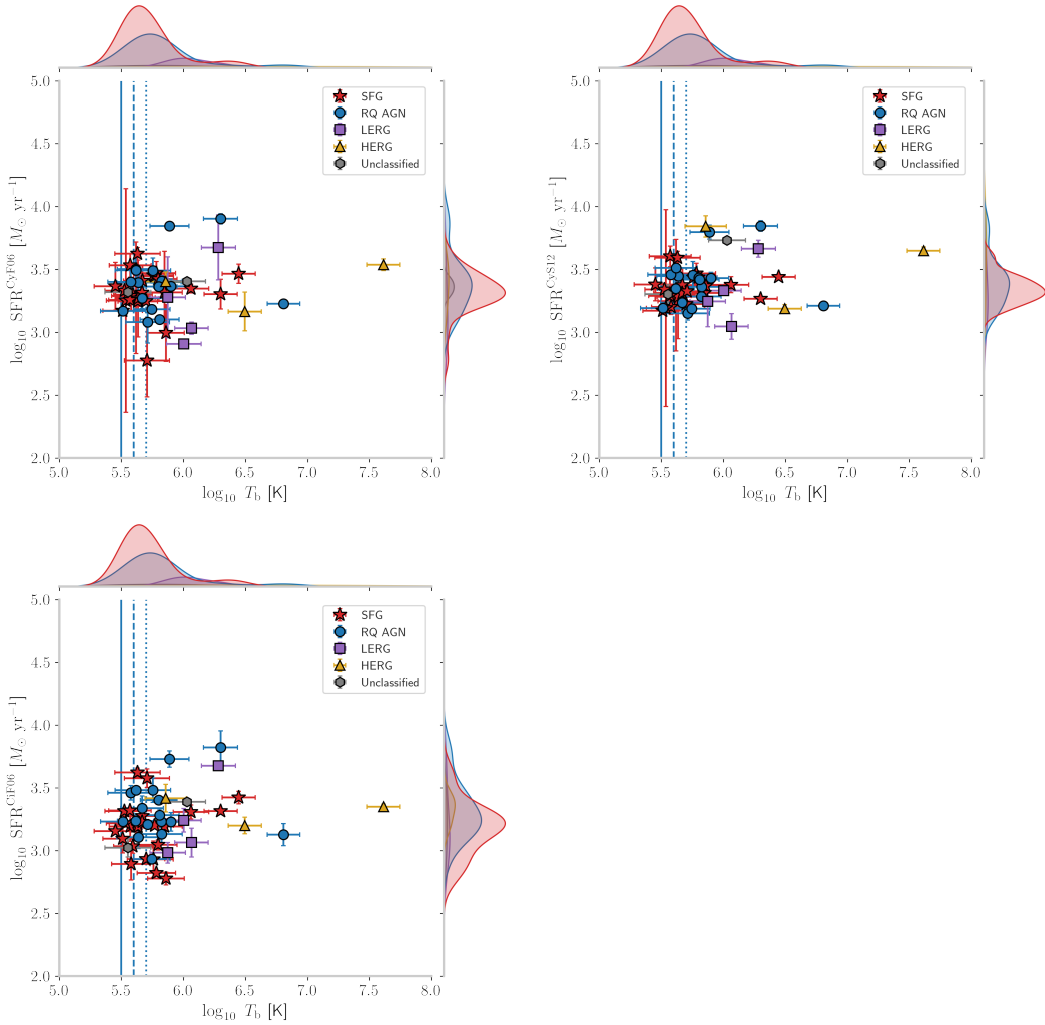


Figure 5.11: Star-formation rate versus brightness temperature for the CyF06, CyS12 and CiF06 models.

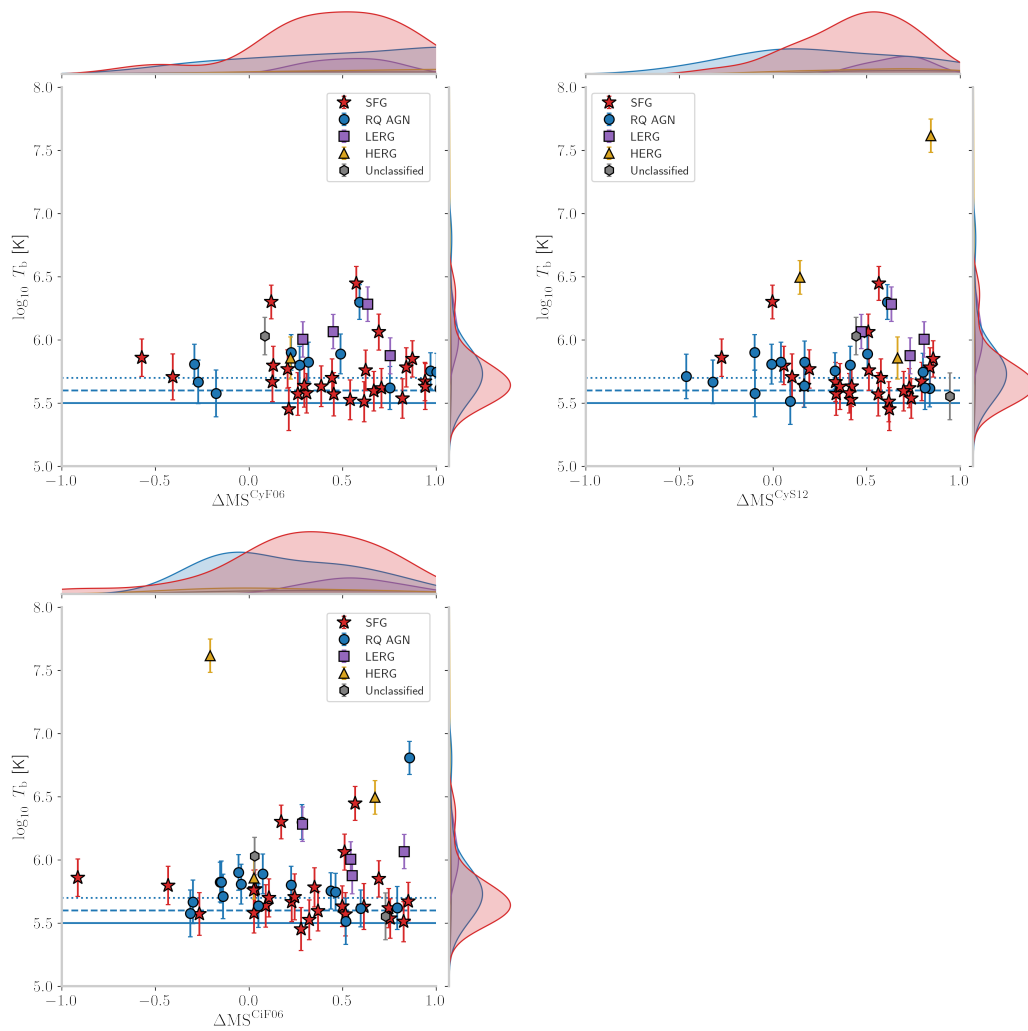


Figure 5.12: Brightness temperature versus distance to the star-forming main sequence for the CyF06, CyS12 and CiF06 models.

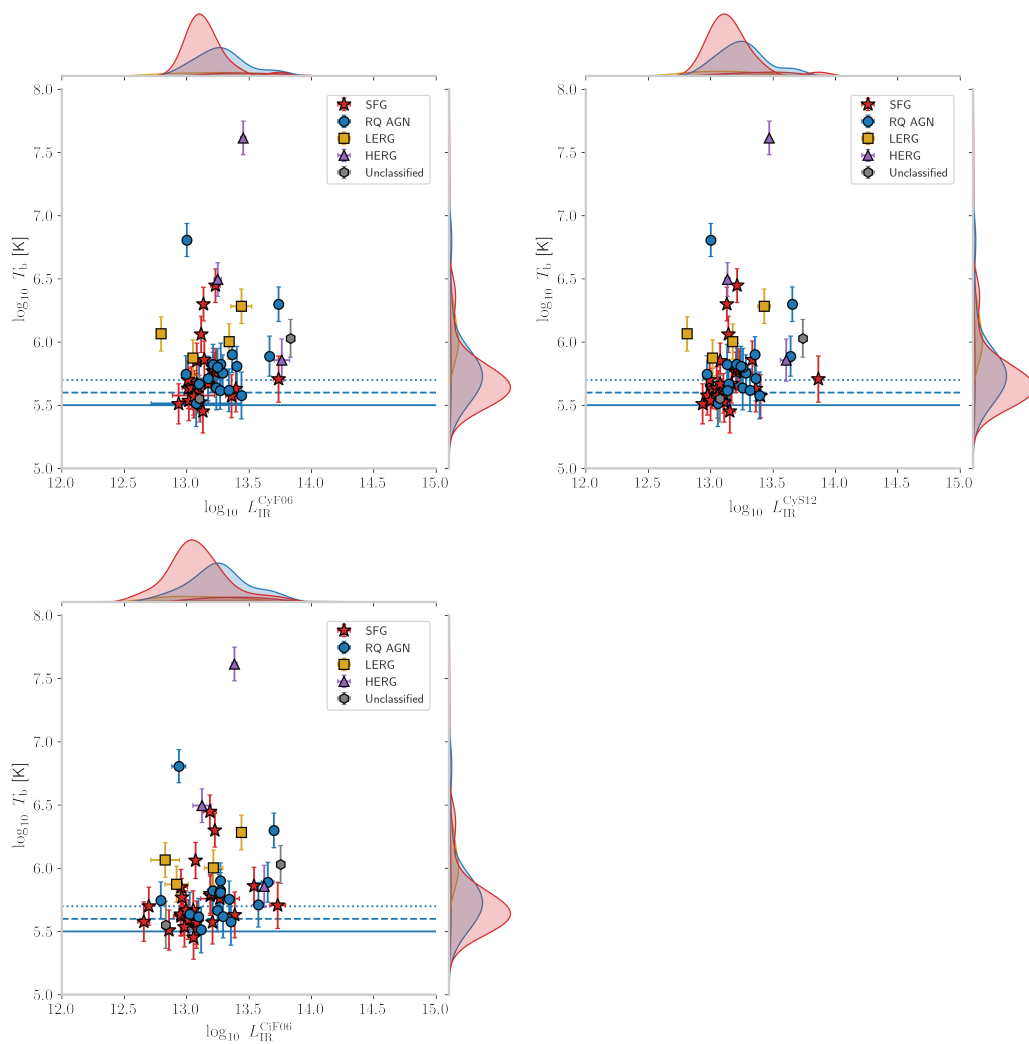


Figure 5.13: Brightness temperature versus infrared luminosity for the CyF06, CyS12 and CiF06 models.

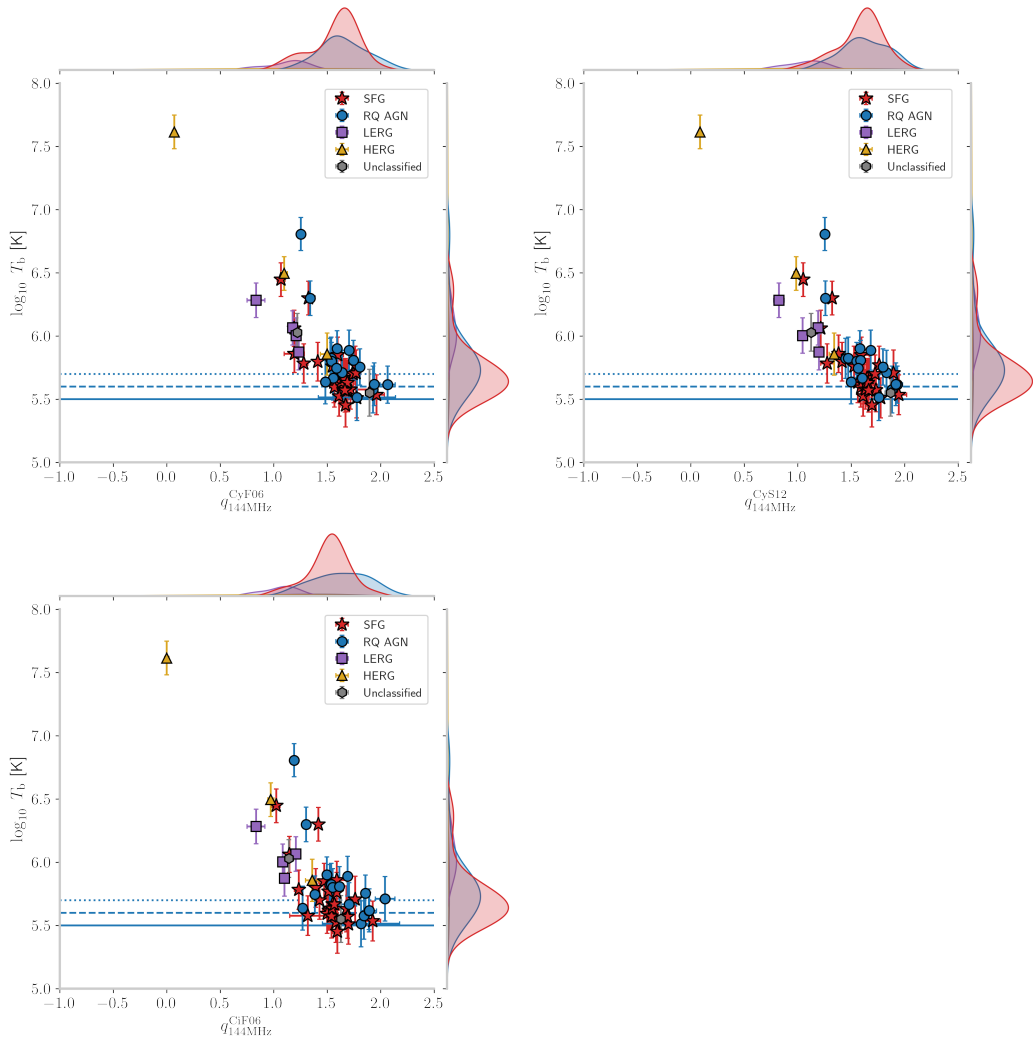


Figure 5.14: Brightness temperature versus radio-excess for the CyF06, CyS12 and CiF06 models.

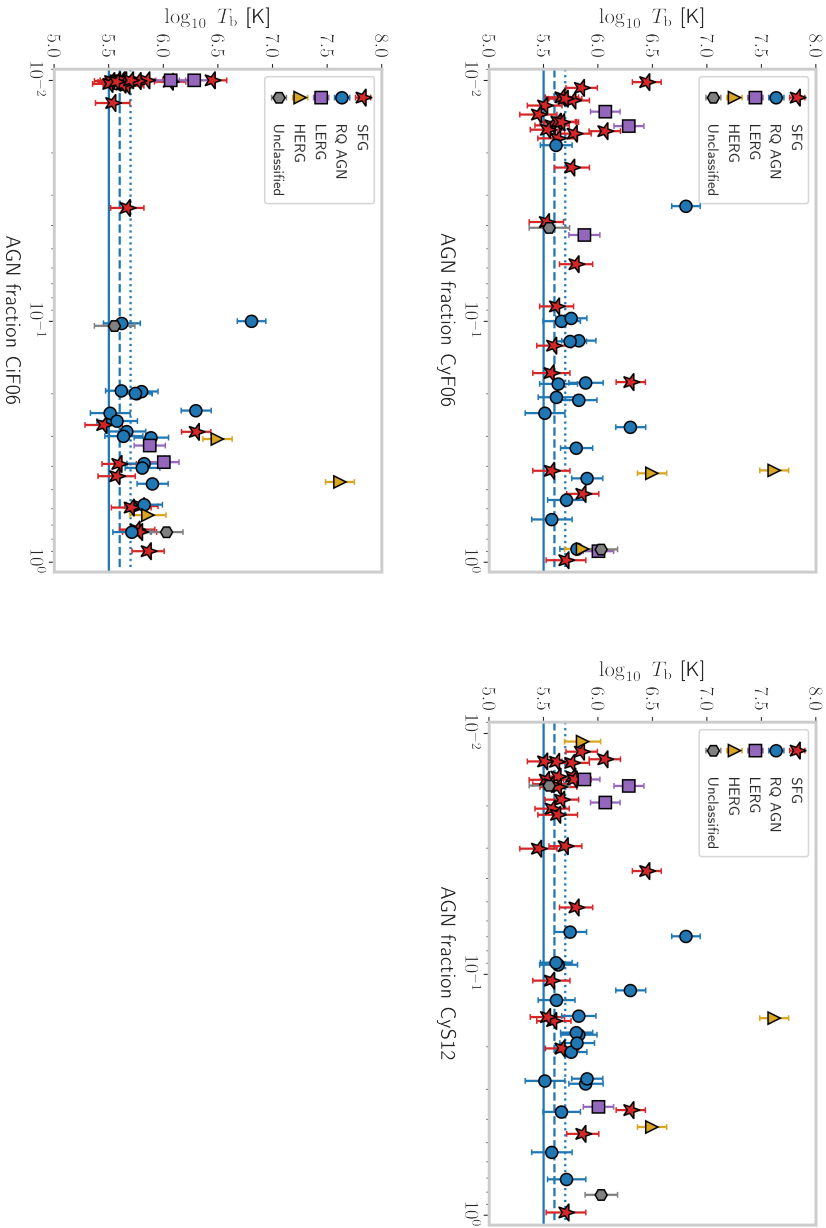


Figure 5.15: Brightness temperature versus AGN fraction for the CyF06, CyS12 and ClF06 models.

Additional plots

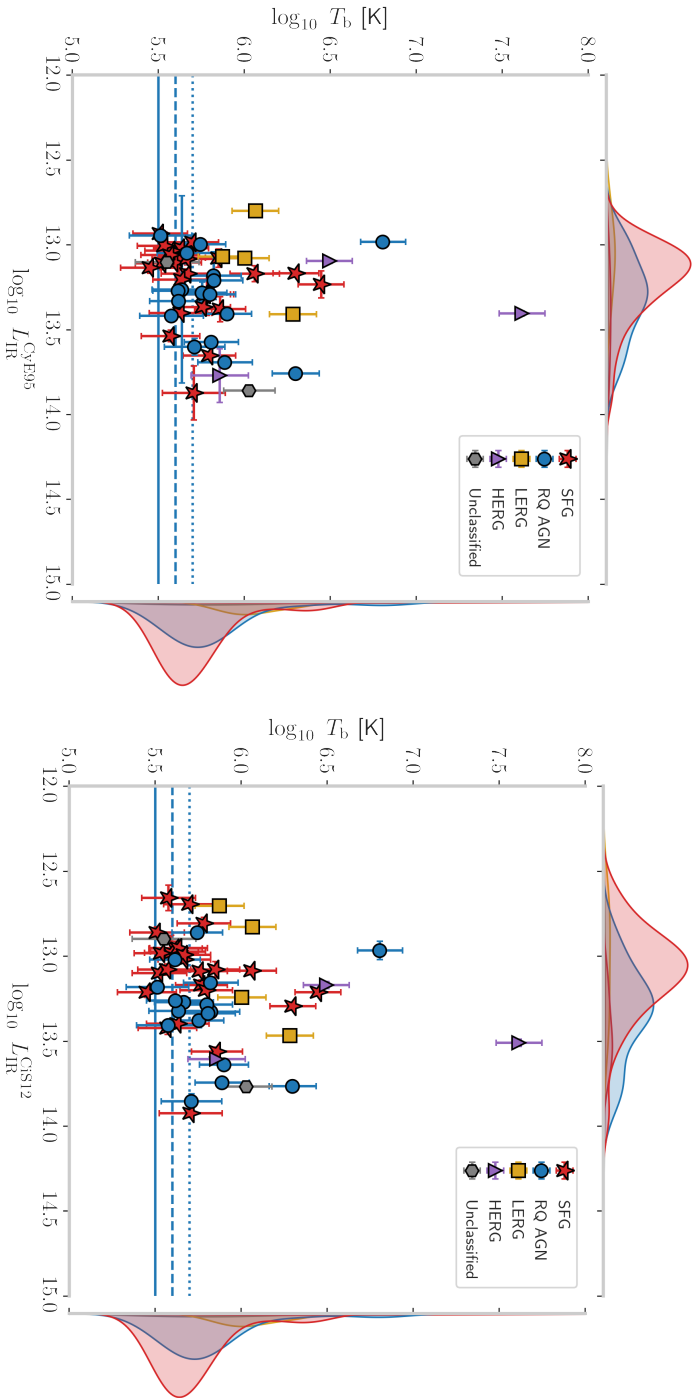


Figure 5.16: Brightness temperature versus infrared luminosity for the CYE95 and GS12 models.

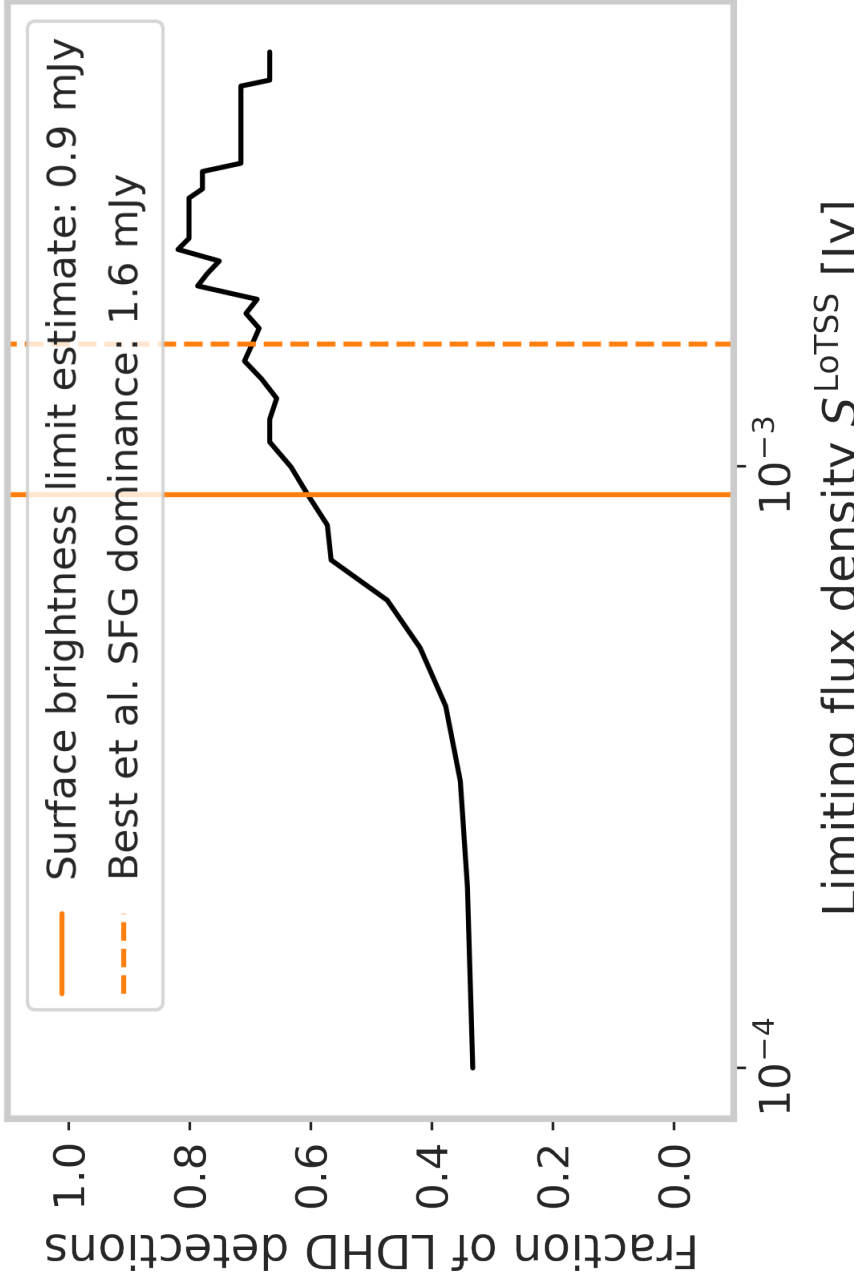
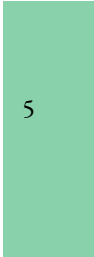


Figure 5.17: Completeness as the fraction of LDHD detections versus LoTSS flux density S_{LoTSS} . The solid line indicates a peak intensity cut while the dashed line indicates a flux density cut. Maximum completeness is 81% at $S_{\text{LoTSS}} > 2.3\text{mJy}$.



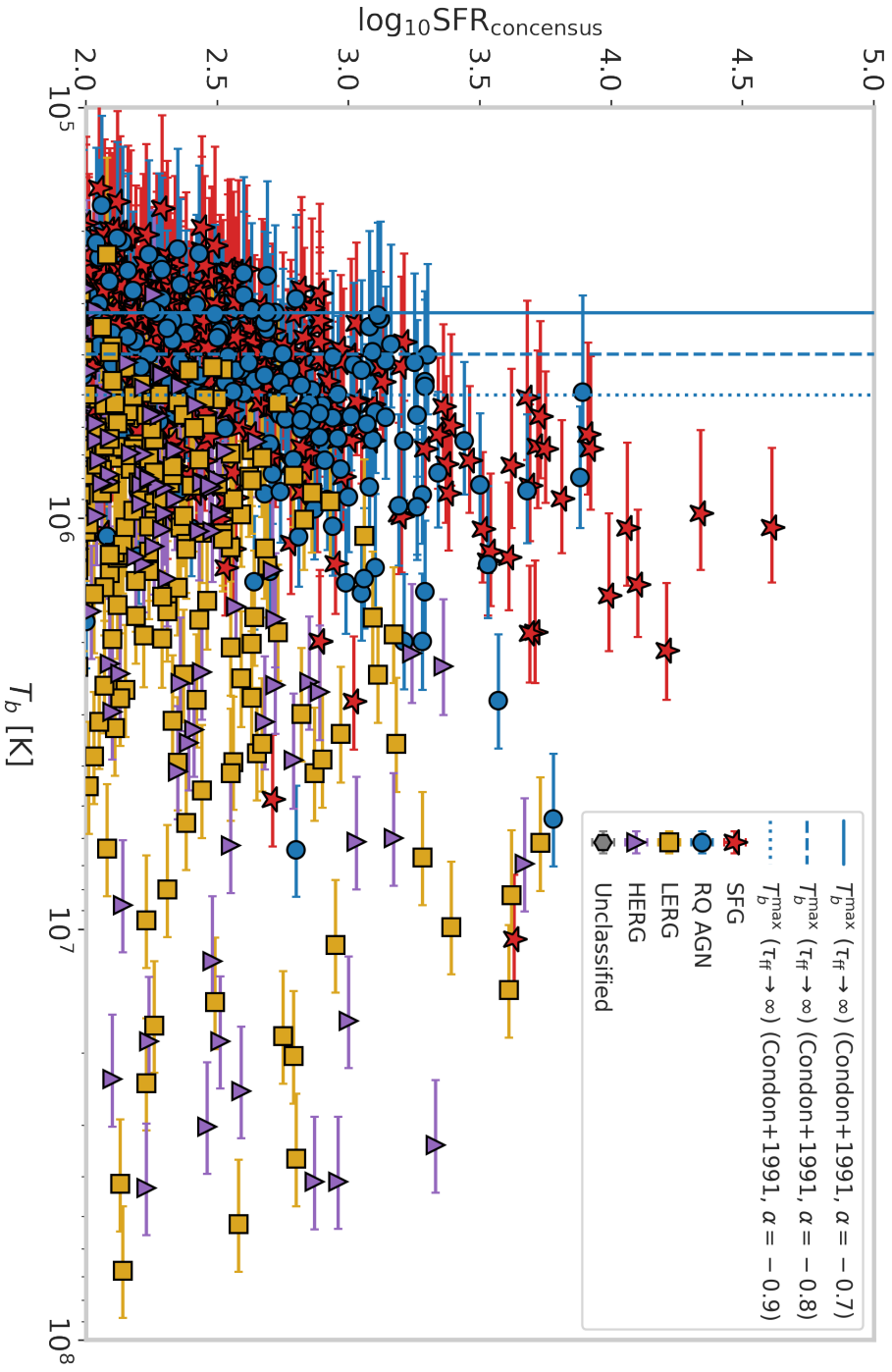


Figure 5.18: Star formation rate versus brightness temperature for the full sample of LDHD sources. Axis ranges are cropped to reflect the same range that our HILIRG sample occupies.

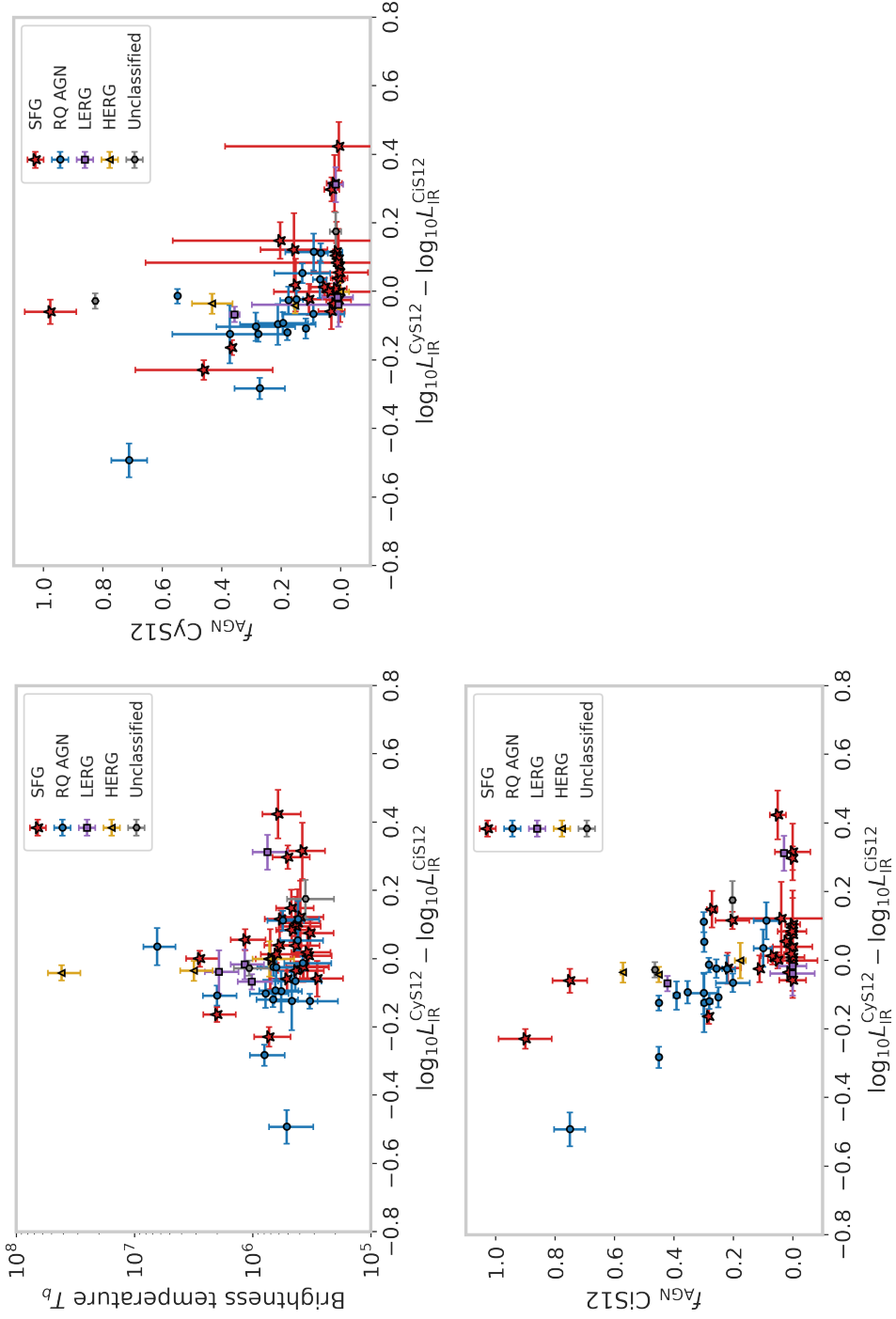


Figure 5.19: Brightness temperature and AGN fractions for the S12 model versus the difference in estimated IR luminosity.

Bibliography

- Ade, P. A. R. et al. (Oct. 2016). “Planck 2015 Results”. In: *Astronomy & Astrophysics* 594, A13. ISSN: 0004-6361. DOI: [10.1051/0004-6361/201525830](https://doi.org/10.1051/0004-6361/201525830). (Visited on 11/07/2018).
- Armus, Lee, Timothy Heckman, and George Miley (Oct. 1987). “Multicolor Optical Imaging of Powerful Far-Infrared Galaxies: More Evidence for a Link Between Galaxy Mergers and Far-Infrared Emission”. In: *AJ* 94, p. 831. DOI: [10.1086/114517](https://doi.org/10.1086/114517).
- Bell, Eric F. (Apr. 2003). “Estimating Star Formation Rates from Infrared and Radio Luminosities: The Origin of the Radio-Infrared Correlation”. In: *ApJ* 586.2, pp. 794–813. DOI: [10.1086/367829](https://doi.org/10.1086/367829). arXiv: [astro-ph/0212121](https://arxiv.org/abs/astro-ph/0212121) [[astro-ph](https://arxiv.org/abs/astro-ph)].
- Best, P N et al. (Aug. 2023). “The LOFAR Two-metre Sky Survey: Deep Fields Data Release 1. V. Survey Description, Source Classifications, and Host Galaxy Properties”. In: *Monthly Notices of the Royal Astronomical Society* 523.2, pp. 1729–1755. ISSN: 0035-8711. DOI: [10.1093/mnras/stad1308](https://doi.org/10.1093/mnras/stad1308). (Visited on 06/07/2023).
- Buat, V. et al. (Dec. 2019). “Cold dust and stellar emissions in dust-rich galaxies observed with ALMA: a challenge for SED-fitting techniques”. In: *A&A* 632, A79, A79. DOI: [10.1051/0004-6361/201936643](https://doi.org/10.1051/0004-6361/201936643).
- Burgarella, D., V. Buat, and J. Iglesias-Páramo (July 2005). “Star formation and dust attenuation properties in galaxies from a statistical ultraviolet-to-far-infrared analysis”. In: *MNRAS* 360.4, pp. 1413–1425. DOI: [10.1111/j.1365-2966.2005.09131.x](https://doi.org/10.1111/j.1365-2966.2005.09131.x). arXiv: [astro-ph/0504434](https://arxiv.org/abs/astro-ph/0504434) [[astro-ph](https://arxiv.org/abs/astro-ph)].
- Calistro Rivera, G. et al. (Aug. 2017b). “The LOFAR window on star-forming galaxies and AGNs - curved radio SEDs and IR-radio correlation at $0 < z < 2.5$ ”. In: *MNRAS* 469.3, pp. 3468–3488. DOI: [10.1093/mnras/stx1040](https://doi.org/10.1093/mnras/stx1040). arXiv: [1704.06268](https://arxiv.org/abs/1704.06268) [[astro-ph](https://arxiv.org/abs/astro-ph).GA].
- Condon, J. J. et al. (Sept. 1991). “Compact Starbursts in Ultraluminous Infrared Galaxies”. In: *ApJ* 378, p. 65. DOI: [10.1086/170407](https://doi.org/10.1086/170407).
- Cutri, Roc M. et al. (Apr. 1994). “IRAS F15307+3252: A Hyperluminous Infrared Galaxy at $Z = 0.93$ ”. In: *ApJ* 424, p. L65. DOI: [10.1086/187276](https://doi.org/10.1086/187276).
- Davé, Romeel et al. (Mar. 2010). “The nature of submillimetre galaxies in cosmological hydrodynamic simulations”. In: *Monthly Notices of the Royal Astronomical Society* 404.3, pp. 1355–1368. ISSN: 00358711. DOI: [10.1111/j.1365-2966.2010.16395.x](https://doi.org/10.1111/j.1365-2966.2010.16395.x). URL: <https://academic.oup.com/mnras/article-lookup/doi/10.1111/j.1365-2966.2010.16395.x>.
- de Jong, T. et al. (June 1985). “Radio continuum and far-infrared emission from spiral galaxies : a close correlation.” In: *A&A* 147, pp. L6–L9.
- Delvecchio, I. et al. (Mar. 2021). “The infrared-radio correlation of star-forming galaxies is strongly M_{\star} -dependent but nearly redshift-invariant since $z \sim 4$ ”. In: *A&A* 647, A123, A123. DOI: [10.1051/0004-6361/202039647](https://doi.org/10.1051/0004-6361/202039647). arXiv: [2010.05510](https://arxiv.org/abs/2010.05510) [[astro-ph](https://arxiv.org/abs/astro-ph).GA].

- Donley, J. L. et al. (Nov. 2005). “Unveiling a Population of AGNs Not Detected in X-Rays”. In: *ApJ* 634.1, pp. 169–182. DOI: 10.1086/491668. arXiv: astro-ph/0507676 [astro-ph].
- Donley, J. L. et al. (Apr. 2012). “Identifying Luminous Active Galactic Nuclei in Deep Surveys: Revised IRAC Selection Criteria”. In: *ApJ* 748.2, 142, p. 142. DOI: 10.1088/0004-637X/748/2/142. arXiv: 1201.3899 [astro-ph.CO].
- Duncan, K. J. et al. (Apr. 2021). “The LOFAR Two-meter Sky Survey: Deep Fields Data Release 1. IV. Photometric redshifts and stellar masses”. In: *A&A* 648, A4, A4. DOI: 10.1051/0004-6361/202038809. arXiv: 2011.08204 [astro-ph.GA].
- Efstathiou, A. and M. Rowan-Robinson (Apr. 1995). “Dusty discs in active galactic nuclei”. In: *MNRAS* 273.3, pp. 649–661. DOI: 10.1093/mnras/273.3.649.
- Farrah, D. et al. (Oct. 2002). “Submillimetre observations of hyperluminous infrared galaxies”. In: *MNRAS* 335.4, pp. 1163–1175. DOI: 10.1046/j.1365-8711.2002.05698.x. arXiv: astro-ph/0205422 [astro-ph].
- Farrah, Duncan et al. (July 27, 2017). “The Role of the Most Luminous Obscured AGNs in Galaxy Assembly at z 2”. In: *The Astrophysical Journal* 844.2. Publisher: IOP Publishing, p. 106. ISSN: 0004-637X. DOI: 10.3847/1538-4357/AA78F2. URL: <https://iopscience.iop.org/article/10.3847/1538-4357/aa78f2> (visited on 11/03/2021).
- Fritz, J., A. Franceschini, and E. Hatziminaoglou (Mar. 2006). “Revisiting the infrared spectra of active galactic nuclei with a new torus emission model”. In: *MNRAS* 366.3, pp. 767–786. DOI: 10.1111/j.1365-2966.2006.09866.x. arXiv: astro-ph/0511428 [astro-ph].
- Gao, F. et al. (July 2021). “The Nature of Hyperluminous Infrared Galaxies”. In: *arXiv e-prints*, arXiv:2107.08703, arXiv:2107.08703. arXiv: 2107.08703 [astro-ph.GA].
- Haarlem, M. P. van et al. (Aug. 2013). “LOFAR: The LOw-Frequency ARray”. In: *Astronomy & Astrophysics* 556, A2. ISSN: 0004-6361, 1432-0746. DOI: 10.1051/0004-6361/201220873. (Visited on 09/20/2023).
- Hardcastle, M. J. et al. (Feb. 2019). “Radio-Loud AGN in the First LoTSS Data Release”. In: *Astronomy & Astrophysics* 622, A12. ISSN: 0004-6361. DOI: 10.1051/0004-6361/201833893. (Visited on 01/24/2020).
- Hayward, Christopher C. et al. (Jan. 2013). “Submillimetre galaxies in a hierarchical universe: number counts, redshift distribution and implications for the IMF”. In: *MNRAS* 428.3, pp. 2529–2547. DOI: 10.1093/mnras/sts222. arXiv: 1209.2413 [astro-ph.CO].
- Heckman, Timothy M. and Philip N. Best (Aug. 2014). “The Coevolution of Galaxies and Supermassive Black Holes: Insights from Surveys of the Contemporary Universe”. In: *Annual Review of Astronomy and Astrophysics* 52, pp. 589–660. ISSN: 00664146. DOI: 10.1146/annurev-astro-081913-035722. arXiv: 1403.4620. (Visited on 10/12/2020).
- Helou, G., B. T. Soifer, and M. Rowan-Robinson (Nov. 1985). “Thermal infrared and nonthermal radio: remarkable correlation in disks of galaxies.” In: *ApJ* 298, pp. L7–L11. DOI: 10.1086/184556.
- Jackson, N. et al. (Feb. 2022). “Sub-arcsecond imaging with the International LOFAR Telescope. II. Completion of the LOFAR Long-Baseline Calibrator Survey”. In: *A&A* 658, A2, A2. DOI: 10.1051/0004-6361/202140756. arXiv: 2108.07284 [astro-ph.GA].
- Jannuzi, B. T. and A. Dey (Jan. 1999). “The NOAO Deep Wide-Field Survey”. In: *Photometric Redshifts and the Detection of High Redshift Galaxies*. Ed. by Ray Weymann et al. Vol. 191. Astronomical Society of the Pacific Conference Series, p. 111.

- Kondapally, R. et al. (Apr. 2021). “The LOFAR Two-meter Sky Survey: Deep Fields Data Release 1. III. Host-galaxy identifications and value added catalogues”. In: *A&A* 648, A3, A3. DOI: 10.1051/0004-6361/202038813. arXiv: 2011.08201 [astro-ph.GA].
- Lockman, F. J., K. Jahoda, and D. McCammon (Mar. 1986). “The Structure of Galactic H i in Directions of Low Total Column Density”. In: *ApJ* 302, p. 432. DOI: 10.1086/164002.
- Lovell, Christopher C. et al. (Mar. 2021). “Reproducing submillimetre galaxy number counts with cosmological hydrodynamic simulations”. In: *MNRAS* 502.1, pp. 772–793. DOI: 10.1093/mnras/staa4043. arXiv: 2006.15156 [astro-ph.GA].
- Morabito, L. K. et al. (Feb. 2022). “Sub-arcsecond imaging with the International LOFAR Telescope. I. Foundational calibration strategy and pipeline”. In: *A&A* 658, A1, A1. DOI: 10.1051/0004-6361/202140649. arXiv: 2108.07283 [astro-ph.IM].
- Morabito, Leah K et al. (Oct. 2022). “Identifying Active Galactic Nuclei via Brightness Temperature with Sub-Arcsecond International LOFAR Telescope Observations”. In: *Monthly Notices of the Royal Astronomical Society* 515.4, pp. 5758–5774. ISSN: 0035-8711. DOI: 10.1093/mnras/stac2129. (Visited on 10/10/2022).
- Narayanan, Desika et al. (Sept. 2015). “The formation of submillimetre-bright galaxies from gas infall over a billion years”. In: *Nature* 525.7570, pp. 496–499. DOI: 10.1038/nature15383. arXiv: 1509.06377 [astro-ph.GA].
- Neugebauer, G. et al. (Mar. 1984). “The Infrared Astronomical Satellite (IRAS) mission.” In: *ApJ* 278, pp. L1–L6. DOI: 10.1086/184209.
- Noll, S. et al. (Dec. 2009). “Analysis of galaxy spectral energy distributions from far-UV to far-IR with CIGALE: studying a SINGS test sample”. In: *A&A* 507.3, pp. 1793–1813. DOI: 10.1051/0004-6361/200912497. arXiv: 0909.5439 [astro-ph.CO].
- Oliver, Seb et al. (2000). “The European Large Area ISO Survey (ELAIS): Latest Results”. In: *ISO Survey of a Dusty Universe*. Ed. by D. Lemke, M. Stickel, and K. Wilke. Vol. 548, p. 28.
- Padovani, Paolo (Sept. 2016). “The faint radio sky: radio astronomy becomes mainstream”. In: *A&A Rev.* 24.1, 13, p. 13. DOI: 10.1007/s00159-016-0098-6. arXiv: 1609.00499 [astro-ph.GA].
- Prandoni, I. et al. (Dec. 2018). “The Lockman Hole Project: new constraints on the sub-mJy source counts from a wide-area 1.4 GHz mosaic”. In: *MNRAS* 481.4, pp. 4548–4565. DOI: 10.1093/mnras/sty2521. arXiv: 1810.03738 [astro-ph.GA].
- Radcliffe, J. F. et al. (May 2021). “The radio emission from active galactic nuclei”. In: *Astronomy & Astrophysics* 649, p. L9. ISSN: 0004-6361. DOI: 10.1051/0004-6361/202140791. URL: https://www.aanda.org/articles/aa/full_html/2021/05/aa40791-21/aa40791-21.html <https://www.aanda.org/articles/aa/abs/2021/05/aa40791-21/aa40791-21.html>.
- Rowan-Robinson, M. (Aug. 2000). “Hyperluminous infrared galaxies”. In: *MNRAS* 316.4, pp. 885–900. DOI: 10.1046/j.1365-8711.2000.03588.x. arXiv: astro-ph/9912286 [astro-ph].
- Rowan-Robinson, M. et al. (Nov. 2018). “Extreme Submillimetre Starburst Galaxies”. In: *Astronomy & Astrophysics* 619, A169. ISSN: 0004-6361. DOI: 10.1051/0004-6361/201832671. (Visited on 10/15/2020).
- Ruiz, A. et al. (Jan. 2013). “Analysis of Spitzer-IRS spectra of hyperluminous infrared galaxies”. In: *A&A* 549, A125, A125. DOI: 10.1051/0004-6361/201015257. arXiv: 1210.3915 [astro-ph.CO].
- Sabater, J. et al. (Apr. 2021). “The LOFAR Two-meter Sky Survey: Deep Fields Data Release 1. II. The ELAIS-N1 LOFAR deep field”. In: *A&A* 648, A2, A2. DOI: 10.1051/0004-6361/202038828. arXiv: 2011.08211 [astro-ph.GA].

- Shimwell, T. W. et al. (Feb. 2017). “The LOFAR Two-metre Sky Survey”. In: *Astronomy & Astrophysics* 598, A104. ISSN: 0004-6361. DOI: [10.1051/0004-6361/201629313](https://doi.org/10.1051/0004-6361/201629313). (Visited on 11/30/2018).
- Shimwell, T. W. et al. (Feb. 2019). “The LOFAR Two-metre Sky Survey - II. First Data Release”. In: *Astronomy & Astrophysics* 622, A1. ISSN: 0004-6361, 1432-0746. DOI: [10.1051/0004-6361/201833559](https://doi.org/10.1051/0004-6361/201833559). (Visited on 02/01/2022).
- Smith, Harding E., Colin J. Lonsdale, and Carol J. Lonsdale (Jan. 1998). “The Starburst-AGN Connection. II. The Nature of Luminous Infrared Galaxies as Revealed by VLBI, VLA, Infrared, and Optical Observations”. In: *ApJ* 492.1, pp. 137–172. DOI: [10.1086/305020](https://doi.org/10.1086/305020).
- Speagle, J. S. et al. (Oct. 2014). “A Highly Consistent Framework for the Evolution of the Star-Forming “Main Sequence” from $z \sim 0-6$ ”. In: *ApJS* 214.2, 15, p. 15. DOI: [10.1088/0067-0049/214/2/15](https://doi.org/10.1088/0067-0049/214/2/15). arXiv: [1405.2041](https://arxiv.org/abs/1405.2041) [[astro-ph.GA](#)].
- Stalevski, Marko et al. (Mar. 2012). “3D radiative transfer modelling of the dusty tori around active galactic nuclei as a clumpy two-phase medium”. In: *MNRAS* 420.4, pp. 2756–2772. DOI: [10.1111/j.1365-2966.2011.19775.x](https://doi.org/10.1111/j.1365-2966.2011.19775.x). arXiv: [1109.1286](https://arxiv.org/abs/1109.1286) [[astro-ph.CO](#)].
- Sweijen, F. et al. (Jan. 2022a). “Deep Sub-Arcsecond Wide-Field Imaging of the Lockman Hole Field at 144 MHz”. In: *Nature Astronomy*, pp. 1–7. ISSN: 2397-3366. DOI: [10.1038/s41550-021-01573-z](https://doi.org/10.1038/s41550-021-01573-z). (Visited on 01/28/2022).
- Symeonidis, M and M J Page (May 2021). “AGN and Star Formation across Cosmic Time”. In: *Monthly Notices of the Royal Astronomical Society* 503.3, pp. 3992–4007. ISSN: 0035-8711. DOI: [10.1093/mnras/stab598](https://doi.org/10.1093/mnras/stab598). (Visited on 02/24/2022).
- (Sept. 2018). “What Powers Hyperluminous Infrared Galaxies at $z \sim 1-2$?” In: *Monthly Notices of the Royal Astronomical Society: Letters* 479.1, pp. L91–L95. ISSN: 1745-3925. DOI: [10.1093/MNRASL/SLY105](https://doi.org/10.1093/MNRASL/SLY105). arXiv: [1806.01336](https://arxiv.org/abs/1806.01336). (Visited on 11/29/2021).
- Tasse, C. et al. (Apr. 2021). “The LOFAR Two-meter Sky Survey: Deep Fields Data Release 1. I. Direction-dependent calibration and imaging”. In: *A&A* 648, A1, A1. DOI: [10.1051/0004-6361/202038804](https://doi.org/10.1051/0004-6361/202038804). arXiv: [2011.08328](https://arxiv.org/abs/2011.08328) [[astro-ph.IM](#)].
- Tsai, Chao-Wei et al. (June 2015). “The Most Luminous Galaxies Discovered by WISE”. In: *ApJ* 805.2, 90, p. 90. DOI: [10.1088/0004-637X/805/2/90](https://doi.org/10.1088/0004-637X/805/2/90). arXiv: [1410.1751](https://arxiv.org/abs/1410.1751) [[astro-ph.GA](#)].
- Wang, L. et al. (Apr. 2021). “The bright end of the infrared luminosity functions and the abundance of hyperluminous infrared galaxies”. In: *A&A* 648, A8, A8. DOI: [10.1051/0004-6361/202038811](https://doi.org/10.1051/0004-6361/202038811). arXiv: [2011.08798](https://arxiv.org/abs/2011.08798) [[astro-ph.GA](#)].

CHAPTER 6

A low-frequency size distribution of radio galaxies in the Lockman hole

Abstract

Supermassive black holes at the hearts of galaxies can launch powerful jets. Such black holes are called active galactic nuclei (AGNs). Depending on this central engine's power, the surrounding interstellar, intergalactic or intracluster medium, and the lifetime of jet activity, these jets can remain confined within or close to the galaxy at kiloparsec scales, or grow to giant radio galaxies on Mpc scales. Measuring the distribution of sizes of radio galaxies can thus help one infer something about their life cycle, jet powers and environment. In this work we aim to measure the angular length distribution of bright radio sources in the Lockman Hole field down to sub-arcsecond scales using the full resolution of the International LOFAR Telescope (ILT). We will then compare our results to those found by using only the Dutch array at a resolution of $6''$. We also touch on possible differences between low-redshift ($z < 0.8$) and higher-redshift ($0.8 \leq z < 2.5$) objects. A combination of methods was used in order to derive source sizes. Compact sources were fitted with a Gaussian intensity profile. Extended sources had sizes estimated by a flood fill algorithm. For sources that were unresolved in the LOFAR Two-metre Sky Survey (LoTSS) and that could not have their size be measured reliably at higher resolutions, a random draw was employed using a surface brightness limit argument and low-resolution deconvolved sizes as lower and upper bounds in order to get an estimate of the true source size distribution. We present a sample of 2,192 sources that have flux densities $S > 600 \mu\text{Jy}$. For the 2,110 with redshift estimates available, we present a power-linear size diagram for sources $0 < z < 2.5$. Using the classification of [PN Best et al., 2023](#) we focus on the 1205 objects not classified as star-forming galaxies. Physical projected lengths in the range $\ell = 0.7 \text{ kpc} - 1 \text{ Mpc}$ are derived. Radio powers span the range $P_{144\text{MHz}} \approx 10^{21} - 5 \times 10^{28} \text{ W Hz}^{-1}$. A qualitative agreement with [Hardcastle et al., 2019](#) is found for sources at redshifts $z < 0.8$. For sources above that, we find they exclusively have radio powers $P_{144\text{MHz}} \geq 10^{24} \text{ W Hz}^{-1}$ and somewhat prefer more compact projected lengths $\ell \lesssim 20 \text{ kpc}$. The ILT's ability to measure sources over a wide range of angular and hence physical lengths makes it a powerful instrument for future large statistical studies of radio galaxy life cycles. We conclude that the apparent preference for objects in the range $0.8 < z < 2.5$ to be more compact could indicate more short-lived bursts of high accretion in the Early Universe compared to times closer to the present day. Finally, we point out the potential benefit of an additional ILT station in the 100 – 200 km distance from the core in an east-west baseline that would fill the last remaining gap in the ILT's uv coverage.

6.1 Introduction

Radio galaxies can span many orders of magnitude in both size and radio luminosity. Their sizes range from compact pc-scale objects (e.g. K. I. Kellermann, 1978; Cotton et al., 2018; Bondi et al., 2018) to Mpc-long giants e.g. Dabhade et al., 2020; Martijn S. S. L. Oei et al., 2022. Compact objects have a range of classifiers associated with them such as peaked spectrum (PS), compact steep spectrum (CSS), compact symmetric object (CSO) and medium symmetric object (MSO). For an in-depth discussion of such objects, we refer the reader to the recent review by Christopher P. O’Dea et al., 2021 and references therein. Here we only focus on the findings that these objects can display double-lobed, jetted or complex disturbed morphologies when studied at higher resolving powers, resulting from possible interaction with a dense interstellar medium, or a dense intracluster medium (tailed radio galaxies). To answer the question about the nature of these objects, whether they are young sources or frustrated jets imprisoned by the dense environment surrounding them, direct probes of their size and morphology are required. The compact nature of the aforementioned sources demands observations with sub-arcsecond angular resolution or higher to resolve their structure (or lack thereof).

The larger end of the scale is occupied by jetted AGNs, whose jets penetrate out to large scales into the extra-galactic medium and form the fiducial double-lobed morphology of radio-loud AGNs. Fanaroff et al., 1974 came up with the now archetypical “FR I” and “FR II” classification based on the intensity distribution of the source. FR I type sources generally have lower luminosities, are brightest close to the galaxy, and become more diffuse further away from the host galaxy (e.g. 3C 31). Conversely, FR II type sources are generally luminous AGNs having most of their brightness in “hotspots” (where the jet terminates in the intergalactic medium) and lobes far(ther) away from the host galaxy (e.g. Cygnus A). Results from deeper, higher resolution surveys question the rigidity of this division, however, with the discovery of a large population of compact objects that cannot be placed in either category (“FR 0s”, Baldi et al., 2015), FR IIs with luminosities below their typical values (Mingo et al., 2019) and sources of hybrid morphology (e.g. Jeremy J Harwood et al., 2020). Figure 2 by Hardcastle et al., 2020 illustrates the various types of radio galaxies and the vast range of sizes and radio powers they exhibit. Surveys that can probe both the faintest and objects of all relevant scales from compact to giants are thus important to gain a complete overview of radio galaxy morphology.

Radio telescopes have an inherently limited angular resolution set by the dish diameter in the case of single-dish telescopes, or the longest baseline for an interferometer. In the early days of radio astronomy, esoteric techniques such as lunar occultations made it possible to measure the positions or angular sizes of compact objects with remarkable accuracy. Hazard et al., 1963 used this technique to determine the size of 3C 273 and Swarup, 1975 derived a relation between the angular size derived from occultations and flux density. Despite this success, they remained cumbersome to use by their nature. It took the construction of large interferometers with widely separated antennas, such as the *Westerbork Synthesis Radio Telescope* (WSRT), the *Very Large Array* (VLA) and *Multi-Element Radio Linked Interferometer Network* (MERLIN) to start pushing towards more routine sample studies and ultimately to move towards analysis in the image domain.

The lack of such advanced instruments did not stop the early radio astronomers from measuring source sizes, however. In the 1950s, Jennison et al., 1953 concluded that Cygnus A had a symmetric double structure and Hanbury Brown et al., 1953a found a number of bright radio sources, some of which had estimated sizes exceeding one degree on the sky (Hanbury Brown et al., 1954). Morris et al., 1957 estimated sizes smaller than a few arcminutes for sources reported by Hanbury Brown et al., 1953a that had no es-

timates. Mills et al., 1960 measured 50 sources and found the smallest ones were less than $15''$ in size. Scaling up, L. R. Allen et al., 1962a studied the size distribution of more than a hundred sources, from which they concluded that a large fraction of sources had two components that had estimated projected angular sizes ranging from $10''$ to $600''$. Bash, 1968 used the a two-element interferometer at the *National Radio Astronomy Observatory* (NRAO) to conduct another large sample study of 234 sources. The interferometer’s angular resolution went down to $2''$ at a frequency of 2695 MHz. Such larger samples allowed for statistical studies of the radio source population, such as done by e.g. G. K. Miley, 1971.

Studies into the structure of radio sources could be expanded into the image domain with the advent of multi-element interferometers and Earth-rotation aperture synthesis e.g. Fomalont, 1973. Exploiting images ($\theta_{\text{syn}} \sim 22''$) from the third 1415 MHz WSRT survey, Katgert, 1976 inferred that approximately half the population of radio sources brighter than 10 mJy were smaller than $10''$. Later, A. J. B. Downes et al., 1981 and A. Downes, 1982 used high-resolution VLA observations to measure angular sizes of sources in the 5C 6, 7 (Pearson et al., 1978) and 12 (Benn et al., 1982) surveys, down to similarly faint levels of 55 mJy at 408 MHz and 20 mJy at 1407 MHz. Expanded on by Fielden et al., 1983, median source sizes of $10.5''$ and $7.5''$ were found in the ranges $0.055 \text{ Jy} < s_{408\text{MHz}} < 0.1 \text{ Jy}$ and $0.1 \text{ Jy} < s_{408\text{MHz}} < 1 \text{ Jy}$, respectively. R. A. Windhorst et al., 1984 augmented the results of Katgert, 1976 using the *Leiden Berkeley Deep Survey*, a deep WSRT survey with longer baselines up to 2.7 km. An angular resolution of $\theta_{\text{syn}} \sim 12.5''$ was achieved and a median angular size of $10''$ was found for sources with flux densities of $0.001 \text{ Jy} < s_{1412\text{MHz}} < 0.2 \text{ Jy}$, consistent with earlier studies.

Knowing the angular size distribution of radio sources benefits our understanding of the Universe in multiple ways. In more abstract ways, the size distribution and related relationships, such as between angular size and flux density or redshift, allow one to derive constraints on cosmological models and investigate whether there is intrinsic evolution within the population aside from cosmological effects (e.g. K. I. Kellermann, 1972; Swarup, 1975; Kapahi, 1975; Kapahi et al., 1987; M. J. A. Oort, 1988). In more direct ways, the size distribution can serve as a proxy for their age (Longair et al., 1979), lifetime distribution and kinetic jet power (Hardcastle et al., 2019) or help study their environment (Croston et al., 2019). This in turn provides input for the theoretical modeling of the evolution of the jets and lobes created by AGNs. Modelling this evolution is a complicated task and as such has long been an active field of study setting up the theoretical frameworks (Longair et al., 1973; Blandford et al., 1974; Scheuer, 1974) and, once computational power increased, simulating their evolution numerically (Turner et al., 2018). Other simulations broaden the scope and aim to provide a realistic mock representation of the radio sky, such as the *SKA Design Study Simulated Skies* (S^3 , Wilman et al. (2008)) or *Tiered Radio Extragalactic Continuum Simulation* (T-RECS, Bonaldi et al., 2019). Finally, size measurements can be used to test predictions based on more theoretical grounds, such as presented by Saxena et al., 2017, and help test the unification theory (e.g. DiPompeo et al., 2013).

With larger samples of resolved radio sources, it became possible to start thinking about their evolution. A key diagram in studying this evolution is the so-called “power-linear size” diagram that compares radio power against physical size Baldwin, 1982. It allows one to infer something about where a source is within its life cycle when combined with predictions from models. The modelling of different scenarios of activity from the central black hole, such as a continuous jet versus a single short-lived outburst will produce different theoretical tracks across this diagram. In order to test such models it is important to directly measure the size of radio sources to populate this diagram.

High angular resolution observations play an important role here. Some early studies based on data taken with an angular resolution of the order of $10''$ or more found that the distribution appeared to approach a constant value roughly between $5''$ and $10''$ (Swarup, 1975). Higher-resolution observations,

however, showed a different trend. (M. J. A. Oort, 1988) found a decreasing trend of angular size down to $s_{1.4\text{GHz}} = 1$ mJy. The data of M. J. A. Oort, 1988 suggested that the median angular size will drop below $1''$ for $s_{1412\text{MHz}} < 1$ mJy ($s_{144\text{MHz}} \lesssim 6$ mJy). A drop in size with decreasing flux density is not unexpected, as the dominant population starts to switch towards SFGs and rq AGNs, which tend to have more compact radio emission compared to RL AGNs. Prominent recent radio surveys such as the *Low Frequency ARray* (LOFAR, Haarlem et al. 2013) *Two-metre Sky Survey* (LoTSS, Shimwell et al. 2017; Shimwell et al. 2019; Shimwell et al. 2022), a deep ($\sim 70 \mu\text{Jy beam}^{-1}$) 144 MHz survey of the northern hemisphere, map the radio sky at unprecedented combinations of sensitivity, area and resolution, but even at its angular resolution of $6''$ over 80% of sources detected in LoTSS remain (close to) unresolved. The new *Very Large Array Sky Survey* (VLASS, Lacy et al. (2020)) at 3 GHz pushes the angular resolution envelope by mapping the northern skies at an angular resolution of $2.5''$ (Gordon et al., 2021). This allows the true size distribution to be approximated more precisely through deconvolved sizes compared to the twice lower resolution of LoTSS, for example. Images at sub-arcsecond angular resolution can push the envelope of deconvolved sizes to less than a few tenths of an arcsecond for sources that remain unresolved at even the arcsecond level.

These projects highlight how observations across a wide range of resolutions and radio powers are needed to properly infer the overall size distribution of radio sources. All-sky surveys are needed to sample the largest or brightest sources that are intrinsically rare. Deeper surveys sample the fainter end of the population. Interferometers with dense short spacings are required to provide the low angular resolution (of the order of tens of arcseconds to an arcminute) and sensitivity to extended structure required to measure the large diffuse sources. Ignoring exotic diffuse structures, these will consist of large and giant radio galaxies. Intermediate resolutions in the arcsecond range extend this to more common smaller radio galaxies and objects like QSOs. Finally, observations with sub-arcsecond angular resolution are needed to observationally verify the compactness of the (nearly) unresolved sources. Various techniques have been employed to recover information about source structure on scales below that of the restoring beam, such as Gaussian fitting with deconvolution and fitting visibility amplitudes or phases as a function of baseline length, but they come with their own caveats. Accurate deconvolution requires accurate knowledge of the effective point spread function (psf)¹. Furthermore, depending on the signal-to-noise ratio of the detection such fitting will become increasingly uncertain. An ideal angular resolution is thus one that resolves the sources of interest, such that ambiguities from calibration or psf effects are removed, but not so much that sensitivity to diffuse emission is reduced too much. Practically this often translates to a desired resolution about an order of magnitude lower than the scale of interest.

In this work, we study the size distribution of low-frequency radio sources in the sub-arcsecond to arcminute range. Section 2 outlines the data used and the sample selected from it. Section 3 describes the methods that were employed to measure the sizes of sources. The results of that are presented in Section 4. Section 5 penultimately discusses the results in a broader context. Finally, Section 6 summarises the conclusions of this work.

We define the synchrotron spectral index α through $S \propto \nu^\alpha$. A Λ CDM cosmology with $H_0 = 70 \text{ km s}^{-1} \text{ Mpc}^{-1}$, $\Omega_m = 0.3$ and $\Omega_\Lambda = 0.7$ is assumed. Quantities indicated with a subscript ν refer to “spectral” or “specific” quantities. For brevity we omit these in the text, e.g. “specific intensity” is referred to as simply “intensity”.

¹Imperfect calibration and time or bandwidth smearing, for example, will degrade the actual psf away from its theoretical shape.

6.2 Data

With the *International LOFAR Telescope* surveys at sub-arcsecond resolution are now becoming possible. The ILT's wide range of baselines between $\sim 10^2$ and $\sim 10^6$ m make it sensitive to a wide range of spatial scales. A single eight-hour synthesis observation (as is typical) can now routinely provide high-quality images at angular resolutions of $6''$, $20''$ and $60''$ (e.g. LoTSS). Recent advances in calibration and imaging techniques have enabled high-quality images down to angular resolutions of arcsecond (Ye et al. *subm.*, de Jong et al. *in prep.*) and sub-arcsecond level (e.g. L. Morabito et al., 2021; Sweijen et al., 2022a). This allows the projected linear sizes of the low-frequency radio population some tens of kpc less in size (depending on their redshift) to be measured directly and stronger upper limits to be placed on sources that remain compact.

One advantage of the ILT over previous studies at higher frequencies is its sensitivity to larger or more diffuse sources due to the dense network of short baselines. For example, VLASS uses the VLA's B configuration, which has a largest angular scale (LAS) of $58''$ at 3 GHz (S-band)² whereas LoTSS DR2 with an inner uv -cut of 100 m (Shimwell et al., 2022) has a LAS of 1.2° .

6.2.1 Radio data

We use ILT data of the Lockman Hole (Lockman et al., 1986) region taken at 144 MHz, centred at $\alpha_{j2000} = 10^{\text{h}}47^{\text{m}}00^{\text{s}}$, $\delta_{j2000} = 58^\circ05'00''$. Three images at angular resolutions of $6''$, $1.8''$ and $0.45''$ were used, which we will refer to as the standard, intermediate and high-resolution images respectively. An initial sample was constructed from high signal-to-noise ratio (SNR) sources, using a flux density cut of $s_{\text{lots}} > 600 \mu\text{Jy}$. This yielded a sample of 2214 sources.

Standard resolution imaging The standard resolution image used is a deep image from the LoTSS Deep Fields DR1. It was generated from 80 hours of data, with a central rms noise of $\sigma_{\text{rms}}^{\text{LoTSS}} \approx 23 \mu\text{Jy beam}^{-1}$ (Kondapally et al., 2021; Tasse et al., 2021).

Intermediate resolution imaging Using the calibration solutions from Sweijen et al., 2022a, we imaged the field at a lower resolution by applying a $1.2''$ taper to the data. The calibration solutions were applied through WSClean's facet functionality. A flux density scaling factor was derived in the same way as described in Sweijen et al., 2022a, by doing source detection with PyBDSF (Mohan et al., 2015a) and comparing the flux density of high-snr sources to the standard resolution image. This yielded an image at an angular resolution of $1.8'' \times 0.8''$ and a central rms noise of $130 \mu\text{Jy beam}^{-1}$.

High resolution imaging The high-resolution image came from a single 8-hour observation (LT10_012, L659948; PI: Best) as presented by Sweijen et al., 2022a. We use a mosaic that has been convolved to a common restoring beam of $0.45'' \times 0.4''$. The rms noise in a small region near the centre is $\sigma_{\text{rms}}^{\text{ILT}} \approx 25 \mu\text{Jy beam}^{-1}$.

²<https://science.nrao.edu/facilities/vla/docs/manuals/oss/performance/resolution>

Table 6.1: Summary of image properties

Image resolution	Restoring beam	Central rms [μ Jy beam $^{-1}$]	Beam area [arcsec 2]	$I_{\text{lim}}^{5\sigma}$ [μ Jy arcsec $^{-2}$]
Standard resolution	$6'' \times 6''@0^\circ$	23	40.79	2.8
Intermediate resolution	$1.8'' \times 0.84''@94^\circ$	50	1.71	146
High resolution	$0.45'' \times 0.40''@0^\circ$	25	0.20	625

Table 6.2: Source classification for the full $S > 600 \mu\text{Jy}$ sample

Classification	No. sources	Fraction	No. redshifts available
SFG	905	41%	905
HERG	165	8%	165
LERG	840	38%	840
RQAGN	160	7%	160
Uncertain	122	6%	40
Total	2192	100%	2110

6.2.2 Sample selection

For this study, a flux density limited sample was constructed in order to ensure good completeness. [Shimwell et al., 2019](#) estimate a 95% completeness of LoTSS for point sources with $S_{144\text{MHz}} > 450 \mu\text{Jy}$ and that the real completeness limit is likely ~ 1.3 times higher. We therefore adopt a slightly more conservative flux density cut of $S_{144\text{MHz}} > 600 \mu\text{Jy}$. This provides a sample of 2192 sources over the area where high-resolution imaging is available. Figure 6.1 shows the fraction of sources that have a peak intensity in LoTSS exceeding three times the local rms noise in the intermediate and high-resolution images, respectively. The noise values were obtained from rms images created by PyBDSF. It can be seen that the intermediate-resolution image has a lower completeness.

To construct an AGN-only sample for comparison with the work of [Hardcastle et al., 2019](#), two additional cuts were made:

- A source classification cut, to eliminate non-AGNs.
- A redshift cut to improve the reliability of the classifications.

For removal of the SFGs, we use the classification by [P N Best et al., 2023](#) who classified sources as star-forming galaxies (SFGs), high and low excitation radio galaxies (HERGs and LERGs) and radio-quiet AGNs (RQAGNs) where possible. The sample's classification is summarised in Tab. 6.2.

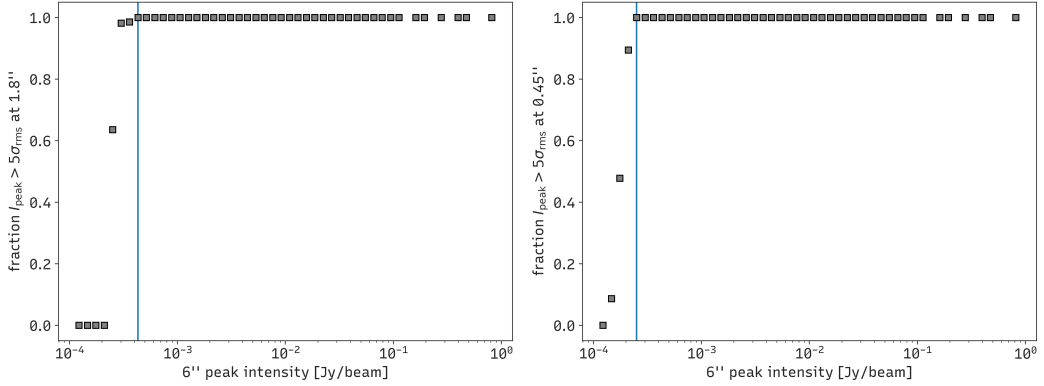


Figure 6.1: Theoretical detectability of LoTSS sources assuming they are genuine point sources. Fraction of sources with a peak intensity exceeding the local $5\sigma_{\text{rms}}$ level in the intermediate resolution (*top*) and high resolution (*bottom*) images. The square points indicate the fraction for each bin. The blue line indicates the last bin for which the fraction still exceeds 99%.

6.3 Methods

Radio luminosities were derived in the usual way through

$$L_{144\text{MHz}} = 4\pi \left(\frac{D_L}{\text{m}} \right)^2 \frac{S_{144\text{MHz}}}{10^{-26} \text{ W m}^{-2} \text{ Hz}^{-1} \text{ Jy}^{-1}} (1+z)^{-(1+\alpha)} \quad (6.1)$$

where D_L is the luminosity distance in metres, $S_{144\text{MHz}}$ is the flux density in Jansky at 144 MHz, z is the redshift and α is the synchrotron spectral index. Redshifts were taken from the Deep Fields DR1 catalogue, while for the synchrotron spectral index a fixed fiducial value of $\alpha = -0.8$ was assumed (Condon, 1992).

Three methods of measuring source sizes were explored: a flood-fill approach, curves of growth and Gaussian fitting. All methods were run on the full sample of sources. Later on, with the help of visual inspection, a final selection of the appropriate measurement was made. More details on each of the size measurement methods used are included in the following subsections. Curves of growth were not used in the final analysis. Each source therefore has either a flood-fill-based size estimate or one based on Gaussian fitting.

6.3.1 Flood-fill size estimates

Flood-fill sizes were estimated based on a flood-fill algorithm, derived from the one used by Mingo et al., 2019. First, a noise threshold was calculated through $\max(5\sigma_{\text{rms}}, I_{\text{peak}}/50)$, where σ_{rms} is the root-mean-square noise below which emission is ignored. After this, the major and minor axes from LoTSS were used to define an elliptical region outside of which source emission is ignored as well to exclude potential emission not associated with the source of interest. This mask provides the starting point for the flood fill. Based on the noise threshold the image is “flooded”, which provides a set of pixels containing source emission. An angular size is then estimated as the maximum (Euclidean) distance between any of the included pixels.

Flux densities were calculated from the non-masked pixels following

$$S = \sum_{x,y} I_{x,y}/A_{\text{beam}} \quad (6.2)$$

where S is the flux density, $I_{x,y}$ is the intensity measured of the pixel at the location (x, y) in the image and A_{beam} is the restoring beam area calculated as

$$\Omega_{\text{beam}} = \frac{2\pi\theta_{\text{maj}}\theta_{\text{min}}}{8 \ln 2} \quad (6.3)$$

where θ_{maj} and θ_{min} are the major and minor axes of the restoring beam in radians.

Size measurements for smaller sources for which the image pixel scale approaches a notable fraction of the linear size will suffer from discretisation. For example, the $1.5''$ pixels of the LoTSS image put an inherent uncertainty of at least $1.5''$ on the size estimate. This technique is therefore most suited for (resolved) sources that are reasonably extended with respect to the pixel size.

6.3.2 Curve-of-growth estimate

With the curve-of-growth method, a flux-density profile is computed by measuring the enclosed flux density in increasingly larger circular apertures. These apertures grow in multiples of the pixel size. By interpolating the resulting curves, the uncertainty limit imposed by the pixel size can be somewhat overcome, allowing a more precise size to be estimated in theory. A source's size is set to the diameter out to which a certain fraction of a reference flux density is recovered. Such a size is similar to the concept of the half-light radius. It has the potential to allow for the recovery of fainter emission that would normally escape a noise threshold, under the assumption that the reference flux density is close to the true total flux density. Given the high flux density cut of our sample (approximately $\text{SNR} > 30$ in the LoTSS Deep Field catalogue), we consider it safe to assume that the $6''$ flux density is close to the true flux density and thus use that as a reference point.

Curves of growth were found to be sensitive to artifacts, however, and rather sensitive to image fidelity. Radio astronomical images are rarely perfect and artifact-free. The background noise therefore does not always exhibit uniform behaviour. Additionally, faint diffuse emission close to the noise threshold may not be properly deconvolved. These effects affect both the stability of the curve of growth and the interpretation of what is measured, as the image intensities are expressed in units of the clean restoring beam while undeconvolved emission has units of the psf. This makes the curve of growth measurements most suited for high-SNR sources, sources that are relatively symmetric in terms of their intensity distribution and artifact-free sources.

6.3.3 Gaussian fitting estimate

With the Gaussian fitting approach, one or more Gaussian profiles were fitted to the emission. For the LoTSS image fitting was done with PyBDSF. One or more Gaussians were fitted to islands of emission identified based on local rms noise thresholds. The resulting size measurement is the FWHM of the Gaussian in the case of a single-component source. In the case where multiple Gaussians were fitted to a source, the reported axes are derived from moment analyses. Moments will be naturally “biased”³ towards bright

³It is not a true bias, in the sense that the moment is by definition an intensity-weighted proxy.

compact emission, hence the choice of employing a flood fill algorithm for larger extended sources. For the intermediate and high-resolution images, CASA's `imfit` was used instead of PyBDSF. Cutouts were made around every source and subsequently `imfit` fitted a single Gaussian to the intensity distribution. This approach is most suited for sources that are relatively compact and thus reasonably approximated by a Gaussian distribution. To be more consistent with the flood-fill algorithm, sizes from Gaussian fitting are reported as $2 \times \theta_{\text{FWHM}}$, or approximately 5σ , containing most of the emission.

6.3.4 Visual inspection and cross-check

Visual inspection was conducted by overlaying size estimates from the different fits and checking if they agreed well visually. For the intermediate-resolution image the Gaussian fits were often rejected due to an overestimate caused by side lobes of the psf. Figure 6.10 compares the deconvolved major axes of Gaussian fits with each other.

6.3.5 Down-scattering sources without reliable higher resolution fits

Sources that are in the $6''$ sample, but could not (reliably) be detected or measured at higher resolutions are re-distributed over the bins using a resampling that we will refer to as “down scattering”. This way we statistically incorporate the information that these failed fits provide. One bound of this down scattering process is set by surface brightness limits in the intermediate-resolution image. The limiting surface brightness was estimated as follows. First, the surface area of the restoring beam is calculated as the area under a two-dimensional Gaussian:

$$\Omega_{\text{beam}} = \frac{2\pi\theta_{\text{maj}}\theta_{\text{min}}}{8 \ln 2} \quad (6.4)$$

Taking the central rms noise level σ_{rms} as a proxy for the limiting surface brightness, we estimate the $5\sigma_{\text{rms}}$ limit as

$$I_{\text{lim}}^{5\sigma} [\text{Jy arcsec}^{-2}] = \left(\frac{5\sigma_{\text{rms}}}{\text{Jy beam}^{-1}} \right) \left(\frac{\Omega_{\text{beam}}}{\text{arcsec}^2 \text{ beam}^{-1}} \right)^{-1}. \quad (6.5)$$

This yields an estimated upper limit on the size for a detection of

$$\theta_{\text{max}}^{\text{SB}} \leq \sqrt{\frac{8 \ln 2}{2\pi} \frac{S_{\text{LoTSS}}}{I_{\text{lim}}^{5\sigma}}} \quad (6.6)$$

where S_{LoTSS} is the LoTSS flux density having units of Jy, I_{lim} has units of Jy arcsec^{-2} and θ_{max} has units of arcsec (see Appendix 6.7 for a brief derivation). Conversely, for non-detections that would be bright enough to be detected based on their LoTSS intensity, this presents a *lower* limit.

As deconvolved size estimates can go to zero, they are taken as the lower bound for the random draws. The upper bound is set by $\theta_{\text{draw}}^{\text{SB}}$, with the added constraint that $\theta_{\text{draw}}^{\text{SB}} < \theta_{\text{LoTSS}}^{\text{DC}}$. This constraint is chosen because the down scattering focuses on sources for which no reliable fit was identified visually. Large sources would have been assigned a different measure otherwise.

The new size was drawn from a log-uniform distribution between these limits, resulting in a random size of $\theta_{\text{LoTSS}}^{\text{DC}} + 3\sigma_{\text{maj}} \leq \ln \theta_{\text{draw}} \leq \theta_{\text{max}}^{\text{SB}}$, where $\theta_{\text{LoTSS}}^{\text{DC}}$ is the estimated deconvolved major axis from LoTSS and σ_{maj} indicates the uncertainty in the fit. These random draws were repeated 1000 times to determine the scatter in the random draws. For the results presented in the following section, an arbitrary realisation was chosen.

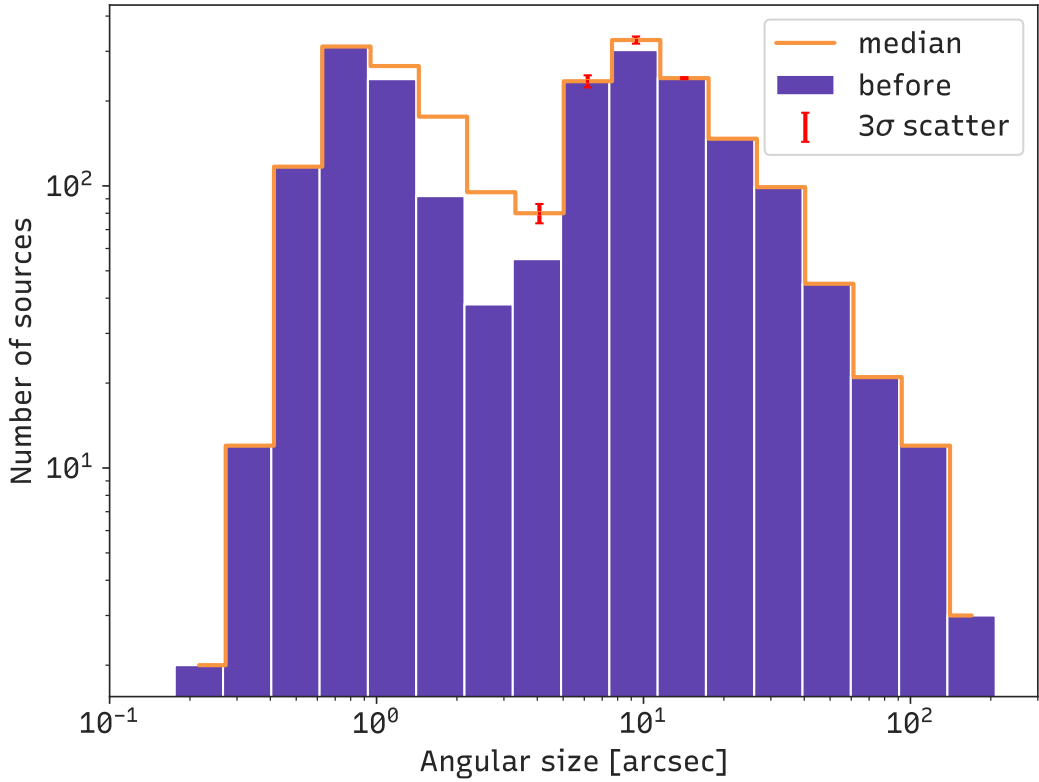


Figure 6.2: *Top*: Distribution of measured angular sizes for the full $S_{\text{LoTSS}} > 600 \mu\text{Jy}$ sample. The histogram indicates the initial measurements. The orange stepped line indicates the median distribution after drawing 1000 random realisations from the resampling process, with the scatter resulting from random draws being indicated in red. For visual clarity, this is *three* times the standard deviation.

6.4 Results

6.4.1 Angular size distribution and flux density versus angular size

Figure 6.2 shows the sample’s overall angular size distribution. The histogram shows the original distribution, while the overplotted line shows the distribution after the resampling process described in the previous section. The error bars indicate the scatter in each bin from drawing 1000 random realisations. The resampling process helps interpolate the distribution over the observed gap, which is discussed more in the Discussion section.

The figure makes it appear as if formally well-resolved sources are scattered down from $\sim 10''$ to smaller sizes. We, therefore, reiterate that for the Gaussian fitted sources and those that are scattered down the size is reported as *twice* the FWHM.

Figure 6.3’s left column shows the sample’s flux density S versus angular length ψ . On each opposing

side, the marginal distributions are shown. The top two histograms in Fig. 6.5 show the flux density and angular size distributions in more detail. In $S - \psi$ space sources conglomerate at the fainter flux density levels of order millijansky. In terms of angular size, a wide range is observed, ranging from $\sim 0.5'' - 200''$.

Figure 6.6 presents the median source size measured versus flux density. It is compared against the results from R. A. Windhorst et al., 1984; R. Windhorst et al., 1990, the *Tiered Radio Extragalactic Continuum Simulation* (T-RECS) and results from VLASS Quick Look data.

6.4.2 Radio power vs linear size

Figure 6.3's right column shows the sample's radio power P versus projected proper length ℓ . Since not all sources had a redshift estimate available, the sample size shrank by 82 sources from 2192 to 2110. In $P - \ell$ space the 2110 sources with redshift estimates spread out over a range of radio powers between $P_{144\text{MHz}} \sim 10^{21} \text{ W Hz}^{-1}$ and $\sim 10^{28} \text{ W Hz}^{-1}$, with an apparent peak between $P_{144\text{MHz}} \sim 10^{25} - 10^{26} \text{ W Hz}^{-1}$ around a proper projected length of $\ell \sim 9 \text{ kpc}$. Figure 6.4 shows this diagram separated by source classification.

Among the SFGs, a number of high-power sources can be seen with $P_{144\text{MHz}} > 10^{25} \text{ W Hz}^{-1}$. This is rather high for these objects (e.g. Gürkan et al., 2018). P N Best et al., 2023 mention that it becomes difficult to distinguish AGN SEDs from SFG SEDs above redshifts of 2.5. They caution that AGN classification is incomplete above this redshift. We therefore introduce this redshift cut to our sample, which removes a significant number of the higher power sources above $P_{144\text{MHz}} \sim 10^{25} \text{ W Hz}^{-1}$, as can be seen in the middle right diagram of Fig. 6.3. Subsequently removing sources that have been classified as SFGs by P N Best et al., 2023, which are outside the scope of this work, mainly removes less powerful sources below this value, in the $\ell \sim 10 - 100 \text{ kpc}$ range. A small number of objects classified as SFGs extend beyond 100 kpc, also noted by Hardcastle et al., 2019. These are suspiciously large.

6.5 Discussion

Three regions that are avoided or sparsely inhabited can be identified in the $P - \ell$ diagram:

- High power, large sources in the top and top right areas of the diagram. Such sources will be intrinsically rare(r) and require a substantial sky area larger than a single field to be surveyed for large number statistics.
- Low power, large sources. Sources will inevitably fall below the surface brightness limit of even low-resolution observations – in this case the $6''$ LoTSS data – once they cross a certain limiting surface brightness. These sources would inhabit the bottom right corner of the plot.
- The smallest sources, which are either rare because they spend only a fraction of their lives in that regime, or are difficult to obtain proper estimates for due to instrumental resolution limitations. These are found to the left of the plot.

6.5.1 Comparison with literature

In this section we compare our findings to those of Hardcastle et al., 2019 (hereafter H19). We first note the large $\ell > 100 \text{ kpc}$ SFGs. Visual inspection revealed AGN-like structures for some sources, which

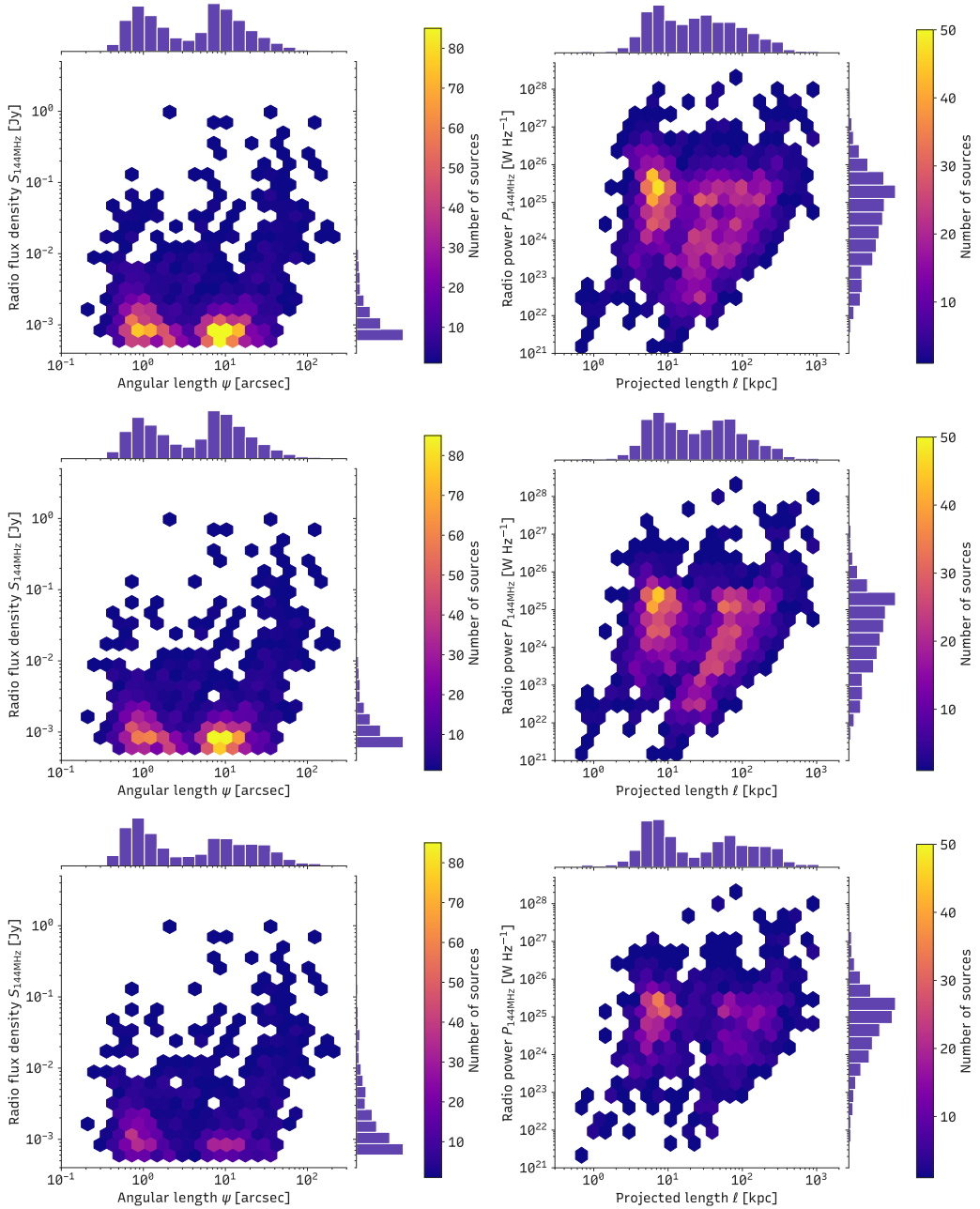


Figure 6.3: Radio brightness versus projected length on the sky. *Left*: flux density versus projected angular length. *Right*: radio power versus projected physical length. *Top*: the full sample. *Middle*: only sources with $z < 2.5$. *Bottom*: sources with $z < 2.5$ and not classified as SFGs.

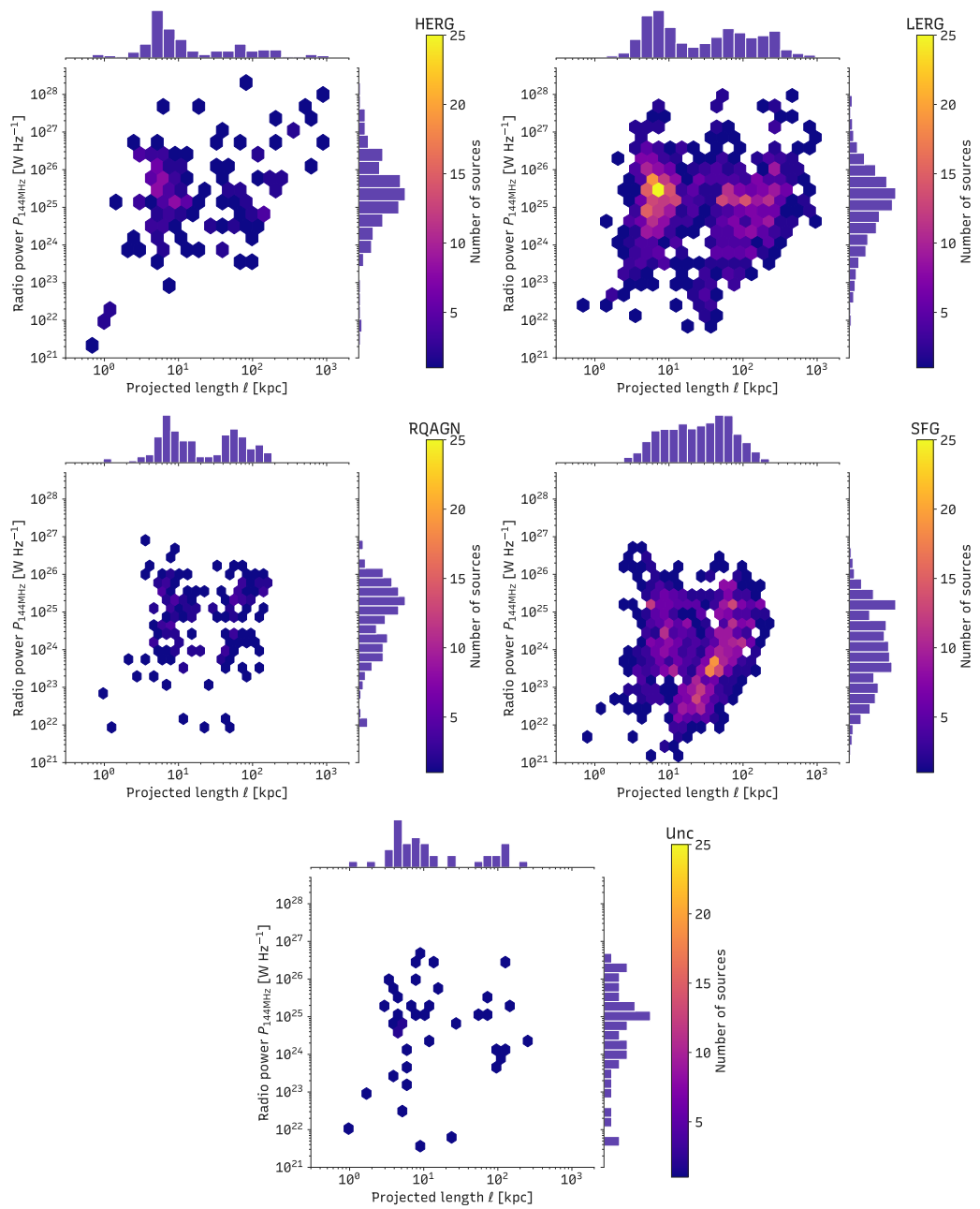


Figure 6.4: Power versus projected linear size for each source classification.

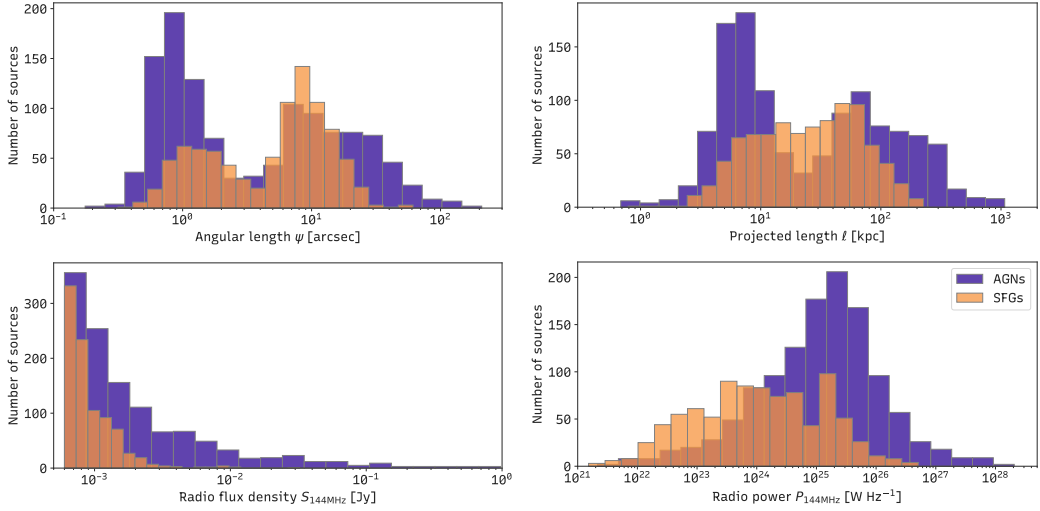


Figure 6.5: Marginal distributions of Fig. 6.3. The left two histograms show the marginal distributions of the angular length and flux density observables. The right two histograms show the respective derived quantities: physical length and power. Yellow bars indicate objects that were classified as SFGs while purple bars those that were classified otherwise.

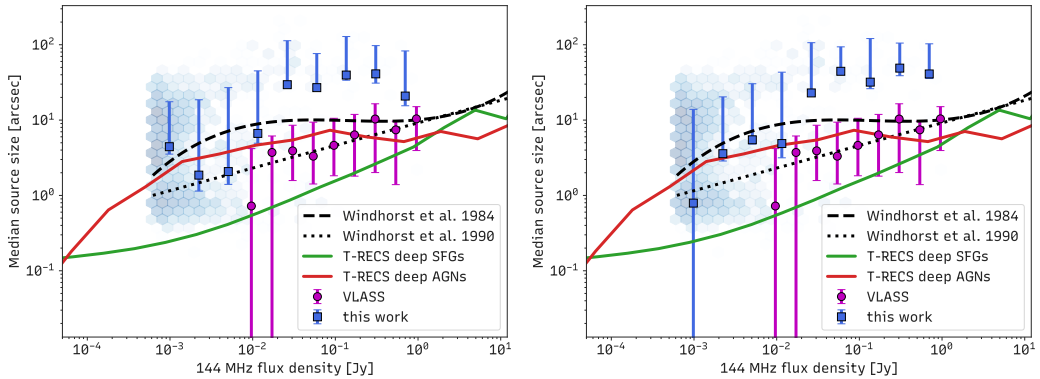


Figure 6.6: Median source size versus flux density. *Left*: as function of LoTSS Deep 6" flux density. *Right*: as a function of flux density derived from the respective size measurement method. Blue squares indicate our work, with the error bars indicating the 16th and 84th percentiles within the bin. The dashed black line indicates the empirical relation found by R. A. Windhorst et al., 1984. The dotted line indicates the relation derived by R. Windhorst et al., 1990. Pink circles indicate measurements derived from VLASS. The two-dimensional histogram in the background visualises the distribution used to derive the blue data points.

indicates complications during the source association, or optical counterparts that were faint, which could have affected the SED fitting or redshift estimates, consequently affecting the derived powers and sizes.

Figure 6.6 compares our findings against those found with the VLASS Quick Look images from Gordon et al., 2021. While an excellent agreement between VLASS and the R. Windhorst et al., 1990 relation is found, our median size is notably higher. Two main caveats are at play here, as mentioned by Gordon et al., 2021. Firstly the configuration used by the VLA prioritises longer baselines. This reduces the sensitivity to extended structures. Secondly, the higher angular resolution causes extended sources to be resolved into multiple components. Source-finding algorithms may not consider these components as belonging to a single source, causing an underestimate of the true size and introducing spurious small(er) sources. Visual comparison of a few large sources in our sample with the catalogue and images of the VLASS Epoch 1 Quick Look images confirms both cases. Some large diffuse sources are not detected at all and those that are indeed break up into multiple components. This issue is not unique to VLASS, but a general source finding and association problem, and part of the reason why for large extended sources we used a different algorithm for our measurements. The significant differences between our results and previous studies that are not sensitive to extended emission have implications for the planning of future studies with e.g. the Square Kilometer Array (SKA).

The main difference between the H19 sample and the sample presented here is that we can now more directly measure sizes of compact sources for which previously only upper limits or deconvolved sizes were available. In their Fig. 8 this corresponds roughly to sources smaller than 20 kpc. A notable difference in our sample is the conglomeration of sources with $\ell = 5 - 10$ kpc and $P_{144\text{MHz}} \sim 10^{25} - 10^{26} \text{ W Hz}^{-1}$. The PD diagram of H19 shows a dearth of sources in this region. One cause can be the difference in redshift coverage. The bulk of that sample resides at $z \lesssim 0.8$, while for this sample we have a notable tail towards (much) higher redshifts. By restricting the sample to below this redshift, we recover a distribution more similar to H19, as can be seen in Fig. 6.7. Few sources now lie above $P_{144\text{MHz}} \approx 10^{25} \text{ W Hz}^{-1}$, except at large projected lengths.

In the bottom panel, the redshift cut is reversed and only sources with $0.8 \leq z < 2.5$ are shown. In this redshift range, sources exclusively inhabit the region with estimated radio powers $P_{144\text{MHz}} > 10^{24} \text{ W Hz}^{-1}$. This exclusiveness is a sensitivity bias from the flux density cut. Despite that, the distributions do imply a tail towards higher radio powers at higher redshifts. If we assume a larger number of high-power radio sources, this may be related to the accretion history of supermassive black holes. The black hole accretion rate density is known to increase towards cosmic noon ($z \sim 2$), matching the cosmic star formation rate density remarkably (Shankar et al., 2008; Madau et al., 2014). The increase in radio power at higher redshifts could then be attributable to short-lived events of high accretion.

In terms of sizes, the derived distribution of projected lengths peaks around $\ell = 6-7$ kpc and it appears approximately log-uniform for $\ell > 10$ kpc. The bump is likely a resolution effect due to a large number of sources being unresolved. Even if unresolved, an increase in the number of smaller sources could be indicative of an increasing fraction of younger, smaller sources. However, cosmological surface brightness dimming may affect the detection of larger sources.

6.5.2 Recovery of (diffuse) emissions

Two systematic effects impact our ability to recover diffuse emission at certain scales. One is the uv -coverage inherently constraining the angular scales that the instrument is sensitive to. The other is the limiting surface brightness at a given resolution. We surmise that it is these limitations that contribute to or drive, the observed dip in the angular size distribution.

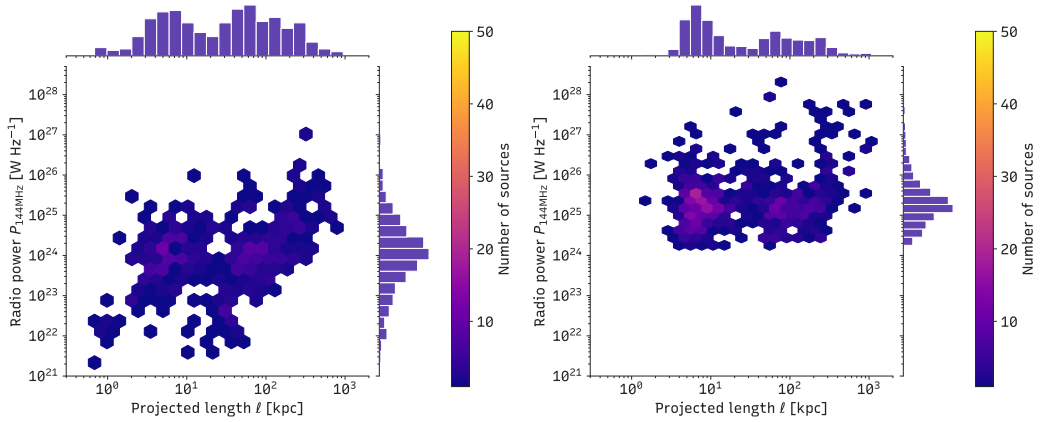


Figure 6.7: Same as the bottom right figure in Fig. 6.3, except now with a redshift cut of $z < 0.8$ (top) and $0.8 \leq z < 2.5$ (bottom).

uv-coverage and sensitivity to angular scales

Where and how well the *uv*-plane is sampled dictates the angular scales that the instrument is sensitive to. Gaps in the *uv*-coverage therefore impact the instrument’s ability to recover structures on certain angular scales. Figure 6.8 shows the Stokes I *uv*-coverage of the observation used in this work. The first three panels illustrate how the core, remote and international stations contribute to the *uv*-coverage separately. Approximately, core stations sample the $80 - 3000 \lambda$ range, remote stations the $3000 - 50,000 \lambda$ range and international stations mostly the $100,000 - 900,000 \lambda$ range (with some extensions inwards to the $50,000 - 100,000 \lambda$ range). The last panel shows the complete *uv*-coverage of all stations. Despite the ILT’s dense sampling of the *uv* plane, a notable gap in the east-west direction remains. Figure 6.9 provides a zoom-in of this gap. It can be seen that, in the east-west direction, the (approximately) $40 - 100 \text{ k}\lambda$ range lacks sampling. This *uv* range corresponds to angular resolutions between $2''$ and $5''$. In the north-south direction a sparsely sampled area around $175 \text{ k}\lambda$, corresponding to an angular scale of $1.2''$ is identified. While not devoid of any sampling, this sparser sampling of the *uv*-plane in the $1'' - 5''$ range will have influenced our ability to recover emission at these scales. We suppose that this has resulted in the diagonal valley separating sources $\ell = 10 \text{ kpc}$ in Fig. 6.3, as such a diagonal line is the result of a constant angular size. Ideally, an additional station would be added to the array that would provide more intermediate east-west baselines to fill the remaining gap in the *uv* coverage.

Resolution bias and surface brightness limitations

One of the limiting factors in recovering diffuse emission is the surface brightness sensitivity; a quantity that decreases with increasing angular resolution. The estimated theoretical sensitivity limits are summarised in Tab. 6.1. This effect not only impacts the recovery of diffuse sources such as SFGs but also biases the extent to which the diffuse jets of FR I type radio galaxies can be measured, for example. To (partially) overcome these biases the resampling discussed in Section 3 was used. Another bias related to resolution comes from the visual inspection, where a more compact size would be preferred in the cases where the intermediate resolution fits were rejected.

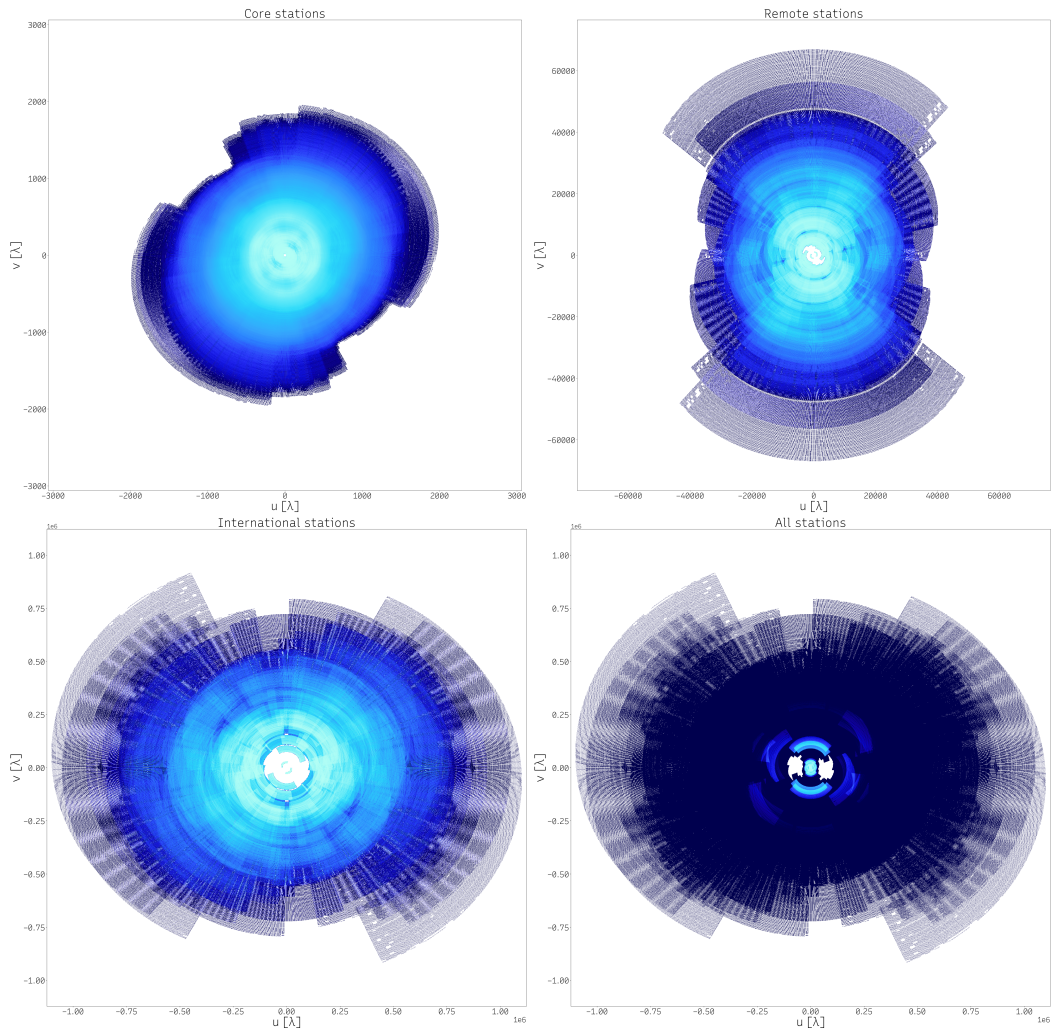


Figure 6.8: Stokes I uv -coverage of the observation used in this work. From top to bottom: core stations only, remote stations only, international stations only, full ILT. The axes show the v and u coordinates in units of wavelength. A brighter colour indicates a higher relative density of points. Panels are not on the same colour scale.

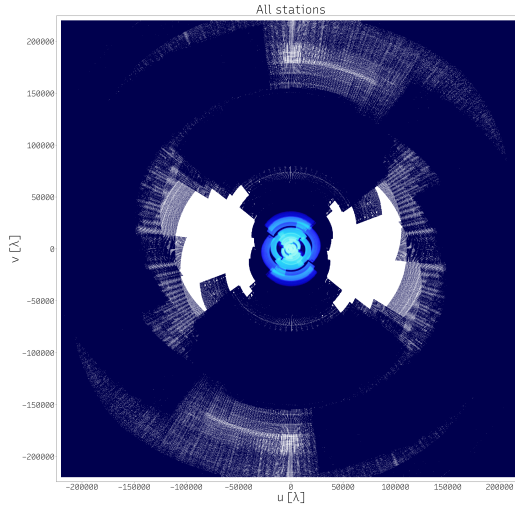


Figure 6.9: A zoom-in on the inner region of the bottom right panel in Fig. 6.8 showing the gap in uv -coverage in the (approximately) $40 - 100 \text{ k}\lambda$ range and the relatively sparse sampling around $175 \text{ k}\lambda$.

6.5.3 Definitions of size

The above-mentioned limitations lead to a more philosophical consideration of what constitutes “the size” of a radio galaxy, also discussed in [Martijn S. S. L. Oei et al., 2023](#). Here we also briefly touch on this. Firstly, a common threshold for source detection is to only consider emission that is brighter than the local (rms) noise level σ_{rms} by some factor. This is unavoidable from a reliability perspective but introduces a survey depth bias where diffuse sources like FR Is or SFGs can “grow” when newer deeper observations would measure the same source. This strengthens the cause for methods such as half-light radii, which (assuming a good fit) will be more robust between various survey depths, but one may argue that those do not reflect the “actual size” of the object. On a similar note, the intensity profiles of any source with a non-zero spectral index will be frequency dependent. Faint emission or that with a steep spectral index may be missed at higher frequencies but is more readily detected at lower frequencies. Comparison between literature values is further complicated when different works use different definitions of “size”.

6.6 Conclusions

In this work, we have attempted to measure the size distribution of radio sources in the Lockman Hole area of the LoTSS Deep survey that has ILT coverage. We build on the results from [Hardcastle et al., 2019](#) by using images with angular resolutions of $6''$, $1.8''$ and $0.45''$, allowing us to probe smaller source sizes. Efforts for optical counterpart identification in the LOFAR Deep fields also allow us to expand the sample to higher redshifts. We summarise our findings as follows:

- We have measured angular sizes between $0.2''$ and $200''$ for radio sources $S_{144\text{MHz}} > 600 \mu\text{Jy}$. Physical projected lengths in the range $\ell = 0.7 \text{ kpc} - 1 \text{ Mpc}$ and radio powers in the range $P_{144\text{MHz}} \approx$

Table 6.3: List of symbols used in this work

Symbol	Meaning
α	synchrotron spectral index
ν	frequency
Ω	solid angle
θ_{maj}	fitted major axis of the synthesised beam
θ_{min}	fitted minor axis of the synthesised beam
ψ	projected angular size of a source
σ_{rms}	local root-mean-square noise in the image
ℓ	projected physical size of a source
I_{ν}	specific peak intensity at frequency ν
L_{ν}	specific luminosity at frequency ν
S_{ν}	specific flux density at frequency ν
z	redshift

$10^{21} - 5 \times 10^{28} \text{ W Hz}^{-1}$ were derived using available redshift information from LoTSS Deep DR1.

- We find a significant disagreement between our measurements and previous studies at higher frequencies such as VLASS, which we argue is, for example, due to the lack of sensitivity to extended emission in the latter.
- We find a qualitative agreement with [Hardcastle et al., 2019](#) for sources classified as AGNs by [P N Best et al., 2023](#) at redshifts $z < 0.8$. At higher redshifts $0.8 \leq z < 2.5$, however, we find a larger number of sources with radio powers $P_{144\text{MHz}} \geq 10^{24} \text{ W Hz}^{-1}$. This could imply more short-lived high accretion events in the Early Universe.
- The ILT's ability to produce science-quality images at both arcsecond and sub-arcsecond scale angular resolutions gives it a unique view of the radio sky, enabling it to detect both compact and diffuse emission from a single observation.

Follow-up work will focus on jet power modelling to study the implications of these sizes on AGN life cycles in more detail. Higher resolution observations down to milliarcsecond scales will be required to directly measure the sizes of the smallest sources in the sample. Work on the other LOFAR deep fields such as the ELAIS-N1 and Boötes fields will increase the sample size to provide increased statistics in sparsely sampled regions. Finally, with additional stations still joining the array, we highlight the value of additional east-west baselines in the 100 – 200 km length range, which would fill a valuable gap in the ILT's uv coverage.

6.7 Derivation of the size limits given a surface brightness limit

We derive an upper limit on the size of a source by demanding that the peak intensity $I = S/\Omega$ of the source exceeds some limiting intensity I_{lim} [Jy arcsec^{-2}], for a given largest size Ω_{max} [arcsec^2]:

$$I_{\text{lim}} \leq \frac{S}{\Omega_{\text{max}}}$$

Using Eqn. 6.3 this can be written as

$$\begin{aligned} \Omega_{\text{max}} &\leq \frac{S}{I_{\text{lim}}} \\ \frac{2\pi\theta_{\text{maj,max}}\theta_{\text{min,max}}}{8\ln 2} &\leq \frac{S}{I_{\text{lim}}} \\ \frac{2\pi\theta_{\text{max}}^2}{8\ln 2} &\leq \frac{S}{I_{\text{lim}}} \end{aligned}$$

where the last simplification comes from assuming a circular source, for which $\theta_{\text{maj,max}} = \theta_{\text{min,max}}$. Rearranging terms to isolate θ_{max} we arrive at the final size criterion

$$\theta_{\text{max}} \leq \sqrt{\frac{8\ln 2}{2\pi} \frac{S}{I_{\text{lim}}}} \quad (6.7)$$

where S has units of Jy , I_{lim} of Jy arcsec^{-2} and θ_{max} of arcsec .

Cross-check between resolutions

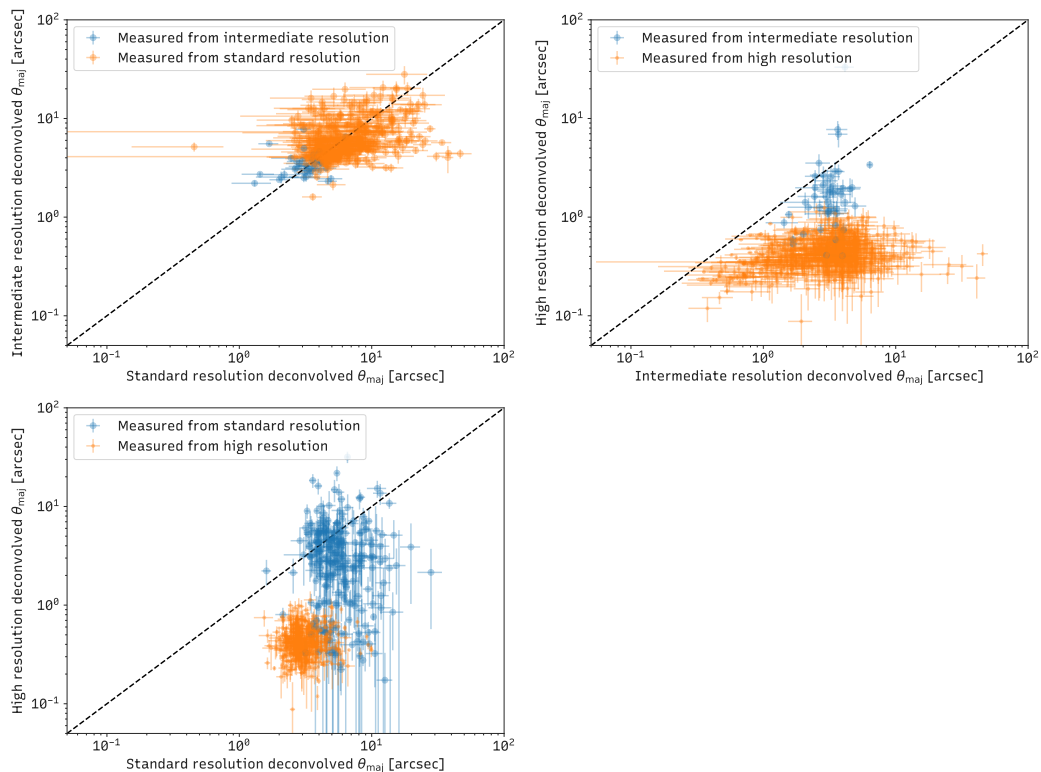


Figure 6.10: A comparison between the major axis of Gaussian fits at standard, intermediate and high resolution. Error bars indicate uncertainties in the fits. Blue points indicate sources for which the intermediate resolution fit was deemed acceptable. Orange points indicate fits for which the high-resolution image was preferred. The deviation from the one-to-one line in the right plot reflects the visual inspection preferring the high-resolution image in situations where the intermediate-resolution fit was compromised by psf side lobes.

Visual inspection plot examples

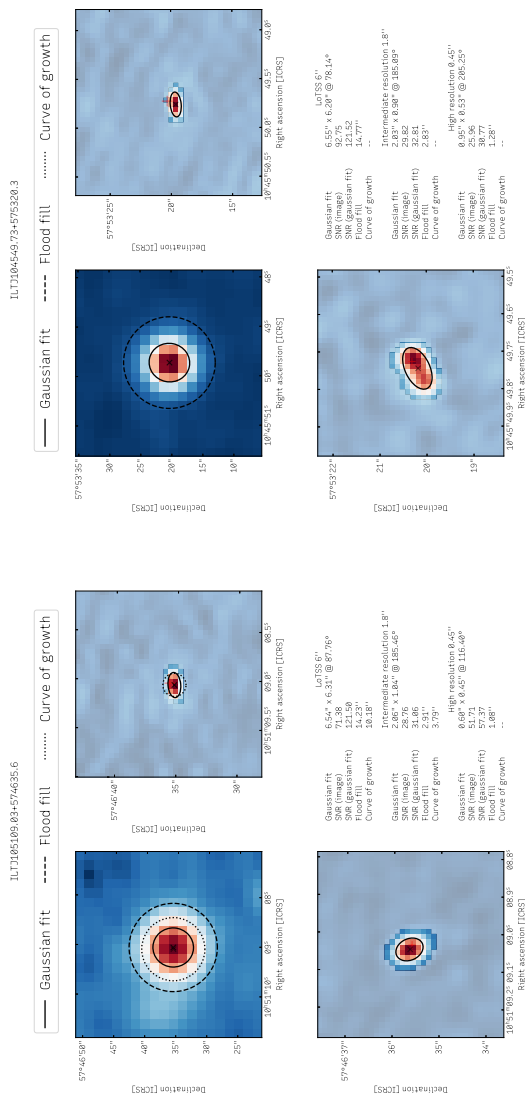


Figure 6.11: Two examples of the plots used to aid visual inspection. The three images show the source at standard resolution (top left), intermediate resolution (top right) and high resolution (bottom left). Solid black lines indicate the Gaussian fit from PyBDSF (for standard resolution) or imfit for the intermediate and high-resolution images. Dotted lines indicate curve-of-growth size if it had converged (not used in the final analysis). Finally, the flood fill sizes are indicated by a dashed line in the standard resolution images or a white semi-transparent overlay on the intermediate and high-resolution images.

Acknowledgements

JP and MJH acknowledge support from the Science and Technology Facilities Council (STFC) via grant ST/V000624/1. RJvW acknowledges support from the ERC Starting Grant ClusterWeb 804208. This paper is based (in part) on data obtained with the International LOFAR Telescope (ILT) under project code LT10_012. LOFAR (van Haarlem et al. 2013) is the Low Frequency Array designed and constructed by ASTRON. It has observing, data processing, and data storage facilities in several countries, that are owned by various parties (each with their own funding sources), and that are collectively operated by the ILT foundation under a joint scientific policy. The ILT resources have benefitted from the following recent major funding sources: CNRS-INSU, Observatoire de Paris and Université d'Orléans, France; BMBF, MIWF-NRW, MPG, Germany; Science Foundation Ireland (SFI), Department of Business, Enterprise and Innovation (DBEI), Ireland; NWO, The Netherlands; The Science and Technology Facilities Council, UK; Ministry of Science and Higher Education, Poland[7]. This work made use of Astropy:⁴ a community-developed core Python package with an ecosystem of tools and resources for astronomy (Astropy Collaboration et al., 2013; Astropy Collaboration et al., 2018; Astropy Collaboration et al., 2022). This work made use of NumPy⁵ (C. R. Harris et al., 2020b).

⁴<http://www.astropy.org>

⁵<https://numpy.org/>

Bibliography

- Allen, L. R., R. H. Brown, and H. P. Palmer (July 1962a). “An Analysis of the Angular Sizes of Radio Sources”. In: *Monthly Notices of the Royal Astronomical Society* 125.1, pp. 57–74. ISSN: 0035-8711, 1365-2966. DOI: [10.1093/mnras/125.1.57](https://doi.org/10.1093/mnras/125.1.57). (Visited on 02/10/2023).
- Astropy Collaboration et al. (Oct. 2013). “Astropy: A community Python package for astronomy”. In: *A&A* 558, A33, A33. DOI: [10.1051/0004-6361/201322068](https://doi.org/10.1051/0004-6361/201322068). arXiv: [1307.6212](https://arxiv.org/abs/1307.6212) [astro-ph. IM].
- Astropy Collaboration et al. (Sept. 2018). “The Astropy Project: Building an Open-science Project and Status of the v2.0 Core Package”. In: *AJ* 156.3, 123, p. 123. DOI: [10.3847/1538-3881/aabc4f](https://doi.org/10.3847/1538-3881/aabc4f). arXiv: [1801.02634](https://arxiv.org/abs/1801.02634) [astro-ph. IM].
- Astropy Collaboration et al. (Aug. 2022). “The Astropy Project: Sustaining and Growing a Community-oriented Open-source Project and the Latest Major Release (v5.0) of the Core Package”. In: *apj* 935.2, 167, p. 167. DOI: [10.3847/1538-4357/ac7c74](https://doi.org/10.3847/1538-4357/ac7c74). arXiv: [2206.14220](https://arxiv.org/abs/2206.14220) [astro-ph. IM].
- Baldi, Ranieri D., Alessandro Capetti, and Gabriele Giovannini (Apr. 2015). “Pilot Study of the Radio-Emitting AGN Population: The Emerging New Class of FR 0 Radio-Galaxies”. In: *Astronomy and Astrophysics* 576. ISSN: 14320746. DOI: [10.1051/0004-6361/201425426](https://doi.org/10.1051/0004-6361/201425426). arXiv: [1502.00427](https://arxiv.org/abs/1502.00427). (Visited on 09/14/2020).
- Baldwin, J. E. (Jan. 1982). “Evolutionary Tracks of Extended Radio Sources”. In: 97, pp. 21–24. (Visited on 08/03/2023).
- Bash, F. N. (May 1968). “Observations of the Angular Structure of Radio Sources”. In: *The Astrophysical Journal* 152, p. 375. ISSN: 0004-637X. DOI: [10.1086/149555](https://doi.org/10.1086/149555). (Visited on 02/03/2023).
- Benn, C. R. et al. (Aug. 1, 1982). “A deep radio/optical survey near the North Galactic Pole. I. The 5C12 catalogue.” In: *Monthly Notices of the Royal Astronomical Society* 200. ADS Bibcode: 1982MNRAS.200..747B, pp. 747–766. ISSN: 0035-8711. DOI: [10.1093/mnras/200.3.747](https://doi.org/10.1093/mnras/200.3.747). URL: <https://ui.adsabs.harvard.edu/abs/1982MNRAS.200..747B> (visited on 01/30/2023).
- Best, P N et al. (Aug. 2023). “The LOFAR Two-metre Sky Survey: Deep Fields Data Release 1. V. Survey Description, Source Classifications, and Host Galaxy Properties”. In: *Monthly Notices of the Royal Astronomical Society* 523.2, pp. 1729–1755. ISSN: 0035-8711. DOI: [10.1093/mnras/stad1308](https://doi.org/10.1093/mnras/stad1308). (Visited on 06/07/2023).
- Blandford, R. D. and M. J. Rees (Dec. 1974). “A “twin-exhaust” model for double radio sources.” In: *MNRAS* 169, pp. 395–415. DOI: [10.1093/mnras/169.3.395](https://doi.org/10.1093/mnras/169.3.395).
- Bonaldi, Anna et al. (Jan. 2019). “The Tiered Radio Extragalactic Continuum Simulation (T-RECS)”. In: *MNRAS* 482.1, pp. 2–19. DOI: [10.1093/mnras/sty2603](https://doi.org/10.1093/mnras/sty2603). arXiv: [1805.05222](https://arxiv.org/abs/1805.05222) [astro-ph. GA].
- Bondi, M. et al. (Oct. 2018). “Linear radio size evolution of μ Jy populations”. In: *A&A* 618, L8, p. L8. DOI: [10.1051/0004-6361/201834243](https://doi.org/10.1051/0004-6361/201834243). arXiv: [1810.04095](https://arxiv.org/abs/1810.04095) [astro-ph. GA].

- Condon, J. J. (Jan. 1992). “Radio Emission from Normal Galaxies.” In: *Annual Review of Astronomy and Astrophysics* 30, pp. 575–611. ISSN: 0066-4146. DOI: [10.1146/annurev.aa.30.090192.003043](https://doi.org/10.1146/annurev.aa.30.090192.003043). (Visited on 08/18/2023).
- Cotton, W. D. et al. (Mar. 2018). “The Angular Size Distribution of μ Jy Radio Sources”. In: *A&J* 856.1, 67, p. 67. DOI: [10.3847/1538-4357/aaec4](https://doi.org/10.3847/1538-4357/aaec4). arXiv: [1802.04209](https://arxiv.org/abs/1802.04209) [astro-ph.GA].
- Croston, J. H. et al. (Feb. 2019). “The environments of radio-loud AGN from the LOFAR Two-Metre Sky Survey (LoTSS)”. In: *A&A* 622, A10, A10. DOI: [10.1051/0004-6361/201834019](https://doi.org/10.1051/0004-6361/201834019). arXiv: [1811.07949](https://arxiv.org/abs/1811.07949) [astro-ph.GA].
- Dabhade, P. et al. (Mar. 2020). “Giant radio galaxies in the LOFAR Two-metre Sky Survey. I. Radio and environmental properties”. In: *A&A* 635, A5, A5. DOI: [10.1051/0004-6361/201935589](https://doi.org/10.1051/0004-6361/201935589). arXiv: [1904.00409](https://arxiv.org/abs/1904.00409) [astro-ph.GA].
- DiPompeo, M. A. et al. (Aug. 2013). “DOES SIZE MATTER? THE UNDERLYING INTRINSIC SIZE DISTRIBUTION OF RADIO SOURCES AND IMPLICATIONS FOR UNIFICATION BY ORIENTATION”. In: *The Astrophysical Journal* 774.1, p. 24. ISSN: 0004-637X. DOI: [10.1088/0004-637X/774/1/24](https://doi.org/10.1088/0004-637X/774/1/24). (Visited on 06/22/2023).
- Downes, A. (Jan. 1, 1982). “The angular size distribution of radio sources at low flux densities”. In: 97. Conference Name: Extragalactic Radio Sources ADS Bibcode: 1982IAUS...97..393D, pp. 393–400. URL: <https://ui.adsabs.harvard.edu/abs/1982IAUS...97..393D> (visited on 01/30/2023).
- Downes, A. J. B., M. S. Longair, and M. A. C. Perryman (Dec. 1981). “High-resolution observations of faint radio sources and the angular size–flux density relation”. en. In: *Monthly Notices of the Royal Astronomical Society* 197.3, pp. 593–626. ISSN: 0035-8711, 1365-2966. DOI: [10.1093/mnras/197.3.593](https://doi.org/10.1093/mnras/197.3.593). URL: <https://academic.oup.com/mnras/article-lookup/doi/10.1093/mnras/197.3.593> (visited on 01/30/2023).
- Fanaroff, B. L. and J. M. Riley (Apr. 1974). “The Morphology of Extragalactic Radio Sources of High and Low Luminosity”. In: *Monthly Notices of the Royal Astronomical Society* 167.1, 31P–36P. ISSN: 0035-8711. DOI: [10.1093/mnras/167.1.31P](https://doi.org/10.1093/mnras/167.1.31P). (Visited on 11/26/2018).
- Fielden, J. et al. (Sept. 1983). “Further high-resolution observations of faint radio sources and the angular size–flux density relation”. en. In: *Monthly Notices of the Royal Astronomical Society* 204.2, pp. 289–315. ISSN: 0035-8711, 1365-2966. DOI: [10.1093/mnras/204.2.289](https://doi.org/10.1093/mnras/204.2.289). URL: <https://academic.oup.com/mnras/article-lookup/doi/10.1093/mnras/204.2.289> (visited on 02/01/2023).
- Fomalont, E.B. (Sept. 1973). “Earth-rotation aperture synthesis”. In: *Proceedings of the IEEE* 61.9. Conference Name: Proceedings of the IEEE, pp. 1211–1218. ISSN: 1558-2256. DOI: [10.1109/PROC.1973.9247](https://doi.org/10.1109/PROC.1973.9247).
- Gordon, Yjan A. et al. (Aug. 2021). “A Quick Look at the 3 GHz Radio Sky. I. Source Statistics from the Very Large Array Sky Survey”. In: *The Astrophysical Journal Supplement Series* 255.2, p. 30. ISSN: 0067-0049. DOI: [10.3847/1538-4365/ac05c0](https://doi.org/10.3847/1538-4365/ac05c0). (Visited on 03/29/2023).
- Gürkan, G. et al. (Apr. 2018). “LOFAR/H-ATLAS: The Low-Frequency Radio Luminosity-Star Formation Rate Relation”. In: *Monthly Notices of the Royal Astronomical Society* 475, pp. 3010–3028. ISSN: 0035-8711. DOI: [10.1093/mnras/sty016](https://doi.org/10.1093/mnras/sty016). (Visited on 01/14/2022).
- Haarlem, M. P. van et al. (Aug. 2013). “LOFAR: The LOw-Frequency ARray”. In: *Astronomy & Astrophysics* 556, A2. ISSN: 0004-6361, 1432-0746. DOI: [10.1051/0004-6361/201220873](https://doi.org/10.1051/0004-6361/201220873). (Visited on 09/20/2023).

- Hanbury Brown, R. and C. Hazard (Apr. 1953a). “A Survey of 23 Localized Radio Sources in the Northern Hemisphere”. In: *Monthly Notices of the Royal Astronomical Society* 113.2, pp. 123–133. ISSN: 0035-8711. DOI: [10.1093/mnras/113.2.123](https://doi.org/10.1093/mnras/113.2.123). (Visited on 02/20/2023).
- Hanbury Brown, R., H. P. Palmer, and A. R. Thompson (May 1954). “Galactic Radio Sources of Large Angular Diameter”. In: *Nature* 173.4411, pp. 945–946. ISSN: 1476-4687. DOI: [10.1038/173945a0](https://doi.org/10.1038/173945a0). (Visited on 08/18/2023).
- Hardcastle, M. J. and J. H. Croston (June 1, 2020). “Radio galaxies and feedback from AGN jets”. In: *New Astronomy Reviews* 88, p. 101539. ISSN: 1387-6473. DOI: [10.1016/j.newar.2020.101539](https://doi.org/10.1016/j.newar.2020.101539). URL: <https://www.sciencedirect.com/science/article/pii/S1387647320300166> (visited on 05/16/2022).
- Hardcastle, M. J. et al. (Feb. 2019). “Radio-Loud AGN in the First LoTSS Data Release”. In: *Astronomy & Astrophysics* 622, A12. ISSN: 0004-6361. DOI: [10.1051/0004-6361/201833893](https://doi.org/10.1051/0004-6361/201833893). (Visited on 01/24/2020).
- Harris, Charles R. et al. (Sept. 2020b). “Array programming with NumPy”. In: *Nature* 585.7825, pp. 357–362. DOI: [10.1038/s41586-020-2649-2](https://doi.org/10.1038/s41586-020-2649-2). URL: <https://doi.org/10.1038/s41586-020-2649-2>.
- Harwood, Jeremy J, Tessa Vernstrom, and Andra Stroe (Jan. 2020). “Unveiling the Cause of Hybrid Morphology Radio Sources (HyMoRS)”. In: *Monthly Notices of the Royal Astronomical Society* 491.1, pp. 803–822. ISSN: 0035-8711. DOI: [10.1093/mnras/stz3069](https://doi.org/10.1093/mnras/stz3069). (Visited on 08/09/2023).
- Hazard, C., M. B. Mackey, and A. J. Shimmins (Mar. 1963). “Investigation of the Radio Source 3C 273 By The Method of Lunar Occultations”. In: *Nature* 197.4872, pp. 1037–1039. ISSN: 1476-4687. DOI: [10.1038/1971037a0](https://doi.org/10.1038/1971037a0). (Visited on 02/01/2023).
- Jennison, R. C. and M. K. Das Gupta (Nov. 1953). “Fine Structure of the Extra-terrestrial Radio Source Cygnus I”. In: *Nature* 172.4387, pp. 996–997. ISSN: 1476-4687. DOI: [10.1038/172996a0](https://doi.org/10.1038/172996a0). (Visited on 03/01/2023).
- Kapahi, V. K. (Sept. 1975). “Cosmology from Angular Size Counts of Extragalactic Radio Sources”. In: *Monthly Notices of the Royal Astronomical Society* 172.3, pp. 513–533. ISSN: 0035-8711, 1365-2966. DOI: [10.1093/mnras/172.3.513](https://doi.org/10.1093/mnras/172.3.513). (Visited on 03/02/2023).
- Kapahi, V. K., V. K. Kulkarni, and C. R. Subrahmanya (Mar. 1987). “On the interpretation of the observed angular-size-flux-density relation for extragalactic radio sources.” In: *Journal of Astrophysics and Astronomy* 8. ADS Bibcode: 1987JApA....8...33K, pp. 33–50. ISSN: 0250-6335. DOI: [10.1007/BF02714250](https://ui.adsabs.harvard.edu/abs/1987JApA....8...33K). URL: <https://ui.adsabs.harvard.edu/abs/1987JApA....8...33K> (visited on 02/02/2023).
- Katgert, P. (June 1976). “Source count, spectral indices and angular sizes of weak radio sources in the 5C 2 region.” In: *Astronomy and Astrophysics* 49. ADS Bibcode: 1976A&A...49..221K, pp. 221–234. ISSN: 0004-6361. URL: <https://ui.adsabs.harvard.edu/abs/1976A&A...49..221K> (visited on 02/01/2023).
- Kellermann, K. I. (Sept. 1972). “Radio Galaxies, Quasars, and Cosmology”. en. In: *The Astronomical Journal* 77, p. 531. ISSN: 00046256. DOI: [10.1086/111314](https://doi.org/10.1086/111314). URL: http://adsabs.harvard.edu/cgi-bin/bib_query?1972AJ....77..531K (visited on 02/21/2023).
- (Mar. 1978). “Structure and Time Variations of Compact Radio Sources in Galaxies and Quasars”. In: *Physica Scripta* 17.3, p. 257. ISSN: 1402-4896. DOI: [10.1088/0031-8949/17/3/019](https://doi.org/10.1088/0031-8949/17/3/019). (Visited on 02/20/2023).

- Kondapally, R. et al. (Apr. 2021). “The LOFAR Two-meter Sky Survey: Deep Fields Data Release 1. III. Host-galaxy identifications and value added catalogues”. In: *A&A* 648, A3, A3. DOI: 10.1051/0004-6361/202038813. arXiv: 2011.08201 [astro-ph.GA].
- Lacy, M. et al. (Jan. 2020). “The Karl G. Jansky Very Large Array Sky Survey (VLASS). Science Case and Survey Design”. In: *Publications of the Astronomical Society of the Pacific* 132.1009, p. 035001. ISSN: 1538-3873. DOI: 10.1088/1538-3873/ab63eb. (Visited on 09/22/2023).
- Lockman, F. J., K. Jahoda, and D. McCammon (Mar. 1986). “The Structure of Galactic H I in Directions of Low Total Column Density”. In: *ApJ* 302, p. 432. DOI: 10.1086/164002.
- Longair, M. S. and J. M. Riley (Sept. 1979). “Statistical evidence on the dynamical evolution of extended radio sources.” In: *MNRAS* 188, pp. 625–635. DOI: 10.1093/mnras/188.3.625.
- Longair, M. S., M. Ryle, and P. A. G. Scheuer (Jan. 1973). “Models of extended radiosources”. In: *MNRAS* 164, p. 243. DOI: 10.1093/mnras/164.3.243.
- Madau, Piero and Mark Dickinson (Aug. 2014). “Cosmic Star-Formation History”. In: *Annual Review of Astronomy and Astrophysics* 52.1, pp. 415–486. ISSN: 0066-4146. DOI: 10.1146/annurev-astro-081811-125615. arXiv: 1403.0007. (Visited on 06/04/2020).
- Miley, G. K. (July 1971). “The Radio Structure of Quasars – A Statistical Investigation”. In: *Monthly Notices of the Royal Astronomical Society* 152.4, pp. 477–490. ISSN: 0035-8711, 1365-2966. DOI: 10.1093/mnras/152.4.477. (Visited on 02/03/2023).
- Mills, B. Y., O. B. Slee, and E. R. Hill (Dec. 1960). “A Catalogue of Radio Sources between Declinations -20° and -50°”. In: *Australian Journal of Physics* 13, p. 676. ISSN: 0004-9506. DOI: 10.1071/PH600676. (Visited on 02/10/2023).
- Mingo, B et al. (Sept. 2019). “Revisiting the Fanaroff–Riley Dichotomy and Radio-Galaxy Morphology with the LOFAR Two-Metre Sky Survey (LoTSS)”. In: *Monthly Notices of the Royal Astronomical Society* 488.2, pp. 2701–2721. ISSN: 0035-8711. DOI: 10.1093/mnras/stz1901. (Visited on 08/09/2023).
- Mohan, Niruj and David Rafferty (Feb. 2015a). *PyBDSF: Python Blob Detection and Source Finder*. Astrophysics Source Code Library, record ascl:1502.007. ascl: 1502.007.
- Morabito, L. et al. (Apr. 2021). “Sub-Arcsecond Imaging with the International LOFAR Telescope. I. Foundational Calibration Strategy and Pipeline”. In: *Astronomy & Astrophysics*. ISSN: 0004-6361. DOI: 10.1051/0004-6361/202140649. (Visited on 07/19/2021).
- Morris, D., H. P. Palmer, and A. R. Thompson (June 1957). “Five radio sources of small angular diameter”. In: *The Observatory* 77. ADS Bibcode:1957Obs....77..103M, pp. 103–106. ISSN: 0029-7704. URL: <https://ui.adsabs.harvard.edu/abs/1957Obs....77..103M> (visited on 02/10/2023).
- O’Dea, Christopher P. and D. J. Saikia (Mar. 2021). “Compact Steep-Spectrum and Peaked-Spectrum Radio Sources”. In: *The Astronomy and Astrophysics Review* 29.1, p. 3. ISSN: 1432-0754. DOI: 10.1007/s00159-021-00131-w. (Visited on 08/08/2023).
- Oei, Martijn S. S. L. et al. (Apr. 2022). “The discovery of a radio galaxy of at least 5 Mpc”. In: *A&A* 660, A2, A2. DOI: 10.1051/0004-6361/202142778. arXiv: 2202.05427 [astro-ph.GA].
- Oei, Martijn S. S. L. et al. (Apr. 2023). “Measuring the Giant Radio Galaxy Length Distribution with the LoTSS”. In: *Astronomy & Astrophysics* 672, A163. ISSN: 0004-6361, 1432-0746. DOI: 10.1051/0004-6361/202243572. (Visited on 05/10/2023).
- Oort, M. J. A. (Mar. 1988). “High-resolution observations of millijansky radio sources : the run of median angular size at low flux densities.” In: *Astronomy and Astrophysics* 193. ADS Bibcode:1988A&A...193...50O, pp. 5–14. ISSN: 0004-6361. URL: <https://ui.adsabs.harvard.edu/abs/1988A&A...193...50O> (visited on 02/01/2023).

- Pearson, T. J. and A. J. Kus (Feb. 1, 1978). “The 5C 6 and 5C 7 surveys of radio sources”. In: *Monthly Notices of the Royal Astronomical Society* 182.2, pp. 273–274. ISSN: 0035-8711, 1365-2966. DOI: [10.1093/mnras/182.2.273](https://academic.oup.com/mnras/article-lookup/doi/10.1093/mnras/182.2.273). URL: <https://academic.oup.com/mnras/article-lookup/doi/10.1093/mnras/182.2.273> (visited on 01/30/2023).
- Saxena, A., H. J. A. Röttgering, and E. E. Rigby (Aug. 2017). “Modelling the luminosities and sizes of radio galaxies: radio luminosity function at $z = 6$ ”. In: *Monthly Notices of the Royal Astronomical Society* 469.4, pp. 4083–4094. ISSN: 0035-8711. DOI: [10.1093/mnras/stx1150](https://academic.oup.com/mnras/article-lookup/doi/10.1093/mnras/stx1150). arXiv: 1705.03449. URL: <https://academic.oup.com/mnras/article-lookup/doi/10.1093/mnras/stx1150><http://arxiv.org/abs/1705.03449>[http://dx.doi.org/10.1093/mnras/stx1150](https://dx.doi.org/10.1093/mnras/stx1150).
- Scheuer, P. A. G. (Mar. 1974). “Models of extragalactic radio sources with a continuous energy supply from a central object”. In: *MNRAS* 166, pp. 513–528. DOI: [10.1093/mnras/166.3.513](https://academic.oup.com/mnras/article-lookup/doi/10.1093/mnras/166.3.513).
- Shankar, Francesco, David H. Weinberg, and Jordi Miralda-Escudé (Dec. 2008). “SELF-CONSISTENT MODELS OF THE AGN AND BLACK HOLE POPULATIONS: DUTY CYCLES, ACCRETION RATES, AND THE MEAN RADIATIVE EFFICIENCY”. In: *The Astrophysical Journal* 690.1, p. 20. ISSN: 0004-637X. DOI: [10.1088/0004-637X/690/1/20](https://academic.oup.com/aj/article-lookup/doi/10.1088/0004-637X/690/1/20). (Visited on 08/13/2023).
- Shimwell, T. W. et al. (Feb. 2017). “The LOFAR Two-metre Sky Survey”. In: *Astronomy & Astrophysics* 598, A104. ISSN: 0004-6361. DOI: [10.1051/0004-6361/201629313](https://academic.oup.com/aas/article-lookup/doi/10.1051/0004-6361/201629313). (Visited on 11/30/2018).
- Shimwell, T. W. et al. (Feb. 2019). “The LOFAR Two-metre Sky Survey - II. First Data Release”. In: *Astronomy & Astrophysics* 622, A1. ISSN: 0004-6361, 1432-0746. DOI: [10.1051/0004-6361/201833559](https://academic.oup.com/aas/article-lookup/doi/10.1051/0004-6361/201833559). (Visited on 02/01/2022).
- Shimwell, T. W. et al. (Mar. 2022). “The LOFAR Two-metre Sky Survey - V. Second Data Release”. In: *Astronomy & Astrophysics* 659, A1. ISSN: 0004-6361, 1432-0746. DOI: [10.1051/0004-6361/202142484](https://academic.oup.com/aas/article-lookup/doi/10.1051/0004-6361/202142484). (Visited on 06/30/2023).
- Swarup, G. (Sept. 1975). “Angular size-flux density relation for extragalactic radio sources.” In: *MNRAS* 172, pp. 501–512. DOI: [10.1093/mnras/172.3.501](https://academic.oup.com/mnras/article-lookup/doi/10.1093/mnras/172.3.501).
- Sweijen, F. et al. (Jan. 2022a). “Deep Sub-Arcsecond Wide-Field Imaging of the Lockman Hole Field at 144 MHz”. In: *Nature Astronomy*, pp. 1–7. ISSN: 2397-3366. DOI: [10.1038/s41550-021-01573-z](https://doi.org/10.1038/s41550-021-01573-z). (Visited on 01/28/2022).
- Tasse, C. et al. (Apr. 2021). “The LOFAR Two-meter Sky Survey: Deep Fields Data Release 1. I. Direction-dependent calibration and imaging”. In: *A&A* 648, A1, A1. DOI: [10.1051/0004-6361/202038804](https://academic.oup.com/aas/article-lookup/doi/10.1051/0004-6361/202038804). arXiv: 2011.08328 [astro-ph.IM].
- Turner, Ross J, Stanislav S Shabala, and Martin G H Krause (Mar. 2018). “RAiSE III: 3C radio AGN energetics and composition”. In: *Monthly Notices of the Royal Astronomical Society* 474.3, pp. 3361–3379. ISSN: 0035-8711. DOI: [10.1093/mnras/stx2947](https://academic.oup.com/mnras/article/474/3/3361/4631166). URL: <http://academic.oup.com/mnras/article/474/3/3361/4631166>.
- Wilman, R. J. et al. (Aug. 2008). “A semi-empirical simulation of the extragalactic radio continuum sky for next generation radio telescopes”. In: *MNRAS* 388.3, pp. 1335–1348. DOI: [10.1111/j.1365-2966.2008.13486.x](https://academic.oup.com/mnras/article-lookup/doi/10.1111/j.1365-2966.2008.13486.x). arXiv: 0805.3413 [astro-ph].
- Windhorst, R. A., G. M. van Heerde, and P. Katgert (Oct. 1984). “A deep Westerbork survey of areas with multicolor Mayall 4 M plates. I. The 1412 MHz catalogue, source counts and angular size statistics.” In: *Astronomy and Astrophysics Supplement Series* 58. ADS Bibcode: 1984A&AS...58....1W, pp. 1–37. ISSN: 0365-0138. URL: <https://ui.adsabs.harvard.edu/abs/1984A&AS...58....1W> (visited on 01/30/2023).

Windhorst, Rogier, Doug Mathis, and Lyman Neuschaefer (Jan. 1990). “The Evolution of Weak Radio Galaxies at Radio and Optical Wavelengths.” In: 10, pp. 389–403. (Visited on 07/14/2023).

Popular scientific summary

The electromagnetic spectrum and an invisible universe

Humans have studied the night sky for thousands of years. Some of the earliest astronomical records we have found are from the Babylonians and date back to hundreds of years before the Common Era (BCE). These records show us that they were already capable of feats like tracking the motion of planets across the night sky. However, we can only practically study what we can see. For the longest time that restricted us to our eyes, but much can already be looked at with just those. Most obvious are stars dotted across the night sky. You may even spot the Milky Way stretching across the sky as a fuzzy band, as is shown in Fig. 7.12. Spotting the Milky Way requires dark skies, however, which can be difficult to find in the modern world with the ever increasing amount of light pollution from lights that we keep running at night. Among those



Figure 7.12: The Milky Way as seen above Cerro Paranal, Chile. This photo is a panorama created from multiple 2-minute exposures using a DSLR camera. Image Credit: Bruno Gilli/ESO

billions of stars visible to us, there are a few that the ancient Greeks referred to as “πλάνητες ἀστέρες” or “wandering stars”. These stars move across the night sky as the year passes by. While to the naked eye they may look like just another star, a small telescope can reveal they are not stars at all, but other planets in our solar system.

The first to start using telescopes to explore the night sky was Galileo Galilei. In the early 1600s he was able to deduce that Jupiter was not only different from a star, it even had moons revolving around it. Christiaan Huygens later observed Saturn, discovering that it also had a moon. He found the largest of Saturn’s moons: Titan. In the late 1700s the French astronomer Charles Messier used a telescope to observe the now famous “Messier objects”. These objects are a variety of objects such as nebulae, star clusters and

nearby other galaxies. When photographic plates and, ultimately, CCD cameras came along fainter and fainter objects could be observed, but we had still only seen a tiny sliver of the Universe.

When thinking of “light” we readily consider *visible* light from the Sun, stars, lightbulbs etc. but there are many other forms of light. The entire range of wavelengths light can have we call the “electromagnetic spectrum”. Figure 7.13 shows a schematic overview of the various types of light and whether that light can reach Earth’s surface. Our eyes are sensitive to wavelengths between roughly 380 nm and 750 nm. Shorter wavelengths correspond to higher energies and cover ultraviolet (UV) radiation, X-ray and gamma rays at the highest energies. Pretty much all of these, except some UV wavelengths, are blocked by Earth’s atmosphere. Longer wavelengths bring us first to the infrared (“heat radiation”) wavelengths, followed by microwave radiation and ultimately radio waves. The latter can have wavelengths of centimetres up to many metres. All of these wavelengths require their own specialised equipment in order to be “seen”, or better said observed.

THE ELECTROMAGNETIC SPECTRUM

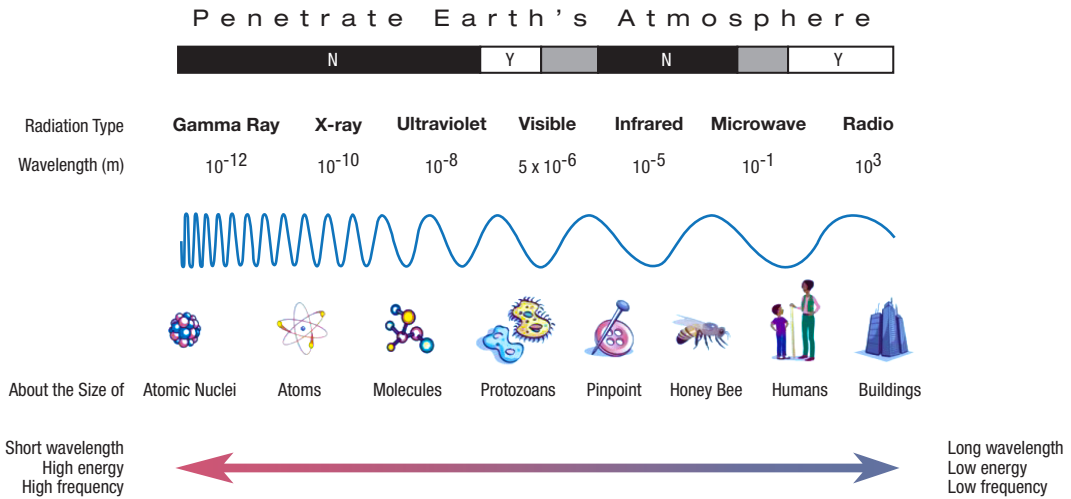


Figure 7.13: A simple overview of the electromagnetic spectrum. The greyscale bar at the top indicates approximately which types of light can be observed from Earth (white), are completely blocked by Earth’s atmosphere (black) or which may still be partially possible to observe (grey). From left to right the wavelength gets longer, the frequency becomes lower and the light carries less energy. Image Credit: NASA.

Figure 7.14 shows a comparison between the Perseus cluster of galaxies as seen in visible light with the recently launched Euclid satellite and what the LOFAR telescope sees in the same region of the sky at radio waves with frequencies of 144 MHz (overlaid on top of the Euclid image). If we had astronomical telescopes as eyes we would see the left image: a rich field of stars and galaxies. If our eyes were sensitive to radio waves, however, the picture changes drastically and we would see the pink-coloured emission seen in the right image. Suddenly a large bubble of radio emission is revealed in the bottom left, surrounding the galaxy at the centre of the cluster, another galaxy near the top middle of the image is seen to be emitting huge plumes of radio emitting material, and dotted around the image we see many other galaxies with smaller plumes.



Figure 7.14: A view of the Perseus cluster. *Left*: a combination of visible light near-infrared light as seen by the Euclid satellite. *Right*: the same image, but now with 144 MHz radio emission as seen by LOFAR overlaid in a pinkish hue. Euclid image credit: ESA/Euclid/Euclid Consortium/NASA, image processing by J.-C. Cuillandre (CEA Paris-Saclay), G. Anselmi, CC BY-SA 3.0 IGO. LOFAR image credit: R. J. van Weeren, processing by F. Sweijen.

A brief background: radio astronomy

First hints of cosmic radio signals came in the early 1930s. Karl Jansky, a telecommunications engineer at Bell Labs, was tasked with the investigation of noise on telephone lines. Understanding the origin of the noise could improve the quality of communications. Two sources of noise he managed to track down to thunderstorms close by or far away. A third source he could not recognise, however: a recurrent hiss, as he put it, that returned every day. He noticed that this hiss became stronger the closer he pointed his instrument to the Milky Way. Eventually he concluded that this interfering signal did not come from the Earth, but had an extraterrestrial origin. It took a long time for astronomers to take interest in it. A few years after Jansky's discovery, Grote Reber detected the signal with his own radio telescope and concluded that the theories of physics we had established so far were not sufficient to explain what Jansky and himself had observed. However, it wasn't until the connection to black holes and quasars was built over the 1950s and '60s before "radio astronomy" started to be considered an interesting and useful branch of astronomy.

From mirrors to antennas

Radio telescopes can look and operate quite different from telescopes built to receive visible light. The idea of a mirror still works and a dish is still often used to focus the incoming light, but it is no longer captured by a camera. Instead antennas are used to "receive" the signal, just like how you tune in to your favourite radio station. This signal creates a small electric current which is then recorded and processed into data that astronomers can ultimately use for science. Due to the long wavelengths of radio waves, the dish also does not need to be as perfect as an actual mirror. In the left photograph in Fig. 7.15 we see the Effelsberg radio telescope. It has a dish with a diameter 100 metres and is one of the largest fully steerable dishes in the world (only surpassed by the Greenbank Telescope which has a 100 m \times 110 m dish). You can see that the dish itself is hardly a mirror by normal standards, but for the radio waves it was built for it suffices. In fact, the dish hardly has to look like a proper dish at all for long wavelengths. The right photograph shows a number of telescopes that make up the *Giant Metrewave Radio Telescope* (GMRT) interferometer in India. They are more hole than dish, but are still perfectly fine for the wavelengths it observes at.

With the *LOW Frequency ARray* (LOFAR) in the Netherlands and across Europe the design has done away with dishes completely. The *International LOFAR Telescope*, as it is called in full, is formed by thousands of antennas on the ground that receive radio waves. Figure 7.16 shows two pictures of the LOFAR antennas with which the data used in this thesis was taken. The left photograph shows the centre of the "core", called the superterp. Two types of antennas can be seen here: the black tiles are the high-band antennas (HBAs) that can receive radio waves between 110 and 240 MHz. The grey/brown squares are the platforms on which the low-band antennas (LBAs) are located. In this thesis we have used data collected with the HBAs. On the right photograph the actual antennas can be seen in the styrofoam skeleton. These metal triangles are what do the actual receiving of radio waves.

Bigger is better: interferometry and a digital telescope

As time went on, astronomers built bigger and bigger telescopes. The reason for this is simple: a bigger telescope has a higher resolving power, meaning it can reveal smaller details in astronomical objects. At the same time longer wavelengths give a lower resolving power. Low frequency telescopes thus have an inherent need to be bigger, but at some point it becomes too impractical to keep increasing the size of a single dish.



Figure 7.15: *Left*: the 100 metre Effelsberg radio telescope in Germany. It is the world's largest fully steerable single-dish radio telescope. *Right*: three of the 30 total 45 metre dish telescopes of the Giant Metre-wave Radio Telescope (GMRT) interferometer in India. Image credit: dr.G.Schmitz (Effelsberg); NCRA-TIFR (GMRT).



Figure 7.16: *Left*: LOFAR's so-called superterp located in Exloo, Drenthe in The Netherlands. The black tiles are the HBA antennas. The gray squares are the platforms of the LBA antennas. *Right*: a close-up of one of the HBA tiles, revealing the actual antennas suspended in styrofoam. Image credit: LOFAR / ASTRON (left); B. Wolba (right).



Figure 7.17: Two examples of the large radio-emitting outflows from an AGN: 3C 31 (*left*) and Cygnus A (*right*). Credit: Volker Heesen and the LOFAR surveys team (*left*); NSF/NRAO/AUI/VLA (*right*).

The 100 m Effelsberg telescope is about as big as they come while remaining steerable. To overcome the issues of building huge single telescopes, multiple smaller telescopes or antennas can be combined to mimic a bigger one. This technique is called interferometry. The main advantage of this technique is that the detail we can see is no longer set by the size of a single telescope, but by how far apart we put them. This way, theoretically, the size of the Earth becomes the limit to how big we can make a telescope. For LOFAR this means we effectively have a radio telescope the size of Europe. This gives it the ability to see incredible detail at MHz radio frequencies.

Interferometers using dishes, like the GMRT shown earlier, can be physically pointed in a certain direction. LOFAR on the other hand has only antennas and no moving parts. “Pointing” LOFAR in a specific direction is more complicated than pointing a traditional telescope, as there are no lenses or mirrors to physically point with. Taking LOFAR as an example, if the telescope is observing eastwards, then an antenna in say Ireland will see a signal from that direction at a slightly later time than an antenna in Germany. We know where the antennas have been placed, so this small time difference can be calculated accurately. This makes LOFAR almost entirely a “software telescope”.

Galaxies, black holes and cosmic fountains

Our own Milky Way is but one of trillions of other galaxies in the Universe. Galaxies consist of stars, gas, dust and at their heart a supermassive black hole. When gas and dust gets too close to this black hole it starts to get eaten up. When this happens the central region of the galaxy, called the nucleus, is said to become active and turns into what we call an “active galactic nucleus”, or AGN. These AGNs have the ability to emit radio waves. They form the largest amount of radio-emitting objects in the sky. Powerful AGNs can also launch so-called jets: strong fountains of material being carried out of the galaxy’s nucleus. These jets travel outwards into space until they fade away, or create large bubble-like structures called lobes. An example of this is show in Figure 7.17. Studying aspects like the brightness, size and age of these radio lobes allows us to study how black holes and galaxies form and grow over the age of the Universe.

Colloquially the terms “radio galaxies” or “AGNs” are often used as a catch-all term, but they come

in all sorts of shapes and sizes. When the radio emission can be associated to a galaxy, we typically say radio galaxy. When the AGN is pointed towards us and we look down the barrel, we start calling them quasars due to their star-like, or “quasi stellar” appearance at optical wavelengths. Finally, depending on their brightness we divided them into radio “loud” and radio “quiet”. Quasars and radio galaxies with jets and large lobes fall under the radio loud category. While they may appear different, they may actually be the same. A popular theory is the so-called unification theory. This proposes that these are actually the same kind of AGN, but just seen from a different angle. This theory is still an active area of research. The radio quiet sources are faint and do not show clear jets or lobes, making them hard to distinguish from a normal galaxy where star formation also produces faint radio emission. The resolving power of the ILT is crucial for separating AGNs from star-forming galaxies. AGNs are compact and located in the centres of galaxies. Star-forming galaxies are extended and “fluffy”.

This thesis

In this thesis we combined technical aspects of low-frequency radio interferometry with scientific studies of AGNs, in order to study the low-frequency radio sky in unprecedented detail. This work is spread out across four chapters. Below we briefly summarise the work done in each.

Chapter 3

In the first scientific chapter we study the distant radio galaxy 4C 43.15. At a redshift of 2.429, the light from this galaxy was emitted when the Universe was only 2.7 billion years old. The expanding Universe has stretched the light emitted by it to longer wavelengths, making it crucial to make measurements at the low frequencies of LOFAR. At such distances, high resolving power is needed as well, in order to distinguish detailed structures from each other. By combining our data with data from the *Very Large Array*, we studied 4C 43.15 at multiple different wavelengths, which allowed us to create a spatial spectrum of the source. The main question of this work revolved around how “steep” its spectrum is and why. The steepness of the spectrum indicates how quickly the object becomes brighter or fainter changes when seen at different wavelengths. Steep means it changes rapidly. The conclusion of this work is that the spectra of objects like 4C 43.15 are steep, likely because of increased interaction of the material in the lobes with photons from the cosmic microwave background radiation.

Chapter 4

This chapter focuses on technical aspects surrounding the calibration of the ILT. Calibration is the process of turning the raw signals of the telescope into something useful for science. Turning that telescope data into an image afterwards is called “imaging”. In chapter 3 we worked with a single source, but the ILT sees an area of the sky of 25 full Moons in size all at once, with thousands of galaxies visible in it, so we would like to make one big image containing all of them. The main enemy of this process is the ionosphere: a layer of charged particles in Earth’s upper atmosphere. This ionosphere makes our images blurry. It is as if we are lying on the bottom of a swimming pool, trying to see clouds sharply through the waves. This chapter focussed on undoing the blurring by improving the calibration in different locations on the sky and finally to make one big image. This resulted in a 7 gigapixel image with a resolving power of $0.3''$; the biggest sub-arcsecond resolution low-frequency radio image at the time of writing.

Chapter 5

In this chapter we studied a sample of a particular type of sources: the so-called hyper luminous infrared galaxies (HLIRGs). As their name alludes to, these types of galaxies are extremely bright at infrared wavelengths. This radiation can have two origins: intense formation of new stars at a rapid pace or an AGN. If it would all come from star formation, the amount of them that has are detected is much higher than we can predict with theoretical models of how we think galaxies form. In this work we used high resolution radio observations to see if an AGN could be identified. We conclude that a third of the sources in the sample do contain an AGN. However, it is not enough to solve the difference with predictions made by models.

Chapter 6

The final scientific chapter of this thesis looks at the size of radio sources. By directly measuring the sizes of radio sources we can gain insight in, for example, their environment or how strong the jets launched by the AGN are. It also provides an input to simulations, such that realistic examples of what the radio sky looks like can be generated. In this study we extend size measurements to small sizes by exploiting the high resolution image of chapter 4. We find that brighter sources are larger than previous studies at gigahertz frequencies found them to be, which we conclude is due to the specific instruments used for those studies not being able to pick up the faint fuzzy structures that the ILT can.

Populairwetenschappelijke samenvatting

Het elektromagnetisch spectrum en een onzichtbaar heelal

Mensen hebben de nachtelijke hemel al voor duizenden jaren bestudeerd. Onder de vroegste sterrenkundige verslagen vinden we die van de Babyloniërs. Deze gaan terug tot honderden jaren voor de gangbare jaartelling. Hieruit kunnen we zien dat zij bijvoorbeeld al in staat waren om de beweging van de planeten over het hemelgewelf te volgen en te berekenen met behulp van geometrie. Praktisch gesproken kunnen we alleen bestuderen wat we kunnen zien. Voor het gros van de menselijke geschiedenis waren we dus beperkt tot onze ogen, maar zelfs daar kunnen we al veel mee zien. Het meest vanzelfsprekend zijn de talloze sterren verspreid over de hemel. Met wat geluk zou je zelfs de Melkweg kunnen zien als een wazige band, zoals te zien in Fig. 7.18. Om de Melkweg te kunnen zien heb je echter een donkere hemel nodig, welke moeilijk te vinden kan zijn in de moderne wereld door de enorme lichtvervuiling van alle lampen die wij 's nachts laten branden. Tussen de miljarden die wij kunnen zien zitten een paar die de oude Grieken “*πλάνητες*



Figure 7.18: De Melkweg zoals deze te zien is in Cerro Paranal, Chili. Deze foto is een panorama die gemaakt is door meerdere foto's met 2-minuten belichtingstijd, gemaakt met een spiegelreflexcamera, aan elkaar te rijgen. Bron: Bruno Gilli/ESO

ἀστέρες”, ofwel “dwalende sterren”, noemden. Gedurende het jaar verplaatsen deze sterren zich over de hemel. Hoewel ze met het blote oog op een andere ster lijken, onthult een kleine telescoop al dat het helemaal geen sterren zijn, maar andere planeten van ons zonnestelsel.

Galileo Galilei was de eerste die met een telescoop de nachtelijke hemel bestudeerde. Aan het begin van de jaren 1600 ontdekte hij niet alleen dat Jupiter geen ster was, maar dat deze planeet zijn eigen manen heeft. Later ontdekte Christiaan Huygens de grootste maan van Saturnus: Titan. Diep in de 18^e eeuw gebruikte Charles Messier een telescoop om de nu bekende “Messier objecten” te bestuderen. Dit zijn

een grote verscheidenheid van objecten zoals nevels, sterrenhopen en andere nabije sterrenstelsels. Toen de fotografische plaat en uiteindelijk de CCD camera uit werden gevonden konden we steeds zwakkere objecten gaan bestuderen. Maar, zelfs daarmee zien we nog maar het puntje van de ijsberg wat ons Heelal is.

Wanneer we aan “licht” denken dan denken we al snel aan licht van de zon, sterren, lampen, etc., maar er zijn vele andere vormen van licht. Het volledige bereik van golflengtes die licht kan hebben noemen we het “elektromagnetisch spectrum”. In Figuur 7.19 is een schematisch overzicht van verschillende types licht weergegeven, en of dat licht uit het Universum het aardoppervlak kan bereiken. Onze ogen zijn gevoelig voor licht met een golflengtes die grofweg tussen 380 nm en 750 nm vallen. Kortere golflengtes corresponderen met hogere energieën. Dit is ultraviolet (UV) licht, röntgenstraling en, bij de hoogste energieën, gammastraling. Deze worden (gelukkig) vrijwel allemaal geblokkeerd door de atmosfeer op een deel van de UV golflengtes na. Wanneer we naar langere golflengtes gaan krijgen we infrarode straling (“warmtestraling”), microgolflstraling en uiteindelijk radiostraling. Radiostralen bestrijken een golflengtegebied met golflengtes tussen enkele centimeters tot vele meters. Voor al deze golflengtes zijn er specifieke technieken nodig om ze te kunnen “zien”, of betere gezegd, te observeren. Bij nog langere golflengtes (buiten het diagram) houdt de ionosfeer alles weer tegen. Om de allerlangste radiogolflengtes te kunnen observeren moeten we dus weer naar de ruimte.

THE ELECTROMAGNETIC SPECTRUM

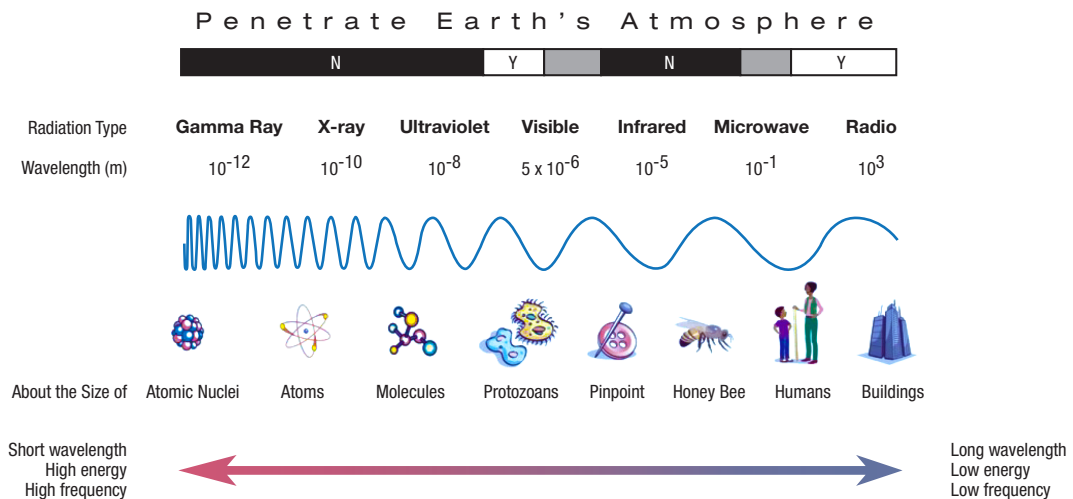


Figure 7.19: Een eenvoudig overzicht van het electromagnetische spectrum. De grijze balk bovenaan geeft grofweg aan welke soorten licht vanaf de aarde geobserveerd kunnen worden (wit), welke compleet geblokkeerd worden door de atmosfeer (zwart) of welke nog deels het oppervlak bereiken (grijs). Van links naar rechts wordt de golflengte langer, de frequentie lager en neemt de energie af. Bron: NASA.

Om het drastische verschil tussen zichtbaar licht en radiostraling te illustreren, zien we in Figuur 7.20 een vergelijking tussen de Perseus cluster van sterrenstelsels in zichtbaar licht en infrarood zoals geobserveerd met de recent gelanceerde Euclid satelliet, en 144 MHz radiostraling zoals LOFAR die waarneemt erover heen geleid in een roze tint. Als onze ogen enorme telescopen waren, dan zouden we het linker beeld zien:

een rijk veld van sterren en sterrenstelsels. Als onze ogen echter radioantennes zouden zijn, dan veranderd het beeld enorm en zouden we alleen de rozekleurige straling zien. Plots verdwijnen de sterren en sterrenstelsels en zien we een enorme bel van radio straling in de linker onderhoek rondom het central sterrenstelsel van de cluster. Bij een ander sterrenstelsel midden aan de bovenkant zien we grote pluimen verschijnen, en verspreid over de afbeelding zien we ook andere sterrenstelsels met pluimen.

Een korte achtergrond: radiosterrenkunde

Een voorproefje van kosmische radio signalen kwam in het begin van 1930. Karl Jansky werkte bij Bell Labs als een technicus voor telecommunicatie. Hier werd hem opgedragen om stoorzenders op de telefoonlijnen te onderzoeken. Als men begreep waar de storing vandaan kwam, kon er wellicht iets tegen worden gedaan. Hiervoor bouwde hij een grote antenne, waar hij uiteindelijk drie oorzaken mee wist te vinden. Twee daarvan bleken onweersbuien te zijn, zowel nabij als ver weg. De derde oorzaak werd niet herkend: een gesis, zoals hij het beschreef, wat elke dag terug kwam. Het viel op dat de sis sterker werd naarmate zijn metingen dichterbij de Melkweg werden gedaan. Uiteindelijk concludeerde hij hieruit dat dit signaal niet van de Aarde kwam, maar dat het een buitenaardse oorsprong had. Het zou vrij lang duren voordat de sterrenkundige gemeenschap er interesse in zou krijgen. Grote Reber detecteerde het signaal met zijn eigen telescoop een aantal jaar na Jansky. Hij ontdekte dat deze straling niet verklaard kon worden met de natuurkundige theorieën die we tot dusver kenden. Echter, radiosterrenkunde werd pas echt als een interessant en nuttig vakgebied binnen de sterrenkunde beschouwd toen tijdens de jaren 1950 en '60 de koppeling met zwarte gaten en quasars gemaakt werd.

Van spiegels naar antennes

Radio telescopen kunnen er heel anders uitzien dan telescopen om zichtbaar licht mee waar te nemen. Een schotel wordt nog steeds gebruikt om het licht te focussen, maar er hangt nu geen camera meer achter. In plaats daarvan, vangt een antenne het signaal op die het vervolgens in een elektrisch stroompje omzet welke gemeten en opgeslagen wordt. Hierna wordt het omgezet in iets waar sterrenkundigen wat mee kunnen. Door de lange golflengtes van radiogolven hoeft de schotel ook lang niet zo perfect te zijn als de spiegel in bijvoorbeeld je eigen badkamer. Op de linker foto in Fig. 7.21 staat de Effelsberg radio telescoop. Met een diameter van 100 meter is het een van de grootste volledig stuurbare radio telescopen ter wereld (alleen overtroffen door de Greenbank Telescope met een $100\text{ m} \times 110\text{ m}$ schotel). De schotel is verre van een spiegel per normale eisen, maar voor de radiogolven waarvoor geobserveerd wordt is het prima. De schotel hoeft niet eens op een schotel te lijken. Op de rechter foto staan een aantal telescopen van de *Giant Metrewave Radio Telescope* (GMRT) interferometer in India. Zoals te zien valt, is de schotel meer gat dan schotel, maar zolang de gaten klein zijn ten opzichte van de golflengte is het wederom geen probleem.

De *LOW Frequency ARray* (LOFAR) in Nederland en Europa gaat nog een stap verder en doet weg met het hele idee van een schotel. De *International LOFAR Telescope* (ILT), zoals hij in zijn geheel heet, bestaat uit duizenden antennes over heel Europa. In Fig. 7.22 zien we twee foto's van de LOFAR antennes, waarmee de data in deze thesis genomen is. De linker foto toont het centrum van de "kern" van LOFAR: de zogeheten superterp. Hierop zijn twee types antennes te zien. De zwarte dozen zijn de *high-band antennas* (HBA's) die radiogolven met een golflengte tussen 110 en 240 MHz kunnen ontvangen. De grijs-bruine vierkanten zijn de *low-band antennas* (LBA's), welke golven tussen 10 en 90 MHz waar kunnen nemen. In deze thesis hebben we data van de HBA's gebruikt. Een close-up van de daadwerkelijke antennes is te zien



Figure 7.20: Een blik op de Perseus cluster in zichtbaar licht en radio straling. *Links*: een combinatie van observaties bij zichtbaar licht en het nabije infrarood zoals geobserveerd door de Euclid satelliet. *Rechts*: dezelfde afbeelding, maar dan nu met een overlay van 144 MHz radio straling zoals LOFAR die observeert in roze. Euclid afbeelding bron: ESA/Euclid/Euclid Consortium/NASA, bewerkt door J.-C. Cuillandre (CEA Paris-Saclay), G. Anselmi, CC BY-SA 3.0 IGO. LOFAR afbeelding bron: R. J. van Weeren, bewerkt door F. Sweijen.



Figure 7.21: *Links*: de 100 meter Effelsberg radio telescoop in Duitsland. Het is 's werelds grootste volledig stuurbare radio telescoop. *Rechts*: drie van de in totaal 30 schotels van 45 meter diameter van de Giant Metrewave Radio Telescope (GMRT) interferometer in India. Bron: dr.G.Schmitz (Effelsberg); NCRA-TIFR (GMRT).

in de rechter foto van Fig. 7.22, overeind gehouden met een skelet van piepschuim. De metalen driehoeken zijn de antennes die de metingen doen. Piepschuim is doorzichtig voor de radiogolven en houden het signaal dus niet tegen.

Groot, groter, grootst: interferometrie met een digitale telescoop

Mettertijd gingen sterrenkundigen steeds grotere telescopen bouwen. De reden hiervoor is simpel: een grotere telescoop heeft een groter oplossend vermogen en kan dus meer detail in objecten aan de hemel zien. Tegelijkertijd schaal het oplossend vermogen omgekeerd met golflengte. Langere golflengtes zorgen voor een lager oplossend vermogen. Radio telescopen die bij lage frequenties observeren moeten dus van nature al groter zijn. Vanaf een bepaald punt wordt het simpelweg te onpraktisch, of zelfs onmogelijk, om een telescoop groter te maken en stuurbaar te houden. Die grens ligt ongeveer bij de 100 meter Effelsberg telescoop. Om dit probleem te overwinnen werd er een nieuwe techniek bedacht: interferometrie. Het idee hierachter is dat twee losse telescopen hetzelfde oplossend vermogen kunnen geven als één grote, met als groot voordeel dat die nu niet meer afhangt van hoe groot de telescopen zijn, maar van hoe ver ze uit elkaar staan. Technisch gezien is de limiet nu de grootte van de Aarde geworden. In het geval van LOFAR betekent dit dat we een telescoop zo groot als Europa hebben kunnen bouwen, zonder het hele continent onder een gigantische schotel te bedekken. Hierdoor heeft het een ongekend hoog oplossend vermogen op megahertz radio frequenties.

Waar telescopen met schotels, zoals de GMRT van eerder, nog fysiek een bepaalde richting op kunnen kijken, heeft LOFAR geen bewegende onderdelen. Het “richten” van de telescoop wordt dus lastiger aangezien er geen lenzen of spiegels zijn om ergens op of mee te richten. Dit richten gebeurt virtueel in de computer: het licht van een radiobron aan de oostelijke hemel komt bijvoorbeeld eerder aan bij een Duitse antenne dan bij een Ierse antenne. Omdat we precies weten waar de antennes staan, kan dit tijdsverschil nauwkeurig uitgerekend worden en kunnen we bepalen waar het signaal vandaan kwam. Dit digitale aspect maakt LOFAR bijna geheel een “software telescoop”.



Figure 7.22: *Links*: LOFARs zogeheten superterp in Exloo, Drenthe. De grijze tegels zijn de HBA antennes. De bruingrijze vlakken zijn de platformen waarop de LBA antennes staan. *Rechts*: een close-up van een HBA tegel waar de antennes te zien zijn, omhult door piepschuim. Bron: LOFAR / ASTRON (links); B. Wolba (rechts).

Sterrenstelsels, zwarte gaten en kosmische fonteinen

Onze Melkweg is maar een van miljarden sterrenstelsels in het Universum. Sterrenstelsels bestaan uit sterren, gas en stof, en hebben een superzwaar zwart gat in hun kern. Het zwarte gat kan stof en gas beginnen te veroveren wanneer het te dichtbij komt. Wanneer dit rap genoeg gebeurt en intens licht vrij begint te komen uit de kern zeggen we dat de kern actief is geworden. Het heet dan een “actieve galactische kern”, ofwel AGN. Deze AGNs kunnen radiostraling uitzenden en vormen het gros van de objecten die we bij radiogolven kunnen detecteren. Krachtige AGNs die bijzonder actief zijn kunnen grote straalstromen lanceren die materiaal ver het sterrenstelsel uit kunnen transporteren. Zij kunnen als een fontein materiaal de ruimte insproeien, of als een boor ver de ruimte in gaan en uiteindelijk grote bellen of “lobben” blazen. Twee voorbeelden hiervan zijn te zien in Fig. 7.23. Door verschillende eigenschappen van AGNs en hun lobben te bestuderen (zoals hun helderheid, grootte en leeftijd) kunnen we iets leren over hoe zwarte gaten zich ontwikkelen tijdens de groei van het Heelal, en hoe hun evolutie gerelateerd is aan die van sterrenstelsels.

De termen “radiosterrenstelsel” of “AGN” worden vaak als brede catch-all termen gebruikt, maar deze objecten komen in vele soorten en maten voor. Om het wat specifiekere te maken, spreken we van een radiosterrenstelsel wanneer de radiostraling te associëren is met een sterrenstelsel. Quasars (voluit quasi-stellar radio objects), daarentegen, danken hun naam aan het feit dat zij er bij zichtbaar licht als een heldere ster uitzien. Tot slot gebruiken we de helderheid ook nog om onderscheid te maken tussen zogeheten radio-luide en radio-stille objecten. Hoewel ze er vrij anders uit zien, is het mogelijk een pot nat. De “quasar unification theory”, ofwel de eenwording van radiosterrenstelsels en quasars, stelt voor dat dit dezelfde objecten zijn, maar dat wij ze gewoon onder een andere hoek zien: radiosterrenstelsels staan meer loodrecht op onze zichtlijn, waardoor we de straalstromen en lobben goed kunnen zien terwijl quasars meer naar ons toe gericht staan, waardoor we bijna recht de loop in kijken. Of deze theorie klopt wordt nog altijd onderzocht. De radio-stille objecten zijn veel minder helder en vertonen ook geen duidelijk, grote straalstromen of lobben. Dit maakt het moeilijk om ze te onderscheiden van normale stervormende sterrenstelsels. Het hoge oplossend vermogen van de ILT komt hierbij goed van pas: een AGN zal compact zijn en zich in het centrum van het sterrenstelsel bevinden. Een stervormend sterrenstelsel zal zich over een groter oppervlak verspreiden en “pluizig” zijn.

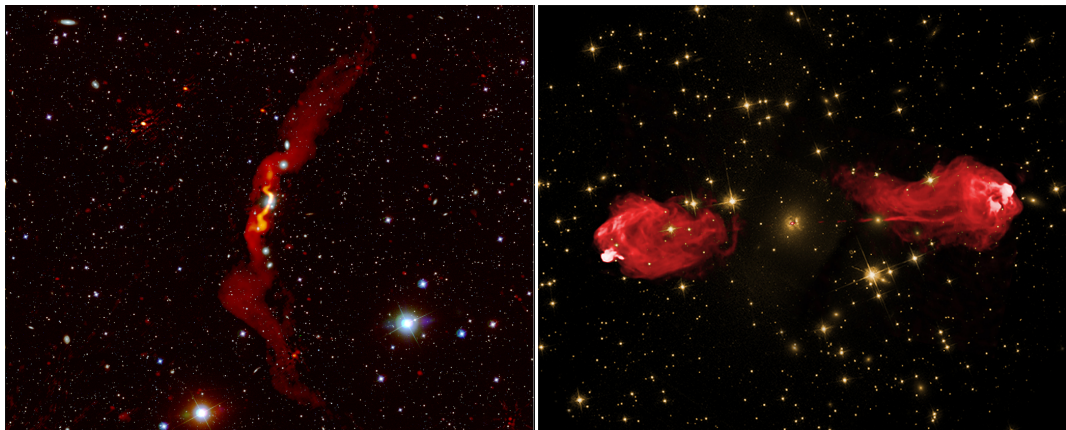


Figure 7.23: Twee voorbeelden van grote straalstromen uit een AGN, welke radiostraling uitzenden: 3C 31 (*links*) en Cygnus A (*rechts*). Bron: Volker Heesen en het LOFAR surveys team (*links*); NSF/NRAO/AUI/VLA (*rechts*).

Dit proefschrift

Dit proefschrift combineert het technische aspect van radiosterrenkunde op lage frequenties, met wetenschappelijke studies van AGNs. Het doel was om de lage-frequentie hemel op ongekend detail te verkennen. Dit werk bevat vier hoofdstukken, welke hieronder elk kort samengevat worden.

Hoofdstuk 3

In het eerste wetenschappelijke hoofdstuk bestuderen we het verwegstaande radiosterrenstelsel 4C 43.15. Op een roodverschuiving van 2,429 was het Heelal nog maar 2,7 miljard jaar oud toen het licht wat wij nu ontvangen uitgezonden werd. De lange golflengtes waarbij LOFAR observeert bevatten cruciale informatie, omdat de uitdijning van het Heelal de golflengte uitgerekt heeft. Op zulke afstanden is ook een hoog oplossend vermogen nodig om nog gedetailleerde structuren te kunnen zien. Door onze observaties te combineren met observaties gedaan met de *Very Large Array* hebben we 4C 43.15 op meerdere radiogolflengtes bestudeerd en zo een spectrum gemaakt. De hamvraag van dit werk was hoe “steil” het spectrum is en waarom. De steilheid van een spectrum vertelt je hoe snel het object helderder of zwakker wordt wanneer je van golflengte verandert: een steiler spectrum wordt sneller helderder naar langere golflengtes. De conclusie van dit werk is dat het steile spectrum van 4C 43.15 waarschijnlijk komt door verhoogde wisselwerking tussen het materiaal in de lobben en fotonen van de kosmische microgolf achtergrondstraling van de Oerknal.

Hoofdstuk 4

Dit hoofdstuk focust op de technische aspecten rondom de kalibratie van de ILT. Kalibratie is het proces om de ruwe data van de telescoop om te zetten in iets bruikbaar om wetenschap mee te doen. In hoofdstuk

3 werd er op één object gefocust. In dit hoofdstuk willen we het hele blikveld van de ILT, 25 volle manen groot, in kaart brengen. Hier staan duizenden sterrenstelsels in, dus was het doel om een grote afbeelding te maken in plaats van vele kleine. De grootste vijand in dit proces is de ionosfeer: een laag geladen deeltjes hoog in de atmosfeer van de aarde. Die zorgt ervoor dat onze afbeeldingen wazig worden. Een analogie hiervoor is alsof je vanaf de bodem van een zwembad de wolken boven je hoofd scherp probeert te zien. Met de techniek beschreven in dit hoofdstuk is er voor deze vervaging gecorrigeerd en hebben we een grote afbeelding kunnen maken. Het resultaat is een 7 gigapixel afbeelding met een oplossend vermogen van 0,3 boogseconden; de grootste sub-boogseconde resolutie lage-frequentie kaart tot nu toe.

Hoofdstuk 5

In dit hoofdstuk bestuderen we een monster van een specifiek type objecten: de *hyper luminous infrared galaxies* (HLIRGs). Deze objecten vertonen, zoals hun naam zegt, een enorm hoge lichtkracht in het infrarood. Dit kan door twee soorten activiteit aangedreven worden: intense stervorming of een AGN. Als alles door stervormingsactiviteit zou komen, dan observeren we een veel groter aantal dan we kunnen voorspellen met theorieën over hoe wij denken dat sterrenstelsels gevormd worden. Aan het eind van dit werk concluderen we dat een derde van het monster een AGN bevat. Echter is dit niet voldoende om de spanning met de voorspelling van de theorie op te lossen.

Hoofdstuk 6

Het laatste wetenschappelijke hoofdstuk van dit proefschrift kijkt naar de grootte van radiobronnen. Door deze direct te meten kunnen wij inzicht verkrijgen in, bijvoorbeeld, hun omgeving of hoe sterk de straalstromen van de AGN zijn. Dit kan weer als invoer dienen voor simulaties om zo een beter kunstmatige monsters van radiosterrenstelsels te kunnen genereren. Wij vinden dat heldere bronnen groter zijn dan voorheen gemeten. Dit kennen wij toe aan het feit dat de instrumenten die eerder gebruikt werden niet zo gevoelig als die ILT waren voor de zwakke pluizige structuren. In combinatie met dat de eerdere metingen ook nog bij hogere frequenties gedaan waren, heeft dit er waarschijnlijk toe geleid dat lobben als individuele bronnen werden geëvalueerd in plaats van als twee componenten van dezelfde bron.

List of publications

First-author publications

- Sweijen, F.**, R. J. van Weeren, H. J. A. Röttgering, L. K. Morabito, N. Jackson, A. R. Offringa, S. van der Tol, B. Veenboer, J. B. R. Oonk, P. N. Best, M. Bondi, T. W. Shimwell, C. Tasse, and A. P. Thomson (Jan. 2022a). “Deep Sub-Arcsecond Wide-Field Imaging of the Lockman Hole Field at 144 MHz”. In: *Nature Astronomy*, pp. 1–7. ISSN: 2397-3366. DOI: [10.1038/s41550-021-01573-z](https://doi.org/10.1038/s41550-021-01573-z). (Visited on 01/28/2022).
- Sweijen, F.**, L. K. Morabito, J. Harwood, R. J. van Weeren, H. J. A. Röttgering, J. R. Callingham, N. Jackson, G. Miley, and J. Moldon (Feb. 2022b). “High-Resolution International LOFAR Observations of 4C 43.15. Spectral Ages and Injection Indices in a High-z Radio Galaxy”. In: *Astronomy and Astrophysics* 658, A3. ISSN: 0004-6361. DOI: [10.1051/0004-6361/202039871](https://doi.org/10.1051/0004-6361/202039871). (Visited on 02/28/2024).
- Sweijen, F.**, Y. Lyu, L. Wang, F. Gao, H. J. A. Röttgering, R. J. van Weeren, L. K. Morabito, P. N. Best, K. Małek, W. Williams, I. Prandoni, M. Bonato, and M. Bondi (Mar. 2023). “Piercing the Dusty Veil of Hyper-Luminous Infrared Galaxies: Sub-arcsecond 144 MHz ILT Observations of HLIRGs in the Lockman Hole”. In: *Astronomy and Astrophysics* 671, A85. ISSN: 0004-6361. DOI: [10.1051/0004-6361/202244378](https://doi.org/10.1051/0004-6361/202244378). (Visited on 02/28/2024).

Contributing-author publications

- Bonnassieux, Etienne, **Frits Sweijen**, Marisa Brienza, Kamlesh Rajpurohit, Christopher John Riseley, Annalisa Bonafede, Neal Jackson, Leah K. Morabito, Gianfranco Brunetti, Jeremy Harwood, Alex Kappes, Huub J. Röttgering, Cyril Tasse, and Reinout van Weeren (Feb. 2022). “Spectral Analysis of Spatially Resolved 3C295 (Sub-Arcsecond Resolution) with the International LOFAR Telescope”. In: *Astronomy and Astrophysics* 658, A10. ISSN: 0004-6361. DOI: [10.1051/0004-6361/202141731](https://doi.org/10.1051/0004-6361/202141731). (Visited on 02/28/2024).
- Callingham, J. R., T. W. Shimwell, H. K. Vedantham, C. G. Bassa, S. P. O’Sullivan, T. W. H. Yiu, S. Bloor, P. N. Best, M. J. Hardcastle, M. Haverkorn, R. D. Kavanagh, L. Lamy, B. J. S. Pope, H. J. A. Röttgering, D. J. Schwarz, C. Tasse, R. J. van Weeren, G. J. White, P. Zarka, D. J. Bomans, A. Bonafede, M. Bonato, A. Botteon, M. Bruggen, K. T. Chyży, A. Drabent, K. L. Emig, A. J. Gloudemans, G. Gürkan, M. Hajduk, D. N. Hoang, M. Hoeft, M. Iacobelli, M. Kadler, M. Kunert-Bajraszewska, B. Mingo, L. K. Morabito, D. G. Nair, M. Pérez-Torres, T. P. Ray, C. J. Riseley, A. Rowlinson, A. Shulevski, **F. Sweijen**, R. Timmerman, M. Vaccari, and J. Zheng (Feb. 2023). “V-LoTSS: The Circularly Polarised LOFAR

- Two-metre Sky Survey”. In: *Astronomy and Astrophysics* 670, A124. ISSN: 0004-6361. DOI: [10. 1051/0004-6361/202245567](https://doi.org/10.1051/0004-6361/202245567). (Visited on 02/28/2024).
- Cordun, C. M., R. Timmerman, G. K. Miley, R. J. van Weeren, **F. Sweijen**, L. K. Morabito, and H. J. A. Röttgering (Aug. 2023). “VLBI Imaging of High-Redshift Galaxies and Protoclusters at Low Radio Frequencies with the International LOFAR Telescope”. In: *Astronomy and Astrophysics* 676, A29. ISSN: 0004-6361. DOI: [10. 1051/0004-6361/202346320](https://doi.org/10.1051/0004-6361/202346320). (Visited on 02/28/2024).
- Groeneveld, C., R. J. van Weeren, G. K. Miley, L. K. Morabito, F. de Gasperin, J. R. Callingham, **F. Sweijen**, M. Brügger, A. Botteon, A. Offringa, G. Brunetti, J. Moldon, M. Bondi, A. Kappes, and H. J. A. Röttgering (Feb. 2022). “Pushing Sub-Arcsecond Resolution Imaging down to 30 MHz with the Trans-European International LOFAR Telescope”. In: *Astronomy and Astrophysics* 658, A9. ISSN: 0004-6361. DOI: [10. 1051/0004-6361/202141352](https://doi.org/10.1051/0004-6361/202141352). (Visited on 02/28/2024).
- Harwood, J. J., S. Mooney, L. K. Morabito, J. Quinn, **F. Sweijen**, C. Groeneveld, E. Bonnassieux, A. Kappes, and J. Moldon (Feb. 2022). “The Resolved Jet of 3C 273 at 150 MHz. Sub-arcsecond Imaging with the LOFAR International Baselines”. In: *Astronomy and Astrophysics* 658, A8. ISSN: 0004-6361. DOI: [10. 1051/0004-6361/202141579](https://doi.org/10.1051/0004-6361/202141579). (Visited on 02/28/2024).
- Jackson, N., S. Badole, J. Morgan, R. Chhetri, K. Prūsīs, A. Nikolajevs, L. Morabito, M. Brentjens, **F. Sweijen**, M. Iacobelli, E. Orrù, J. Sluman, R. Blaauw, H. Mulder, P. van Dijk, S. Mooney, A. Deller, J. Moldon, J. R. Callingham, J. Harwood, M. Hardcastle, G. Heald, A. Drabent, J. P. McKean, A. Asgekar, I. M. Avruch, M. J. Bentum, A. Bonafede, W. N. Brouw, M. Brügger, H. R. Butcher, B. Ciardi, A. Coolen, A. Corstanje, S. Damstra, S. Duscha, J. Eislöffel, H. Falcke, M. Garrett, F. de Gasperin, J.-M. Griessmeier, A. W. Gunst, M. P. van Haarlem, M. Hoefl, A. J. van der Horst, E. Jütte, L. V. E. Koopmans, A. Krankowski, P. Maat, G. Mann, G. K. Miley, A. Nelles, M. Norden, M. Paas, V. N. Pandey, M. Pandey-Pommier, R. F. Pizzo, W. Reich, H. Rothkaehl, A. Rowlinson, M. Ruiter, A. Shulevski, D. J. Schwarz, O. Smirnov, M. Tagger, C. Vocks, R. J. van Weeren, R. Wijers, O. Wucknitz, P. Zarka, J. A. Zensus, and P. Zucca (Feb. 2022). “Sub-arcsecond imaging with the International LOFAR Telescope. II. Completion of the LOFAR Long-Baseline Calibrator Survey”. In: *A&A* 658, A2, A2. DOI: [10. 1051/0004-6361/202140756](https://doi.org/10.1051/0004-6361/202140756). arXiv: [2108.07284](https://arxiv.org/abs/2108.07284) [astro-ph.GA].
- Jurlin, N., R. Morganti, **F. Sweijen**, L. K. Morabito, M. Brienza, P. Barthel, and G. K. Miley (Feb. 2024). “Nuclear Regions as Seen with LOFAR International Baselines. A High-Resolution Study of the Recurrent Activity”. In: *Astronomy and Astrophysics* 682, A118. ISSN: 0004-6361. DOI: [10. 1051/0004-6361/202245821](https://doi.org/10.1051/0004-6361/202245821). (Visited on 02/28/2024).
- Kukreti, Pranav, Raffaella Morganti, Timothy W. Shimwell, Leah K. Morabito, Robert J. Beswick, Marisa Brienza, Martin J. Hardcastle, **Frits Sweijen**, Neal Jackson, George K. Miley, Javier Moldon, Tom Oosterloo, and Francesco de Gasperin (Feb. 2022). “Unmasking the History of 3C 293 with LOFAR Sub-Arcsecond Imaging”. In: *Astronomy and Astrophysics* 658, A6. ISSN: 0004-6361. DOI: [10. 1051/0004-6361/202140814](https://doi.org/10.1051/0004-6361/202140814). (Visited on 02/28/2024).
- Morabito, L. K., N. J. Jackson, S. Mooney, **F. Sweijen**, S. Badole, P. Kukreti, D. Venkattu, C. Groeneveld, A. Kappes, E. Bonnassieux, A. Drabent, M. Iacobelli, J. H. Croston, P. N. Best, M. Bondi, J. R. Callingham, J. E. Conway, A. T. Deller, M. J. Hardcastle, J. P. McKean, G. K. Miley, J. Moldon, H. J. A. Röttgering, C. Tasse, T. W. Shimwell, R. J. van Weeren, J. M. Anderson, A. Asgekar, I. M. Avruch, I. M. van Bemmell, M. J. Bentum, A. Bonafede, W. N. Brouw, H. R. Butcher, B. Ciardi, A. Corstanje, A. Coolen, S. Damstra, F. de Gasperin, S. Duscha, J. Eislöffel, D. Engels, H. Falcke, M. A. Garrett, J. Griessmeier, A. W. Gunst, M. P. van Haarlem, M. Hoefl, A. J. van der Horst, E. Jütte, M. Kadler, L. V. E. Koopmans, A. Krankowski, G. Mann, A. Nelles, J. B. R. Oonk, E. Orru, H. Paas, V. N. Pandey, R. F. Pizzo, M. Pandey-Pommier, W. Reich, H. Rothkaehl, M. Ruiter, D. J. Schwarz, A. Shulevski, M.

-
- Soida, M. Tagger, C. Vocks, R. A. M. J. Wijers, S. J. Wijnholds, O. Wucknitz, P. Zarka, and P. Zucca (Feb. 2022). “Sub-arcsecond imaging with the International LOFAR Telescope. I. Foundational calibration strategy and pipeline”. In: *A&A* 658, A1, A1. doi: [10.1051/0004-6361/202140649](https://doi.org/10.1051/0004-6361/202140649). arXiv: [2108.07283](https://arxiv.org/abs/2108.07283) [[astro-ph](https://arxiv.org/archive/ph). [IM](https://arxiv.org/archive/ph)].
- Morabito, Leah K, F Sweijen, J F Radcliffe, P N Best, Rohit Kondapally, Marco Bondi, Matteo Bonato, K J Duncan, Isabella Prandoni, T W Shimwell, W L Williams, R J van Weeren, J E Conway, and G Calistro Rivera (Oct. 2022). “Identifying Active Galactic Nuclei via Brightness Temperature with Sub-Arcsecond International LOFAR Telescope Observations”. In: *Monthly Notices of the Royal Astronomical Society* 515.4, pp. 5758–5774. ISSN: 0035-8711. doi: [10.1093/mnras/stac2129](https://doi.org/10.1093/mnras/stac2129). (Visited on 10/10/2022).
- Shimwell, T. W., M. J. Hardcastle, C. Tasse, P. N. Best, H. J. A. Röttgering, W. L. Williams, A. Botteon, A. Drabent, A. Mechev, A. Shulevski, R. J. van Weeren, L. Bester, M. Brügger, G. Brunetti, J. R. Callingham, K. T. Chyży, J. E. Conway, T. J. Dijkema, K. Duncan, F. de Gasperin, C. L. Hale, M. Haverkorn, B. Hugo, N. Jackson, M. Mevius, G. K. Miley, L. K. Morabito, R. Morganti, A. Offringa, J. B. R. Oonk, D. Rafferty, J. Sabater, D. J. B. Smith, D. J. Schwarz, O. Smirnov, S. P. O’Sullivan, H. Vedantham, G. J. White, J. G. Albert, L. Alegre, B. Asabere, D. J. Bacon, A. Bonafede, E. Bonnassieux, M. Brienza, M. Bilicki, M. Bonato, G. Calistro Rivera, R. Cassano, R. Cochrane, J. H. Croston, V. Cuciti, D. Dallacasa, A. Danezi, R. J. Dettmar, G. Di Gennaro, H. W. Edler, T. A. Enßlin, K. L. Emig, T. M. O. Franzen, C. García-Vergara, Y. G. Grange, G. Gürkan, M. Hajduk, G. Heald, V. Heesen, D. N. Hoang, M. Hoeft, C. Horellou, M. Iacobelli, M. Jamrozy, V. Jelić, R. Kondapally, P. Kukreti, M. Kunert-Bajraszewska, M. Magliocchetti, V. Mahatma, K. Małek, S. Mandal, F. Massaro, Z. Meyer-Zhao, B. Mingo, R. I. J. Mostert, D. G. Nair, S. J. Nakoneczny, B. Nikiel-Wroczyński, E. Orrú, U. Pajdosz-Śmierciak, T. Pasini, I. Prandoni, H. E. van Piggelen, K. Rajpurohit, E. Retana-Montenegro, C. J. Riseley, A. Rowlinson, A. Saxena, C. Schrijvers, **F. Sweijen**, T. M. Siewert, R. Timmerman, M. Vaccari, J. Vink, J. L. West, A. Wołowska, X. Zhang, and J. Zheng (Mar. 2022). “The LOFAR Two-metre Sky Survey - V. Second Data Release”. In: *Astronomy & Astrophysics* 659, A1. ISSN: 0004-6361, 1432-0746. doi: [10.1051/0004-6361/202142484](https://doi.org/10.1051/0004-6361/202142484). (Visited on 06/30/2023).
- Timmerman, R., R. J. van Weeren, A. Botteon, H. J. A. Röttgering, B. R. McNamara, **F. Sweijen**, L. Birzan, and L. K. Morabito (Dec. 2022a). “Measuring Cavity Powers of Active Galactic Nuclei in Clusters Using a Hybrid X-ray-radio Method. A New Window on Feedback Opened by Subarcsecond LOFAR-VLBI Observations”. In: *Astronomy and Astrophysics* 668, A65. ISSN: 0004-6361. doi: [10.1051/0004-6361/202243936](https://doi.org/10.1051/0004-6361/202243936). (Visited on 02/28/2024).
- Timmerman, R., R. J. van Weeren, J. R. Callingham, W. D. Cotton, R. Perley, L. K. Morabito, N. A. B. Gizani, A. H. Bridle, C. P. O’Dea, S. A. Baum, G. R. Tremblay, P. Kharb, N. E. Kassim, H. J. A. Röttgering, A. Botteon, **F. Sweijen**, C. Tasse, M. Brügger, J. Moldon, T. Shimwell, and G. Brunetti (Feb. 2022b). “Origin of the Ring Structures in Hercules A. Sub-arcsecond 144 MHz to 7 GHz Observations”. In: *Astronomy and Astrophysics* 658, A5. ISSN: 0004-6361. doi: [10.1051/0004-6361/202140880](https://doi.org/10.1051/0004-6361/202140880). (Visited on 02/28/2024).

Curriculum Vitae

I was born on November 14, 1994 in the Frisian village Drachten⁶. After primary school, I went to high school at the CSG Liudger, where I followed the VWO (Gymnasium). In the final year we had to choose the university track we were going to follow. This is the point where I am supposed to say I finally got to pursue my life-long dream of becoming an astronomer... except that would be a lie. As a child I was convinced my career would be a surgeon, always enjoying episodes of “Ingang Oost”; a Dutch TV show following happenings in the emergency room of various hospitals. In high school my interests moved more towards the physical sciences. A big driver for this were a great teacher for chemistry, whose name I do not remember at the time of writing, and my physics teacher Mr. Couperus, who always had time after school to show some more fun experiments. Throughout high school I was reasonably convinced I would pick something in the direction of chemistry. When the list of available studies came in, however, I saw astronomy on there. On a whim I decided that I was going to study astronomy; because why not?

My university studies took me to the next province over: Groningen. I started my three-year BSc. Astronomy at the *Rijksuniversiteit Groningen* (RUG; University of Groningen) there in 2012. In my first year I did follow an optional chemistry course “just in case”, but alas here I am writing my astronomy thesis. At the end of the three years I teamed up with three other fellow students for a bachelor research project with dr. John McKean. It was a practically oriented radio-astronomy project with an ambitious scope: build a radio telescope and measure the temperature of the CMB. In true experimental fashion we made the ground-breaking finding of the CMB actually having a sub-zero absolute temperature... Suffice to say accounting for all instrumental effects is not straightforward. In 2015 I started the two-year MSc. Astronomy. My first foray into radio astronomy had peaked my interest, so for the research project in the final year I once again ended up with John, but this time for a more data-oriented project involving observations from the *Very Large Array*. This is where I realised my love for programming and data reduction problems.

On the quest for a PhD, I saw a position advertised at Leiden observatory by prof. Huub Röttgering, dubbed “Exquisite LOFAR Images to Study the Distant Universe”, which caught my attention. It felt like a natural continuation of my interest in radio astronomy. Under the supervision of both Huub and dr. Reinout van Weeren, I started this PhD in 2017 where we worked on calibration of and imaging with LOFAR’s international stations to produce detailed images of the 144 MHz radio sky. Near the end of 2022 I joined the *Netherlands Institute of Radio Astronomy* (ASTRON) as a part-time software developer, while in the mean time finishing up my PhD. Starting April 2024 I will be joining dr. Leah Morabito in Durham as a postdoc, once again continuing along the line of high-resolution imaging with LOFAR.

⁶Although it can be called a city by modern means, it never obtained borough rights and thus failed to become one of “the eleven cities”.

Acknowledgements

Acknowledgements; probably the hardest chapter of this work. What do you say? Who do you thank first? Have you forgotten anybody? We may never know, but here it goes.

Firstly, a word of thanks has to be given to my supervisors, despite hearing through the grapevine that one shouldn't. Huub, you are quite the character. I remember your phone call to tell me you would like to offer me the position, where (if memory serves me right) you were in a bit of a hurry, because you were about to board the SOFIA observatory. The sky was also the limit for the aspirations we wrote in our *Education and Supervision Plan* that we ambitiously drafted at the start which we in hindsight could not possibly have met. You gave me plenty of freedom, probably too much, but that did allow me to follow my interests. Reinout, your technical insight and know-how were invaluable to the success of the works in this thesis. I don't think we have ever had a regularly scheduled meeting, because you always made time for a "quick" question about a problem or radio astronomical concept even though they often did not end up being all that quick.

Alright, on to the most dangerous part. Patrick, thank you for introducing me to some DnD together with Hiddo, Kirsty, Niloo, Omar and Sanjana. It was fun learning about it and we had some good times. Erik: we will always have Sfinx. Thank you for introducing me to kapsalon. I don't know how I managed to live without it until now. Martijn and Rafaël: we had some great dinners together. Jurjen and Roland: what can I say, ABBA is not the only dancing queen. I also need to thank the many people in or around the Leiden LOFAR group over the years both at work and outside of that — Alex, Andrea, Anniek, Christian, Duy, Gabriella, George, HaoYang, Huib, Ian, Jit, Joe, Josh, Ken, Kim, Maolin, Maria, Raymond, Sai, Tong, Sarah, Xuechen, Wendy and many students — for contributing to a vibrant atmosphere. Yipeng, I hope your career is going well. The results of your MSc project that I helped supervised led to the paper in Chapter 5.

Then I should mention the people in the VLBI working group: Emmy, thank you for introducing us the phenomenon that is Nando's, and together with James showing us the Durham night life; and thank you Alex, Deepika, Etienne, James, Jonny, Leah, Marco, Matthijs, Neal all for making the busyweeks fun and interesting. This extends, of course, to the wider LOFAR collaboration as well: Cyril, thank you for showing us Paris; Marco, I'm glad I got an Italian to try pizza Hawaii; Bohan, Corey, Francesco, Nika, Pranav, Rohit, Vijay and many others I have met along the way, you have all contributed to the experience one way or another.

Of course I should not forget the people at Leiden observatory: Andrés, Bas, Dario, Dilovan, Evgenii, Fraser, Gijs, Ivana, Jeroen, Josh, Jelle (surviving the "LOFAR office" was not easy), Jeroen, Joey, Lýdia, Mantas, Marta, Martijn, Matus, Mihal, Nicco, Piyush, Roi, Stella, Stijn, Thijs, Thomas, Turgay, Willeke (the resident pastry chef; I will miss your cakes dearly). You all contributed to a bustling atmosphere, always ready to finish the same puzzle for the however many-th time. If you are not in this list, don't take it personally. There are just too many of you. Big Dipper, thank you for dutifully organising the vrijmibo's. Finally I thank the right coffee machine for making the better coffee.